ENHANCED LIFE PREDICTION TECHNOLOGY FOR ENGINE ROTOR LIFE EXTENSION (ERLE)

Stephen J. Hudak, Jr., Michael P. Enright, R. Craig McClung, Luc J. Huyse, Harry Millwater, Tom Conquest, Ana Del Amo, and Simeon Fitch

Southwest Research Institute

SEPTEMBER 2008
Final Report

THIS IS A DUAL USE SCIENCE AND TECHNOLOGY (DUST) PROGRAM REPORT.

STINFO COPY

AIR FORCE RESEARCH LABORATORY
MATERIALS AND MANUFACTURING DIRECTORATE
WRIGHT-PATTERSON AIR FORCE BASE, OH 45433-7750
AIR FORCE MATERIEL COMMAND
UNITED STATES AIR FORCE

NOTICE AND SIGNATURE PAGE

Using Government drawings, specifications, or other data included in this document for any purpose other than Government procurement does not in any way obligate the U.S. Government. The fact that the Government formulated or supplied the drawings, specifications, or other data does not license the holder or any other person or corporation; or convey any rights or permission to manufacture, use, or sell any patented invention that may relate to them.

This report was cleared for public release by the Wright-Patterson Air Force Base (WPAFB) Public Affairs Office and is available to the general public, including foreign nationals. Copies may be obtained from the Defense Technical Information Center (DTIC) (http://www.dtic.mil).

AFRL-RZ-WP-TR-2008-4287 HAS BEEN REVIEWED AND IS APPROVED FOR PUBLICATION IN ACCORDANCE WITH THE ASSIGNED DISTRIBUTION STATEMENT.

This report is published in the interest of scientific and technical information exchange, and its publication does not constitute the Government's approval or disapproval of its ideas or findings.

*Disseminated copies will show "//signature//" stamped or typed above the signature blocks.

1. **REPORT DATE** *(DD-MM-YY)*	2. **REPORT TYPE**	3. **DATES COVERED** *(From - To)*
September 2008	Final	08 June 2003 – 31 March 2008

4. **TITLE AND SUBTITLE**	5a. **CONTRACT NUMBER**
ENHANCED LIFE PREDICTION TECHNOLOGY FOR ENGINE ROTOR LIFE EXTENSION (ERLE)	F33615-03-2-5203
	5b. **GRANT NUMBER**
	5c. **PROGRAM ELEMENT NUMBER** 62102F

6. **AUTHOR(S)**	
Stephen J. Hudak, Jr., Michael P. Enright, R. Craig McClung, and Luc J. Huyse (Southwest Research Institute)	5d. **PROJECT NUMBER** 4347
Harry Millwater (University of Texas at San Antonio)	5e. **TASK NUMBER** 27
Tom Conquest and Ana Del Amo (GE Aviation Systems) Simeon Fitch (Mustard Seed Software)	5f. **WORK UNIT NUMBER** 43472702

7. **PERFORMING ORGANIZATION NAME(S) AND ADDRESS(ES)**		8. **PERFORMING ORGANIZATION REPORT NUMBER**
Southwest Research Institute 6220 Culebra Road San Antonio, TX 78238-5166	- University of Texas at San Antonio - GE Aviation Systems - Mustard Seed Software	

9. **SPONSORING/MONITORING AGENCY NAME(S) AND ADDRESS(ES)**	10. **SPONSORING/MONITORING AGENCY ACRONYM(S)**
Air Force Research Laboratory Materials and Manufacturing Directorate Wright-Patterson Air Force Base, OH 45433-7750 Air Force Materiel Command United States Air Force	AFRL/RXLM
	11. **SPONSORING/MONITORING AGENCY REPORT NUMBER(S)** AFRL-RX-WP-TR-2008-4287

12. **DISTRIBUTION/AVAILABILITY STATEMENT**
Approved for public release; distribution unlimited.

13. **SUPPLEMENTARY NOTES**
PAO case number 88ABW 2008-0475, cleared 10 October 2008. This is a Dual Use Science and Technology (DUST) Program Report. Report contains color.

14. **ABSTRACT**
The Air Force Research Laboratory (AFRL) conceived of the Engine Rotor Life Extension (ERLE) program as a sound science and technology investment that offers the potential for significant cost avoidance. The strategy for meeting this goal is to extend the life of certain life-limiting components, without increasing risk, by systematically improving, and more effectively integrating, a number of life management technologies -- life prediction, nondestructive inspection, engine health monitoring, maintenance, and repair. The current program has developed physics-based, deterministic and probabilistic, fatigue life prediction models that support the objectives of ERLE, as well as the broader goals of Condition Based Maintenance Plus (CBM+). The new models incorporate small crack effects and enable enhanced fracture mechanics analysis of high stress radients associated with residual contact and thermal stresses. The importance of uncertainty in mission usage is highlighted, and a statistical method to automatically identify mission type from usage data is introduced. Probabilistic simulations incorporating input from an embedded sensor model are used to demonstrate the effectiveness of engine health monitoring. Mature technology from the program has been incorporated into the DARWIN probabilistic life prediction code to facilitate technology transfer to AFRL and the turbine engine community.

15. **SUBJECT TERMS**
turbine engine, fatigue, crack growth, probabilistic analysis, life prediction, life extension, diagnostics, prognostics, sensor input, usage, missions, CBM+

16. **SECURITY CLASSIFICATION OF:**			17. **LIMITATION OF ABSTRACT:**	18. **NUMBER OF PAGES**	19a. **NAME OF RESPONSIBLE PERSON** (Monitor)
a. **REPORT** Unclassified	b. **ABSTRACT** Unclassified	c. **THIS PAGE** Unclassified	SAR	172	Patrick J. Golden 19b. **TELEPHONE NUMBER** *(Include Area Code)* N/A

i

Table of Contents

Table of Contents (Continued)

Table of Contents (Concluded)

Section   **Page**

List of Figures

List of Figures (Continued)

List of Figures (Continued)

List of Figures (Continued)

List of Figures (Continued)

List of Figures (Concluded)

List of Tables

Acknowledgements

1.   Summary

The United States Air Force (USAF) is facing a potentially large wave of turbine engine disc replacement costs over the next eight to ten years that are inconsistent with anticipated budgets. Consequently, the Engine Rotor Life Extension (ERLE) program was conceived by the AFRL as a sound science and technology investment that offers the potential for significant cost-avoidance by extending the life of certain life-limiting components. The concept is to extend the life of these components by recovering the conservatism believed to exist in current design and life management practices, without increasing risk, by systematically improving and more effectively integrating a number of life management technologies—life prediction, non-destructive inspection, engine health monitoring, maintenance and repair. Enhancements in engine life management technology would also be applicable to developmental and future military engines, commercial engines, and land-based combustion turbines where safety, reliability, and cost of ownership are of paramount importance. SwRI had lead a team with unique capabilities to enhance, as well as integrate, several of the above life management technologies. Other team members include Smiths Aerospace, The University of Texas at San Antonio, and Mustard Seed Software.

The general approach and technical objectives of this program were to: 1) develop and validate a new family of physically-based, deterministic life prediction models for treating total fatigue life including crack nucleation, microcrack growth and large crack growth; 2) develop and demonstrate an efficient probabilistic life prediction methodology based on the stochastic nature of each of the above phases of fatigue life; and 3) explore methods for enhanced engine life management based on hybridisation of state-of-the-art probabilistic life prediction and classical engine health monitoring.

The program has developed and validated a new deterministic fatigue crack nucleation and growth (FaNG) model. Model predictions were found to be in good agreement with measured fatigue lives for notched Ti-6Al-4V specimens over a wide range of loading conditions. The effectiveness of the FaNG model has been demonstrated by predicting the beneficial effect of residual stresses introduced by shot peening and low plasticity burnishing on enhancing fatigue life. Methods have also been developed and implemented to perform probabilistic sensitivity analyses to rank the impact of key random variables on component reliability. Probabilistic tools were also developed to automatically identify missions from engine usage data from aircraft flight data recorders, as well as use this information in combination with the newly developed fatigue models to forecast future damage resulting from changes in the mission planning. Probabilistic modelling using Bayesian updating has also been used to quantify the potential benefits of fusing information from on-board health monitoring of turbine engine discs. This analysis fuses data from probabilistic FaNG model predictions and continual input from a crack detection sensor to forecast current and future probability of failure.

To facilitate technology transfer to the U.S. Air Force and turbine engine community, the above-mentioned developments that were judged to be sufficiently mature and adequately

validated were added to the commercial computer code Design Assessment of Reliability With INspection (DARWIN®) which is available royalty-free to the government and through commercial licensing to industry; these methods, which are accessible through the user friendly Graphical User Interface (GUI), include: FaNG model; FaNG residual stress analysis for surface cracks; enhanced mission mixing, and probabilistic sensitivities

2.   Introduction

2.1   Background

The USAF is facing a significant wave of turbine engine disc replacement costs in the next eight to ten years that are inconsistent with anticipated budgets. Consequently, the ERLE program was conceived by the AFRL as a sound science and technology investment that offers the potential for significant cost-avoidance by extending the life of certain life-limiting components. The concept is to extend the life of these components by recovering the conservatism believed to exist in current design and life management practices, without increasing risk, by systematically improving and more effectively integrating a number of life management technologies—life prediction, non-destructive inspection, engine health monitoring, maintenance and repair.

The current DUST program was focused on developing enhanced deterministic and probabilistic methods for predicting remaining life and component reliability; the program also addressed various probabilistic methods for enhancing engine health monitoring and prognosis.

2.2   Program Objectives

The overall technical objectives of the program were to develop and demonstrate: 1) a new family of physically-based, deterministic life prediction models for treating total fatigue life including crack nucleation, microcrack growth and large crack growth; 2) an efficient probabilistic life prediction methodology based on the differing stochastic nature of each of the above phases of fatigue life; and 3) an integrated methodology for enhanced engine life management based on combining and hybridizing state-of-the-art probabilistic life prediction and classical engine diagnostics and prognostics.

The specific life prediction enhancements pursued in the current program, and outlined below, were selected from candidate tasks that were judged to be both technically feasible and consistent with the goals of the ERLE program as identified in a prior study performed for AFRL by SwRI [1].

2.3   Methods, Assumptions, and Procedures

The program was organized into three distinct but interrelated technical tasks each of which was aimed at achieving one of the above three program objectives. The three tasks were as follows:

Task 1: Enhanced Deterministic Life Modelling: This task developed physically-based models of crack nucleation, microcrack growth and large crack growth phases of the fatigue process. These models were validated by applying them to the prediction of fatigue damage at high stress gradients including those that can occur at notches induced by foreign object damage (FOD), and well as residual stresses resulting from beneficial

3

surface treatments. The newly developed models were validated by comparing predicted lives against available laboratory test data. Computational simulations were also performed to demonstrate the benefits of tracking fatigue damage based on actual usage from flight data recorders versus the use of Total Accumulated Cycles (TAC(s)) to track damage and manage inspection and maintenance decisions. See Section 3.0 for further details.

Task 2: Enhanced Probabilistic Life Modelling: This task utilized the deterministic models from Task 1 to formulate and implement a fully-probabilistic approach to total fatigue life considering the stochastic nature of crack nucleation, microcrack growth and large crack growth. Statistical methods were also developed for identifying mission types, characterizing usage, and forecasting the effect of mission mixing changes on remaining life. Computationally efficient probabilistic methods were also developed and implemented for computing the effect of the above factors on component reliability so that inspection, maintenance, and retirement decisions can be made on a reliability basis. See Section 4.0 for further details.

Task 3: Integration of Damage-Based Probabilistic Methods with Diagnostic and Prognostics Methods: This task attempted to fuse the newly developed physics-based probabilistic life prediction methods in Task 2 with classical diagnostic and prognostic methods. The goal was to enhance the engine health management process by combining the rigor and accuracy of the damage-based life prediction methods with the broader system perspective and overall efficiency of classical health monitoring techniques based on artificial intelligence, neural networks, and Bayesian updating. Bayesian updating was employed to demonstrate the benefits of on-board monitoring of fatigue damage on component reliability. Limitations were encountered in attempting to hybridize classical data driven methods of diagnostics and prognostics with physics-based methods and barriers to this hybridization are discussed. See Section 4.7 for further details.

2.4   Program Team

A diverse and highly qualified team was assembled to address the technical challenges of the proposed program. The program team was led and managed by Southwest Research Institute, who served as prime contractor. Team members included the University of Texas at San Antonio (UTSA), Smiths Aerospace, and Mustard Seed Software. This team provided expertise in fundamental understanding of fatigue damage processes in turbine engine materials (SwRI); development and implementation of deterministic and probabilistic life prediction methods (SwRI and UTSA); ongoing working relationships with the major domestic and foreign engine manufacturers (SwRI and Smiths); expertise in flight data recording and engine health monitoring using on-line data acquisition, data fusion, and advanced reasoning methods (Smiths); and development of commercially successful engineering software tools for industry (SwRI, Smiths, and Mustard Seed Software).

2.5   Dual-Use Benefits and Technology Transfer

The proposed program directly addresses several of the technologies crucial to the ERLE goal of doubling the useful life of military engines. Studies by the USAF and engine manufacturers have estimated that successful science and technology investments of this type could reduce the disk replacement costs by 50%, which would amount to a cost savings of $600M over five years. In addition, enhancements in engine life management technology would also be applicable to developmental and future engines. This is particularly true of the hybridization of life prediction and health monitoring since new engines tend to contain more sensors with advanced sensing capability.

Similar benefits would be expected to accrue in the commercial sector, where safety, reliability, and cost of ownership are of paramount importance for the turbine engines that power commercial airliners. In fact, safety of flight was the primary driving force for Federal Aviation Administration (FAA) and industry support of the Turbine Rotor Material Design (TRMD) program, which led to the initial development and commercialization of DARWIN. The technologies and associated software developed in the current program are also expected to penetrate the power generation industry where availability and cost of ownership are high priorities, particularly in the deregulated market.

Technology demonstration and transfer of the enhanced probabilistic life prediction methodologies developed in the current program were achieved by integrating selected new methodologies as capabilities in SwRI's DARWIN code, which is available to government agencies under a royalty-free license, as well as to turbine engine and power generation communities under commercial licensing.

3. Results and Discussion on Enhanced Probabilistic Life Modeling

The primary objective of this task was to develop and demonstrate a new family of advanced deterministic life prediction methods for total fatigue. These methods would be guided by physical mechanisms and insights, and they would be capable of treating the various phases of fatigue life including crack nucleation, small-crack growth, and large-crack growth. They would also be amenable to practical engineering use and statistical treatment. Once these models were developed, they would be implemented in a suitable computational platform, calibrated with available baseline test data, and then demonstrated by comparison with available feature test data. These goals have all been met, as described in the pages that follow.

3.1 Development of Fatigue Nucleation and Growth (FaNG) Model

The traditional paradigm for fatigue life prediction modeling applied to engine rotors is summarized in Figure 1. So-called "crack initiation" analysis is based on strain-life or stress-life methods and is often calibrated by total fatigue life results on small cylindrical specimens. The end of the crack initiation life phase is commonly assumed to correspond to the formation of an 0.030" surface crack. In order to account for normal material scatter, lower bound design curves (perhaps corresponding to 0.001 failure rates) are constructed through statistical analysis of the available smooth specimen data.

In many cases, the end of the crack initiation phase is assumed to represent the end of the useful life of the component. However, in some situations, there is a desire to account for at least some fraction of the useful remaining life of the cracked part following the initiation event. This is typically accomplished with an independent fatigue crack growth life computation that starts with a 0.015" x 0.030" surface crack and ends at fracture. The two analyses share geometry and stress history information and some material properties, although the primary materials databases that support the independent "initiation" and "growth" calculations are themselves usually largely independent.

In this work, a new paradigm has been defined for the development of new life models. The paradigm is the simple summation of crack nucleation and crack propagation life phases, with the transition occurring at a physically meaningful crack nucleation size. The paradigm can be applied to empirical models, micromechanical models, or physically-informed engineering models. The new paradigm is illustrated generally in Figure 2. Here history information may include stress, strain, and temperature; and material information may include both traditional empirical mechanical properties and microstructural information. The three crack growth regimes shown may reduce to two regimes or even one regime for certain problems. The initial crack size may be random (e.g., defined in terms of a random microstructure), fixed, or dependent on the nucleation and/or growth models. Typically the initial crack size will be much smaller than the traditional 0.030" flaw often used at the start of a conventional damage tolerance analysis.
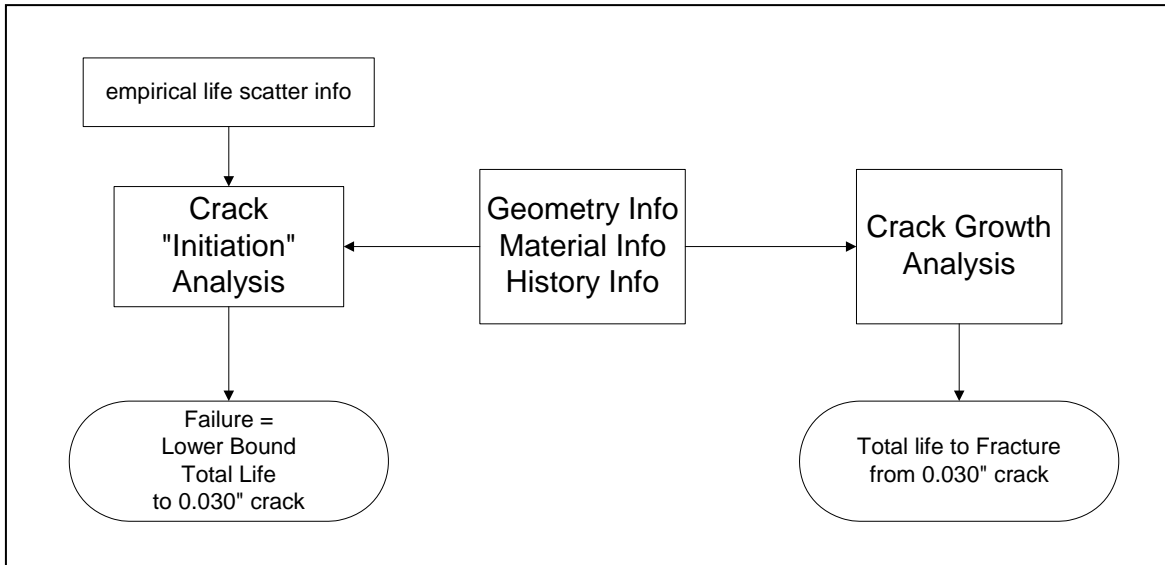
Figure 1. Traditional Paradigm for Engine Rotor Fatigue Life Prediction
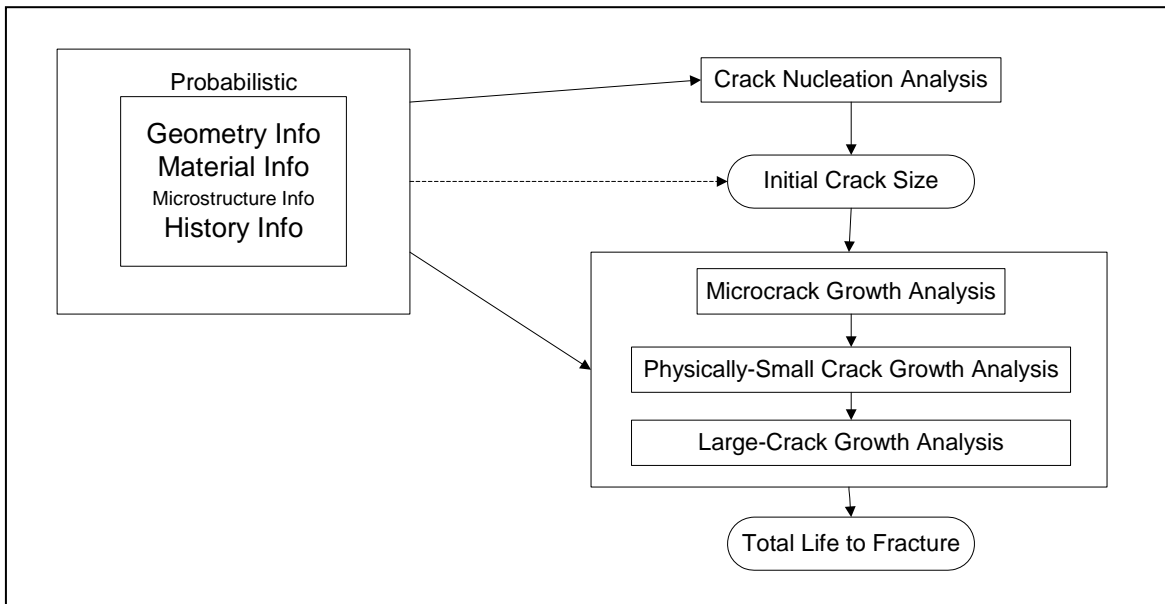
Figure 2. New Paradigm for Total Fatigue Life Analysis

This new paradigm can be applied to conventional empirical life models, as shown in Figure 3. Since the traditional "crack initiation" models (strain-life or stress-life) estimate life to some macrocrack size usually associated with the failure of a smooth laboratory specimen, some portion of this life is actually crack growth. It is possible to back-calculate the crack growth fraction of the "initiation" life for some specified "little" crack size using fracture mechanics models, deriving a true "nucleation" curve. A total crack growth life to failure can then be calculated, using this curve as a starting point. The total fatigue life is then the summation of the nucleation and growth calculations, which are joined by the nucleation crack size. This construction also permits a realistic assessment of crack nucleation vs. crack growth contributions to total life.
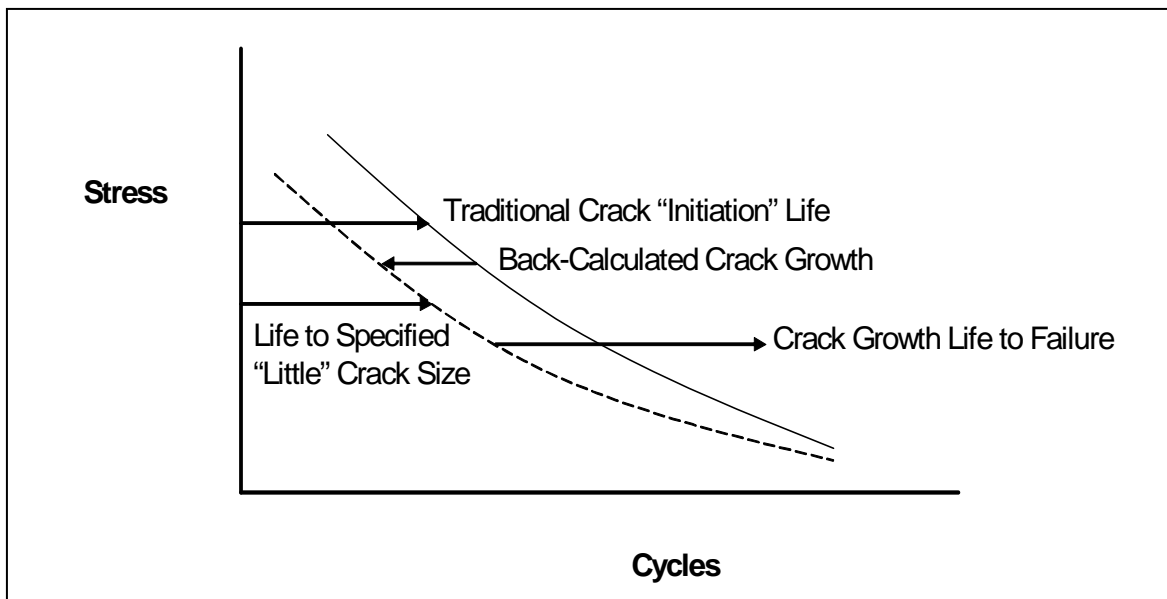
Figure 3. New Total Life Paradigm Applied to Traditional Empirical Models

One of the strengths of this construction is that it is possible to treat directly the physical damage growth mechanisms for various crack sizes. Another strength is that the true nucleation calculation is primarily driven by the stress at the surface. Both of these advantages may be especially relevant when the application problem contains significant stress gradients, as will be shown.

This general paradigm was demonstrated and calibrated with available data on Ti-6Al-4V generated in the large USAF High Cycle Fatigue (HCF) program during the previous decade [2]. The Ti-6Al-4V forgings had been solution treated at 1710 °F and then fan cooled and vacuum annealed at 1300 °F for 2 hours. The resulting microstructure contained approximately 60% primary alpha and transformed beta lamellas. The yield and ultimate tensile strengths averaged 134.9 ksi and 141.8 ksi, respectively.

Smooth Specimen Behavior. A large number of fatigue tests on 0.25-in. diameter smooth cylindrical specimens were performed by various engine companies at four different stress

ratios (R = 0.8, 0.5, 0.1, and -1) as part of the Program Research and Development Announcement (PRDA)(industry) program [2, 3]. The R = 0.8 smooth specimen tests were later determined to exhibit significant time-dependent bulk deformation effects, and so they were excluded from this study. A modified Smith-Watson-Topper (SWT) life model had been fit to the available data by one of the engine companies. This regression gave

$$\sqrt{\sigma_{max}\varepsilon_{a,max}E} = 7611\,N^{-0.59} + 65.39\,N^{-0.023}$$

(1)

where $\varepsilon_{a,max}$ is the maximum principal strain amplitude, σ_{max} is the maximum normal stress on the critical plane of $\varepsilon_{a,max}$, E is Young's modulus, stress and modulus have units of ksi, and N is total cycles to failure. The experimental data and SWT fits are shown in Figure 4.

<u>Large Fatigue Cracks.</u> All available Ti-6Al-4V fatigue crack growth (FCG) rate data generated in the PRDA HCF program were also collected [2, 4]. After tests involving potentially anomalous load shed effects were eliminated, a total of thirty-four large-crack tests at four different stress ratios remained in the PRDA data base. A large number of tests were performed at R = 0.1 and R = 0.8 (exhibiting substantial scatter in growth rates), but only two tests were conducted and reported at R = 0.5 and R = -1. The R = 0.5 test data, in particular, addressed a very limited range of ΔK.

In order to address this shortfall, additional FCG rate data were obtained from Ritchie and Boyce based on their large-crack investigations in the Multidisciplinary University Research Initiative MURI (university) HCF program [5]. They had generated extensive data at R = 0.1, 0.5, and 0.8, including tests at both 50 Hz and 1000 Hz (no frequency effects were observed). The MURI FCG rate data at R = 0.1 agreed with the central tendencies of the PRDA data but exhibited substantially less scatter. The MURI data at R = 0.5 and R = 0.8 exhibited slightly slower growth rates than the limited PRDA data. Both the PRDA and MURI FCG rate data have also been statistically analyzed in the current program, and these results are presented and discussed in Section 4.1.

Tabular representations of the average large-crack data suitable for implementation in DARWIN were constructed. These tabular representations are compared with the original PRDA and MURI experimental data in Figures 5, 6, and 7 for R = 0.1, 0.5, and 0.8, respectively.

Only limited fatigue crack growth data—two surface crack tests—were available for R = -1. These tests were conducted at significantly different applied stresses and therefore exhibited significantly different crack growth rates. Test "8375A" was conducted at maximum stresses ranging from 6 to 17 ksi, and gave FCG rates ranging from 10^{-9} in./cycle to 10^{-7} cycle. Test "70-22-a" was conducted at maximum stresses ranging from 58 to 70 ksi, and gave growth rates ranging from around 10^{-6} in./cycle to nearly 10^{-4} in./cycle.
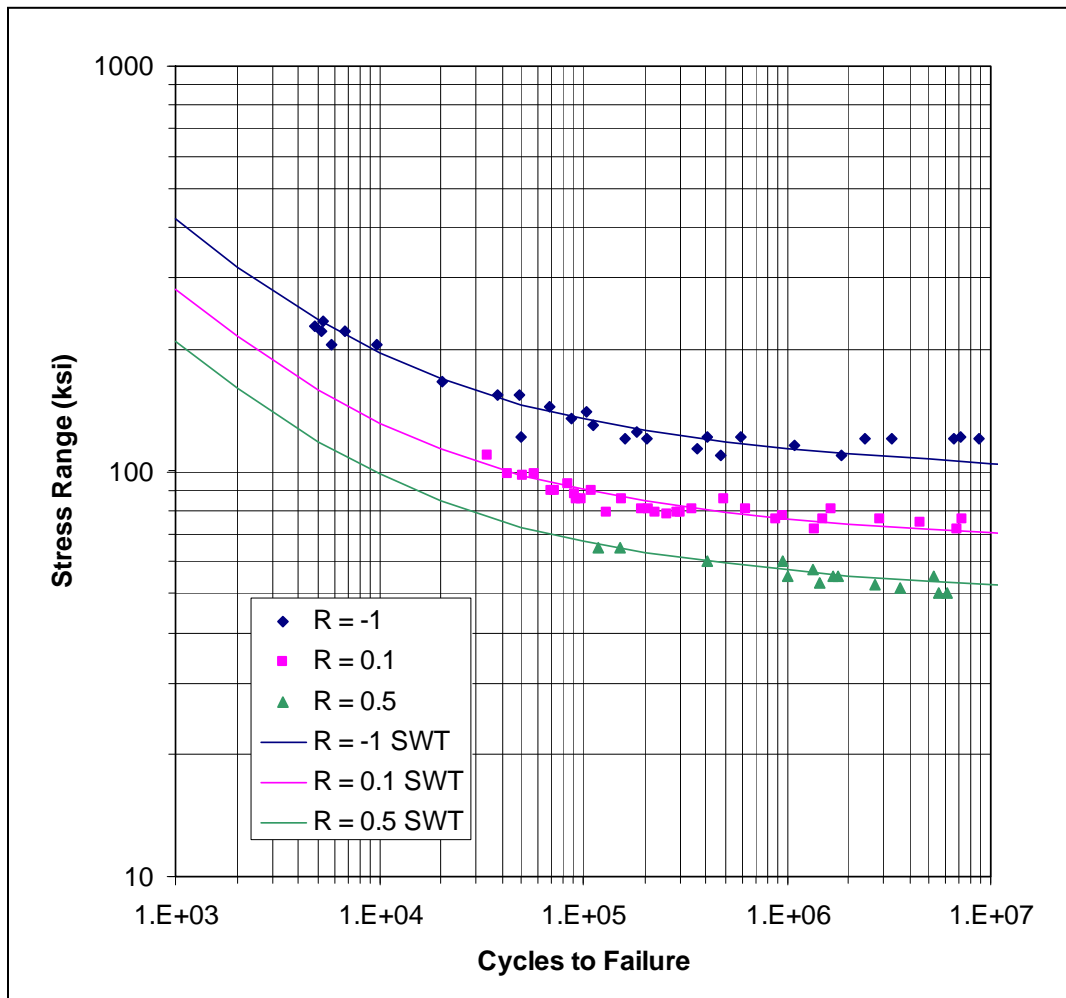
Figure 4. Smooth Specimen Fatigue Life Data and Smith-Watson-Topper Fits for Ti-6Al-4V
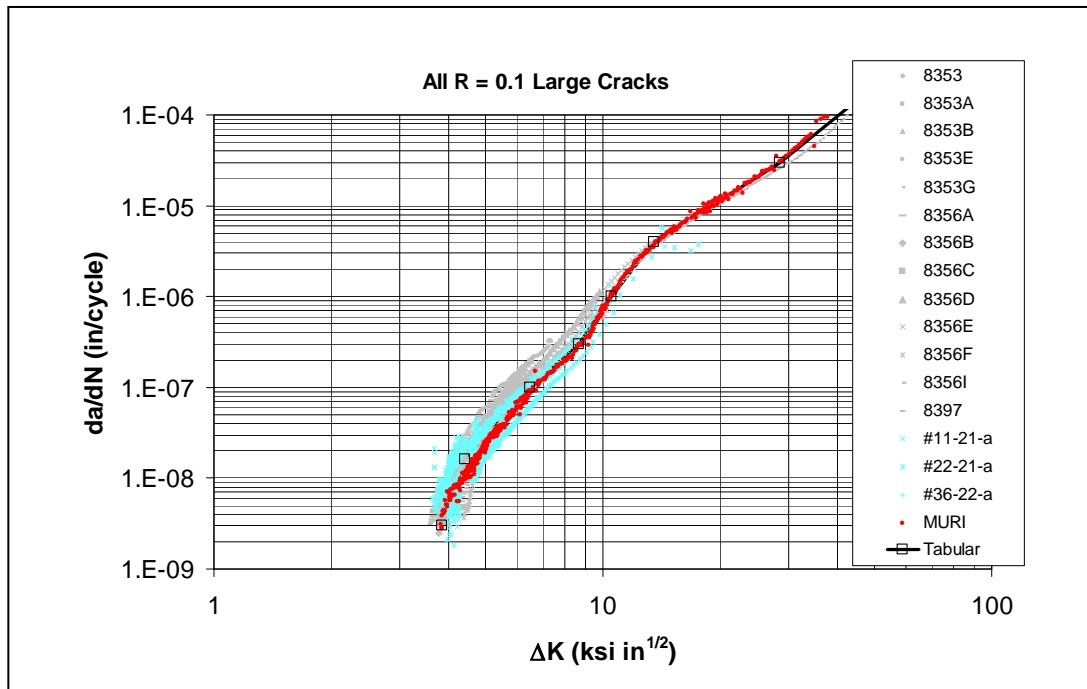
Figure 5. Large-Crack FCG Rate Data and Tabular Model for Ti-6Al-4V at R = 0.1
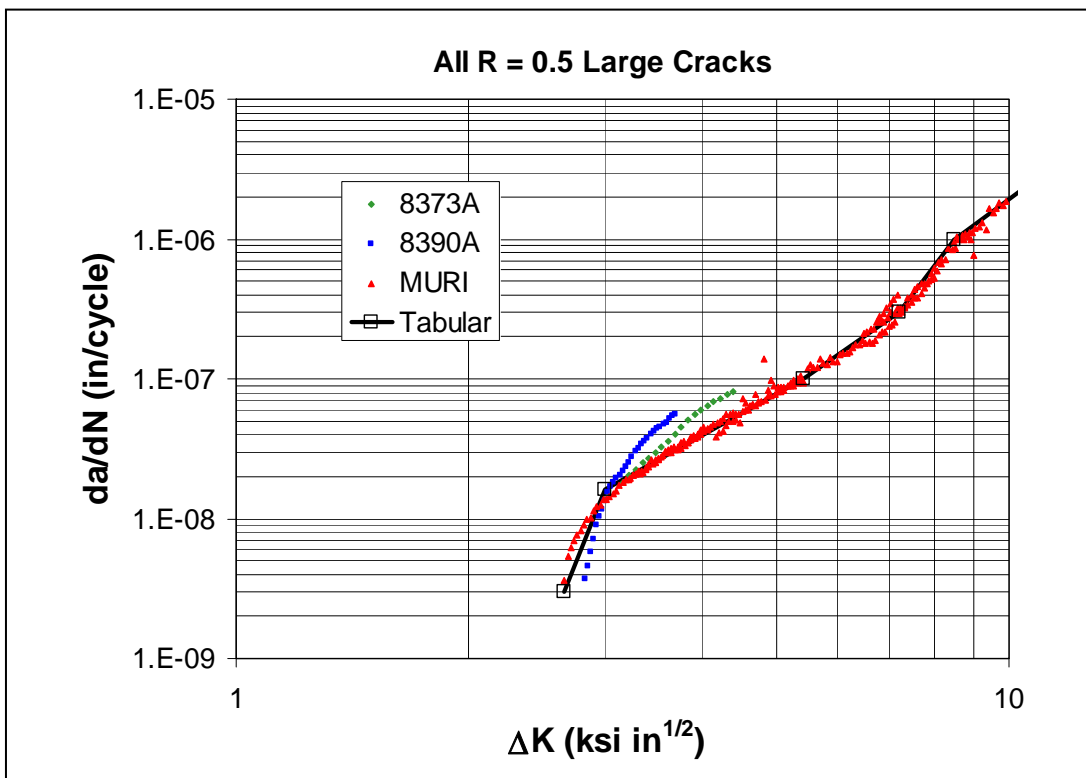
Figure 6. Large-Crack FCG Rate Data and Tabular Model for Ti-6Al-4V at R = 0.5
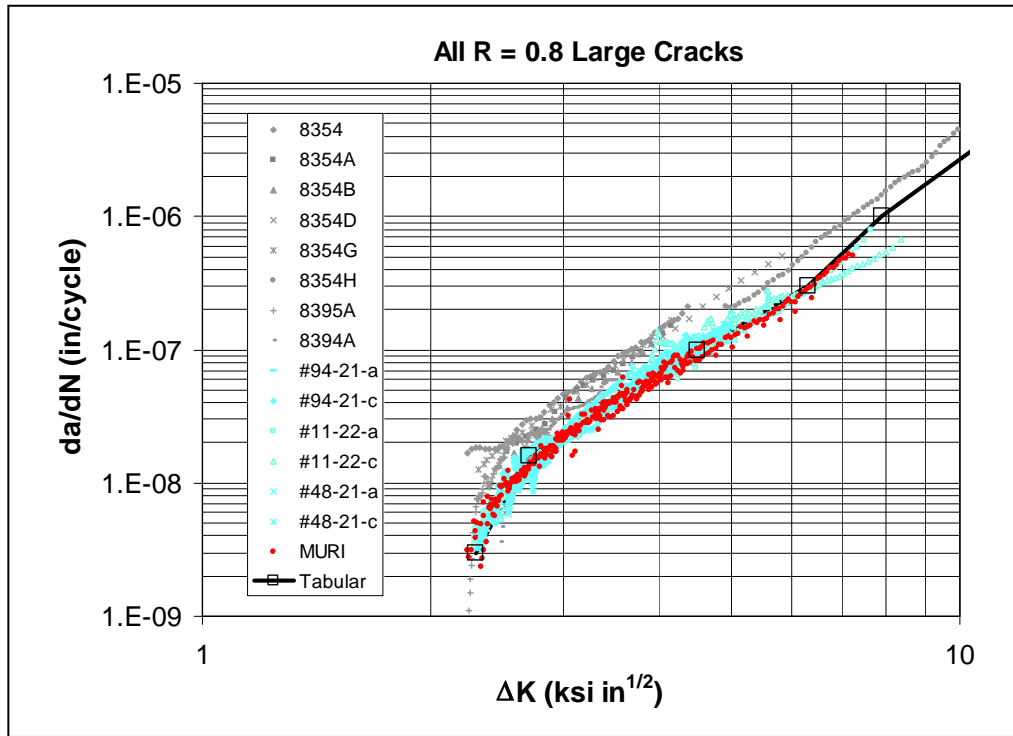
Figure 7. Large-Crack FCG Rate Data and Tabular Model for Ti-6Al-4V at R = 0.8

Arguments based on fatigue crack closure theory suggest that stress level effects on fatigue crack growth rates, which are minimal at higher stress ratios, can be significant at lower stress ratios. For example, the closure-based equations developed by Newman [6] indicate that the effective stress range ratio, U, which indicates the fraction of the stress intensity factor range that is effective in growing the crack, changes by 30% to 50% between low stresses typical of threshold testing and high stresses typical of low-cycle fatigue (LCF) conditions at R = -1. In contrast, U changes only about 10% at R = 0.1 between vanishingly small stress levels and typical LCF stress levels.

Therefore, stress-level effects were considered during the construction of representative tabular curves for R = -1, based on the two available tests. The Newman closure equations were used to estimate crack opening levels and then the closure-corrected range of the stress intensity factor for both tests. The results of this analysis are shown in Figure 8, along with a tabular representation of the tabular FCG rate curve in terms of ΔK_{eff}. Figure 9 then shows the corresponding representation of the R = -1 data in terms of ΔK, along with hypothetical growth rate curves for two larger values of σ_{max}. Here σ_{max} = 110 ksi corresponds to the largest fully-reversed stress amplitude that will not introduce appreciable cyclic plasticity, while σ_{max} = 83 ksi corresponds approximately to an LCF life of 20,000 cycles at R = -1. The final tabular representation of the R = -1 data was constructed at a stress range that was representative of the available smooth specimen and feature test data for R = -1. All of the tabular curves are summarized in Figure 10.
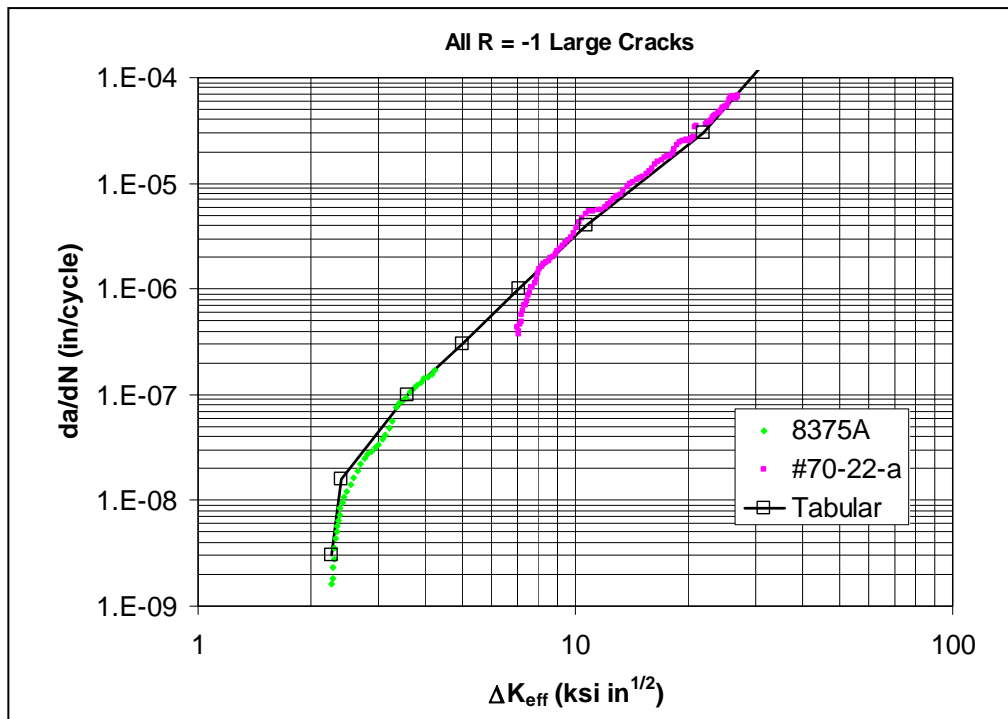
Figure 8. Closure-Corrected FCG Rate Data for Ti-6Al-4V at R = -1
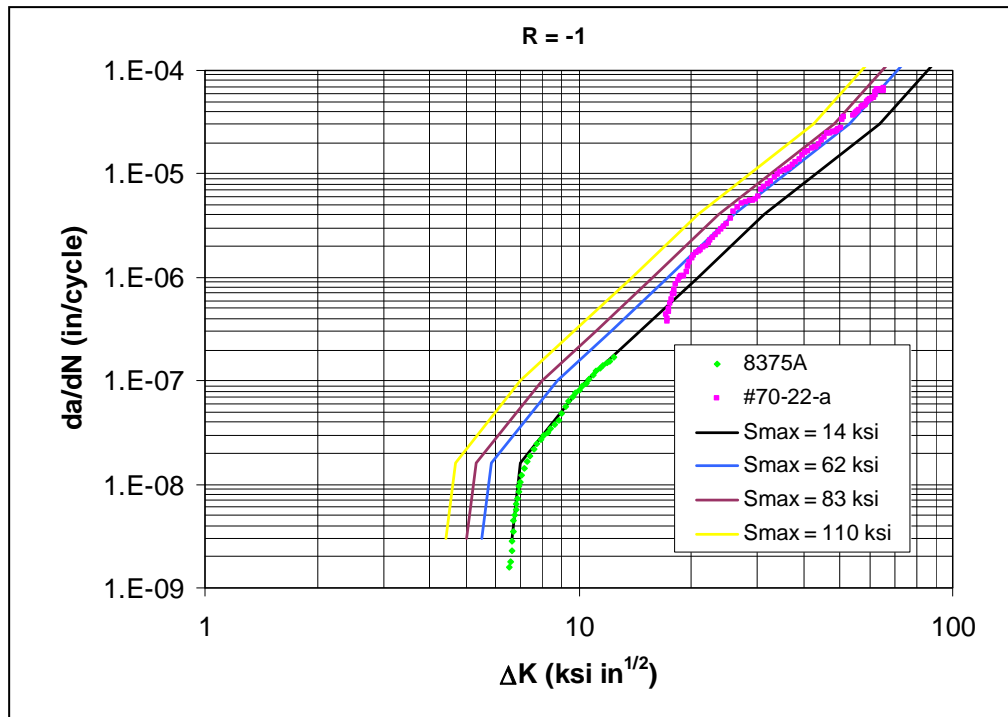
Figure 9. Predictions of FCG Rate Behavior in Ti-6Al-4V at R = -1 Based on Two Tests and the Newman Crack Closure Equations

13
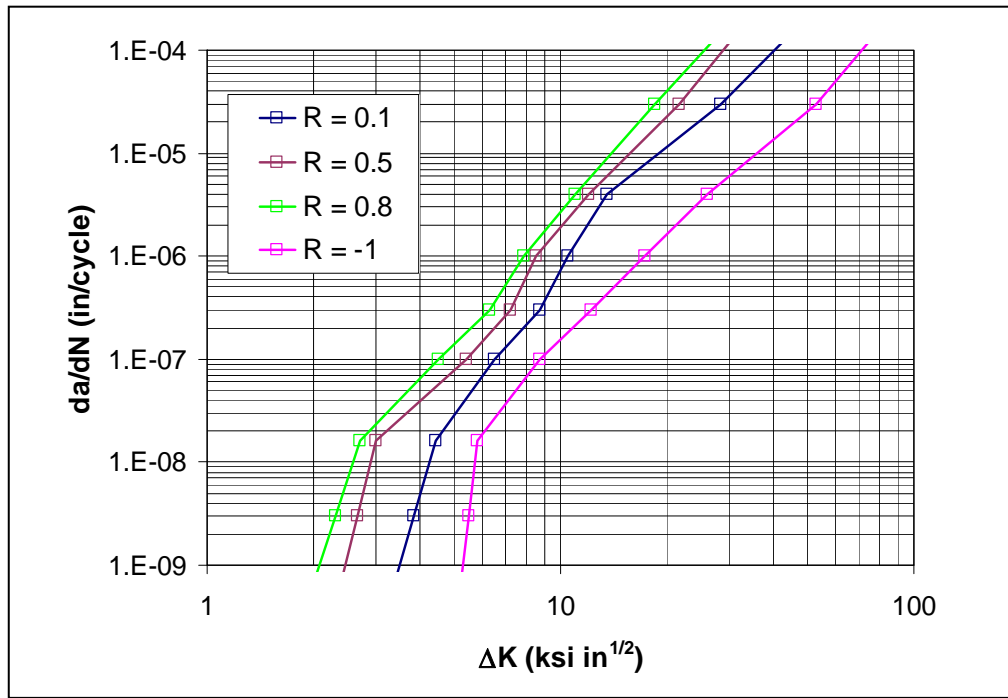
**Figure 10. Summary of Tabular Representations for Ti-6Al-4V
Large-Crack FCG Rate Data**

Small Fatigue Cracks. Small-crack FCG rate data for the same Ti-6Al-4V were generated at R = 0.1, σ_{max} = 88 ksi by Honeywell (then called AlliedSignal) in the PRDA program [2, 7]. These small-crack data are compared with the PRDA large-crack data in Figure 11 (small-crack data in red). The small-crack data exhibit accelerated growth rates compared to the large-crack data at the same nominal ΔK values. Also note that the small cracks grew at nominal ΔK values significantly lower than the apparent large-crack threshold.

A simple engineering approach to address small-crack behavior was developed based on the Kitagawa [8] diagram construction, Figure 12. The Kitagawa diagram integrates the traditional large crack fracture mechanics threshold, ΔK_{th}, with the traditional smooth specimen endurance limit, $\Delta\sigma_e$. The region on the Kitagawa diagram both above the horizontal endurance limit line and above the sloping threshold line is "unsafe" in that fatigue failure is predicted to occur. The region below both lines is "safe" in that fatigue failure is predicted not to occur. The intersection of the two lines, defined as a_0, is given by the equation

$$a_0 = \frac{1}{\pi}\left(\frac{\Delta K_{th}}{F\Delta\sigma_e}\right)^2$$

(2)

where, for consistency with the smooth specimen endurance limit data, $F = 1.12\ (2/\pi)$ is the geometry correction factor in the K solution for the semi-circular surface crack in the smooth specimen.
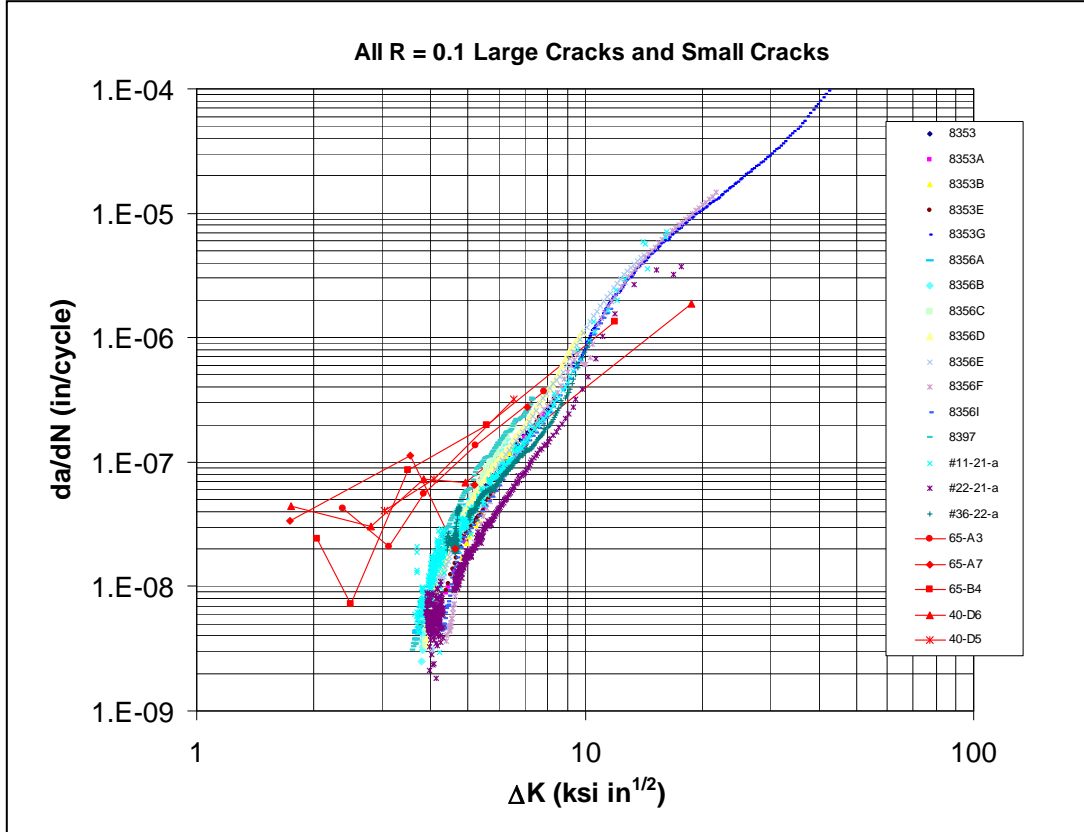
Figure 11. Large-Crack (Multi-Colored Symbols) and Small-Crack (Red Symbols) Fatigue Crack Growth Rate Data for Ti-6Al-4V at R = 0.1
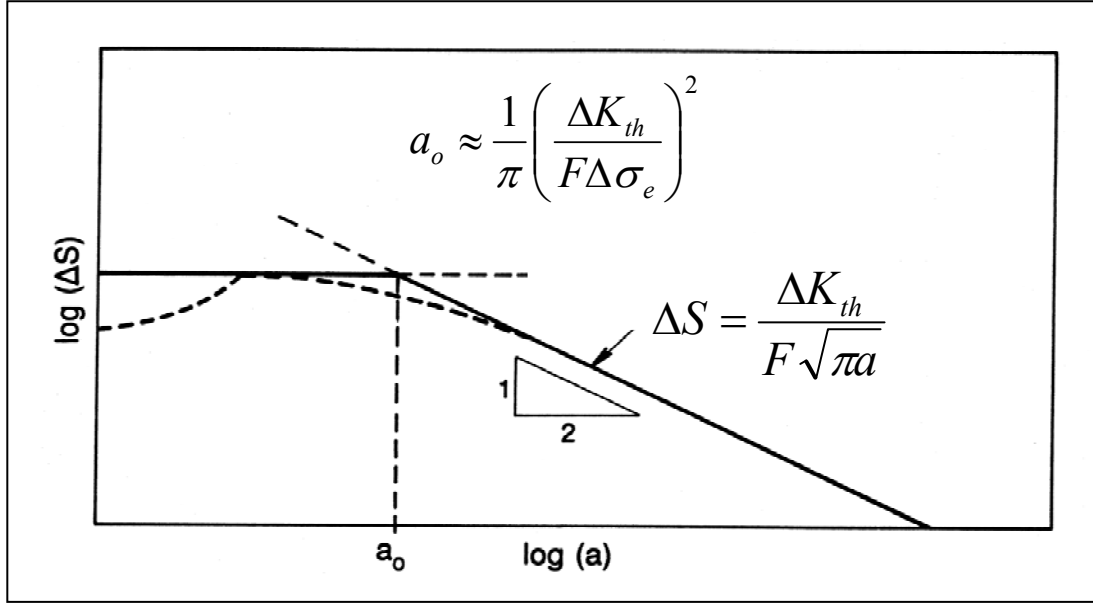
Figure 12. Schematic Kitagawa Diagram Relating Smooth Specimen Fatigue Endurance Limit ($\Delta\sigma_e$) and Large-Crack Threshold (ΔK_{th})

The Kitagawa diagram indicates that cracks smaller than a_0 must be able to grow at nominal stress intensity factors that are less than the large crack threshold, since smooth specimens fail by the initiation and growth of microcracks to failure in this regime. El Haddad [9] suggested that small cracks could grow below the large crack threshold because the effective driving force of the small cracks was larger than expected from traditional large crack fracture mechanics. He proposed that the actual effective driving force was

$$\Delta K_{eq} = F(a)\Delta S\sqrt{\pi\left(a + a_0\right)}$$

(3)

Here $F(a)$ is the crack shape and specimen/component geometry correction factor for the component of interest; a_0 is not included in $F(a)$. Note that the a_0 contribution is negligible for large values of a, but becomes increasingly significant for smaller values of a. The El Haddad construction can also be interpreted as a crack-size dependent *threshold* rather than a crack-size dependent *driving force.* In this case, the crack-size dependent threshold is given as

$$\Delta K_{th}\left(a\right) = \Delta K_{th}\sqrt{\frac{a}{a + a_0}}$$

(4)

The El Haddad construction can be represented on the Kitagawa diagram as a dashed line which transitions between the endurance limit and large-crack threshold lines.

16

Although the El Haddad concept has been criticized for its apparent lack of physical justification, several researchers [10, 11] have independently derived similar formulations based on detailed micromechanical considerations, and these have been shown to be numerically identical to the El Haddad formulation under typical conditions. Chan [10] related a_0 to dislocation pileups and mode II shear cracks, and found satisfactory agreement with small-crack data from titanium aluminides. Tanaka [11] formulated the problem in terms of a crack-tip slip band propagating across one or more grain boundaries, and demonstrated reasonable agreement between his formulation and a variety of experimental data. While titanium was not included in the Tanaka comparisons, Brown and Taylor [12] have shown good agreement with the El Haddad formulation for a mill-annealed Ti-6Al-4V.

In the HCF program, this small-crack formulation was explored primarily from the standpoint of crack-size dependent thresholds, and it found some success in predicting fatigue crack behavior associated with foreign-object damage and fretting fatigue [13]. In the current program, it appears to be more convenient to apply the formulation from the standpoint of a crack-size dependent driving force, Equation (3), since the focus is on predicting fatigue crack growth life rather than threshold stresses (associated with crack arrest) as in [13].

The small-crack parameter a_0 was estimated to be approximately 0.002" at R = 0.1 from Equation (2) and the available experimental data on the endurance limit and the large-crack threshold for Ti-6Al-4V generated in the HCF program. A similar value was calculated at R = 0.5. The ability of the crack-size dependent driving force ΔK_{eq} to correlate the R = 0.1 small-crack data with the baseline R = 0.1 large-crack data is shown in Figure 13. The corrected small-crack data at even the smallest crack sizes shown here (on the order of 0.001", or slightly less than twice the average size of the primary alpha grains) agree well with the large-crack data.
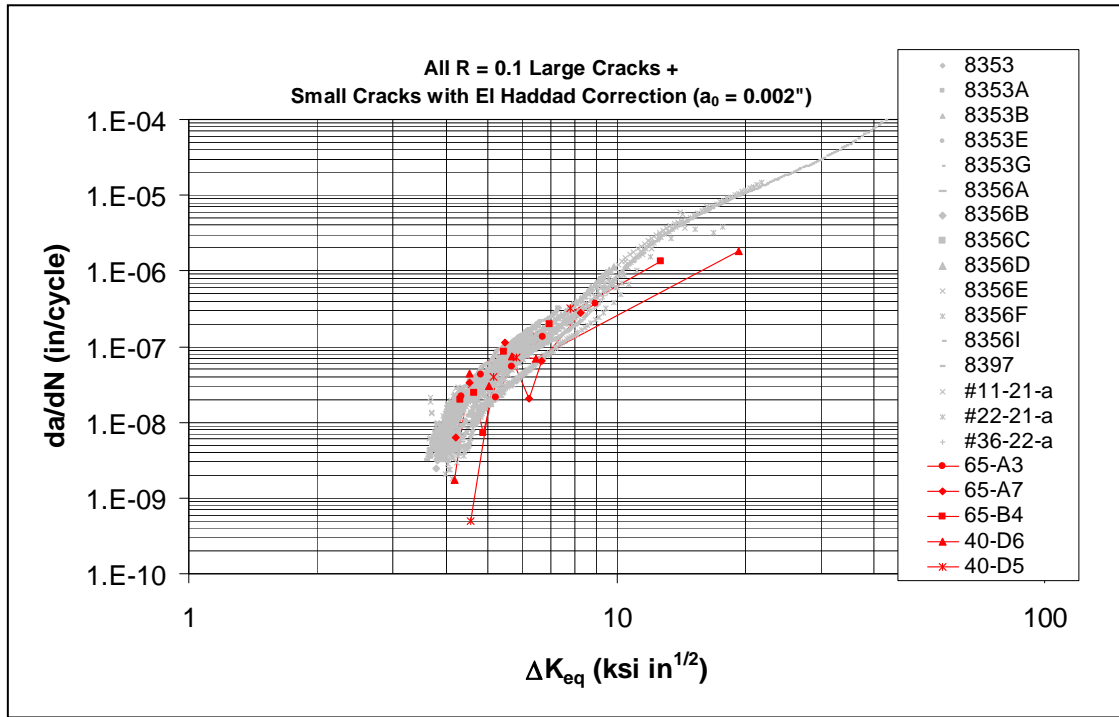
**Figure 13. Large-Crack (Gray Symbols) and Small-Crack (Red Symbols)
Fatigue Crack Growth Rate Data for Ti-6Al-4V at R = 0.1, Correlated in
Terms of the El Haddad Crack-Size Modified Driving Force (ΔK_{eq})**

Crack growth rate data published by Hines, Peters, and Lutjering [14] appear to provide some further evidence of both the small-crack effect and the stress-level effect for Ti-6Al-4V. Figure 14, taken directly from their cited paper, compares R = -1 small-crack data at three different stress levels with large-crack data at R = 0.1. The small cracks exhibited accelerated growth rates in comparison to the large-crack data, along with a systematic layering of increasing growth rate with increasing stress amplitude. Direct analysis of the Hines et al. data is not possible since their bi-modal microstructure is slightly different from the standard HCF program material condition, and since Hines et al. published only idealized trend lines, and not the actual data points. However, it is possible to emulate the Hines et al. results using the available crack growth rate properties for the HCF program Ti-6Al-4V, and employing both the El Haddad small-crack correction as well as the Newman stress-level correction. The resulting "predictions" of the Hines et al. behavior are shown in Figure 15 and exhibit the same general trends. Note that SI units are used in these two figures, whereas US units were used in the previous figures.

18
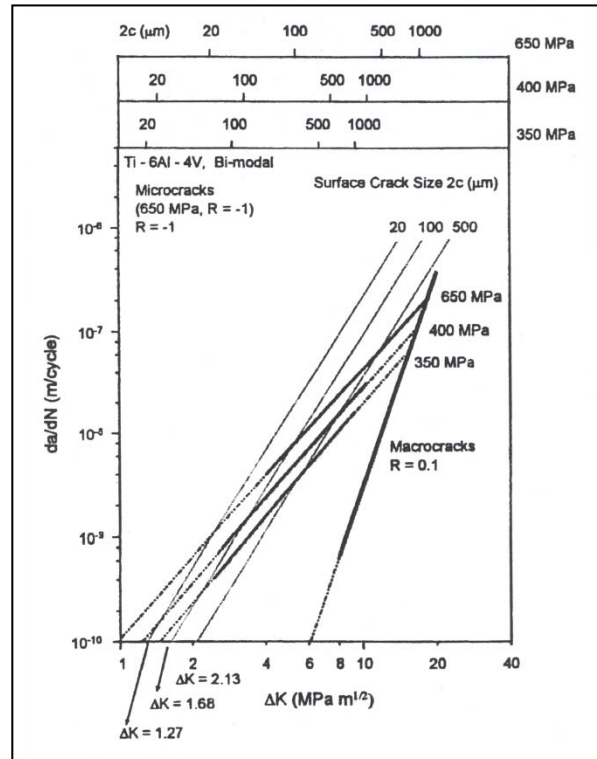
Figure 14. Hines et al. (1999) FCG Rate Data for Small Cracks in Ti-6Al-4V Under R = -1 Loading at Three Different Stress Amplitudes, in Comparison to Large-Crack R = 0.1 Behavior
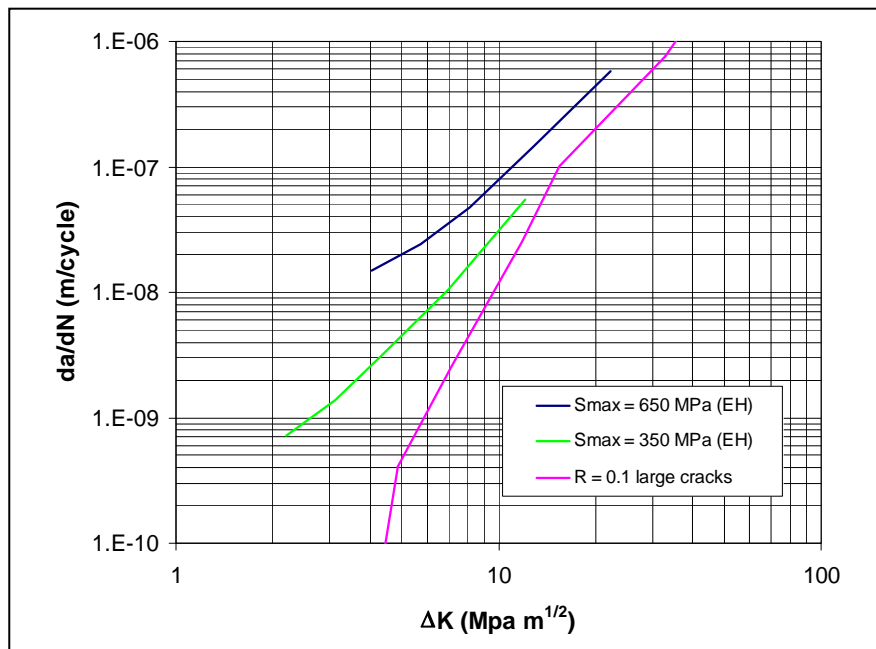
Figure 15. Predicted FCG Rates in Ti-6Al-4V for R = -1 Conditions Considered by Hines et al. (1999), Demonstrating Apparent Small-Crack Effects and Stress-Level Effects

FaNG Results. Crack nucleation curves were constructed for smooth fatigue specimens according to the following procedure. First, the FCG life from a specified nucleation crack size to specimen fracture was calculated for a specified uniform stress using the tabular large-crack FCG rate data and the El Haddad small-crack correction to the crack driving force. This calculation was performed using the stress intensity factor for a surface crack in a cylinder (crack case SC07) available in the National Aeronautics and Space Administration (NASA) Flaw Grow (NASGRO) computer code [15]. Then, this calculated crack growth life was subtracted from the calculated total life determined from the modified SWT fit to the PRDA smooth specimen data. The result was denoted as the "nucleation life" associated with the specified nucleation crack size. All of these algorithms and materials data were implemented in a custom version of the DARWIN computer code [16].

The results are shown in Figure 16 for R = 0.1 and Figure 17 for R = 0.5, each for various values of the nucleation crack size. The smallest nucleation crack size considered here is 0.001", which (as noted earlier) is slightly less than twice the average size of the primary alpha grains. This may be the lower limit of applicability of conventional fracture mechanics analyses. Some rules-of-thumb suggest a slightly larger lower limit, around five times the average grain diameter (in this case, about 0.003"). The nucleation lives approach 100 percent of the total life at the lowest maximum stresses considered (approximately the endurance limit) for both stress ratios. The nucleation lives are a smaller fraction of the total life at higher maximum stresses. Note that the largest maximum stresses represented on these graphs approach the monotonic yield strength of the material (135 ksi). The same results are represented in terms of the relative proportion of nucleation life to total life for R = 0.1 in Figure 18. Nucleation life fractions are compared at R = 0.1 and R = 0.5 for a fixed nucleation crack size in Figure 19.
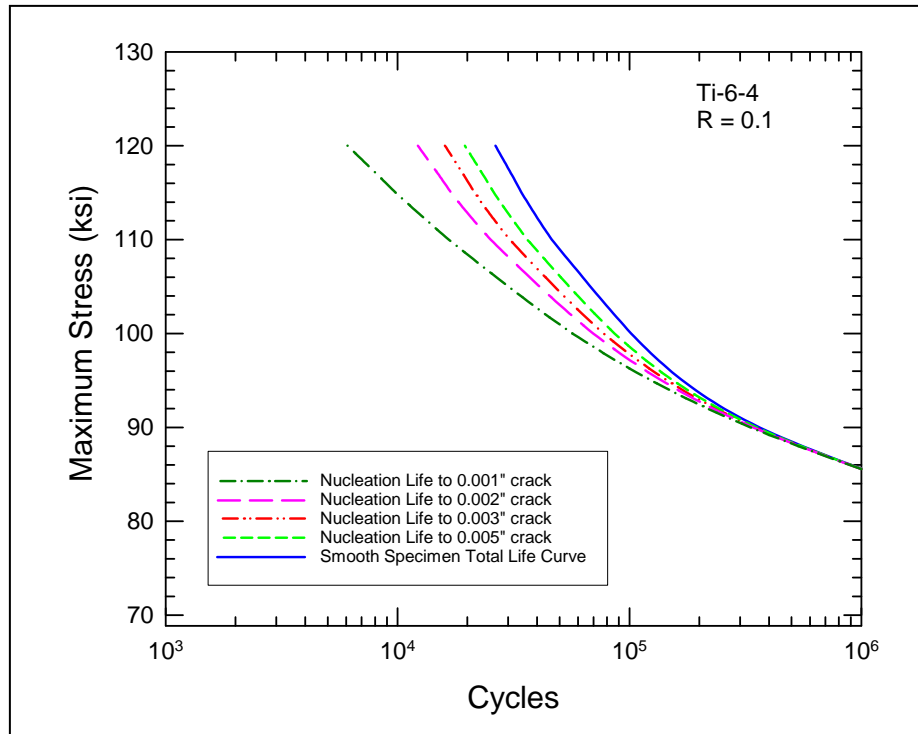
Figure 16. Estimated Crack Nucleation Life and Total Life for Ti-6Al-4V Smooth Specimens at R = 0.1
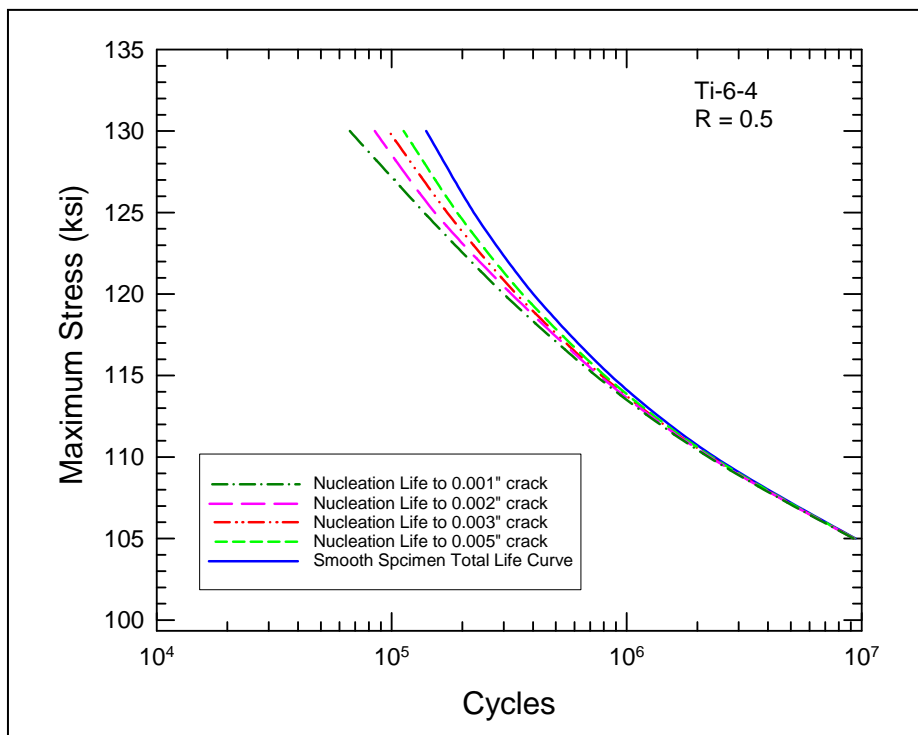
Figure 17. Estimated Crack Nucleation Life and Total Life for Ti-6Al-4V Smooth Specimens at R = 0.5

21
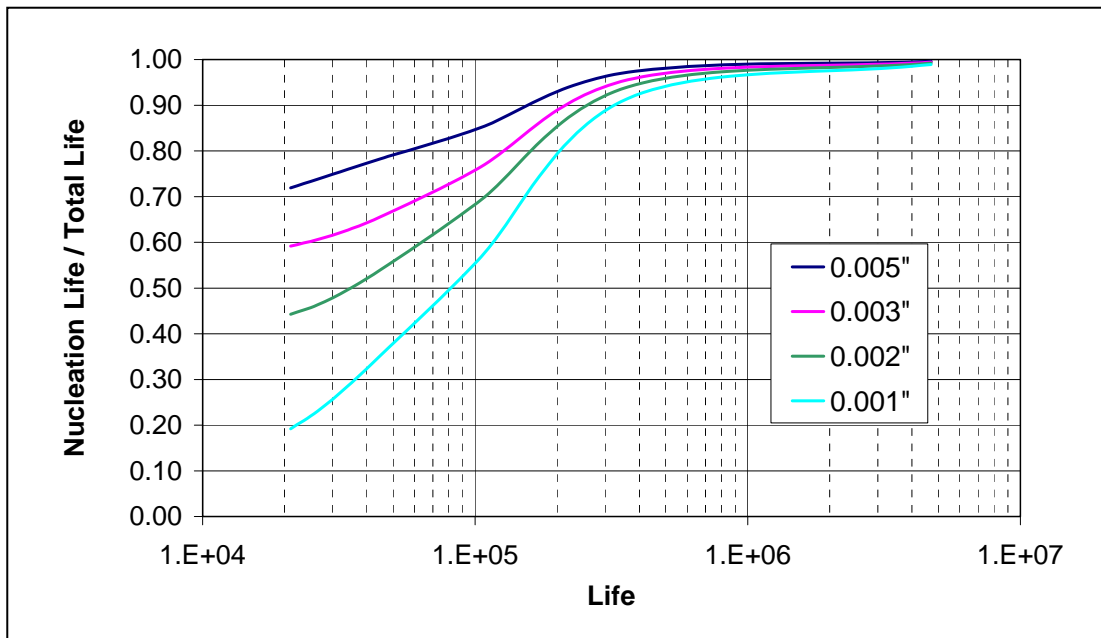
Figure 18. Estimated Nucleation Life Fraction as a Function of Total Fatigue Life at R = 0.1 for Different Nucleation Crack Sizes, Calculated Using the FaNG Model
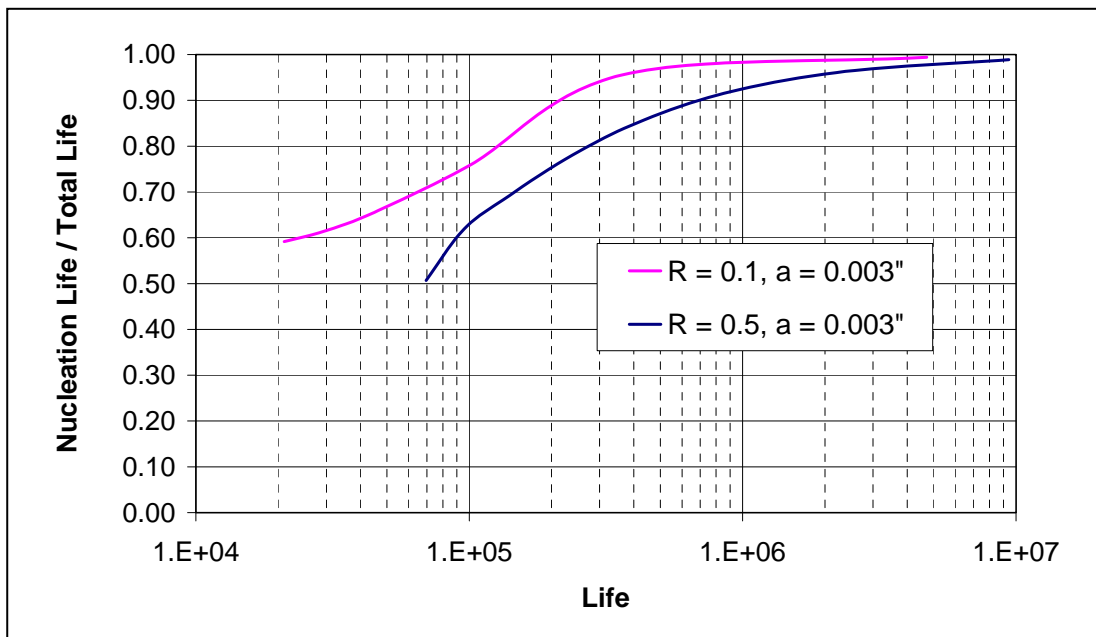
Figure 19. Estimated Nucleation Life Fraction as a Function of Total Fatigue Life at R = 0.1 and 0.5 for a Nucleation Crack Size of 0.003 in.

3.2   Model Validation

3.2.1   Fatigue Crack Growth at Notches

Prediction of fatigue life at stress concentrations is a classical problem.   Traditional stress-life approaches in which smooth specimen behavior is modified by the theoretical stress concentration factor (k_t) give overly conservative results. Semi-empirical corrections to this approach employing a diminished "fatigue notch factor" (k_f) give improved results but do not account for some stress level and geometry effects.

Better methods directly address the partitioning of life into crack "initiation" and "propagation" phases, independently calculating each phase with appropriate methods and then summing the two to obtain total life. Socie et al. [17] and Dowling [18] are representative notable early treatments of this type. The transition length at which initiation and propagation methods are joined in these methods can vary significantly with notch geometry and stress level.

As noted earlier, it is common in engine rotor life management to associate crack "initiation life" with the formation of a crack with some significant (fixed) engineering size (e.g., 0.030 in. or 1 mm). This "initiation life" is often related to the fatigue failure of a smooth cylindrical specimen under uniform axial loading. A corresponding crack "propagation life" is then calculated using this same size as the initial crack size. However, this scheme can also give over-conservative life results, especially for small stress concentrations and steep stress gradients. This method neglects two important phenomena: much of the "initiation life" is actually consumed by the growth of a very small crack, and the stresses may decrease substantially over the initiation length.

The FaNG model demonstrated earlier for smooth specimens can easily be extended to cracks growing at notches or, more generally, in stress gradient fields. The crack nucleation calculation for the application problem with a significant stress gradient (such as a sharp notch) is performed by determining the local stresses at the nucleation length in the corresponding (uncracked) application geometry, and then determining the nucleation life (at this nucleation length) for a smooth specimen subjected to the same local stresses. The local stress calculation in the application geometry should address any elastic-plastic behavior that may occur if local stresses exceed yield at the stress concentration. The crack growth life in the application geometry is performed using customary fracture mechanics analysis methods, employing stress intensity factor solutions that address the local geometry and stress gradients in the application problem. The same small-crack correction used to derive the nucleation curves must be used here to compute crack growth life. Finally, the total fatigue life for the application geometry is determined by summing nucleation and growth contributions. Because both life phases are physically-meaningful values, it is also possible to make a realistic assessment of the relative importance of nucleation and growth for total life.

Note that the fracture mechanics calculation should not be performed and small-crack corrections should not be used at crack sizes so small that severe microstructural influences come into play. A traditional rule-of-thumb is at least two times the grain size, and preferably about five times the grain size. This serves to define a practical lower limit on the nucleation crack size. In principle, the nucleation crack size could be decreased further if suitable fracture mechanics methods were available to characterize the growth of microstructurally-small fatigue cracks. On the other hand, it is not clear that macroscopic calculations of the local stresses (employed in the nucleation calculation) would be meaningful at this microscopic level, and so it may be prudent to maintain the same practical lower limit.

The FaNG model was applied to predict the total fatigue lives of a series of tests performed on double-edge-notch (DEN) specimens in the HCF PRDA program [2]. Two different notch geometries were used. The notch in one specimen (the so-called "V-notch" or "small volume" configuration) had a depth of 0.047", a root radius of 0.021" and a width of 0.142", with an original specimen width (neglecting the notch) of 0.236". The notch in the other specimen ("U-notch" or "large volume") had a depth and radius of 0.032" and a width of 0.250", with an original specimen width (neglecting the notch) of 0.36". The nominal (net-section) stress concentration factor was approximately 2.5 for both geometries. Tests were performed at four different stress ratios: R = 0.1, 0.5, 0.8, and -1.

In preparation for performing the FaNG model predictions, three-dimensional elastic finite element analyses were performed to obtain the stress gradients ahead of the notch root. The nominal (net-section) stress concentration factor was approximately 2.5. The maximum elastic stress decreased from its maximum value at the notch root by a factor of two within 0.013" (0.33 mm) of the notch root. The calculated gradients are shown in Figure 20.

If the elastic maximum stress in the notched specimen was calculated to be greater than yield, then the DARWIN shakedown algorithm was invoked to calculate the elastic-plastic stress relaxation and redistribution near the notch root. When shakedown occurred, the local stress ratio was (in general) different from the nominal (applied) stress ratio, and the actual local stress ratio was considered in both the crack nucleation and growth calculations. The cyclic stress-strain properties of Ti-6Al-4V were employed in the shakedown calculations; the cyclic yield strength is about 113 ksi. An example of the original elastic and shakedown elastic-plastic stress gradients is provided in Figure 21 for nominal R = 0.5 loading with a maximum nominal applied stress of 57.5 ksi. This figure also illustrates the definition of the "nucleation stress" at the specified nucleation length (in this case, 0.003").
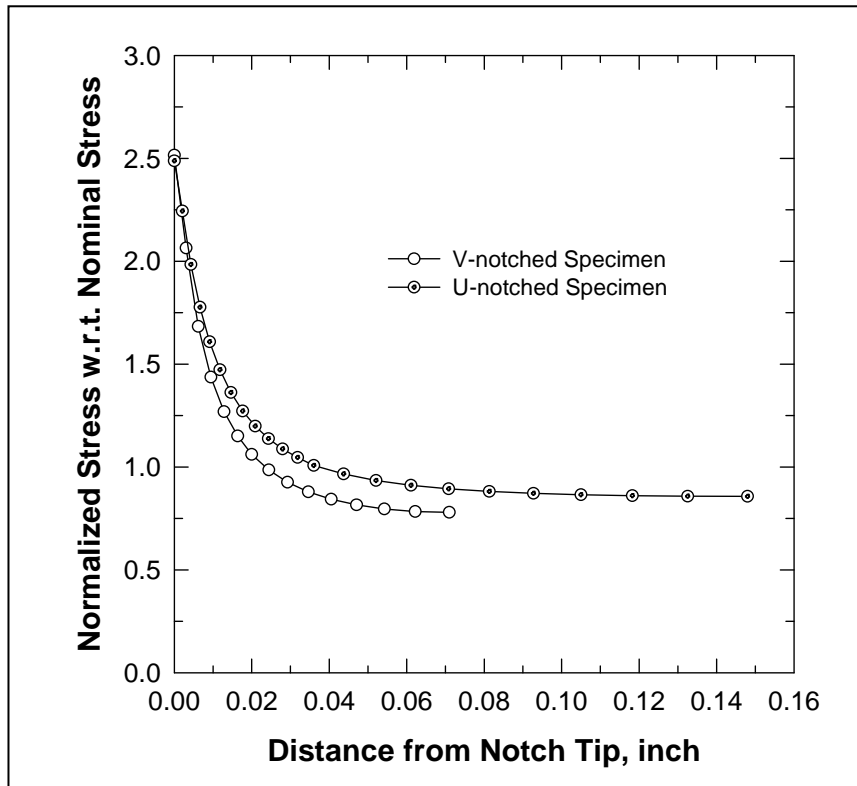
**Figure 20. Calculated Elastic Stress Gradients for
Two Double-Edge-Notch Specimen Geometries**
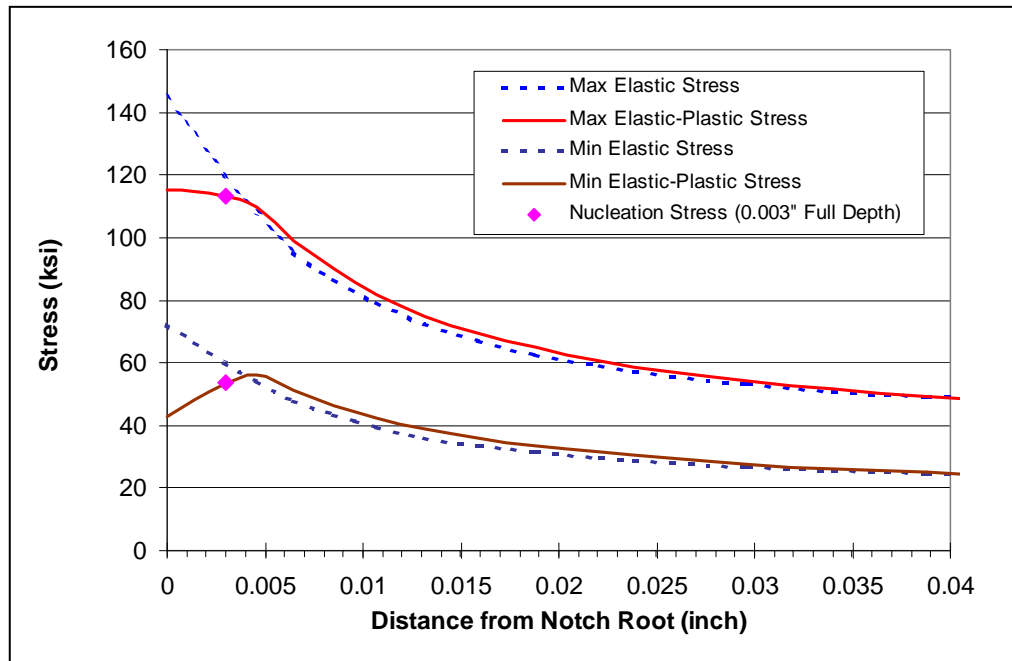
**Figure 21. Calculated Elastic and Elastic-Plastic Shakedown Stress Gradients
at Maximum and Minimum Load for Nominal R = 0.5 Loading
with a Remote Applied Stress of 57.5 ksi**

The test reports indicated that most of the observed cracking initiated as a dominant semi-elliptical surface crack near the center of the notch root, so the initial conditions for the crack growth analysis were selected as a semi-circular crack (with depth equal to the nucleation length) at mid-section. The DARWIN stress intensity factor solution SC17, a weight function solution for a semi-elliptical surface crack growing in a univariant stress gradient field, was used for the calculations.

Several different values of the nucleation length were considered during early investigations. Note that as the nucleation length is decreased, the nucleation life associated with that length decreases, but the crack growth life to failure associated with that nucleation length increases. The calculated total life (nucleation + growth) will not change with nucleation length in the absence of a stress gradient. When the local nucleation stress changes significantly with nucleation length, however, the calculated total life will change with nucleation length.

Comparisons of model predictions for total life with DEN test data at R = 0.1 for three different values of the nucleation length are shown in Figure 22. The three different values of nucleation length give similar total life predictions at higher maximum stresses, because yielding near the notch root (which causes stress relaxation and redistribution) substantially reduces the severity of the stress gradient. At lower maximum stresses, the different nucleation lengths had a larger effect on the predicted total life, although the differences in predicted life were still sometimes within the scatter of the experimental life results. A nucleation length of about 0.003" generally gave the most accurate predictions.

Also shown in Figure 22 for reference purposes are total life predictions based on a conventional stress-life approach in which the modified SWT model is applied to the elastically-calculated stresses and strains at the notch root itself (essentially, the SWT model is scaled by the peak stress concentration factor). As noted previously, this type of simple approach substantially overestimates the fatigue damage caused by the notch and gives over-conservative total life estimates. Plastic corrections to the local stresses and strains (non-negligible only above 45 ksi) would be inadequate to reconcile the differences.

Figure 23 shows comparisons of predictions and test data at R = 0.1 for the two notch geometries, considering only the 0.003" nucleation length. The two geometries are shown to be quite similar, exhibiting only minor life differences in both test and model.

Model predictions and test data for R = 0.5 (all employing the V-notch geometry) are compared in Figure 24. Again, the normalized SWT model is very conservative. Similar results are shown for R = -1 conditions (all V-notch) in Figure 25.
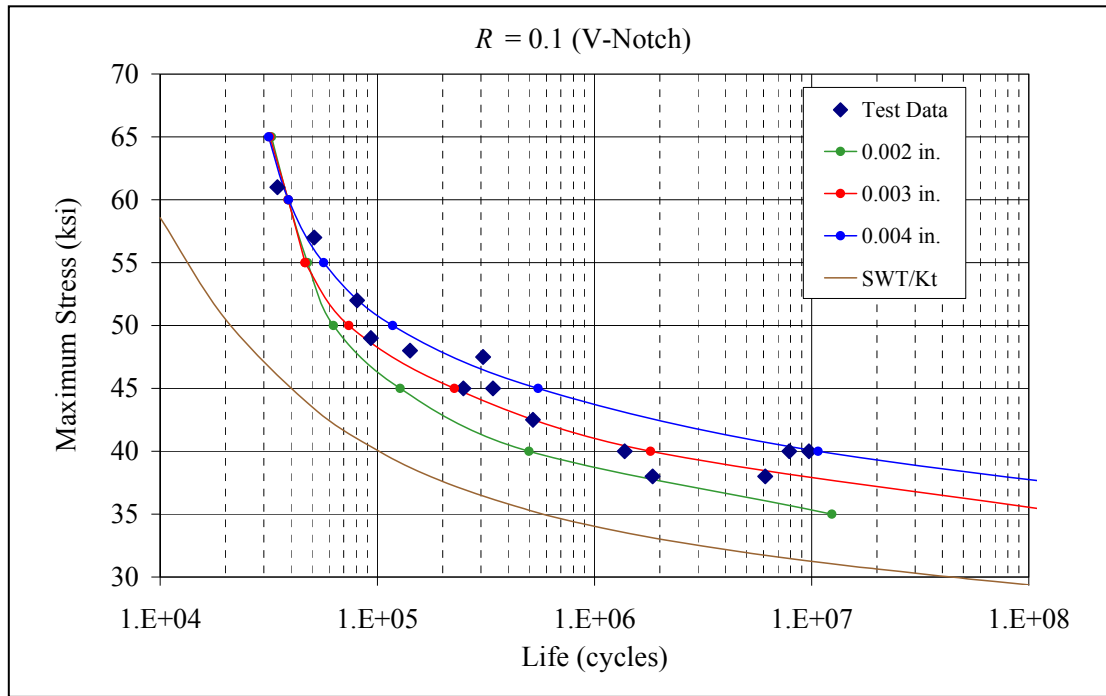
Figure 22. Comparison of FaNG Model Total Life Predictions and Test Data for V-Notch Specimens at R = 0.1 with Different Nucleation Sizes
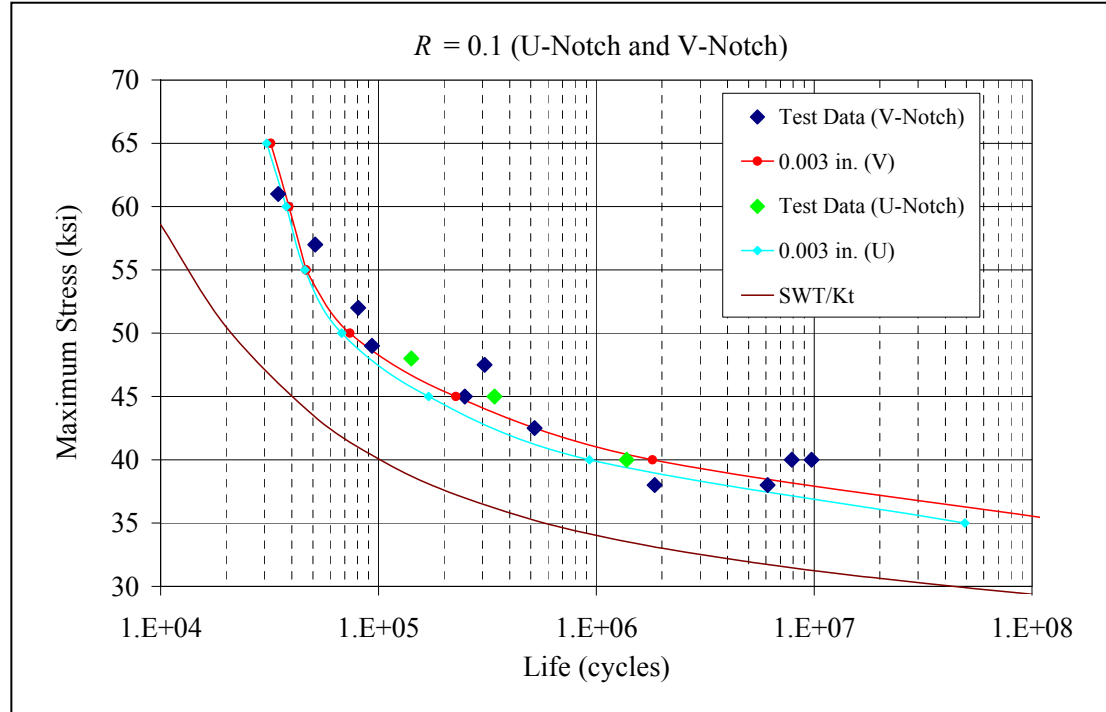
Figure 23. Comparison of FaNG Model Total Life Predictions and Test Data for V-Notch and U-Notch Specimens at R = 0.1

27
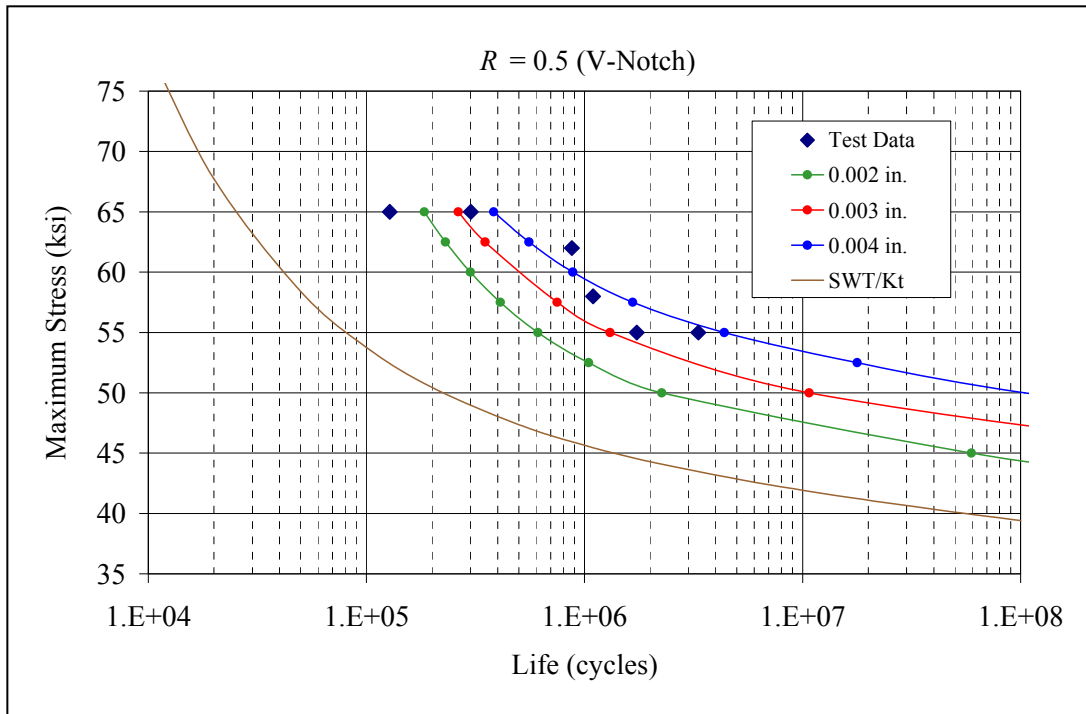
Figure 24. Comparison of FaNG Model Total Life Predictions and Test Data at R = 0.5
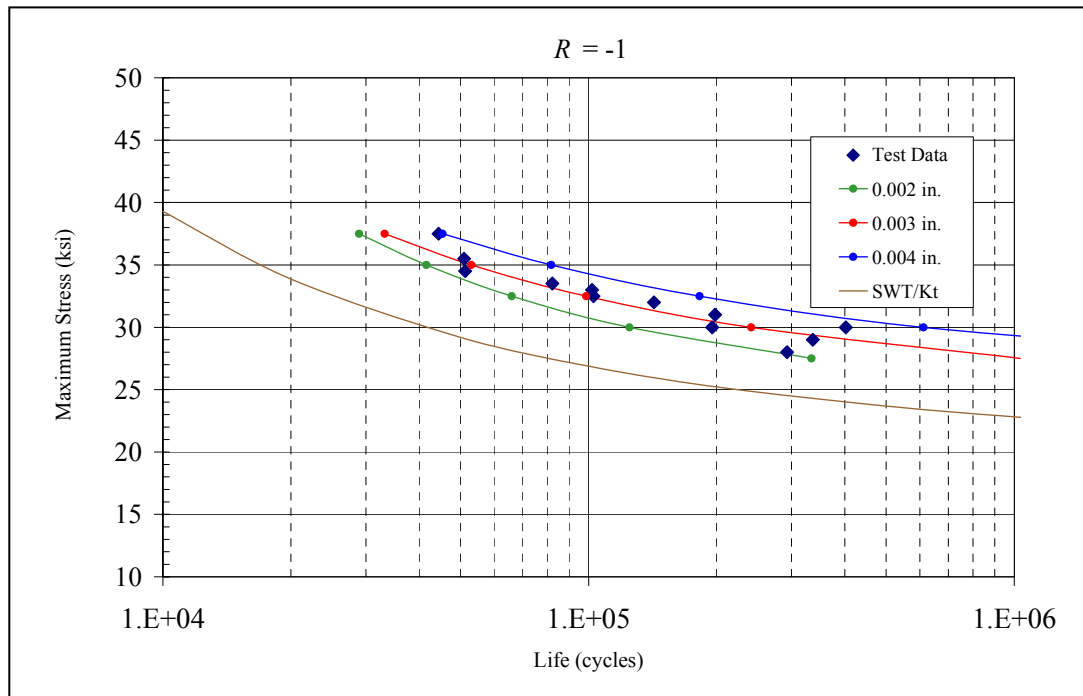
Figure 25. Comparison of FaNG Model Total Life Predictions and Test Data at R = -1

FaNG model predictions of the V-notch fatigue data for all three stress ratios are summarized in Figure 26, considering only the 0.003" nucleation length. Agreement between test and model is generally strong under all conditions. It should be emphasized that the predictions shown here are in no way a fit to the notch test data (other than the selection of a common nucleation length), because the material constants are derived only from smooth specimen and fracture mechanics tests.

The model facilitates evaluation of the fraction of total fatigue life consumed by crack nucleation, for the specified nucleation length. These predictions are summarized in Figure 27 for the same three stress ratios and the same nucleation length (0.003"). In the long life regime, the total life is dominated by crack nucleation, but in the low cycle regime (total lifetimes of 10^5 cycles and less), the crack growth phase consumes 30% and more of the total life. It is interesting to note that, for this particular geometry, the crack nucleation life fraction for a given total life does not change significantly with stress ratio.

This study must be regarded as a preliminary investigation due to its limited scope. Further work is needed to evaluate the method for other materials and other feature geometries. Selection of the optimum "nucleation length" also requires further study. It is not yet clear if this length is dependent on material parameters, geometry parameters, stress gradient parameters, or some combination of the three. Although the nucleation length does not always appear to play a significant role in the quality of the life prediction, it is not yet possible to make an *a priori* determination of the only free parameter in the analysis scheme.

Nevertheless, the results of this first study are encouraging. In principle, the method should apply not only to stress concentrations, but also to other problems with significant stress gradients. For example, many surface enhancement methods (such as peening) induce a severe stress gradient very close to the surface. These applications will be explored in the following section. The new method provides a rational basis to partition the problem into physically-meaningful nucleation and growth phases, to assess the relative importance of each, and to obtain improved life predictions.
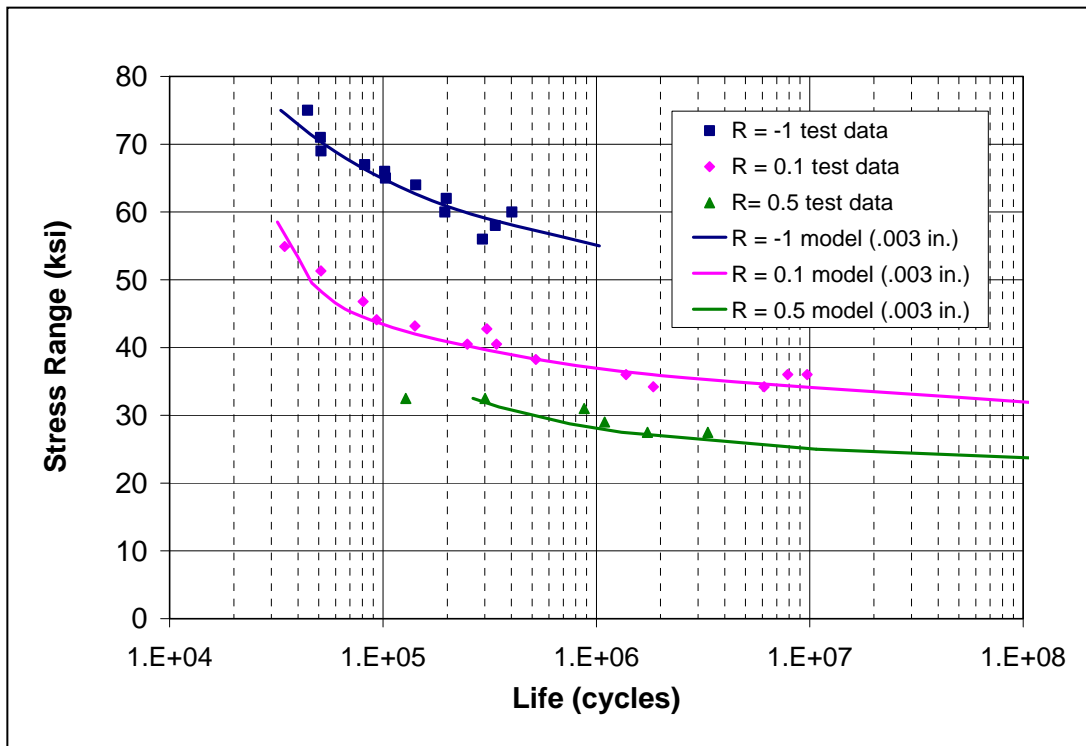
Figure 26. Summary Comparison of FaNG Model Total Life Predictions and Test Data at Three Stress Ratios for 0.003" Nucleation Size
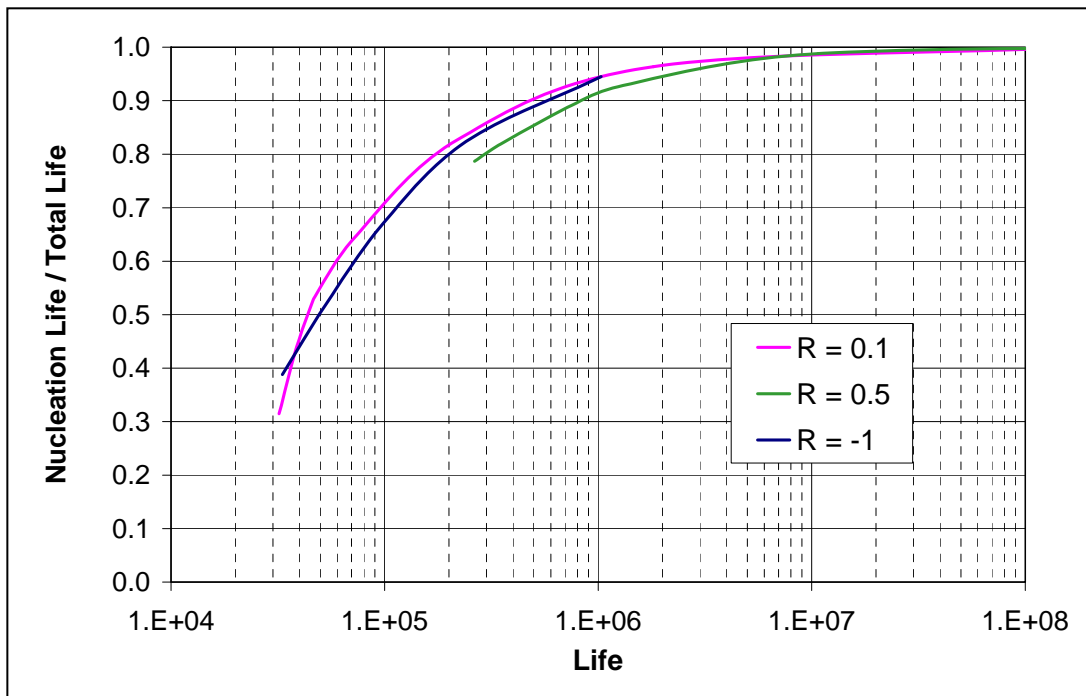
Figure 27. Predicted Nucleation Life Fraction for Notched Geometry and 0.003" Nucleation Size at Three Stress Ratios

3.2.2 Near-Surface Residual Stresses

Another significant class of fatigue problems involving significant stress gradients at the surface is the general category of surface enhancements such as shot peening, laser shock peening, or low plasticity burnishing. These surface enhancements are applied for the specific purpose of inducing a pronounced compressive residual stress at the surface. This residual stress, along with the associated local plastic deformation, generally leads to a substantial increase in fatigue life. However, analysis of these benefits is difficult because of the severity of the stress gradients over very small length scales.

The FaNG model appears to be an appropriate analytical choice to address this class of problems. However, the severity of the local stress field introduces some practical difficulties in performing the fatigue crack growth calculation using weight functions. The local stress values in these problems can change dramatically and even reverse sign over very small distances. At the same time, the component may contain an applied stress field with a gradient operative over a much longer length scale. These stress fields with dissimilar length scales present a computational challenge to the life prediction calculation. Highly irregular point spacing can compromise computational efficiency, which is especially critical for probabilistic analysis. For this reason, the DARWIN weight function solutions were originally configured for stresses defined at equally-spaced points along the gradient line. This approach was feasible for applications problems in which stress gradients exhibited a single length scale, but the approach breaks down for problems involving multiple gradients with multiple length scales. Sparse point spacing appropriate for a large length scale does not provide enough resolution to accurately define a local gradient over a small length scale; but fine spacing appropriate for the local gradient will require an excessively large number of points for the gradient over the large length scale.

In order to address this problem, a new optimum point spacing (OPS) algorithm was developed for weight function stress intensity factor solutions in DARWIN. The goal of the algorithm is to define the smallest number of points and the optimum spacing of those points to represent stress variations with high fidelity and without impacting the efficiency of search routines in the stress intensity factor solutions. The OPS algorithm uses Hermite interpolation to define a reference curve which is optimized such that the OPS and user-defined stresses agree within 0.1%. The point density of the OPS representation increases at locations with sudden change in stress gradient.

Figure 28 (left-hand side) illustrates the limitations of equal point spacing. The point spacing is insufficient to capture the actual stress variation near the origin, but excessive in describing the constant stress field farther away from the origin. The right-hand side of Figure 28 demonstrates how the OPS algorithm selects 29 points to describe the entire curve accurately and efficiently.
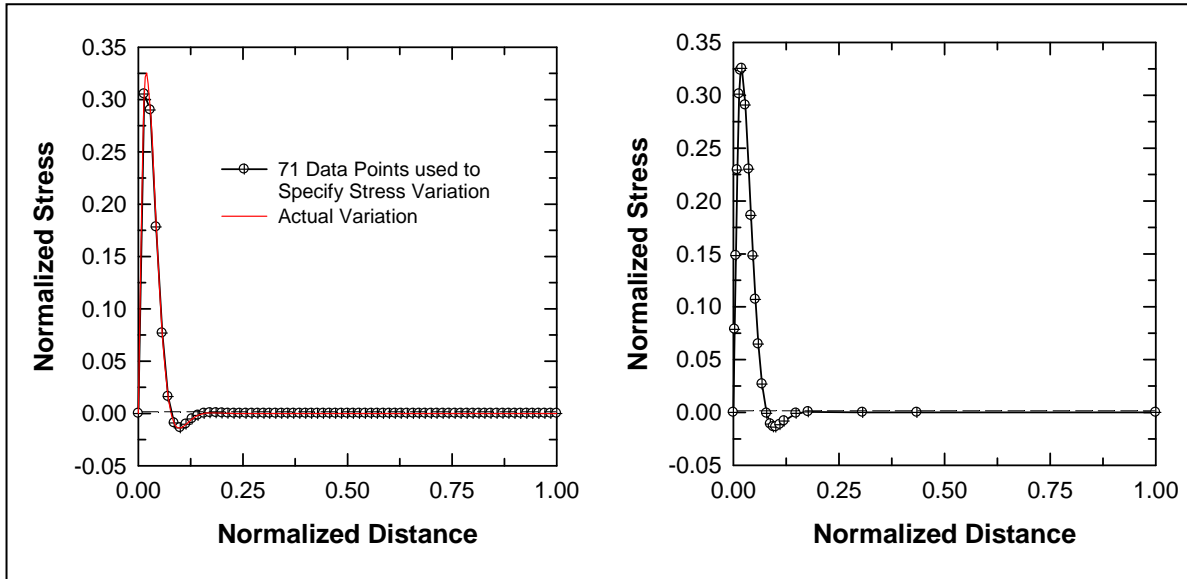
**Figure 28. Illustration of Equal Point Spacing (Left)
and Optimum Point Spacing Algorithm (Right)**

Fatigue data [19] provided by Lambda Research were available for coupons machined
from the same Ti-6Al-4V material used in the HCF program and then subjected to shot-
peening (SP) or low-plasticity burnishing (LPB). Following surface enhancement but prior
to fatigue testing, the coupons were also thermally exposed for 10 hours at 795 °F
(425 °C). Residual stress measurements were made on similar specimens after peening,
both before and after thermal exposure. The residual stress measurements following
thermal exposure are shown in Figure 29. The thermal exposure caused significant
relaxation of the original SP residual stresses, but relatively little relaxation of the original
LPB residual stresses. The fatigue tests were conducted at R = 0.1.

As shown in Figure 30, a comparison of the Lambda fatigue test results with the original
HCF PRDA smooth specimen stress versus number of cycles to failure (S-N) data revealed
that the observed fatigue lives for the SP specimens were actually shorter than the observed
fatigue lives for the baseline (unpeened) specimens tested in the industry HCF program
(these are the tests that were used earlier in this program to calibrate the FaNG model).
The LPB specimens exhibited slightly higher fatigue strengths than the original baseline
specimens from the industry program. Lambda Research has not published any baseline
(unpeened) data of their own for this material under similar testing conditions (four-point
bend with a trapezoidal cross-section). Not included in this figure are runout (usually
around 2E6 cycles) results (LPB tests with max stresses from 85 to 93 ksi, and SP tests
with max stresses from 65 to 70 ksi); the only data shown here are the actual failures.
Lambda specimens with FOD damage have also been excluded from consideration here.
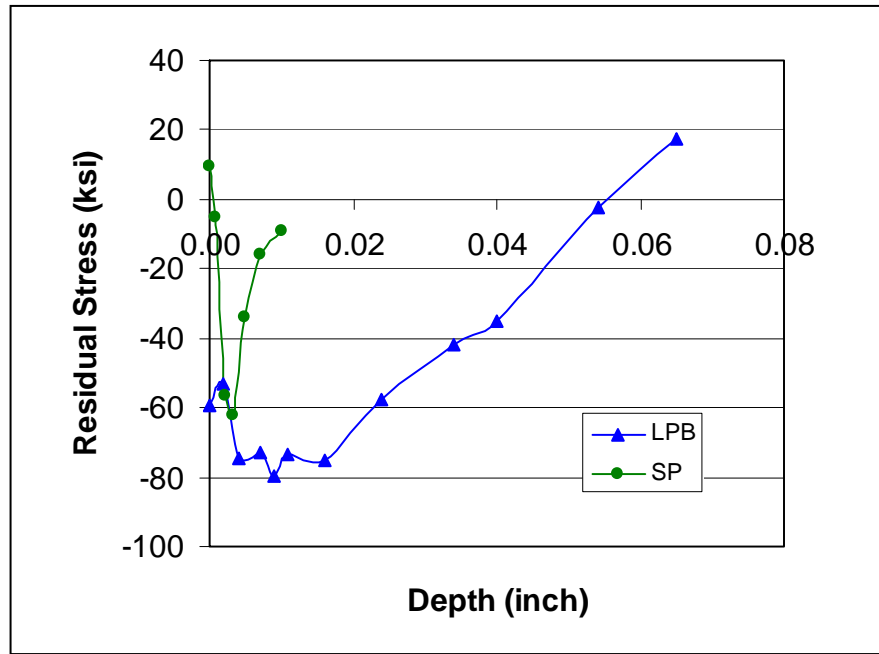
Figure 29. Measured Residual Stress Profiles in Ti-6Al-4V Coupons for Shot-Peening (SP) and Low-Plasticity Burnishing (LPB) Followed by Thermal Exposure
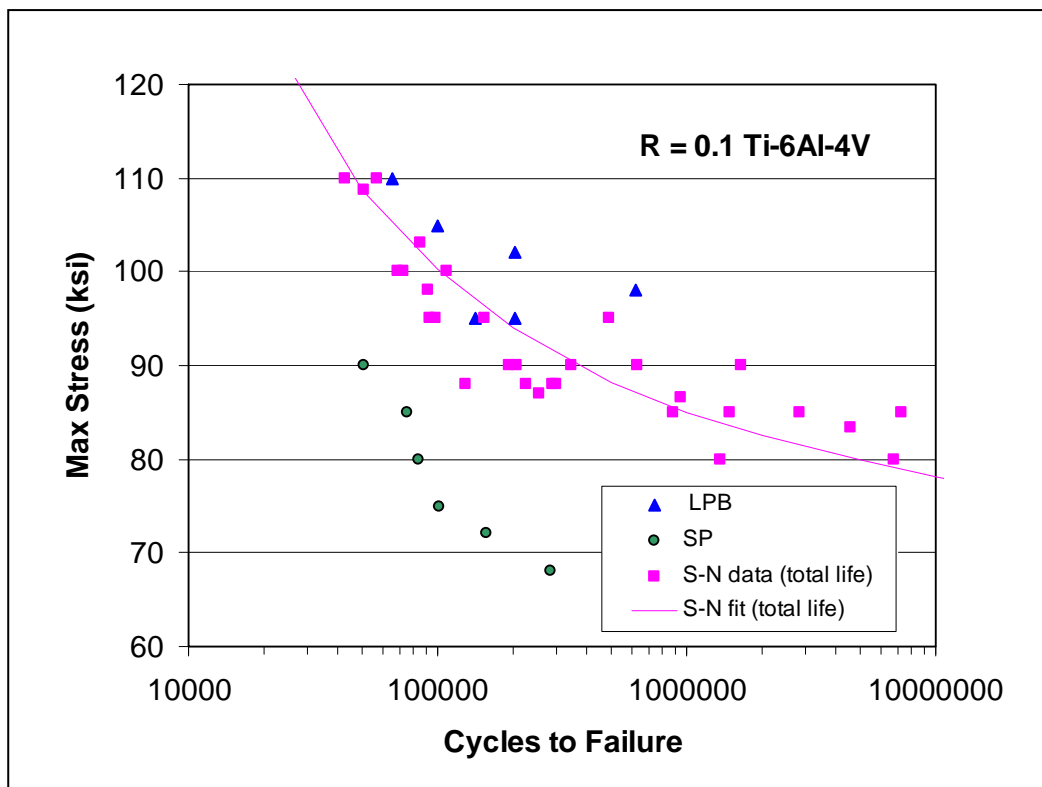
Figure 30. Comparison of Lambda Data for SP and LPB Specimens with HCF PRDA Baseline Smooth Specimen Fatigue Data

33

Preliminary studies with the conventional FaNG model found that the severe compressive stresses associated with the engineered residual stresses led to calculated nucleation lifetimes that were much longer than the observed total fatigue lifetimes; in fact, the calculated nucleation lifetimes were infinite in many cases, because the local stresses were below the smooth specimen endurance limit.

Therefore, it was postulated that the crack nucleation lifetime was zero for both SP and LPB. This might be consistent, for example, with heavy shot peening causing damage to the specimen surface and resulting in immediate crack formation. The physical motivation for this assumption is less clear for LPB, but it is interesting to explore the implications of the assumption. The usual FaNG crack growth life calculation was then performed using the same tabular fatigue crack growth data, the same small-crack model, the same weight function stress intensity factor approach, and the same crack nucleation length (initial crack length) as in the previous validation study on notched Ti-6AL-4V specimens from the HCF PRDA program. The measured residual stress field (SP followed by thermal exposure) reported by Prévey et al. was superimposed with a uniform tensile applied stress at R = 0.1. The actual Lambda geometry is a four-point bend specimen, but the differences between a bend or uniform tension field are negligible at the shortest crack sizes that control the fatigue life. The OPS algorithm was used to superimpose the stress fields.

The calculated local stress ratios for the smallest cracks in the presence of residual stresses are sometimes strongly negative (lower than R = -1). However, baseline FCG rate data are not available at stress ratios lower than R = -1. In order to perform FCG analyses at these low stress ratios, tabular FCG rate curves at R = -2, -3, and -5 were derived from the available R = -1 data using the Newman equations [6] (based on crack closure theory) for the effect of stress ratio.

Figure 31 compares the Prevéy et al. Ti-6Al-4V HCF data for both SP and LPB conditions with the baseline smooth specimen data from the PRDA program and the predictions of the FaNG crack growth model. The agreement between the test data and the FCG predictions is striking. It should be emphasized that these predictions are entirely independent of the test results against which they are compared in this figure; there is no fitting or calibration involved, and all of the material properties used in the predictions were derived from completely independent tests. The implication of these results is that, at least for these coupons, the crack nucleation life (to these small initial crack sizes) appears to be negligible.

Although the LPB predictions agreed well with the central tendencies of the test data, the test data exhibited considerable scatter about this central tendency, and further studies were conducted to investigate the probable sources of this scatter.
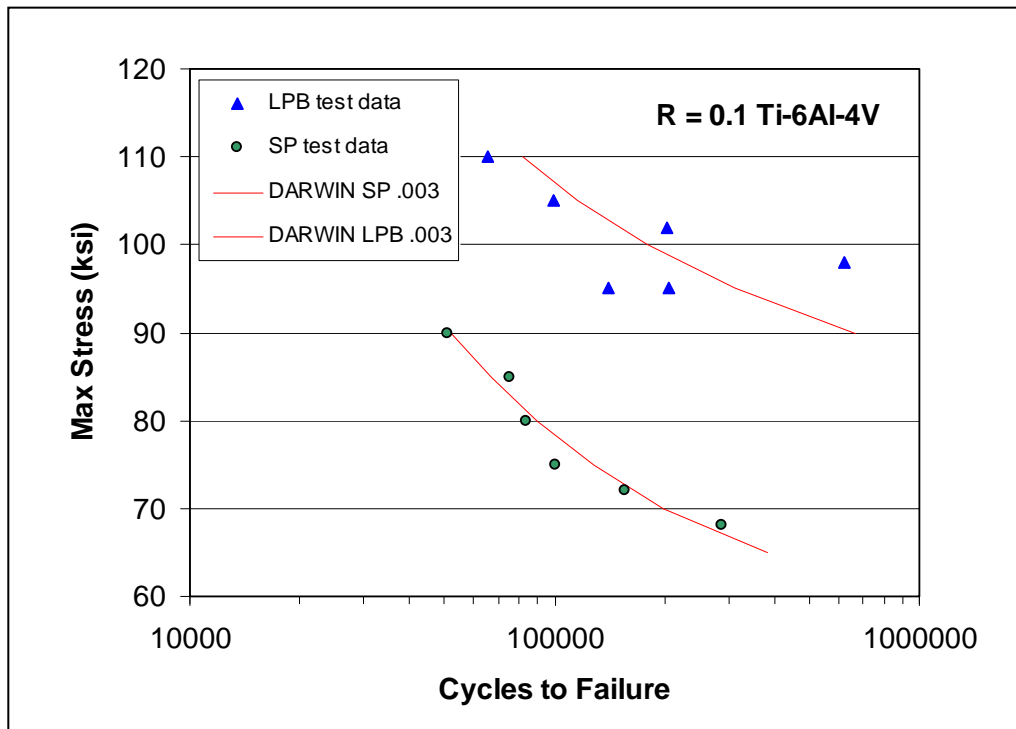
Figure 31. Comparisons of Experimental Fatigue Life Data and FCG Life Predictions for SP and LPB Coupons After Thermal Exposure

In the first sensitivity study, the initial crack size (the nucleation crack size) was varied between 0.002" and 0.006". The resulting family of predicted life curves is shown in Figure 32. Although the small variability in life for these different nucleation crack sizes is consistent with the small variability in observed test life for the SP coupons, the variability in test life for the LPB coupons is generally larger than would be explained by reasonable variability in initial crack sizes. Therefore, other sources of variability were investigated.

Lambda Research has published another study [20] of thermal residual stress relaxation including Ti-6Al-4V. In this study, the residual stress profiles were measured for both SP and Laser Shock Peened (LSP) coupons immediately after surface enhancement and then after various times of thermal exposure at 615 °F (325 °C). The residual stress measurements are shown in Figure 33 for SP coupons and Figure 34 for LSP coupons. Although there is clearly a relaxation in the residual stresses between the baseline (unexposed) and thermally exposed coupons, there does not appear to be a consistent change in the residual stress profile for progressively longer exposure times. Although a progressive decrease in the residual stresses with longer exposure times is physically reasonable, it is possible that it is confounded by measurement error or by location-to-location variability in the initial residual stress field (no replicate measurements were published in this study). The logical next question is how much impact this variability in the residual stresses themselves might have on fatigue life variability for treated coupons.
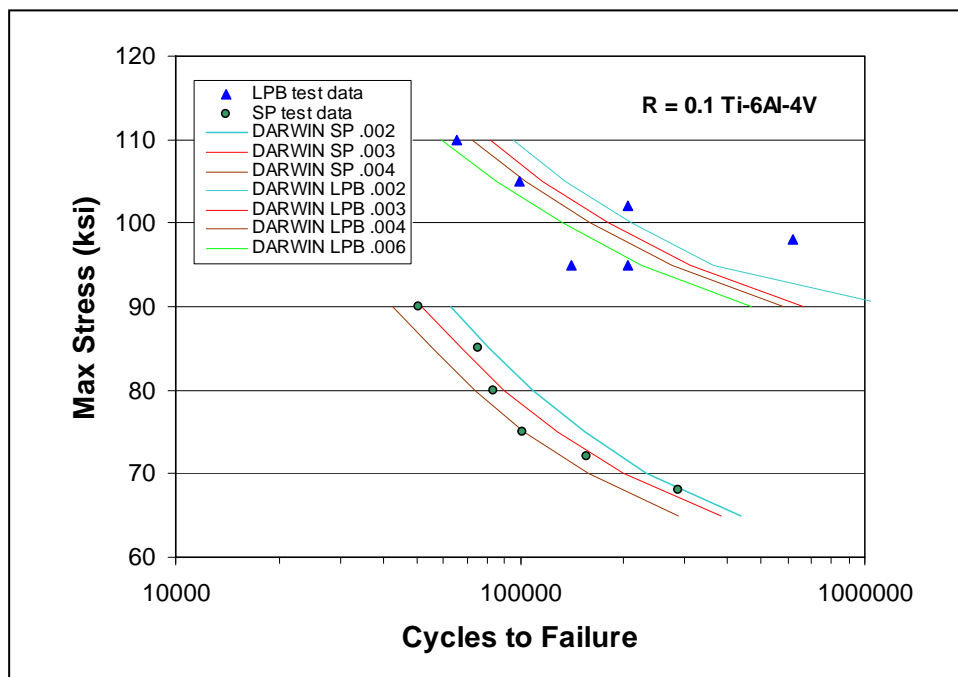
Figure 32. Comparisons of Experimental Fatigue Life Data for SP and LPB Coupons After Thermal Exposure with Fatigue Crack Growth Life Predictions Using Different Initial Crack Sizes
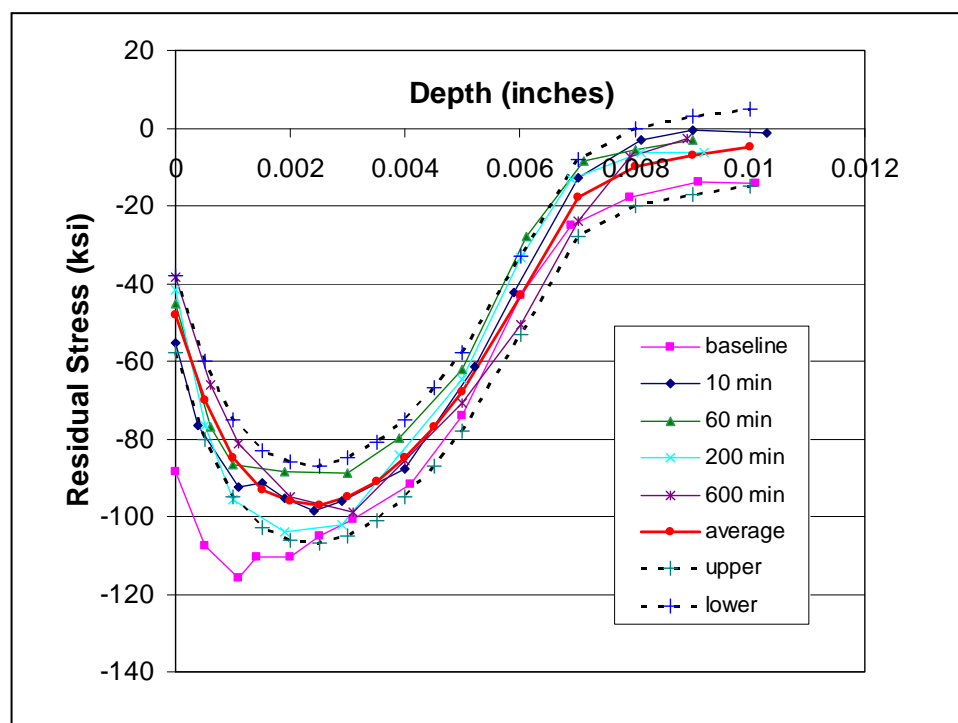
Figure 33. Measured Residual Stresses for Ti-6Al-4V Test Coupons After Shot Peening (Baseline) and After Subsequent Thermal Exposure (615 °F) for Various Lengths of Time
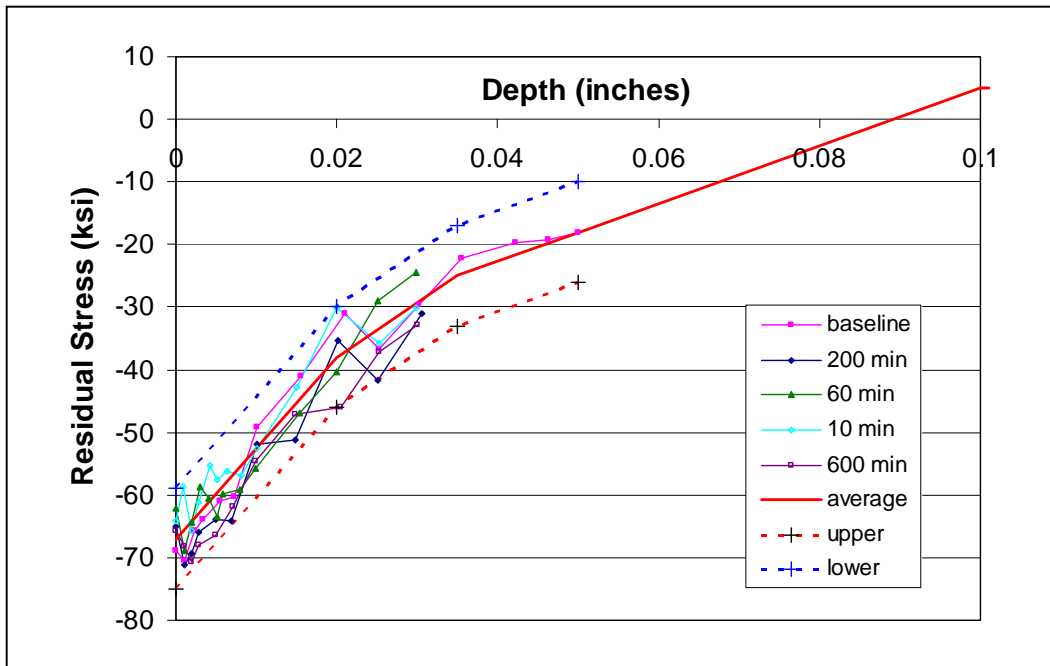
Figure 34. Measured Residual Stresses for Ti-6Al-4V Test Coupons After Laser Shock Peening (Baseline) and After Subsequent Thermal Exposure (615 °F) for Various Lengths of Time

A simple sensitivity study was conducted to address this question. It was observed that the various measured residual stress profiles in Figures 33 and 34 could be enveloped by "bounding" curves that deviated from the "central tendency" curve by either ±10 ksi (SP) or ±8 ksi (LPB). Here the central tendency and bounding curves were informally constructed by eye, not with any formal regressions. Then the residual stress measurements shown in Figure 29 (and used to generate the life predictions in Figure 30) were arbitrarily adjusted by shifting the entire curve up or down by 9 ksi. Finally, the adjusted residual stress curves were used to perform similar fatigue crack growth life predictions, using the same nucleation crack size employed earlier (0.003"). The resulting predictions are shown in Figure 35. The variability in fatigue life observed in the experiments is similar to the life variability predicted by this relatively minor variability in residual stress. This is no proof, of course, but it suggests that further investigations of residual stress variability and its implications for fatigue life variability may be warranted.

Again, this study must be regarded as a preliminary investigation due to its limited scope. Further work is needed to evaluate the method for other materials and other residual stress fields. However, these first results are encouraging and suggest that a careful treatment of fatigue crack growth, following well-defined methodologies, offers promise for accurate evaluation of surface enhancement effects on fatigue life. Other applications involving steep stress gradients, such as those generated by large thermal gradients, should also be explored.
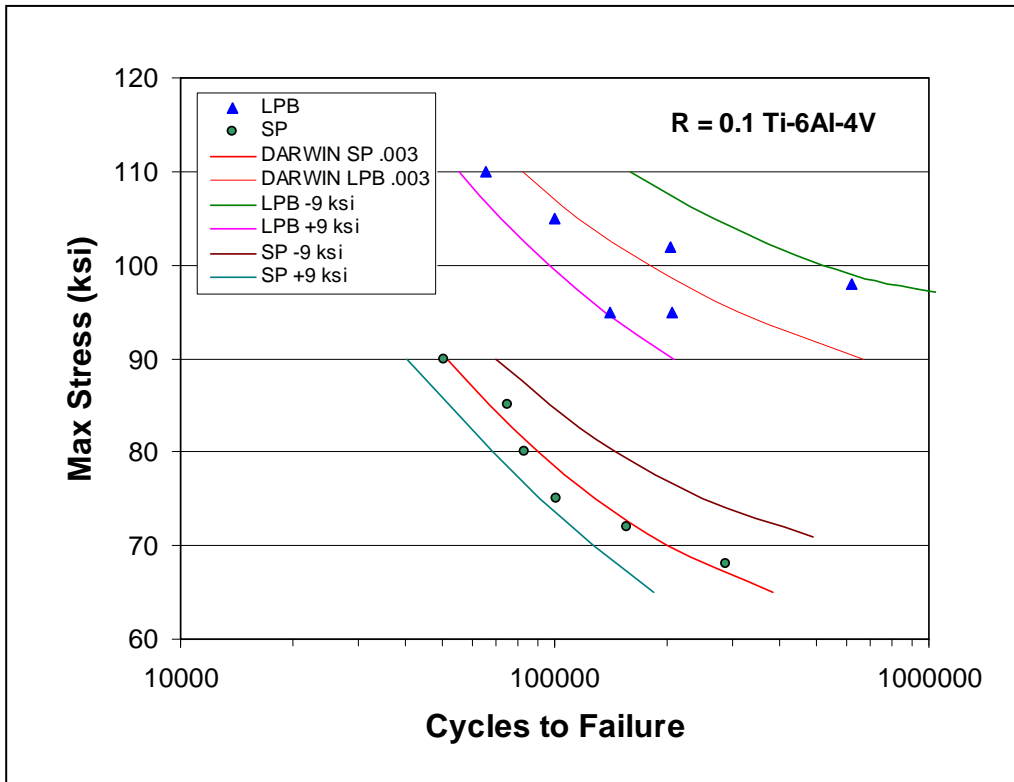
Figure 35. Comparisons of Experimental Fatigue Life Data for SP and LPB Coupons Tested After Thermal Exposure with FCG Life Predictions Using the Measured Residual Stress Profile Shifted Up or Down by 9 ksi

3.3　Predicting Fatigue Life from TACs Versus Usage

The US Department of Defense has traditionally used the concept of TACs for maintenance and inspection scheduling, fatigue life management, and life warranty assessment of fatigue and fracture critical turbine engine components. This concept attempts to characterize the often complex engine usage by a number of effective single-amplitude, LCF cycles. The basic definition of a TAC is provided by an industry consensus Society of Automotive Engineering (SAE) International standard as follows [21]:

$$TAC = LCF + FTC/4 + PTC/40 \qquad\qquad (5)$$

where

   LCF = Low-cycle fatigue cycles ("Intermediate" and above and back to "off")

   FTC = Full-throttle cycle ("Intermediate" and above and back to "idle")

   PTC = Part-throttle cycle ("Cruise" to Intermediate and above and back to "cruise")

and the specific revolutions per minute (RPM) values for these terms are engine specific. As can be seen from Equation (5), the FTC cycles are assumed to be ¼ as damaging as the LCF cycle, consequently four of these FTC cycles would be required to produce damage equivalent to the single LCF cycle. Analogously, 40 of the much small amplitude PTC cycles would be required to produce damage equivalent to the single LCF cycle.   Equation (5) was developed by comparing computed damage from actual measured usage with that from TACs using classical fatigue "crack initiation" analyses, where "crack initiation" is defined as the failure of a smooth, approximately 0.25 in. diameter, fatigue specimen. In other words, the best constants (1/4 and 1/40) in Equation (5) were calibrated using the above analyses for a usages from a variety of different missions.

The work summarized in the remainder of this section is based on a similar analysis using several different fatigue models including classical "crack initiation", growth of small and large cracks, as well as selected combinations of the above, as described in more detail later. The object of this study was develop a better understanding of fatigue lives computed from TACs, as well as to assess whether or not lives computed from TACs are in general conservative relative to those computed from actual mission usage experienced by engines.

3.3.1　Mission Usages Considered

Actual mission usage time histories were provided from Flight Data Recorders (FDRs) by Smiths Aerospace. Since these FDRs include algorithms that counts events (i.e., LCF, FTC, PTC) associated with TACs based on RPM-level crossings, the algorithms employ a modified expression for TACs to account for level crossings that occur within multiple events. For example, an LCF cycle includes also the level crossings associated with a FTC and a PTC, but should be counted as a single TAC. The modified TAC expression that takes this into account is as follows:

$$TAC = LCF + (FTC - LCF)/4 + (PTC - FTC)/40 \qquad (6)$$

where for the engine of interest here the events are defined in terms of either low speed (N1) or high speed (N2) spools of the engine as follows:

N1 Spool:
LCF - RPM below 2000 to above 9500 and back below 2000
FTC - RPM below 5900 to above 9500 and back below 5900
PTC - RPM below 7700 to above 9500 and back below 7700

N2 Spool:
LCF - RPM below 6500 to above 12500 and back below 6500
FTC - RPM below 10250 to above 12500 and back below 10250
PTC - RPM below 11500 to above 12500 and back below 11500

An application example problem was developed to investigate the relationship between TACs and the number of flights to failure. Stress values were obtained by applying N2 (high speed) RPM values from F100 usage histories provided by Smiths Aerospace to a 3D finite element engine disk model calibrated to reference stress and RPM values. Nearly 200 usage histories were considered initially. However, many of the histories were eliminated for various reasons (e.g., mission type could not be identified, usage history was incomplete or was not an actual airborne mission). Of the remaining 31 histories, indicated in Table 1, most of the data were in the Live Fire and Instruments & Navigation categories.

Table 1. F100 Engine Usages Considered for Crack Growth Life Comparisons

Mission Type	Elmendorf	Lakenheath	Mtn. Home	Total
Live Fire	4	0	4	8
Live Fire Missiles	0	2	1	3
ACBT	0	2	0	2
Air to Ground Weapons	0	1	1	2
Instruments & Navigation	0	8	5	13
Transition & Proficiency	0	0	2	2
Functional Check Flight	0	1	0	1
Total	4	14	13	31

3.3.2   Computed Fatigue Lives from Actual Mission Usage Versus TACs

Crack growth life and TAC values were computed for a representative disk using stresses based on the N2 RPM values from F100 usage histories provided by Smiths Aerospace (See Table 1).

To facilitate comparison of computed results for different mission usages a normalization constant N_f^* was selected based on the crack growth life associated with the maximum (0-100%) design RPM for the F100 engine (14,300 RPM for N2 spool), combined with the number of TACs per flight, as shown below:

$$N_f^* = \frac{\textit{Flights to Failure at } 100\% \textit{ Design RPM}}{\textit{TACs per flight}} \tag{7}$$

Fatigue life predictions were performed using several different fatigue models as follows:

1) Classical "crack initiation" using the SWT parameter

$$N_f = N_i^{SWT} \tag{8}$$

2) Classical long-crack fracture mechanics

$$N_f = N_{LC} \tag{9}$$

3) SWT "crack initiation" plus larger crack growth from a 0.030 in. "initiation" crack size

$$N_f = N_i^{SWT} + N_{LC} \tag{10}$$

4) The "true" FAtigue Nucleation and Growth model described in Section 3.1

$$N_f = N_{tn} + (N_{SC} + N_{LC}) \tag{11}$$

where N represents the number of cycles and superscript SWT = SWT parameter and subscripts f = failure, i = initiation, tn = true nucleation, LC = large crack, and SC = small crack.

Figure 36 shows results based on classical crack initiation and the SWT parameter. As can be seen all of these normalized results are greater than 1 indicating the use of TACs is conservative by at least a factor of two on life. This is likely due to the fact that the mean life curve of SWT versus N_f was employed in these calculations, whereas using a mean minus standard deviation curve would reduce to lives.

In comparison Figure 37 shows results based on the classical long-crack fracture mechanics (Equation (8)) with an assumed initial surface flaw size of 15 x 30 mils. As can be seen, many of the normalized life values fall below one indicating that results can be non-conservative when using TACs to compute fatigue life for this case. However, as one might expect the behavior changes significantly when nucleation plus long crack growth is considered as shown in Figure 38; these results are equivalent to adding the results from Figures 36 and 37. Now the predicted lives based on TACs are again conservative and in fact are very similar to the results from the initiation only calculations shown in Figure 36.

41

This similarity is due to the fact that when one assumes a relatively long transition crack size between initiation and growth of 15 X 30 mils, most of the fatigue life is dominated by "initiation". This is the reason for the commonly held perception in the turbine engine industry that LCF of discs is an "initiation" event.

Figure 39 compares the SWT initiation lives with the true nucleation lives as defined within the context of the FaNG model. As can be seen, the resulting livers from the two models are noticeably different since the true nucleation lives are for a nucleation crack depth of 3 mils (see Section 3.2) versus that corresponding to failure of a smooth S-N specimen, which is closer to 30 mils.

If we now compare the total fatigue lives computed from Equations (10) versus (11) as shown in Figure 40 we see that results are very similar. This is because the stress gradient in this problem is rather mild and thus the definition of the transition crack size does not measurably affect the computed fatigue lives. However if we tried to compare results from these same two models for a strip stress gradient, the results would be significantly different since the classical initiation crack size of 30 mils would likely be well outside the region of stress concentration. This is precisely why the classical fatigue initiation methods have difficulty with correctly predicting notch effects particularly when the gradient (or notch root radius) varies from one case to the next.

It is interesting to note that for the missions considered, as well as for most of the models, the normalized life values are significantly greater than one and increase with an increasing number of TACs. This suggests that the TACs-based relationship is conservative when applied to total life values, and conservatism increases as the number of TACs increases. Consequently, the benefit from employing actual usage, rather than TACs, in tracking remaining fatigue life is that some of this conservative margin in the calculations could be used to extend the component life.
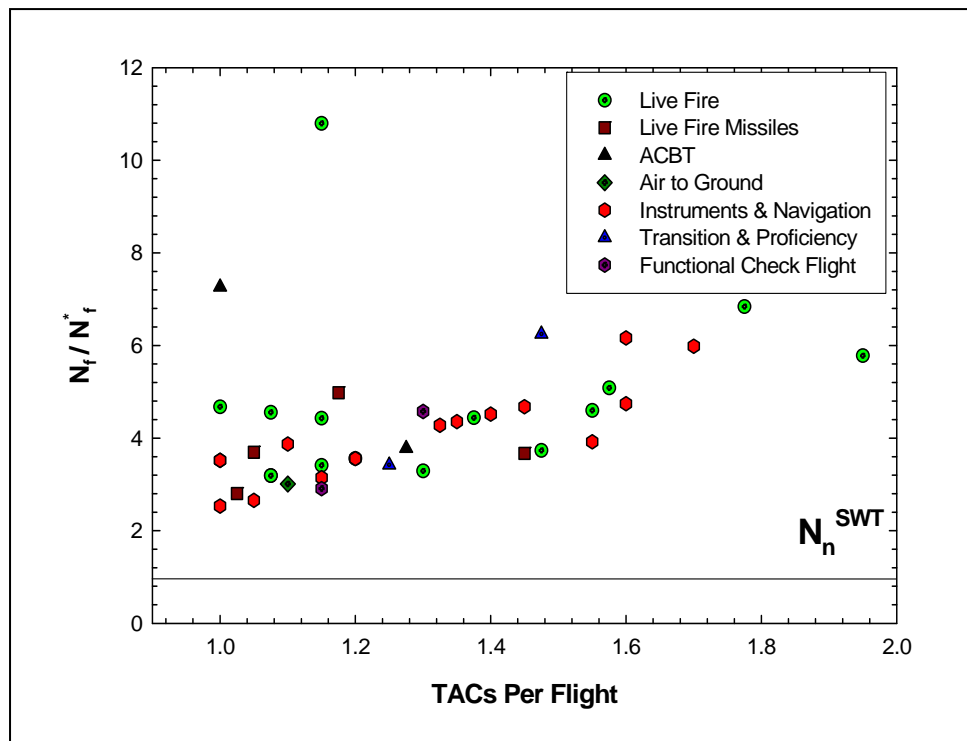
Figure 36. Normalized Nucleation Life (Smith-Watson-Topper Model) Associated with F100 Engine Usage Versus Total Accumulated Cycles per Flight
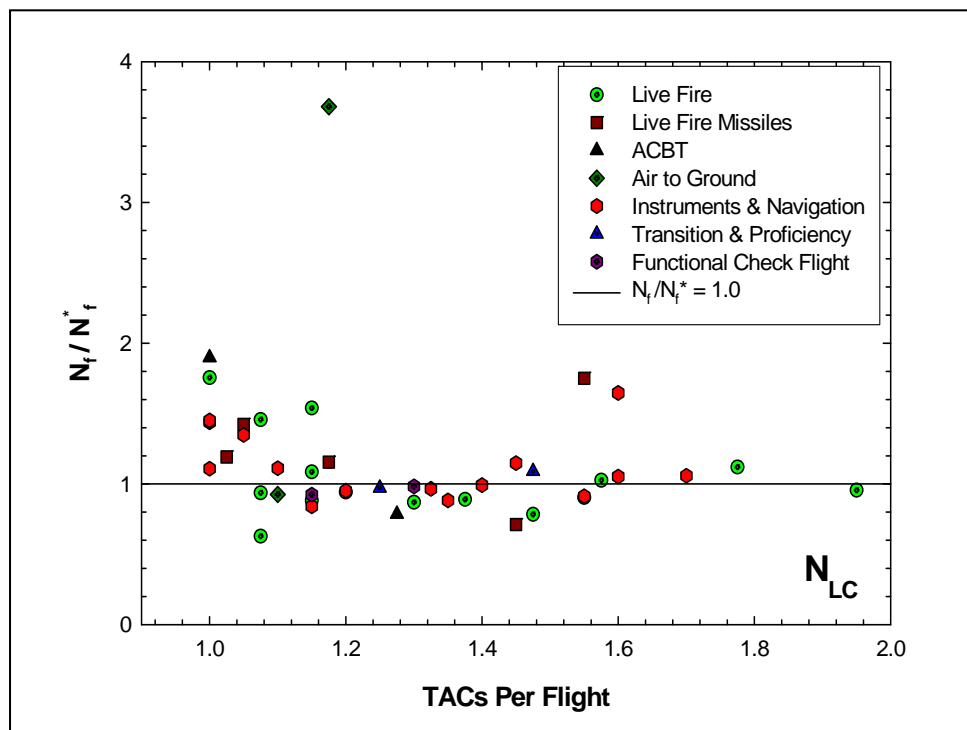
Figure 37. Normalized Large Crack Propagation Life Values Associated with F100 Engine Usage Versus Total Accumulated Cycles per Flight

43
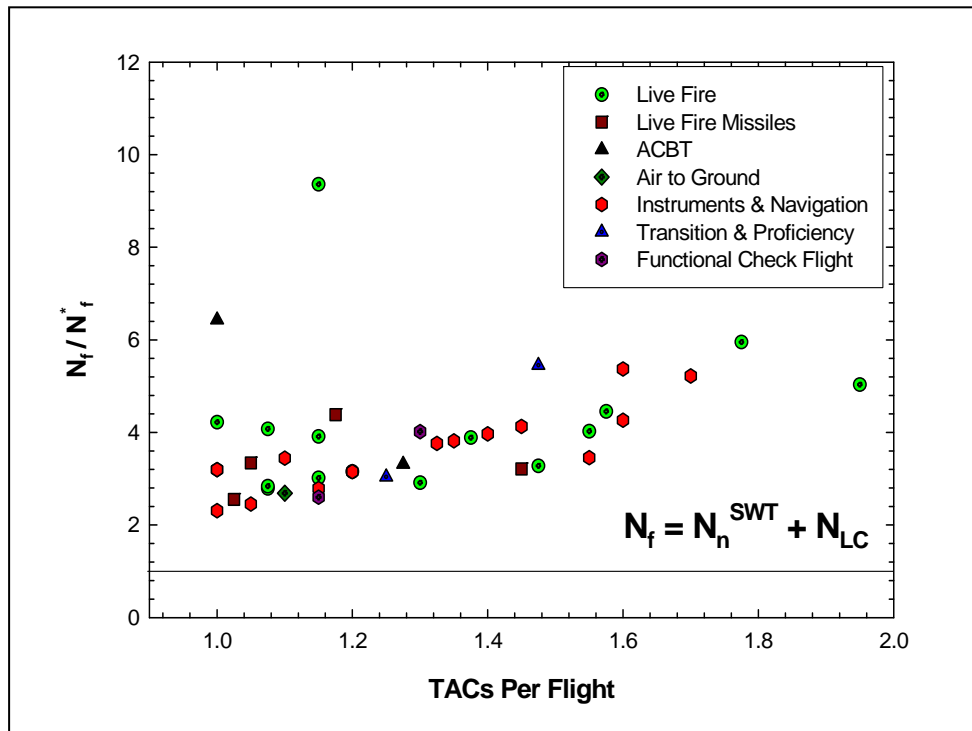
Figure 38. Normalized Nucleation (Smith-Watson-Topper) Plus Propagation Life Associated with F100 Engine Usage Versus Total Accumulated Cycles per Flight
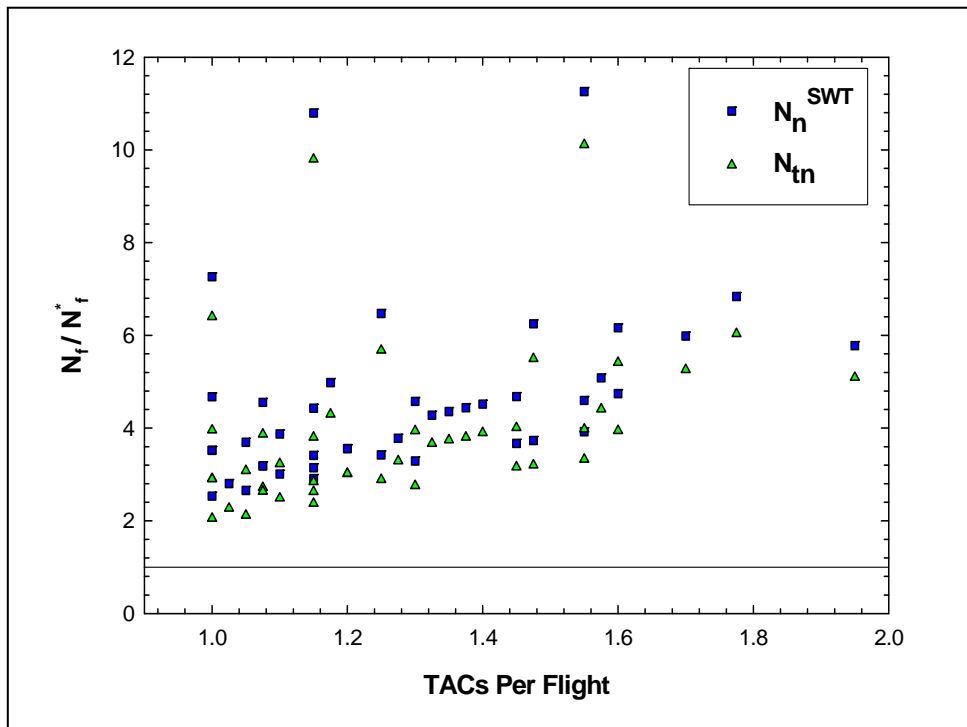
Figure 39. Normalized Crack Nucleation Lives Associated with Smith-Watson-Topper and FaNG Models
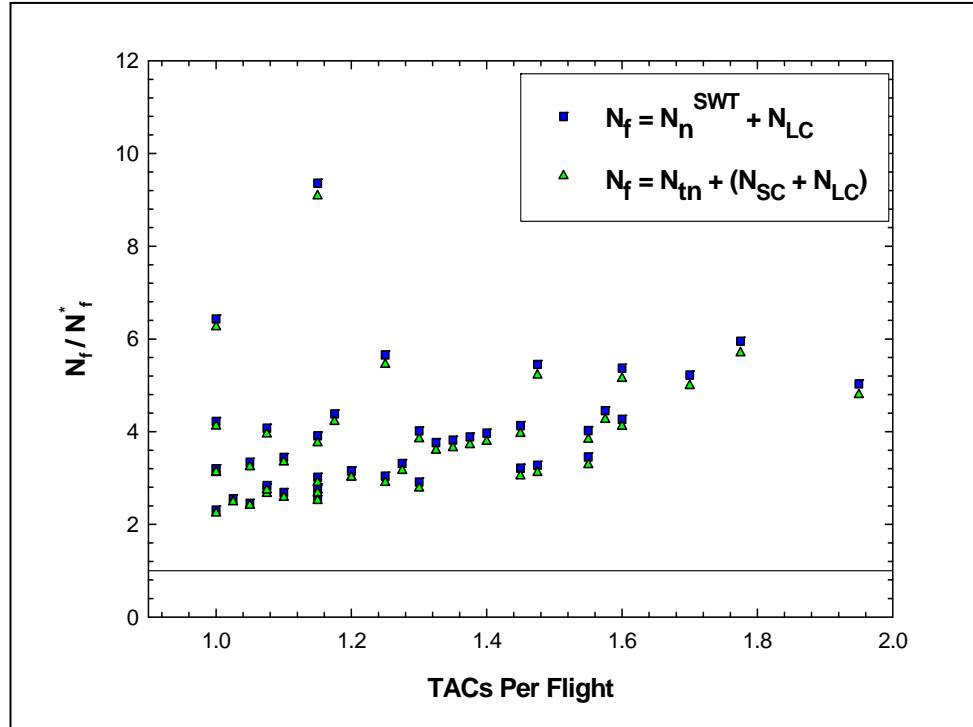
Figure 40. Normalized Crack Nucleation Plus Propagation Lives Associated with Smith-Watson-Topper and FaNG Models

4. Results and Discussion on Enhanced Probabilistic Life Modeling

4.1 Modeling Uncertainty in Fatigue Crack Growth Rates

The dependence of fatigue crack growth rates on ΔK and R-value, $da/dN(\Delta K, R)$, is highly non-linear and often difficult to model over the entire domain from the fatigue crack growth threshold at very low growth rates (10^{-9} mm/cycle) to the approach to crack instability as the material toughness is approached at high growth rates (near 10^{-2} mm/cycle). The response can become even more complex when aggressive environments are present (e.g. seawater or elevated temperature) since under these conditions the cyclic frequency and waveform can influence the rates. Because of the general sigmoidal shape of $da/dN(\Delta K)$ several investigators have employed mathematical function with a similar shape to model fatigue crack growth rate data using additional shape factors, rotational factors and asymptotes at the crack growth rate extremes. However, as has been pointed out [22, 23] these asymptotic models are problematic in the near-threshold regime where they often over-estimate the fatigue crack growth threshold and under estimate the crack growth rates, both of which are non-conservative. Moreover, these lower asymptotes present practical problems when attempting to quantify their uncertainty for use in probabilistic analysis of components and structures.

In this section, Ti-6-4 fatigue crack growth rate data generated in air at room temperature by three different laboratories under the Air Force Office of Scientific Research–High Cycle Fatigue (AFOSR–HCF) program [2, 4, 5] were analyzed. Their uncertainty was also quantified such that the results could be used to characterize fatigue crack growth rates as a random material variable in a probabilistic life assessment. Near the fatigue crack growth threshold accuracy was modeled in terms of ΔK, whereas for higher crack growth rates accuracy was modeled in terms of the crack growth rates themselves. The two-phase procedure to fit the parameters is outlined below. Due to the functional form of the multicomponent model employed, the parameters that describe the behavior near the threshold can be estimated independently from the parameters in the Paris regime. Once the best-fit parameters are identified, the variations in the best-fit parameters among individual specimens and from the different labs are described using random variables.

Ideally the random variable model is specifically tailored to the application and takes maximum advantage of the model form and physics behind the data; e.g.: based on physical considerations, one may decide to keep the Paris slope independent of the stress-ratio R. Although many crack growth data were available, rather few complete fatigue crack growth rate curves, covering the entire domain from the crack growth threshold to the fracture toughness instability limit, were available. The data set was somewhat limited, particularly for the largest crack growth rates; nevertheless, uncertainty quantification could be performed near the threshold and at intermediate crack growth rates, which are often of most interest in fatigue crack growth analyses of components and structures.

The uncertainty modeling approach and its implementation is described below. First, the model relating fatigue crack growth rate (da/dN) as a function of crack-tip stress intensity range (ΔK) is described, model coefficients and their R-dependence are estimated, and finally the overall uncertainty is quantified.

4.1.1   The Multicomponent Model

Typical Ti-6Al-4V fatigue crack growth rate data are shown in Figure 41 [2, 4, 5]. Because of the modeling difficulties and errors associated with asymptotic models a multicomponent crack growth rate equation is employed. This multicomponent model is a generalization of the three-component model previously developed by Saxena and Hudak [22]. Multicomponents are required for application to T-6Al-4V because of the complex behavior exhibited, as shown in Figure 41. These multicomponents are associated with the following crack growth rate regimes:

- Region 1: The near-threshold regime at very small crack growth rates (roughly below 3×10^{-7} mm/cycle), where the da/dN–ΔK slope is very steep.
- Region 2: The classical Paris crack growth rate region.
- Region 3: An accelerated crack growth region.
- Region 4: A crack growth region similar to Paris region.
- Region 5: The accelerated crack growth corresponding to the onset of instability.

The transition between Region 1 and 2 is marked by different physical crack growth phenomena on the micro-structural scale. Also the acceleration in crack growth rates in Region 3 may be due to an environmental effect. Therefore, a series of two-component models is proposed: one for the Region 1-2 transition and one for the Region 3-4 behavior.

$$
\frac{da}{dN} = \max \left\{
\begin{array}{l}
\left[\dfrac{1}{C_1 \Delta K^{m_1}} + \dfrac{1}{C_2 \Delta K^{m_2}} - \dfrac{1}{C_2 \left[(1-R) K_c\right]^2 \Delta K^{m_2 - 2}} \right]^{-1}, \\[4ex]
\left[\dfrac{1}{C_3 \Delta K^{m_3}} + \dfrac{1}{C_4 \Delta K^{m_4}} - \dfrac{1}{C_4 \left[(1-R) K_c\right]^2 \Delta K^{m_4 - 2}} \right]^{-1}
\end{array}
\right\}
$$

(12)

The model is set up such that the largest crack growth rate predicted by the series of two-component models is selected. Note that both two-component models have the same fracture roughness K_c; this ensures that the Region 1-2 component produces da/dN rates below the Region 3-4-5 da/dN rates. It should also be noted that unless R is very high, the instability term of the Region 1-2 model is never exercised.

In this equation, C_1 and m_1 are constants in the first component that describes crack growth in the near-threshold regime, C_2 and m_2 are constants in the second component that describes crack growth in the classical Paris regime, and the third term allows for accelerated growth near instability due to the onset of monotonic failure modes. R is the stress ratio, K_{min}/K_{max}, and K_c is the fracture toughness. Note that this three-component model does not require an asymptotic in the near-threshold (Region 1), although as discussed later it is useful to define an operational threshold when comparing results with data or defining the influence of load ratio in this regime. Analogous parameters exist for the component that describes the Region 3-4-5 behavior.
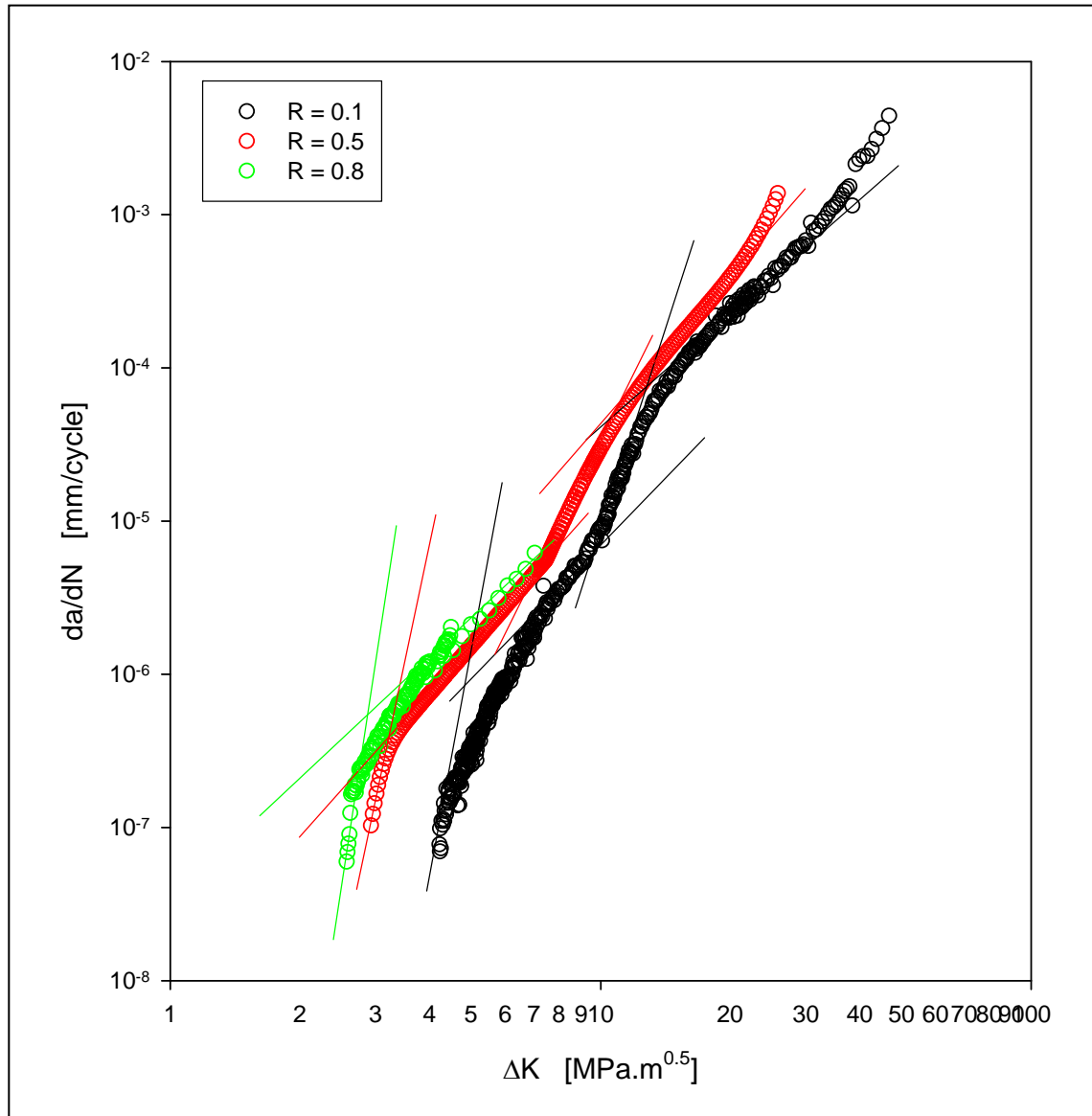
Figure 41. Ti-6Al-4V Data Obtained at Various R-Values by Lab 1

4.1.2 Estimating Model Coefficients

Least squares fits of da/dN(ΔK) data are usually accomplished by minimizing the squared difference between the observed and predicted da/dN values. This is still applicable in Region 2-3-4 and perhaps 5; for Region 1, however, it makes more sense to minimize the error on ΔK for a given da/dN crack growth rate.

Also, it is more convenient to estimate $\log(C_i)$ as a parameter than the intercept value C_i itself. Because the intercept values are orders of magnitude different from the slopes m_i, the least squares problem is numerically much better behaved.

In principle it is possible, though numerically somewhat unstable, to estimate all coefficients simultaneously in a single least squares optimization problem. The process can be much improved, however, by separating the fitting into the two physical components or regions of most interest (Region 1, Region 2, and Regions 3-4-5). Since the model is asymptotic near the upper end instability, an inequality constraint must be introduced for K_c. It suffices to require K_c to be greater or equal to the largest measured value of ΔK/(1-R).

In Region 1, the error is measured on ΔK. For ΔK values, close enough to the threshold the second and third component of the crack growth equation do not significantly contribute to the total crack growth rate. This is shown in Reference [23]. Although the use of this approximation (ignoring the second and third terms in the crack growth equation) requires the analyst to judge the crack growth rate da/dN at which the transition to Region 2 begins, it greatly simplifies the computational process.
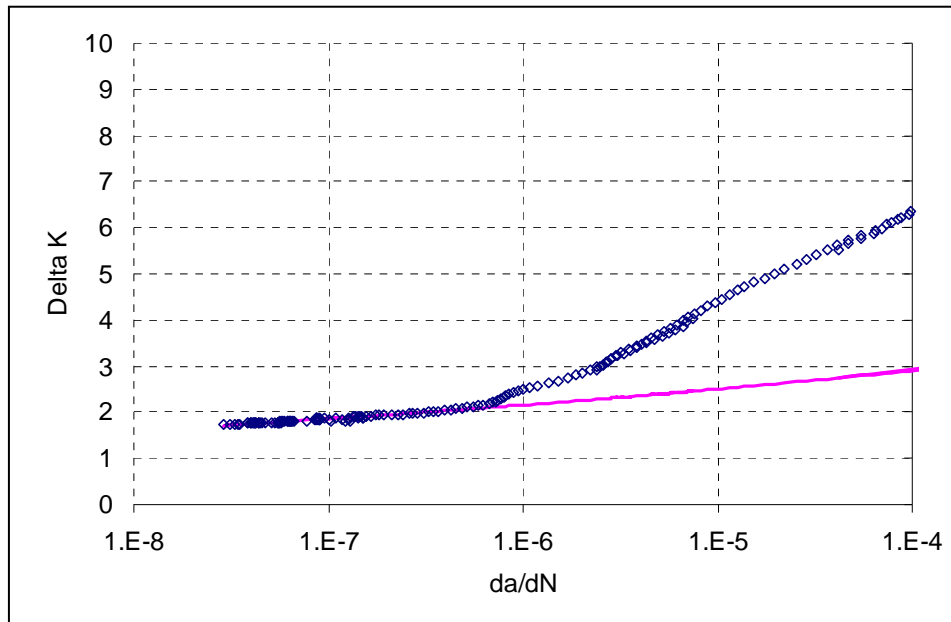
Figure 42. Fitting of ΔK in Terms of da/dN near the Threshold

49

In Region 2, the error in measured on the crack growth rate. For ΔK values in the Paris regime, the first and third components do not significantly contribute to the total crack growth rate. Although the use of this approximation (ignoring the first and third terms in the crack growth equation) requires the analyst the judge the crack growth rate da/dN at which the transition to and from Region 2 begins, it greatly simplifies the computational process. The quality of the combined fit is readily assessed by plotting the combined three components against the experimental data (see Figure 43). It should be noted that – for fitting purposes – there might be some gap between the end of the threshold fit region and the beginning of the Paris region. This "gap region" in the least-square analysis represents the gradual transition between the threshold and Paris regions.
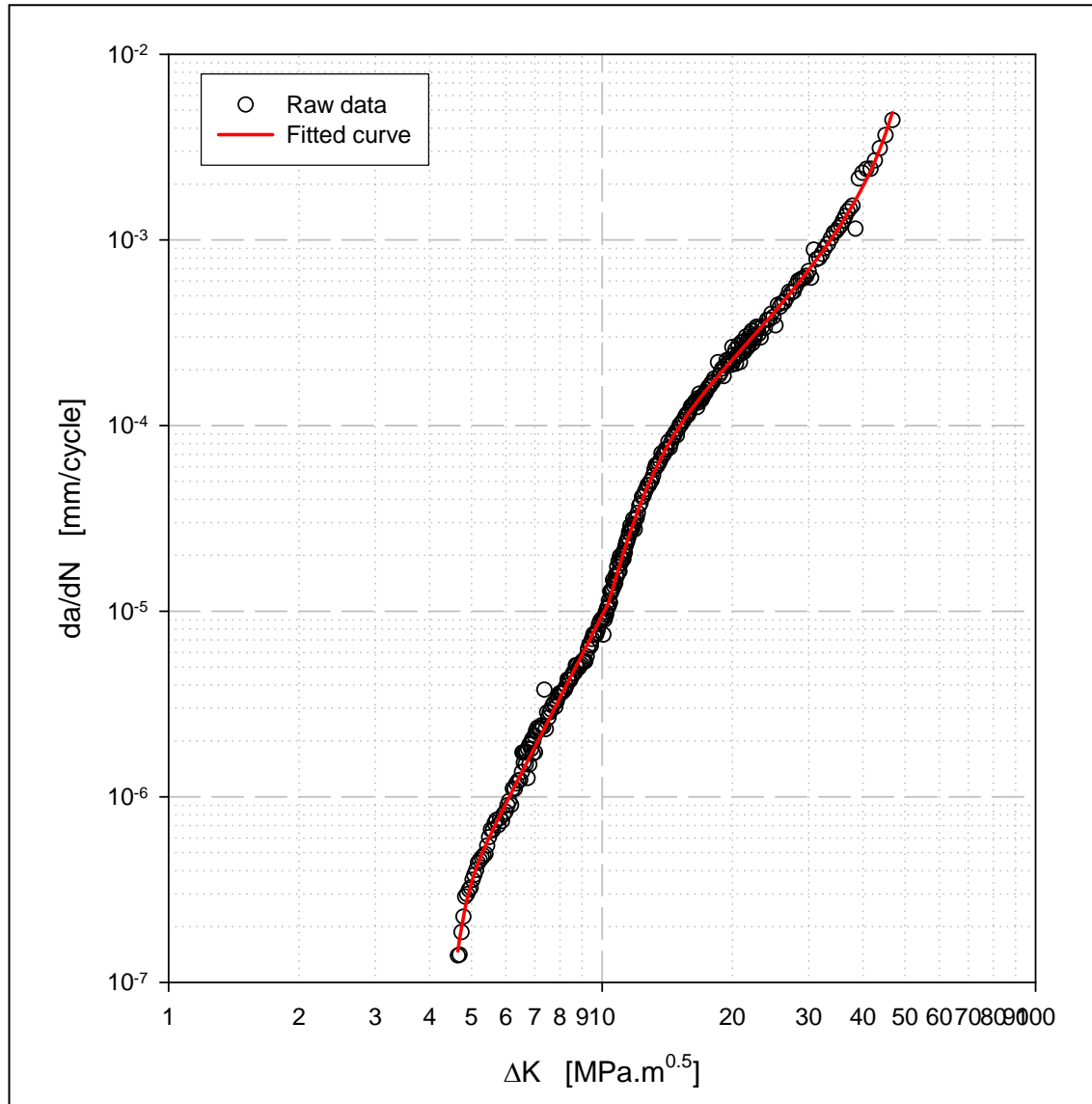
Figure 43. **Comparison of Experimental Data and Model Predictions (Lab 1, R = 0.1)**

Although considerable scatter exists between lab results (crack growth rates differ by up to half an order of magnitude), the raw data for all labs generally overlap. This is shown in Figure 44. Several Lab 2 specimens were analyzed (see Figure 45). Testing a specimen consists of several start-stop segments; each of these start-stop sequences introduces measurement error (see Figure 45) and also some transient effects (see Figure 50). In some cases, it was readily apparent which segments should be eliminated from the database (Figure 49). In many cases it was not possible to discern which individual pieces should be used and in these circumstances all data were used and a single best-fit curve was determined (see specimen 2 in Figure 45). It should be noted that this procedure may underestimate the inherent variability of the data.

Figure 43, Figure 45, and Figure 46 reveal that the multicomponent model is capable of accurately following the transitions between all zones and can adequately capture the environmental effects observed in the raw data for R = 0.1. Figure 47 illustrates the data fit at R = 0.5 Figure 48, Figure 49, and Figure 50 illustrate the data fits for R = 0.8; for the high R very few data sets were available over the entire da/dN(ΔK) domain; consequently, in many cases the fits had to be limited to the Regions 1 and 2 .

The "bulge" associated with Regions 3 and 4 is readily visible in Figure 43, Figure 45, and Figure 46 for R = 0.1, Figure 47 for R = 0.5 and Figure 49 for R = 0.8. The "bulge" becomes less pronounced with increasing R, which is a further indication that this is an environmental effect. The effect seems to be ΔK related and not rate dependent; it occurs near 11-13 MPa.m$^{0.5}$ for all R-values.
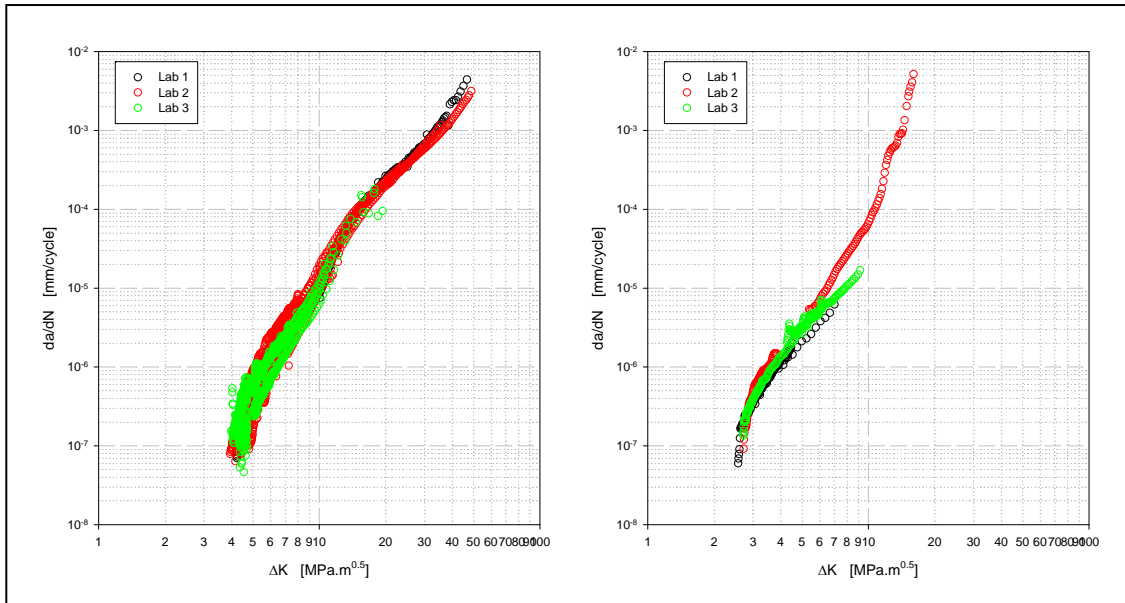
Figure 44. **Comparison Between Results from Different Labs at R = 0.1 (Left) and R = 0.8 (Right)**
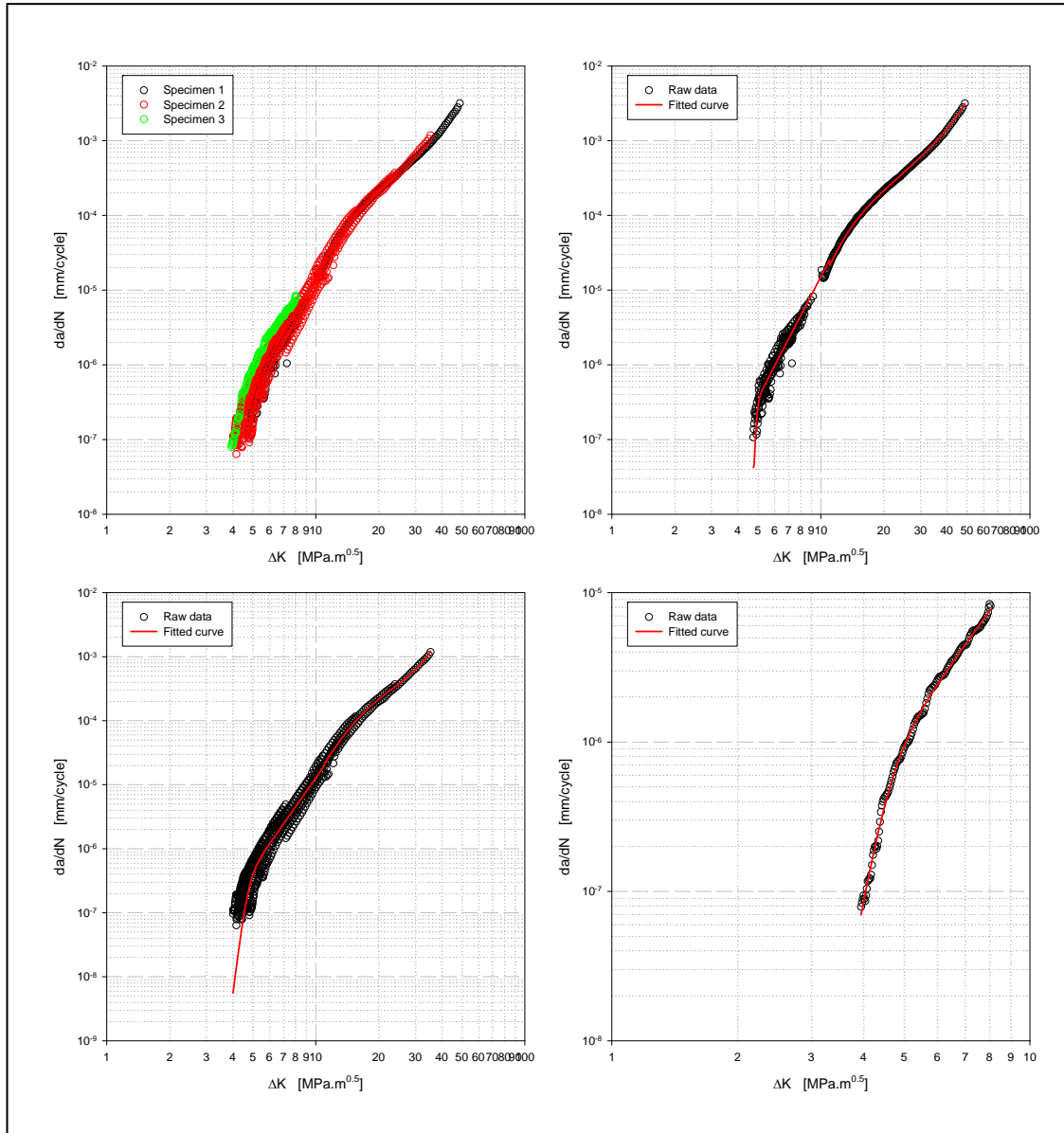
Figure 45. **Comparison of Individual Experimental Data Sets and Model Predictions (Lab 2, R = 0.1)**
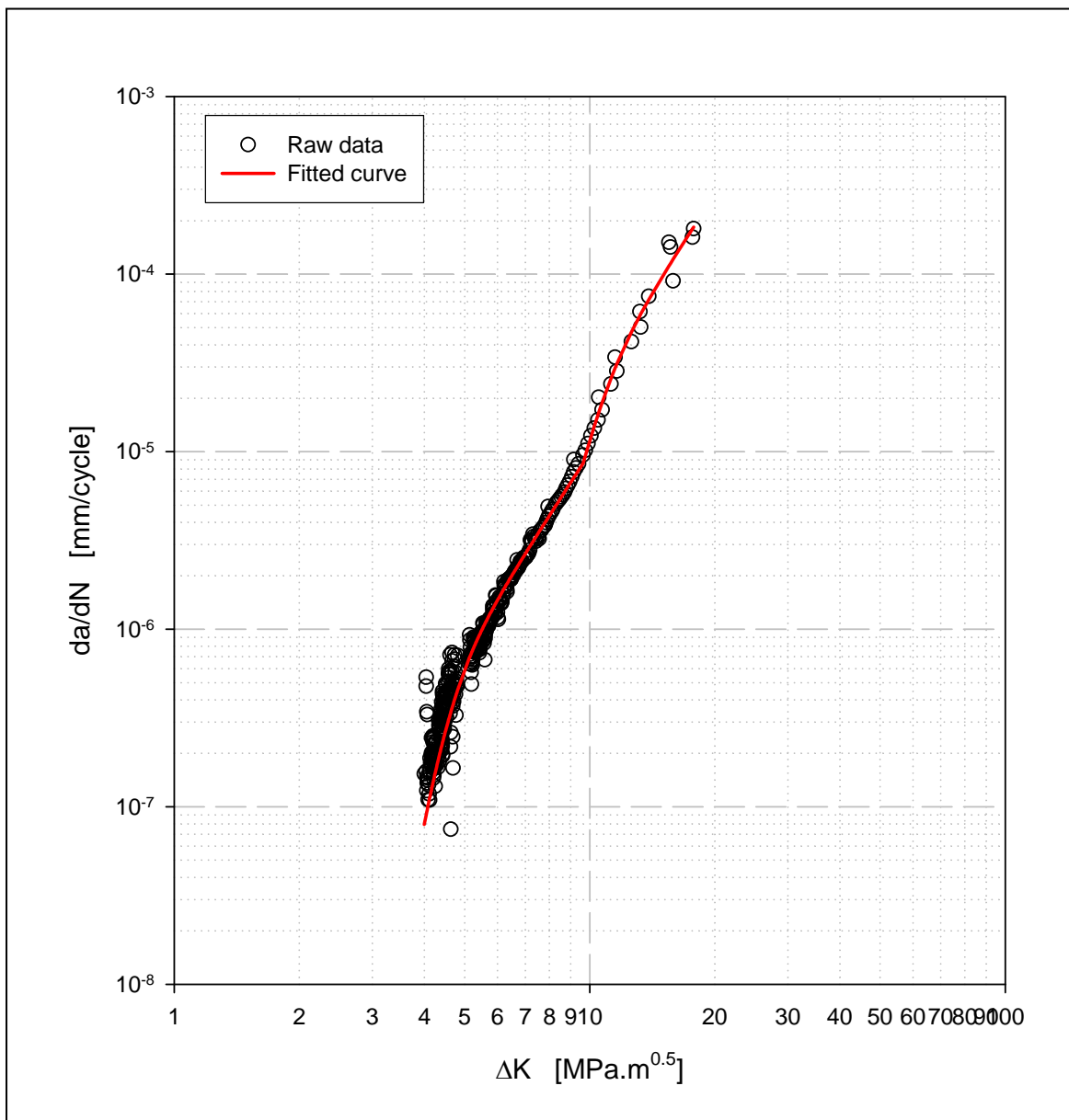
Figure 46. Comparison of Experimental Data and Model Predictions (Lab 3, R = 0.1)
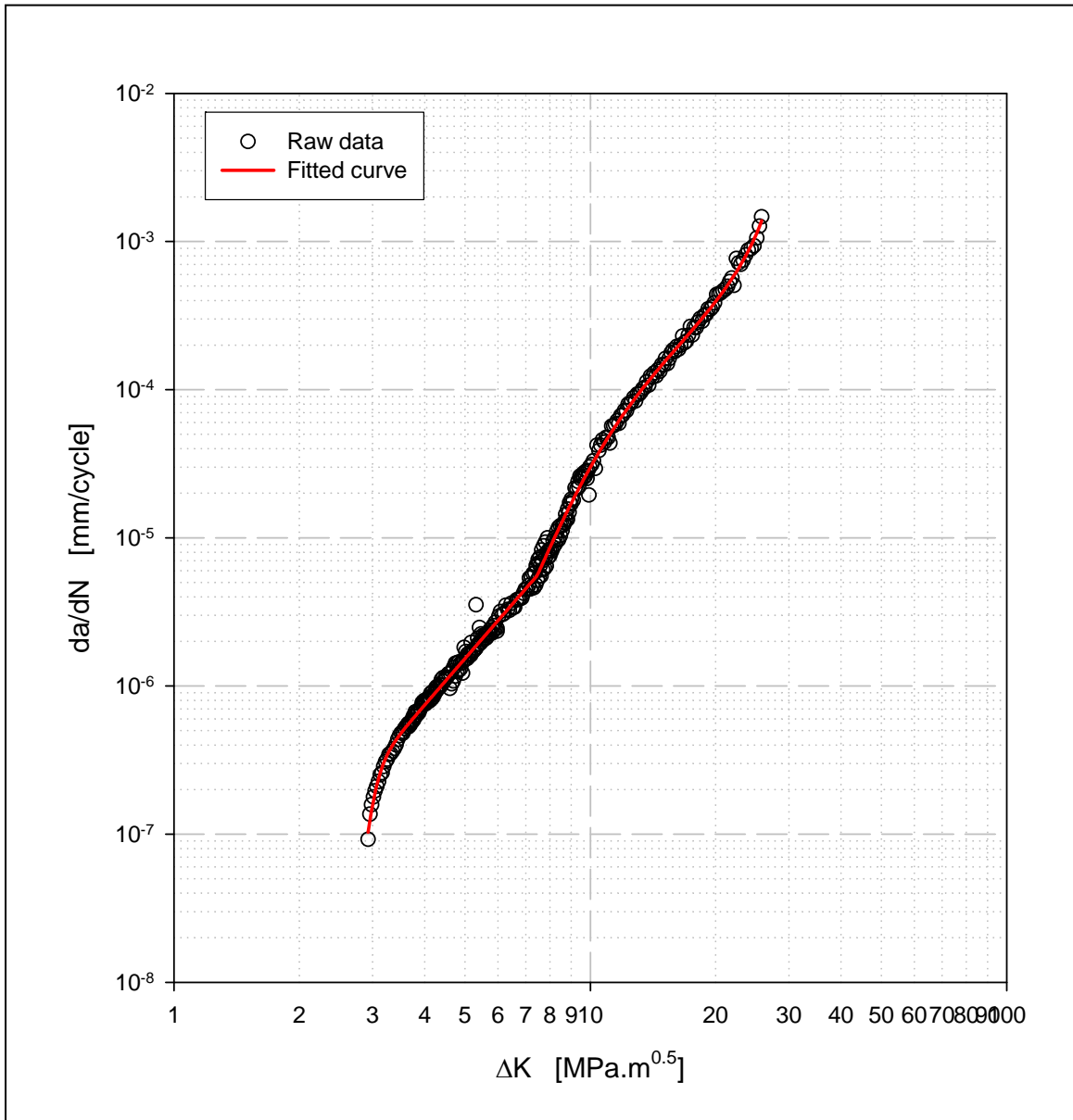
Figure 47. Comparison of Experimental Data and Model Predictions (Lab 1, R = 0.5)
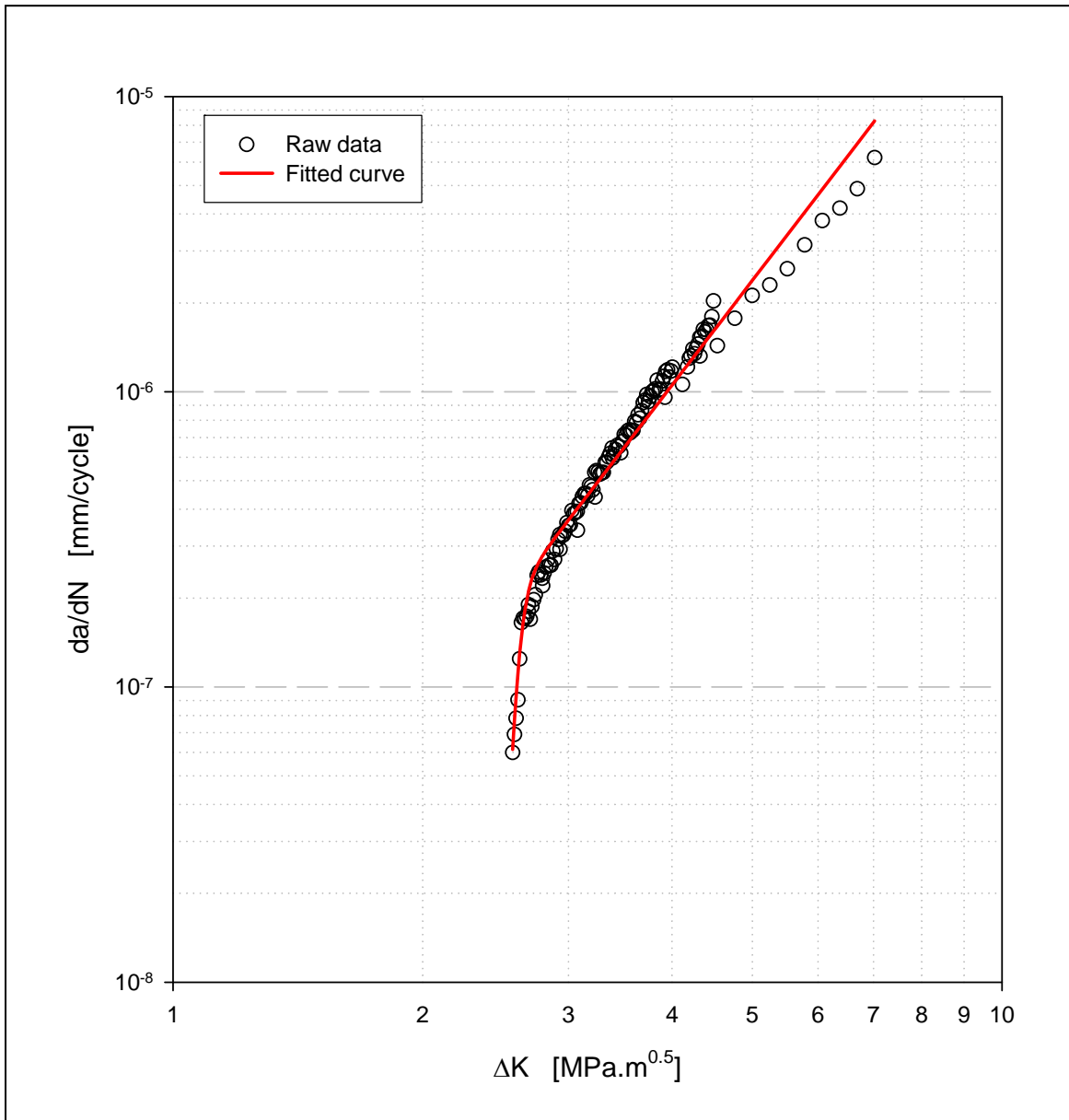
Figure 48. **Comparison of Experimental Data and Model Predictions (Lab 1, R = 0.8)**
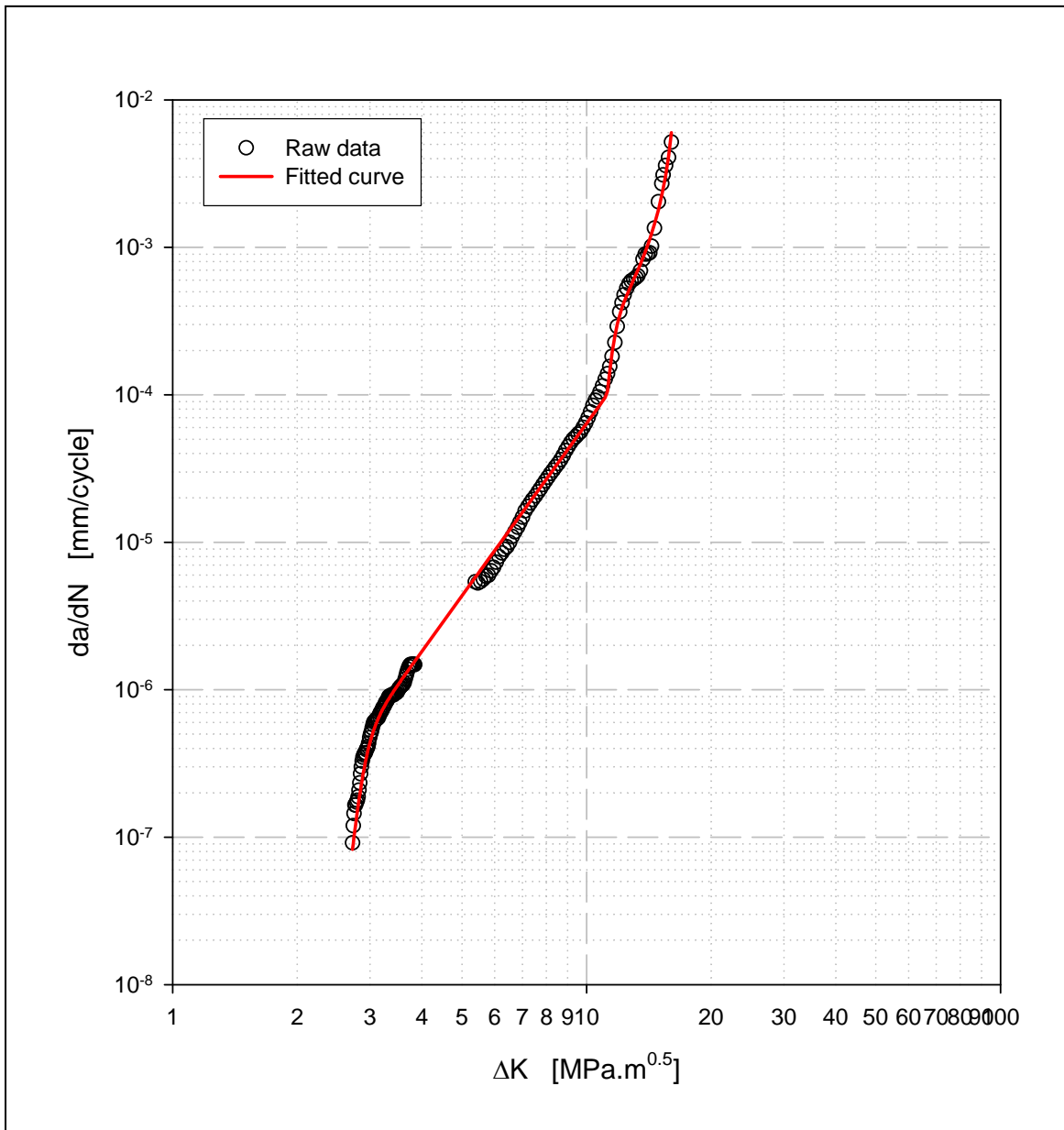
Figure 49. **Comparison of Experimental Data and Model Predictions (Lab 2, R = 0.8)**
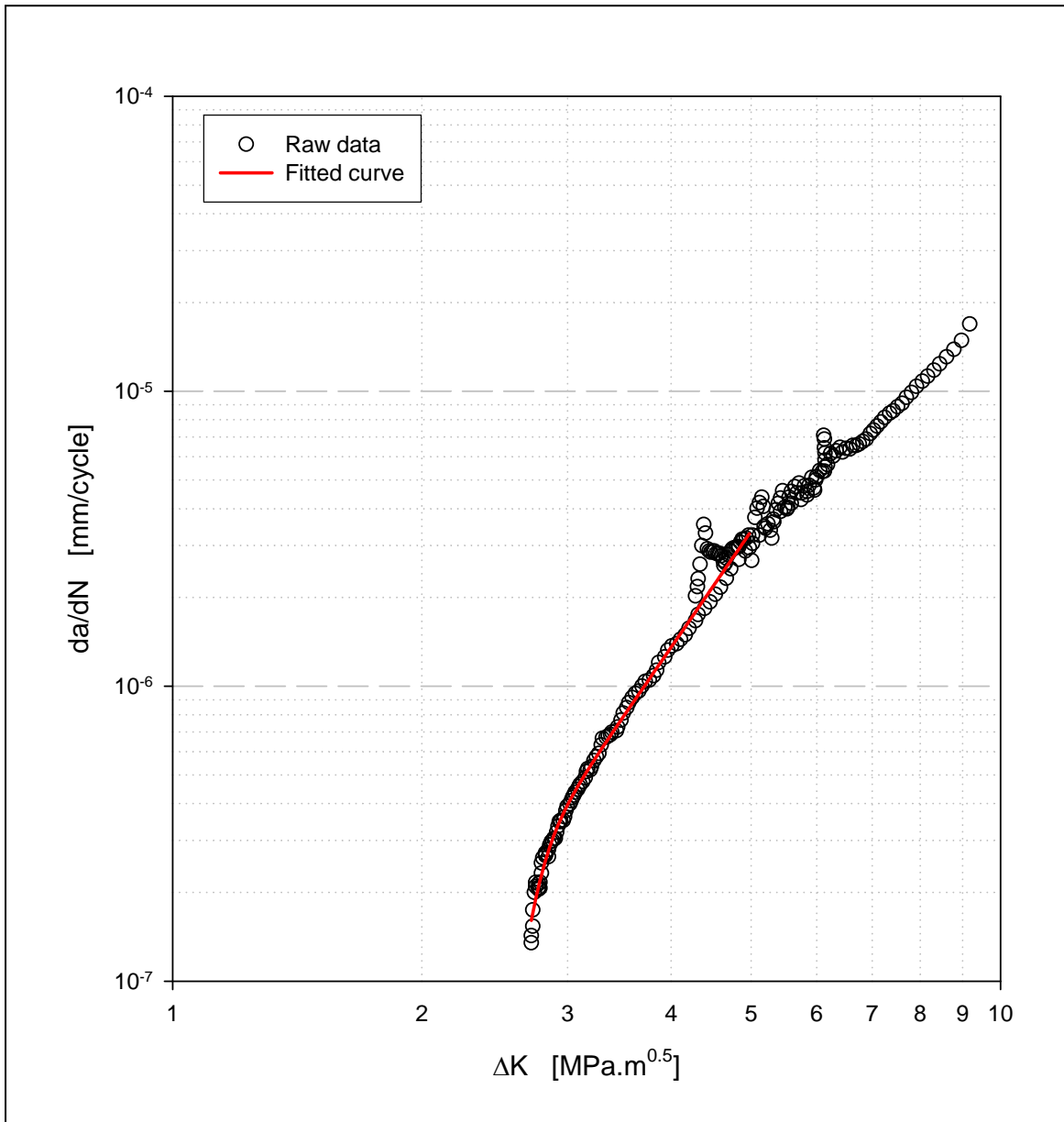
Figure 50. Comparison of Experimental Data and Model Predictions (Lab 3, R = 0.8)

4.1.3   R-Dependence of the Model

Often an effective ΔK (ΔK_{eff}) is used to correct the experimental data for crack closure. in attempting to collapse fatigue crack growth rates obtained at various R-values onto a single curve for which the crack growth parameters can then be estimated. Figure 41 indicates that the necessary closure correction would not only be R-dependent but also very non-linear with ΔK, or crack growth regime.

An alternative approach, which is proposed here, is to account for the R-dependence by making certain of the crack growth rate modeling parameters' functional dependence on R. Figure 51 shows the fluctuation of the Paris slope and log(intercept) as functions of R. Due to the limited data, it is difficult to unequivocally determine whether or not the Paris slope is a function of R. The following questions will be addressed:

-   Are the mean values of the crack growth parameters independent of R?
-   Is the uncertainty on the crack growth parameters independent of R?
-   Is there a statistical dependence (e.g. correlation) between the crack growth parameters?

Different modeling approaches are certainly possible. If, for instance, it is believed that the Paris slope should be R-independent, the individual data sets could be refitted while setting the Paris slope equal to the average values obtained for all specimens, and subsequently recomputing the intercepts using least squares. Alternatively, based on the data presented in Figure 41 one could require that the slope in Region 2 and 4 be equal since both segments represent the Paris regime. In that case, Region 3 is interpreted as a temporary acceleration of the crack growth due to environmental effects. However, none of these alternate modeling approaches have been pursued.
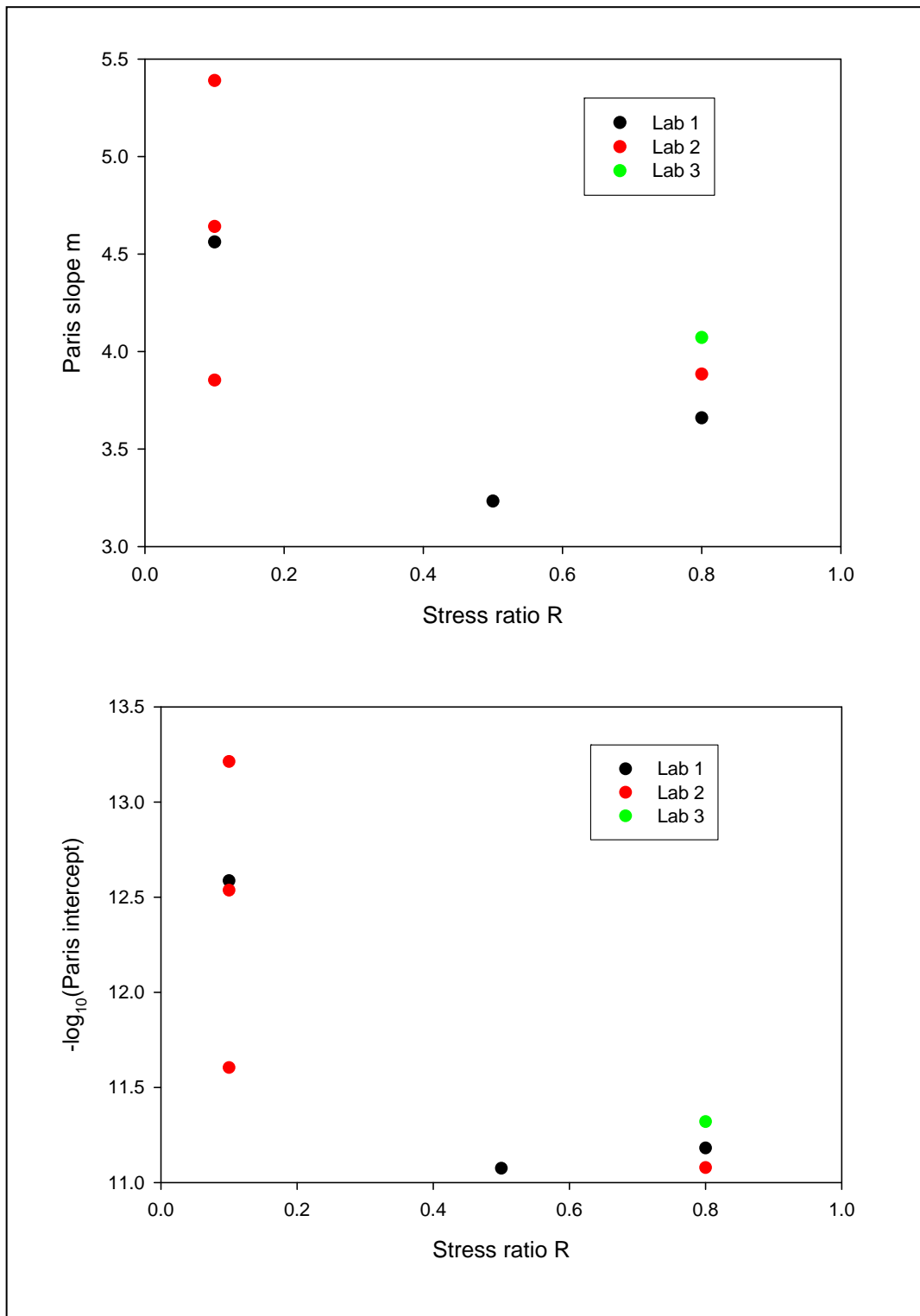
Figure 51. R-Dependence of Crack Growth Parameters in Paris Regime

Figure 52 shows the dependence of the operational threshold ΔK_{th} on R. The operational threshold is defined here as the ΔK value at a crack growth rate equal to 1×10^{-7} mm/cycle to be consistent with the definition employed by ASTM when measuring fatigue crack growth rates and ΔK_{th} values. Again, insufficient data are available to determine whether a linear R-dependence can be applied to ΔK_{th}.
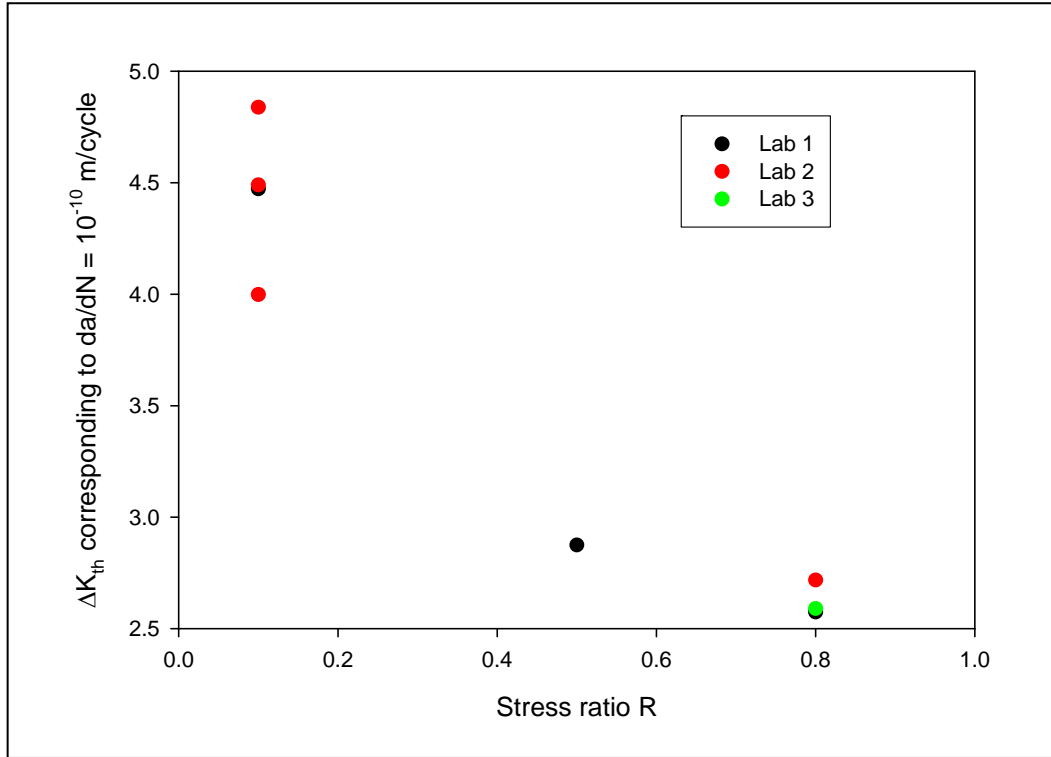
Figure 52. **R-Dependence of Threshold Parameter ΔK_{th}**
(Corresponding to da/dN = 1 x 10^{-7} mm/cycle)

4.1.4 Uncertainty Quantification

It should be mentioned that the rapid fluctuation along a specific da/dN curve is generally not of much interest in the prediction of lives. The main consideration is to quantify the uncertainty on the best fit curves. Although the data set is somewhat limited, particularly when it comes to estimating the uncertainties in Regions 3-4-5, some uncertainty quantification can be performed in Regions 1 and 2 (which were the focus of the HCF program and are of most interest to fatigue in aircraft components and structures. A more comprehensive data set would also enable the uncertainties in Regions 3-4-5 to be assessed in similar fashion.

For Region 1 the discussion will be limited to the threshold parameter: ΔK_{th} (Figure 52). The coefficient of variation on the threshold parameter ΔK_{th} coefficient of variation (COV) is 7% for R = 0.1 and 3% for R = 0.8. Insufficient data are available to determine the COV

of ΔK_{th} at R = 0.5. Because of the additional amount of closure, and the micro-scale deformations due to this closure, it is quite typical to observe more scatter for R = 0.1 than for R = 0.8. Although limited data are available at both R = 0.1 and R = 0.8, the standardized normal probability plot in Figure 53 suggests that a Normal distribution may be a reasonable assumption for distribution of ΔK_{th}. A summary of all parameters and their uncertainty is given in Table 2.

Table 2. Summary Statistics of the Crack Growth Parameters
in the Threshold (Region 1) and Paris Regimes (Region 2)

	R = 0.1		R = 0.5	R = 0.8	
	Mean	**Sigma**	**Value**	**Mean**	**Sigma**
Threshold ΔK_{th}	4.43	0.30	2.87	2.63	0.08
-Log_{10}(intercept)	12.48	0.57	11.07	11.19	0.12
Paris Slope	4.60	0.54	3.23	3.87	0.21

In Region 2, the Paris slope and intercept are highly correlated as shown in Figure 54. Specifically, Figure 55 indicates that lowering the slope is offset by an increase in the intercept (i.e. lowering –log(intercept)). The correlation coefficient between –$\log_{10}$(intercept) and the Paris slope is equal to 0.98 at R = 0.1, and equal to 0.53 at R = 0.8. Thus, there is an almost perfect linear dependence (correlation coefficient = 0.98) between the Paris slope and intercept at R = 0.1. This inverse correlation between the power-law slope and intercept has been observed in a variety of materials (for example, see Reference [24]). The COV of the log(intercept) is 5% at R = 0.1, and only 1% at R = 0.8. The standardized normal probability plot in Figure 56 suggests that a Normal distribution may be a reasonable assumption for the log(intercept) and, by extension, the Paris slope as well – due to its strong correlation with –log(intercept).
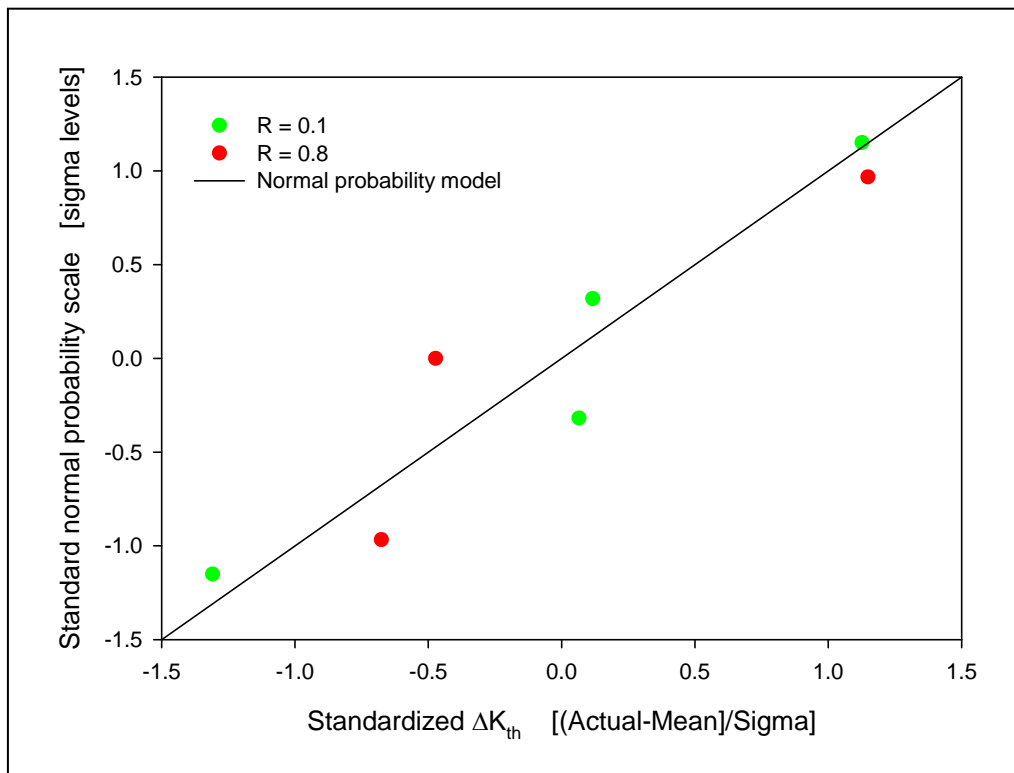
Figure 53. **Standardized Normal Probability Plot for the Threshold ΔK$_{th}$**
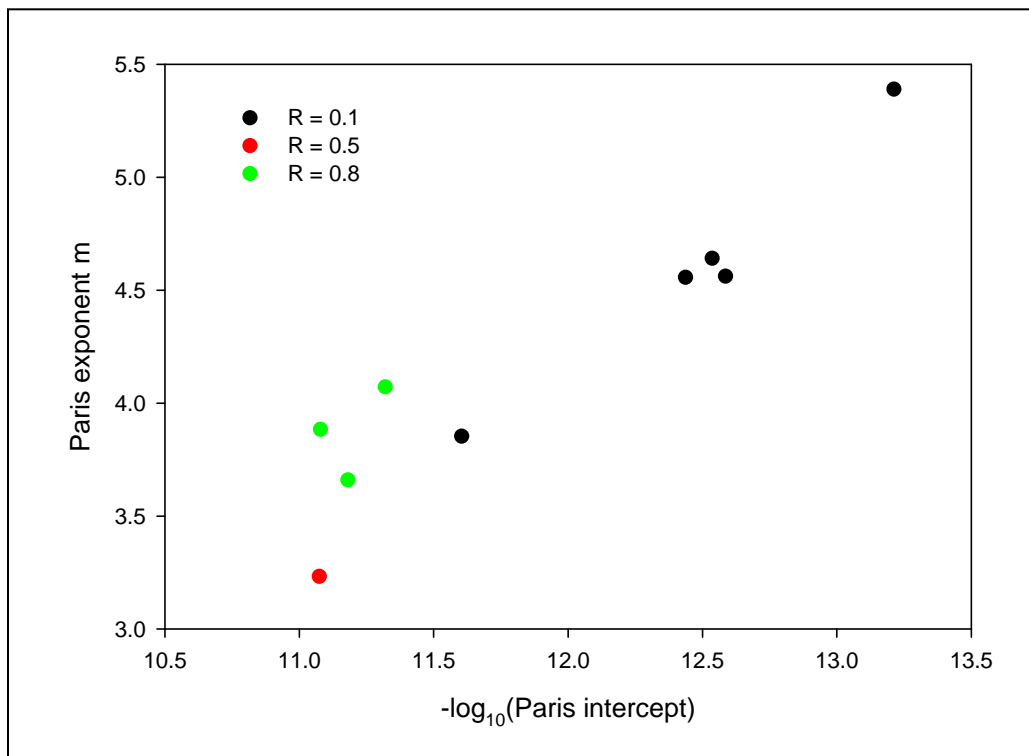
Figure 54. Paris Coefficients for Various R-Values
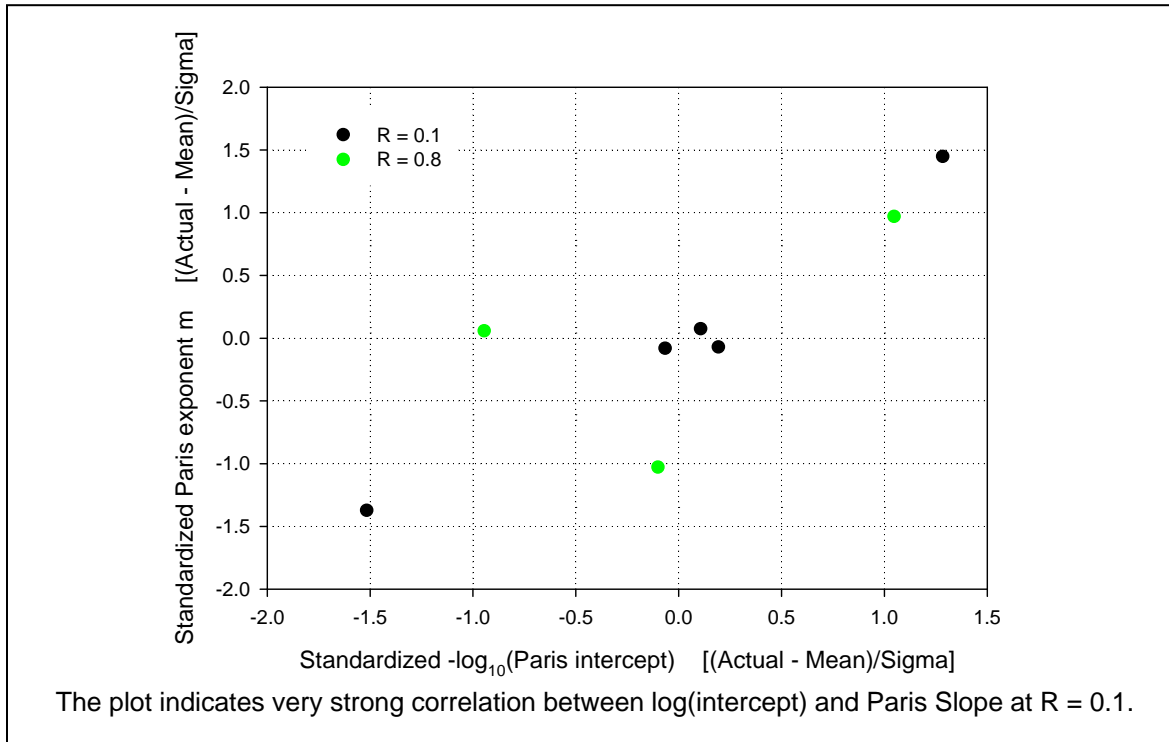
Figure 55. Joint Plot of Standardized Intercept and Slope in Region 2 (Paris Region)
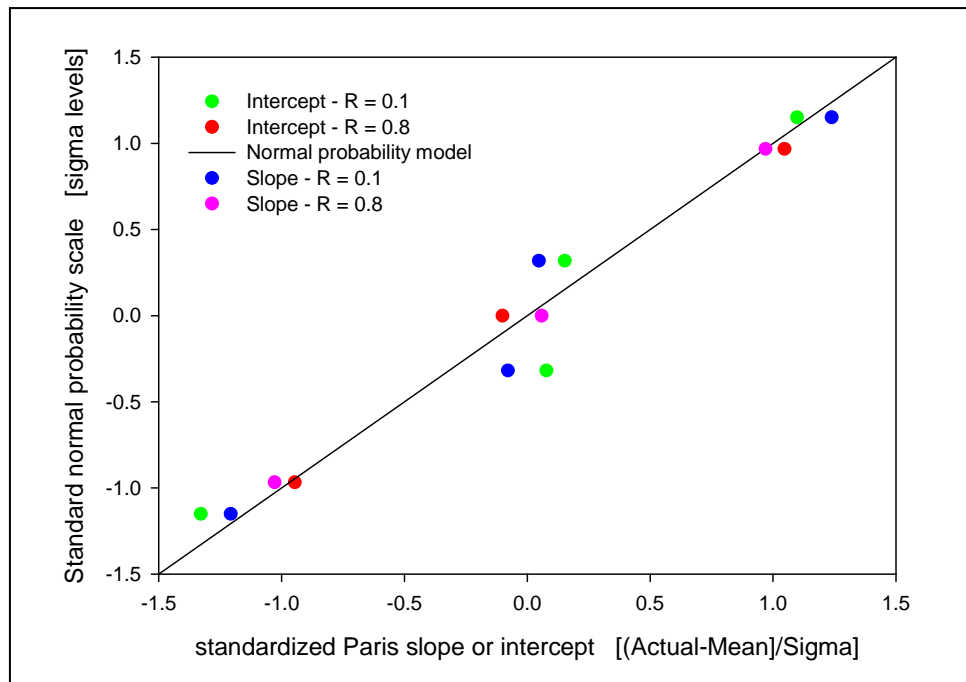
Figure 56. Standardized Normal Probability Plot for Coefficients in Region 2 (Paris Region)

4.2   Statistical Modeling of Mission Variability

The crack growth life associated with a gas turbine engine disk is influenced by a number of random variables (e.g., material properties, inherent/induced anomalies, applied stress, among others). The dispersion associated with each of these variables influences the probability of fracture. The accuracy of predicted risk is highly dependent on the statistical models used to represent each of the individual random variables. Parametric models (i.e., probability density functions such as normal, lognormal, Weibull) are commonly used to represent the random variables in which the accuracy of each variable is dependent on a regression fit of the data. Since experimental data are typically most plentiful near the mean value, the regression curve can be biased towards the mean and is often a poor fit near the tails of the distribution. Also, parametric models contain values that are often physically impossible to achieve in physical systems (e.g., $\pm \infty$). In addition, although the regression approach can be used to estimate the degree of correlation among two or more random variables, it may not adequately address general relationships among multiple random variables (e.g., multimodality, skewed discontinuities, among others).

In this section, a nonparametric method is presented for density estimation of rainflow stress profiles associated with aircraft gas turbine engine usages. A brief summary of the adaptive kernel density estimator is presented including details regarding a specific algorithm. Algorithm performance is illustrated using data generated from parametric uni- and multi-variate probability density functions and is compared to parametric estimates based on the same data. The adaptive kernel density estimator is applied to rainflow stress pairs associated with F-16/F100 engine usages and compared to parametric estimates, including a hybrid approach based on separate treatment of maximum stress pairs associated with engine startup and aircraft takeoff.

Usage histories for commercial aircraft are often well established with known stress pair magnitudes. A stress scatter factor can be used to account for the bias between predicted and measured stress values. This factor can be modeled as a random variable to address the variability associated with the measured values. As shown in Figure 57(a), the influence of stress scatter on the probability of fracture is commonly estimated by applying it repeatedly to the deterministic stress values over the entire life of a disk.

For military usages, the number and magnitude of stress pair values are not always well defined, and may have greater variability compared to commercial usages. Since the stress pair values could vary significantly from flight to flight, a more accurate model (Figure57(b)) is needed to estimate the influence of stress variability on the probability of fracture.

For gas turbine engines, the applied stress is a stochastic variable that is often difficult to measure and predict. Two primary approaches have been proposed for density estimation of rainflow stress values: parametric and nonparametric. The parametric approach consists of a regression fit of the data plotted on a cumulative probability scale [25, 26, 27]. The primary drawback to this approach is that it is often difficult to apply to multimodal

64

densities. On the other hand, nonparametric methods provide a direct fit to the data and are routinely used to estimate multimodal densities. The kernel density estimator, the most commonly used nonparametric method, has been recently applied to rainflow stress data [28, 29].
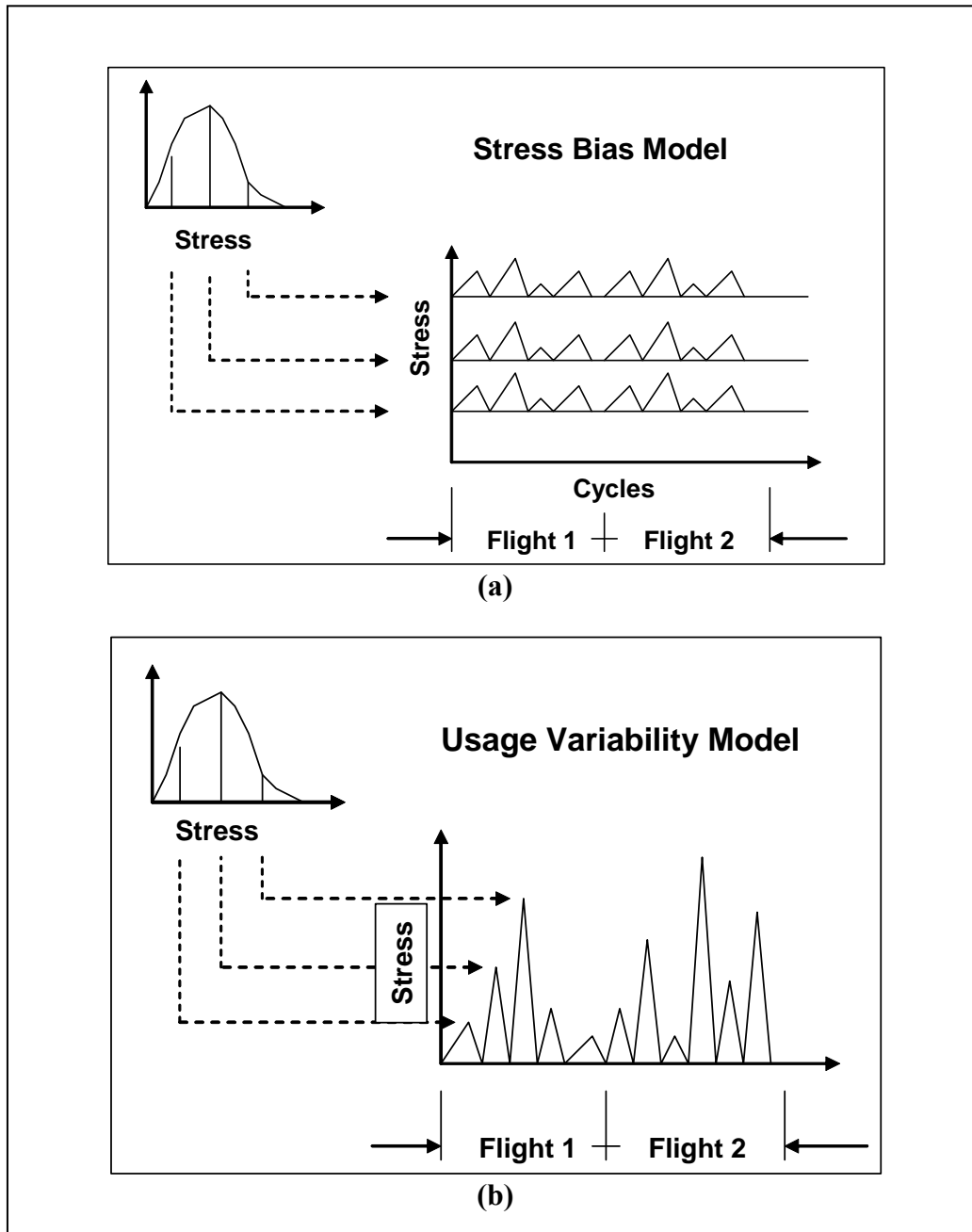
Figure 57. Approaches for Modeling Variability Associated with Applied Loads: (a) Stress Bias Model, and (b) Cycle-by-Cycle Usage Variability Model

A number of nonparametric methods can be used to estimate the probability density associated with a data set, such as the nearest neighbor method [30], convex intensity [31], and orthogonal series estimators [32], among many others. Many of the nonparametric methods are related to the histogram, which is commonly used to provide a measure of the relative occurrences of discrete data values. However, as shown in Figure 58, histograms are highly dependent on the bin width selected for sampling. Furthermore, a histogram is not a true probability density function, and therefore cannot be used for probabilistic computations.
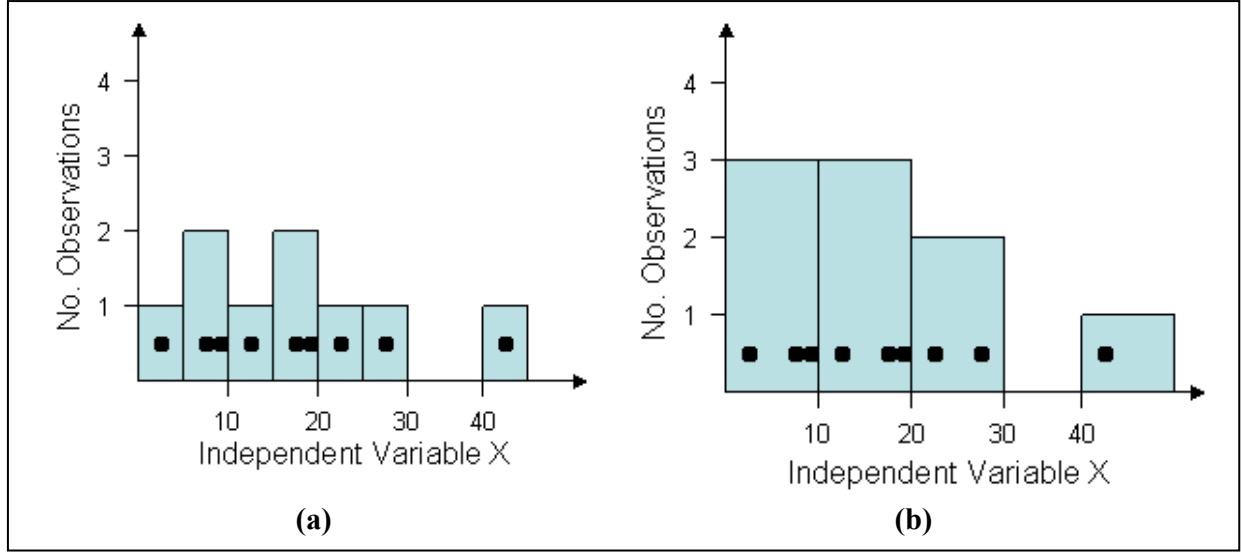
Figure 58. Bin-Width Dependency Associated with Histogram Density Estimates: (a) Bin Width = 5 Units, and (b) Bin Width = 10 Units

The kernel density estimator is one of the most commonly used nonparametric methods to estimate probability densities. As illustrated in Figure 59(a), each data point is assumed to have an associated probability density within a specified range of values. If data points are relatively close together, their probability densities can overlap (Figure 59(b)). The probability density at a given location can be estimated as the sum of the contributions of the kernels associated with each data point [30]:

$$\tilde{f}(t_1, t_2) = \frac{1}{nh^2} \sum_{i=1}^{n} K\left(\frac{t_1 - X_{1i}}{h}, \frac{t_2 - X_{2i}}{h} \right)$$

(13)

where t_1, t_2 = coordinates of evaluation point, n = number of data points, h = window width (smoothing parameter), K = kernel estimator, and $X_{1,i}, X_{2,i}$ = coordinates of data point i.

Equation 13 provides an initial density estimate associated with a fixed window width h. The window width can be adaptively adjusted to account for the number of data points within a region using the following equation [32]:
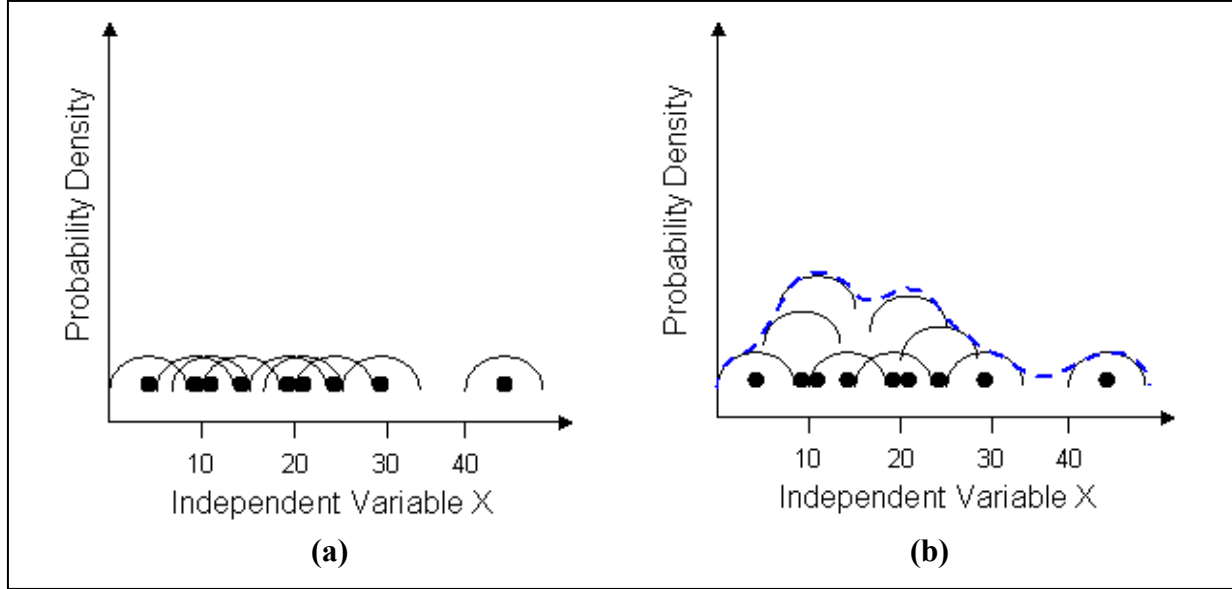
Figure 59. Nonparametric Approach to Probability Density Estimation:
(a) Epanechnikov Kernal Density at Individual Data Points, and
(b) Combined Density of All Data Points

$$\tilde{f}(t_1, t_2) = \frac{1}{n} \sum_{i=1}^{n} \frac{1}{(h\lambda_i)^d} K\left(\frac{t_1 - X_{1i}}{h\lambda_i}, \frac{t_2 - X_{2i}}{h\lambda_i}\right) \qquad (14)$$

where λ_i is a bandwidth parameter that is identified adaptively based on previous probabilistic density function (PDF) estimates:

$$\lambda_i = \frac{\left(\prod_{i=1}^{n} \tilde{f}(\mathbf{X}_i)\right)^{\frac{1}{2n}}}{\sqrt{\tilde{f}(\mathbf{X}_i)}} \qquad (15)$$

An Epanechnikov kernel function can be used to describe the probability density associated with rainflow stress values [29, 32]:

$$K\left(\frac{t_1 - X_{1i}}{h}, \frac{t_2 - X_{2i}}{h}\right) = \frac{2}{\pi}\left\{1 - \frac{1}{h^2}\left[(t_1 - X_{1i})^2 + (t_2 - X_{2i})^2\right]\right\} \geq 0 \qquad (16)$$

67

An adaptive kernel numerical algorithm based on Equations 13-16 was developed and verified using a number of established probability density functions. For example, consider the univariate lognormal distribution (LN(3,2)) shown in Figure 60(a). The initial kernel PDF estimate based on Equation 13 (and 200 Monte Carlo samples from the parent distribution) is very similar to the parent PDF near the median, but differs near the right tail of the distribution. However, when the window width is adaptively adjusted using Equation 14, it converges to the parent distribution over most of the right tail. The parametric density estimate (LN(2.89, 1.81) is very similar to the parent both at the mode and tails of the distribution.

The algorithm was applied to the bivariate lognormal distribution (LN(3,1.5) + LN(9,1.5)) shown in Figure 60(b). Both the initial and adaptive kernel density estimates predict the location of the modes and provide reasonable treatment at the tails of the distribution. On the other hand, the parametric estimate is a poor fit both at the modes and tails of the distribution.

The algorithm was also verified for the bivariate normal distribution shown in Figure 61 ($X = N(100,10)$, $Y = N(100,10)$, uncorrelated X and Y) based on 200 samples from the parent distribution. The parametric fit, shown in Figure 61(a), is nearly identical to the parent distribution. The kernel density estimate (Figure 61(b)) has an overall shape that is similar to the parent, but is quite different in the tails of the distribution. Standard algorithms are available to assess the accuracy of the kernel estimate [30] which should be strongly considered before applying the density estimate for risk predictions.

The adaptive kernel algorithm was applied to the density estimation of rainflow stress pairs associated with actual aircraft gas turbine engine usages. Raw RPM values were obtained from engine flight data recorder data [33] for a variety of F-16/F100 missions. RPM values are shown in Figure 62 for representative flights of missions classified as "Live Fire" and "Instruments & Navigation". The RPM values were converted to stress values using an empirical algorithm including a shakedown procedure to address stress values that fall above the material yield stress [34]. The stress values were sorted into min-max pairs using an established rainflow cycle counting algorithm [35].

As shown in Figure 62, a typical engine usage history can consist of thousands of RPM data points. However, the data can often be reduced to a few hundred values following application of the rainflow cycle counting algorithm. For example, the rainflow stress pairs associated with each of the individual flights shown in Figure 63 are based on usages similar to the ones shown in Figure 62. Most of the stress pairs are clustered in a region of minimum and maximum stress values ranging from 350 to 750 MPa. However, a few stress pairs associated with the aircraft major stress cycle are located in the region where the minimum stress is zero (associated with engine startup and aircraft takeoff).
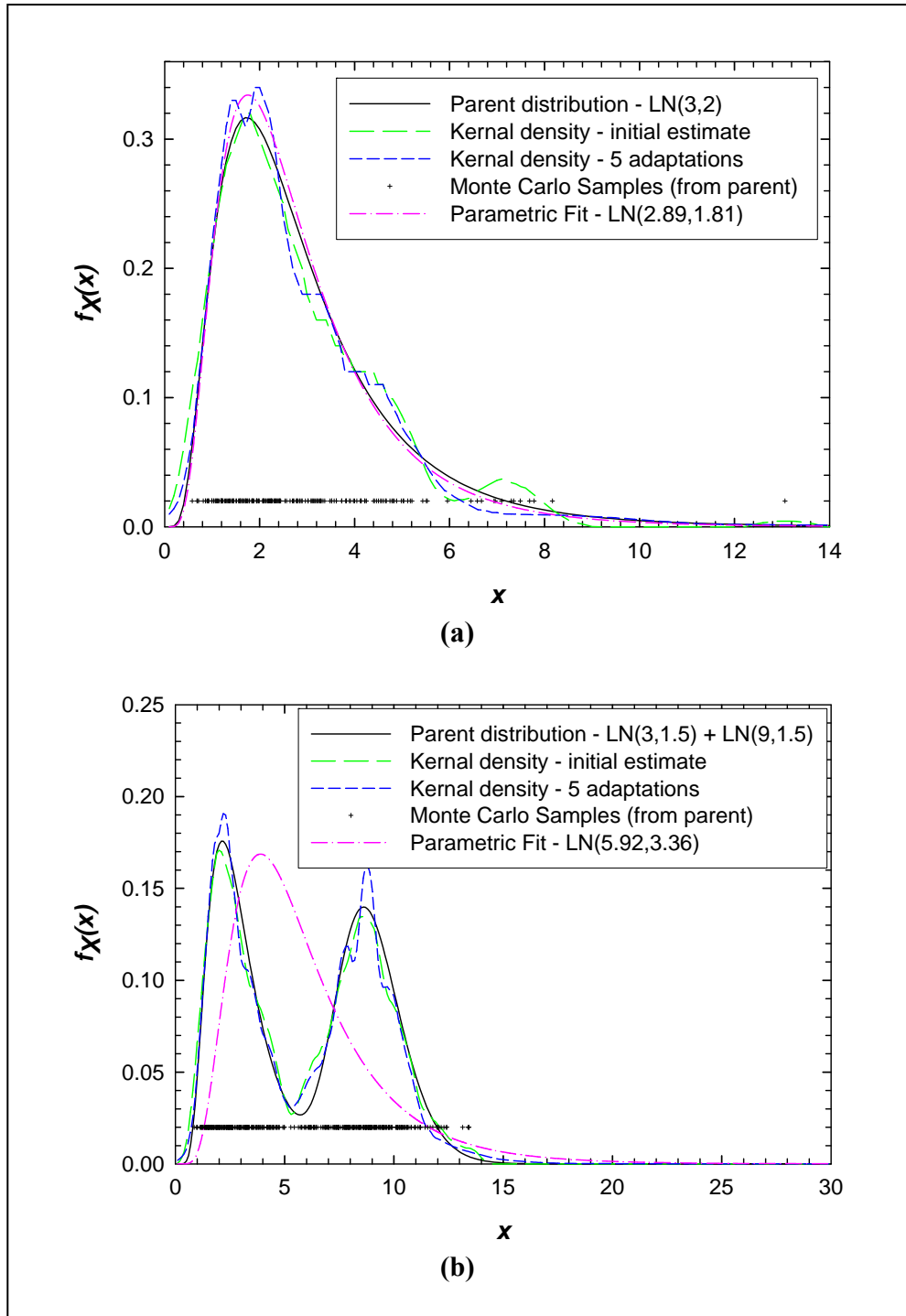
Figure 60. Comparison of Parametric and Nonparametric Density Estimation Methods for (a) Univariate Unimodal Lognormal Parent Distribution, and (b) Univariate Bimodal Parent Distribution
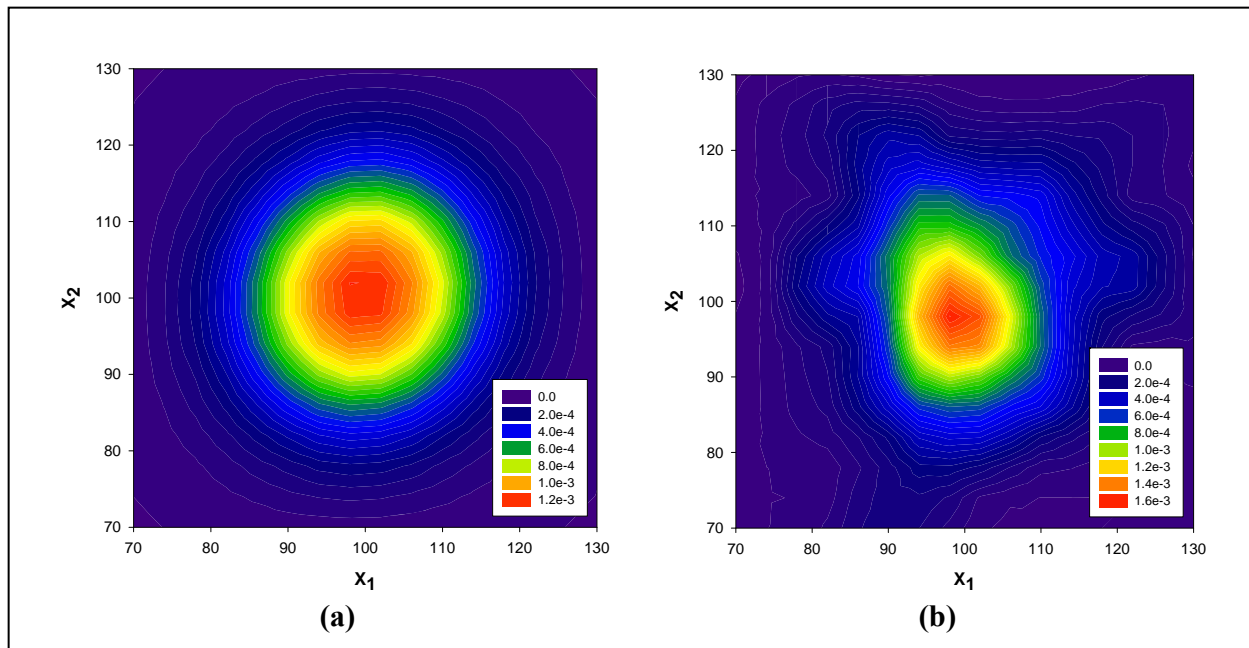
Figure 61. Comparison of Density Estimation Methods for a Multivariate Normal Distribution: (a) Parametric Density Estimate, and (b) Kernel Density Estimate
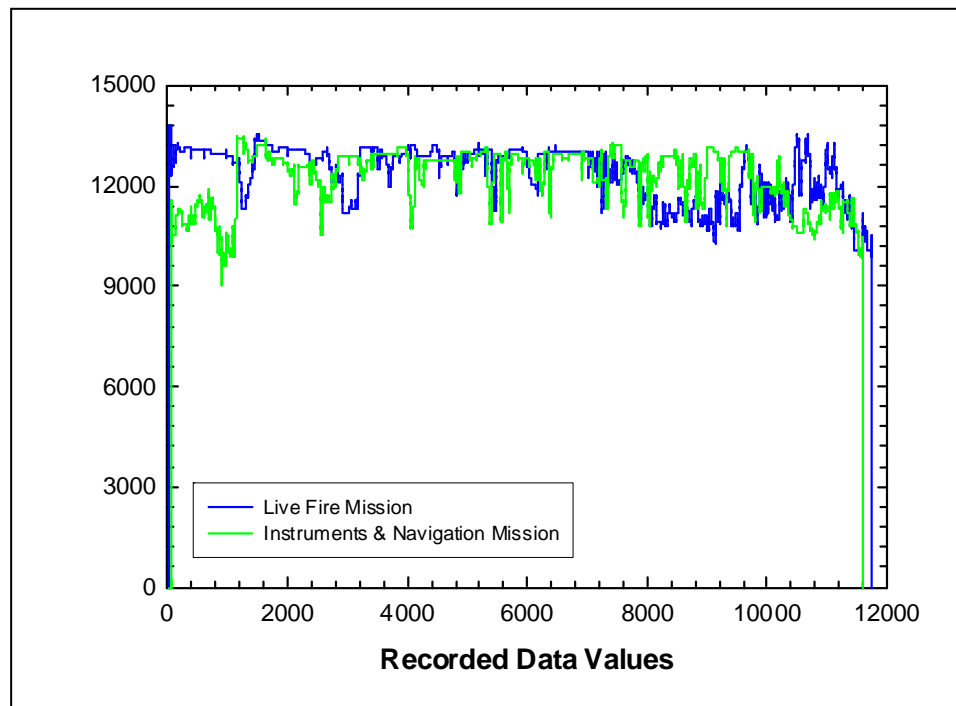
Figure 62. F-16/F100 Aircraft Engine Usage Histories Associated with Representative Flights of the Live Fire and Instruments & Navigation Missions
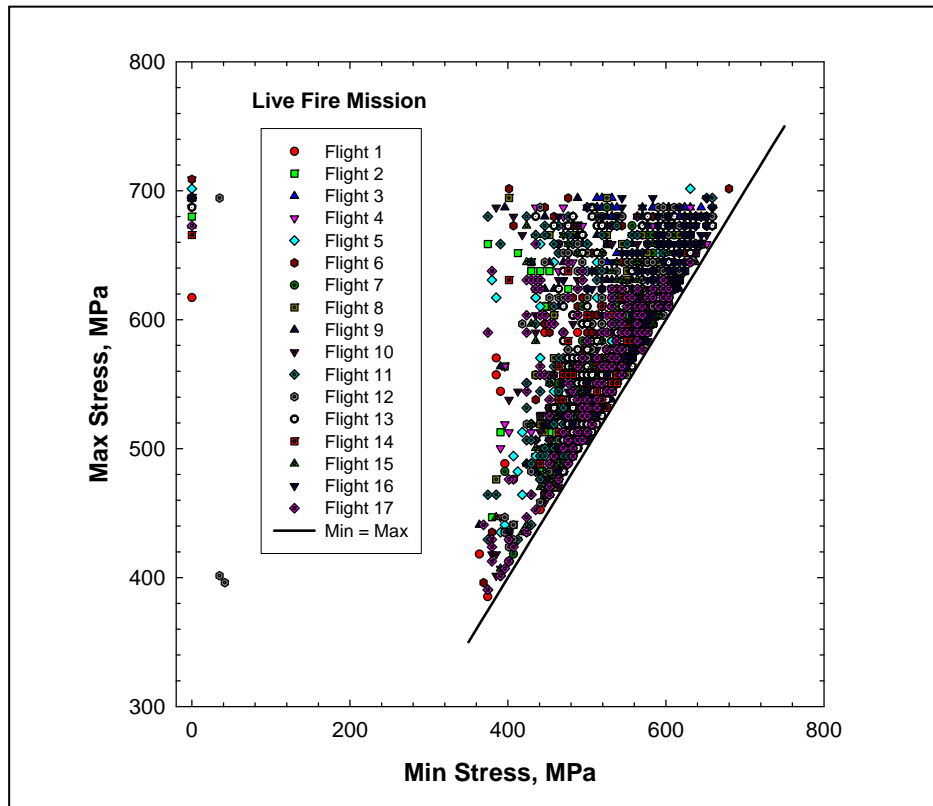
Figure 63. Rainflow Stress Pairs Associated with Representative Flights for the F-16/F100 Aircraft Live Fire Usage Classification

If the stress pairs can be completely described by a probability density function, then the influence of usage variability on the probability of fracture can be quantified by sampling directly from the rainflow stress PDF. The desired PDF must provide a probability density for each region of the population that is consistent with the clustering of data points shown in Figure 63. It must attempt to describe the population from which the data points were drawn to reflect the influence of data points not included in the current sample.

The stress pairs associated with startup/takeoff can be considered separately from the remaining data because they must be applied only once per flight (this cannot be guaranteed if they are included in the sampling population). In addition, since the minimum stress values associated with these stress pairs are always zero (to reflect the zero RPM value prior to engine startup), they can be modeled as a univariate (and probably unimodal) distribution. A parametric probability density estimate of the sub-population of Live Fire rainflow stress pairs that does not include values associated with startup/takeoff is shown in Figures 64(a) and (c). The parametric PDF appears to address the correlation structure of minimum and maximum stress values presented in Figure 63.

A kernel density estimate of the Live Fire mission rainflow stress pairs is shown in Figures 64(b) and (d). It provides explicit treatment of the stress pairs associated with engine startup, as indicated by the stress values that are separated from the primary cluster that appear near zero on the min stress axis. It also appears to capture the correlation structure of the minimum and maximum stress values. It is interesting to note that the parametric method predicts a unimodal density for the rainflow data, whereas the kernel method predicts a bimodal density. Since it is expected that extreme stress values will have more influence on the probability of fracture, it may be more appropriate to assess the accuracy of the methods in the tails of the distributions.

In Figure 63, it can be observed that the maximum and minimum stress pair values associated with the Live Fire mission appear to be correlated random variables. If these values were modeled as random variables for risk assessment, a correlated sampling technique would be required to capture this relationship. Although correlated sampling is well established for parametric random variables, significant errors may be introduced when the random variables are non-Gaussian. Correlated sampling is not as mature for nonparametric variables, and the errors and limitations are not as well known.

Common correlated sampling techniques involve transformation of a vector of correlated variables into a vector of uncorrelated variables using matrix algebra methods (e.g., Rosenblatt transformation) that are similar to coordinate transformation [36]. In some instances, a coordinate transformation can be identified for the original random variables that eliminates the need for uncorrelated sampling. For example, consider the max-min stress pair values shown in Figure 63. If the coordinate system is transformed from max-min stress to delta stress-R ratio (Figure 65), it can be observed that the data exhibit strong negative correlation (correlation coefficient = -0.992). If it is assumed that the transformed variables are perfectly negatively correlated, then uncorrelated sampling techniques can be used to simulate these variables. This approach avoids the errors associated with correlated sampling, and applies to both parametric and nonparametric variables. The density estimation of stress pair values is greatly simplified when modeled as delta stress and R ratio. If the PDF is simulated using uncorrelated sampling techniques, the density estimation can be performed on each random variable individually.
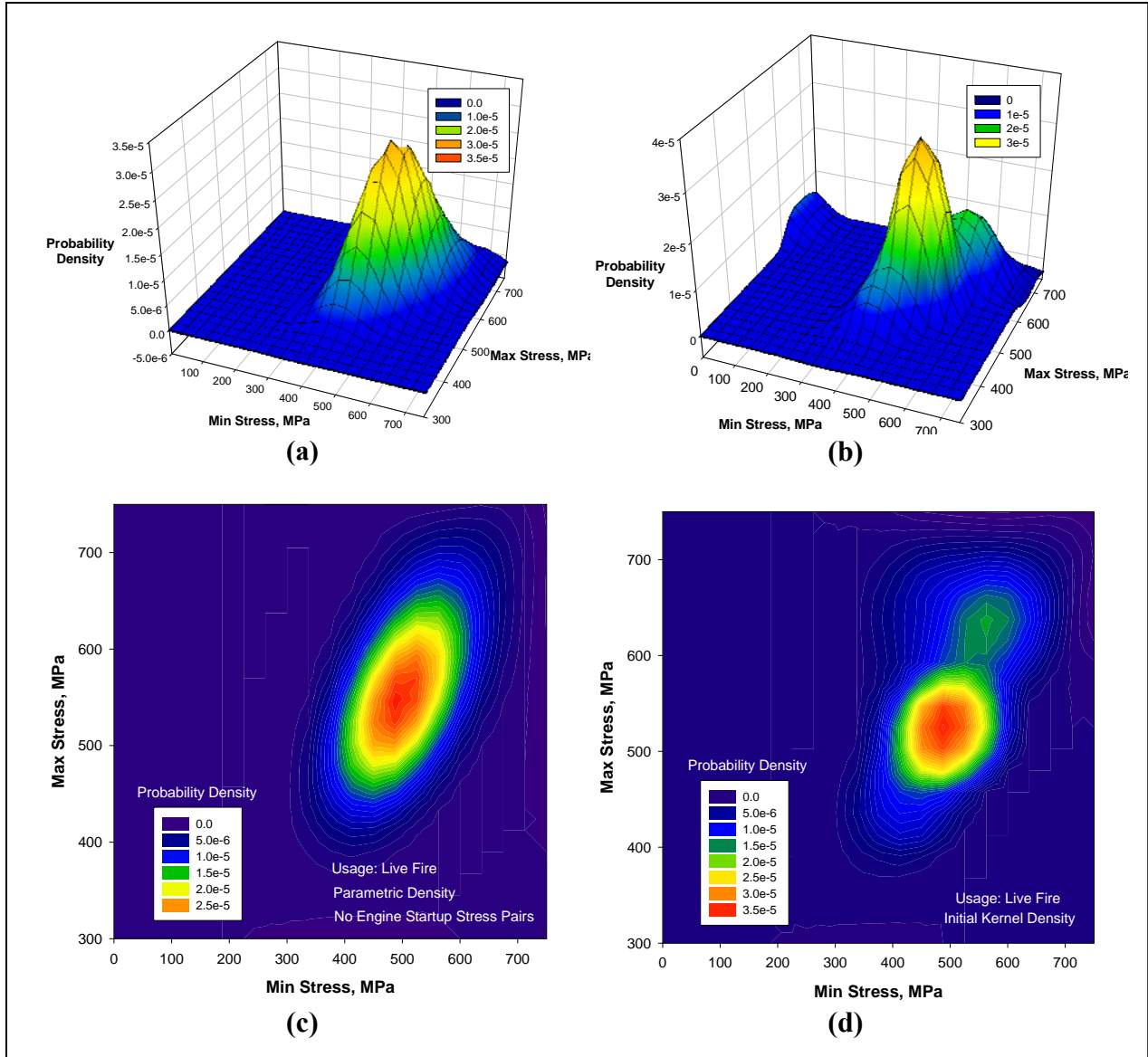
Figure 64. Comparison of Density Estimation Methods for Rainflow Stress Pairs Associated with Live Fire Usage Histories: (a) and (c) Parametric Density Estimate (No Engine Startup Stress Pairs); (b) and (d) Kernel Density Estimate
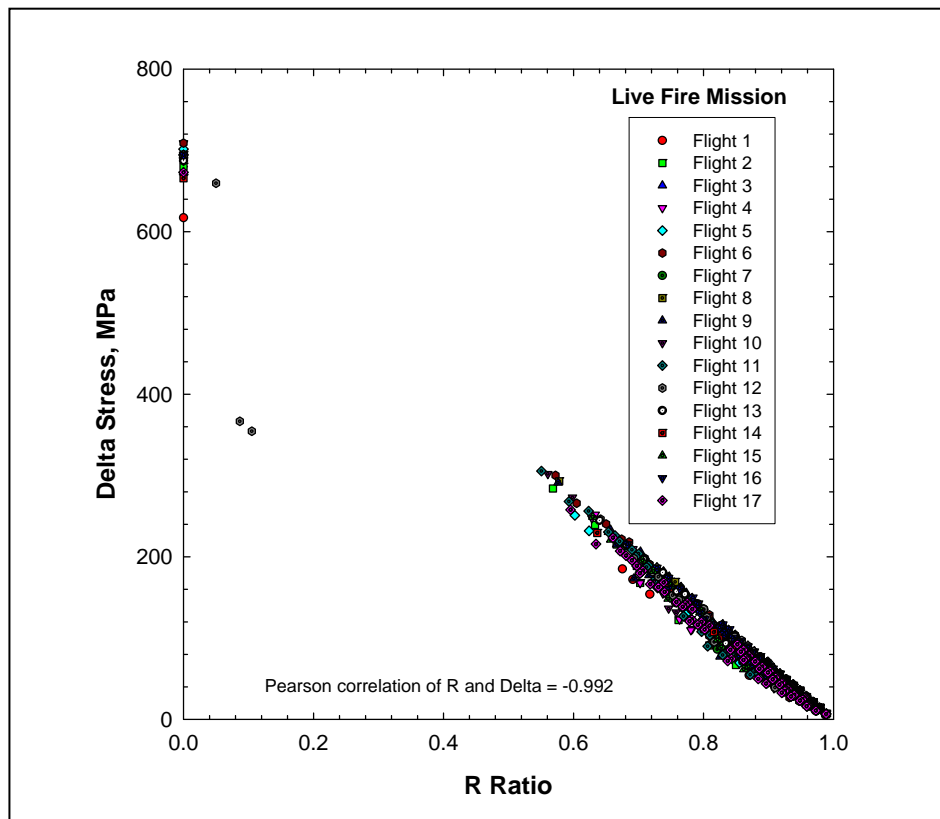
Figure 65. The Rainflow Stress Values for the Live Fire Mission Exhibit Strong Negative Correlation When Transformed to Delta Stress Versus R-Ratio Space

When sampling transformed random variables, special care must be taken to ensure that the stress values selected are consistent with the field data values. For example, consider the delta stress versus stress pair number values for the Live Fire mission flights shown in Figure 66. The rainflow procedure provides stress pair values that decrease in magnitude with increasing stress pair number for an individual flight. The range of stress pair values associated with each stress pair number must also be considered. In Figure 67, mean, 5th and 95th percentile delta stress magnitudes are shown for each stress pair number for the Live Fire mission. Based on the data shown in Figure 67, it appears that the delta stress values associated with each stress pair could be modeled as random variables.

The main descriptors (mean, standard deviation, COV) for each stress pair are shown in Figure 68 (shown as normalized values). The relationship among delta stress values associated with successive stress pairs must also be considered. In Figure 69, delta stress values are shown for two representative stress pairs of the Live Fire mission, indicating strong correlation among delta stress values. This relationship is confirmed in Figure 70, where delta stress values are shown for representative individual flights. It can be observed that all of the delta stress values are either above the mean or below the mean stress values for at least some of the flights. However, it should be noted that for some of the flights, the delta stress values appear both above and below the mean values, which suggests that stress pair values are partially correlated.

74
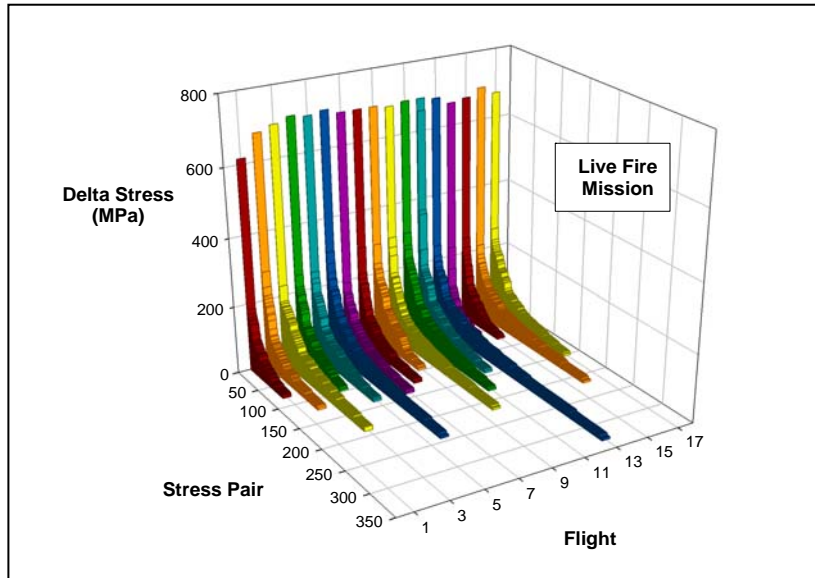
Figure 66. Delta Stress and Stress Pair Number Associated with Individual Flights of the Live Fire Mission
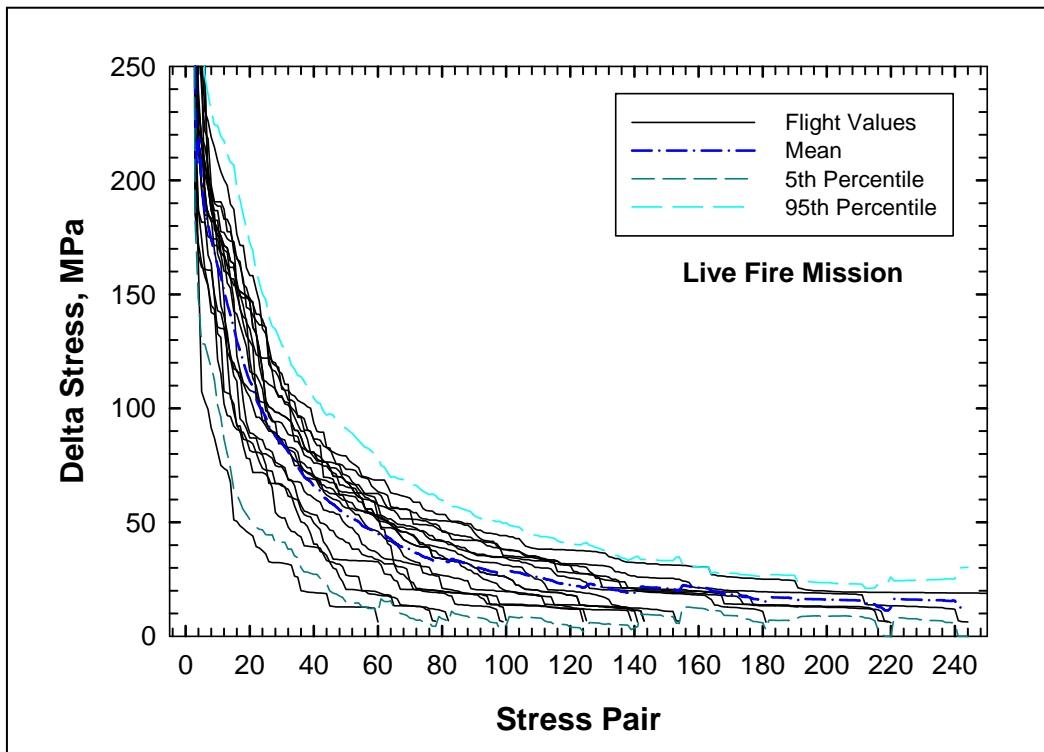
Figure 67. Delta Stress Versus Stress Pair Number for All Flights Associated with the Live Fire Mission
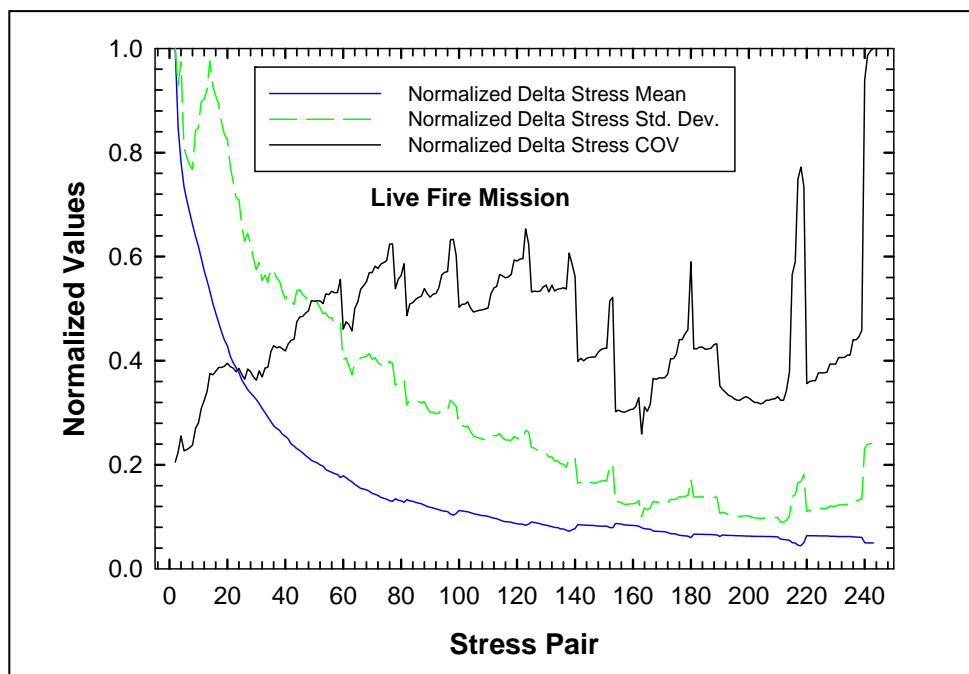
Figure 68. Normalized Mean, Standard Deviation, and Coefficient of Variation (COV) Associated with Delta Stress Values for the Live Fire Mission

Note the strong correlation among delta stress values.
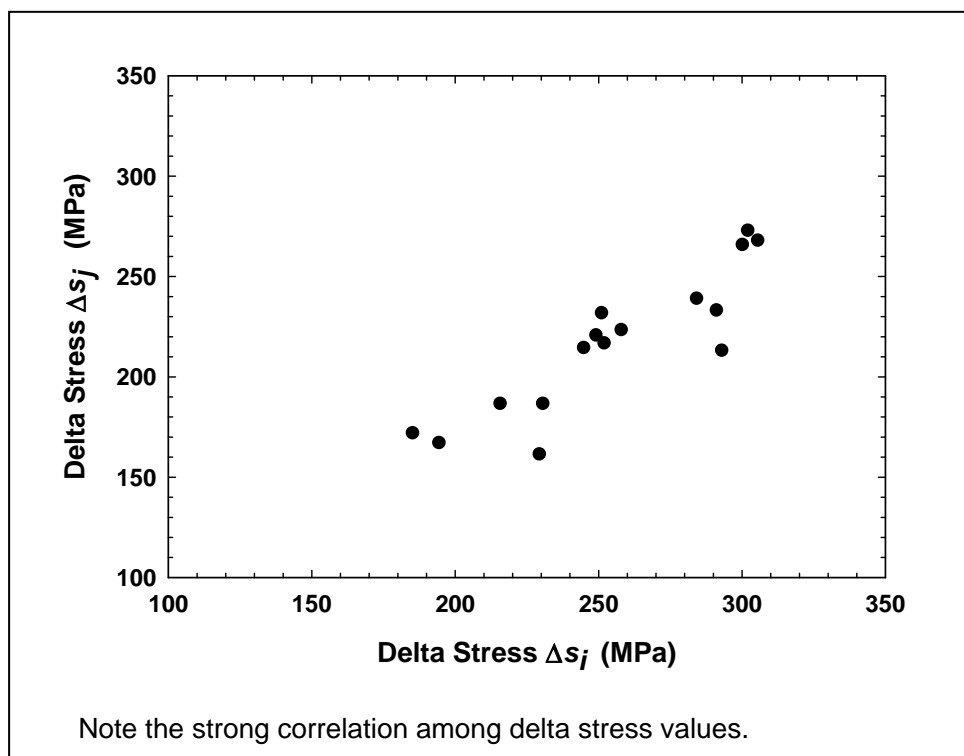
Figure 69. Delta Stress Values Associated with Two Stress Pair Numbers for Each Flight of the Live Fire Mission
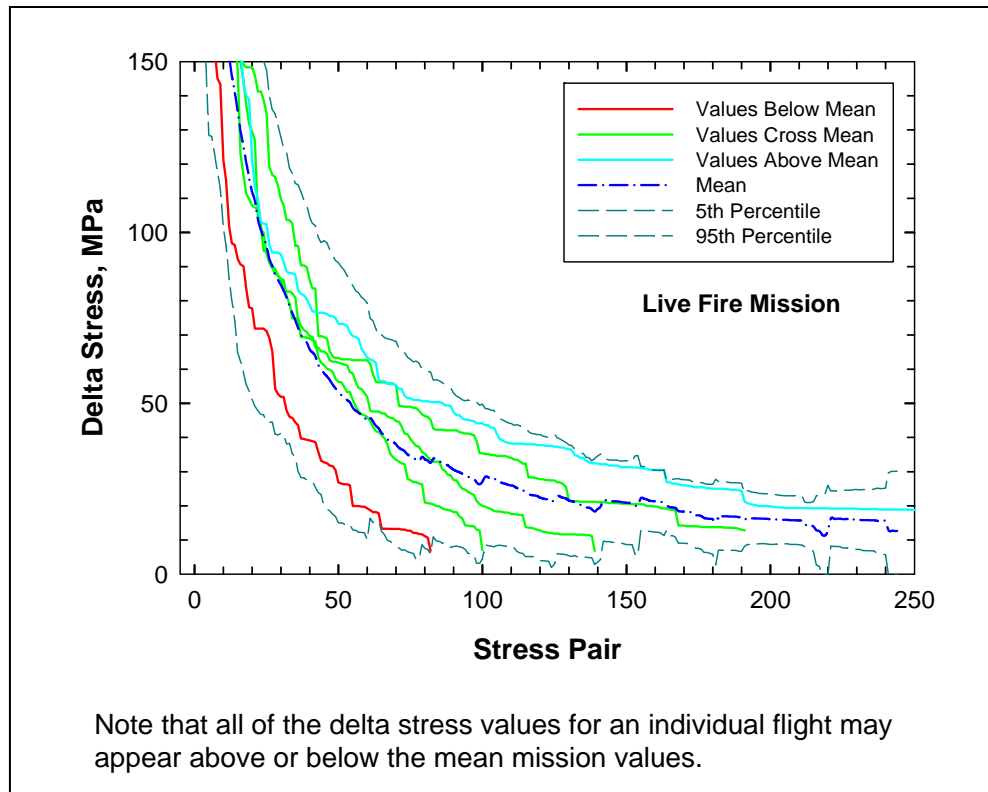
Figure 70. Delta Stress Values for Selected Flights of the Live Fire Mission

4.3   Probabilistic Mission Identification (PMI)

Fatigue life prediction of aircraft gas turbine engine rotating components requires estimates of the applied stress values throughout the life of the component. These values may vary considerably from flight-to-flight, and are highly dependent upon the mission type. Unfortunately, engine flight data recorders currently do not have the capability to identify the mission type for a given flight history. Instead, the aircraft pilot must manually enter the mission type in a log book, which can lead to errors and omissions of this critical information. In addition, a single flight may have characteristics that are similar to multiple mission types. Thus, the mission identification problem consists of selecting the most likely mission type from a set of established standard missions. An automated mission identification method would greatly improve risk assessment estimates, particularly if it were based on quantitative methods.

A quantitative probabilistic method has been developed to identify the mission type for a given flight history. The method is based on a comparison of the rainflow stress PDF of a specific flight history with previously developed PDFs of standard mission types. The method, called PMI, predicts the most likely mission type based on volume integration of the region common to both the flight history and the standard mission.

A description of the probability densities associated with one or more random variables is necessary for probabilistic risk assessment. A number of parametric models are available to estimate probability density based on a statistical fit of the available data. The appropriate distribution is based on the statistical error associated with the data fit that is quantified using classical goodness-of-fit tests (e.g., chi-square, Kolmogorov-Smirnov, among others [25, 26]). These tests provide a quantitative measure of the relationship among a data set and a parametric distribution.

The mission identification problem consists of identifying the distribution that most closely resembles the available data. Consider mission M_i (ith unknown mission) and fleet F_j (jth fleet of known mission type) shown in Figure 71. The volume of the region over which the probability densities of the stress values (s_i, s_2) associated with mission M_i and fleet F_j overlap can be used as a measure of the likelihood that mission M_i is a member of fleet F_j. The overlap probability can be expressed as:

$$P\left(M_i \subset F_j\right) = \frac{\int\limits_{S_1}\int\limits_{S_2} \min\left[f_{M_i}\left(s_1,s_2\right), f_{F_j}\left(s_1,s_2\right)\right] ds_1 ds_2}{\int\limits_{S_1}\int\limits_{S_2} f_{F_j}\left(s_1,s_2\right) ds_1 ds_2} \tag{17}$$

Noting that the denominator in Equation 17 has a value of 1 when integrated over the entire domain of F_j, Equation 17 can be simplified as:

$$P\left(M_i \subset F_j\right) = \int_{S_1} \int_{S_2} \min\left[f_{M_i}\left(s_1, s_2\right), f_{F_j}\left(s_1, s_2\right)\right] ds_1 ds_2 \qquad (18)$$

Note that Equation 18 applies to both parametric and nonparametric probability densities.
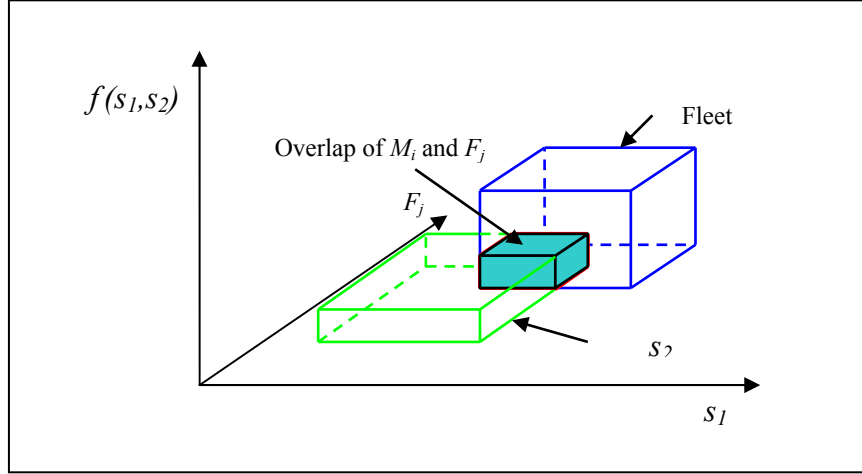
Figure 71. The Volume of the Region Over Which the Probability Densities of the Stress Values (s_i, s_2) Associated with Mission M_i and Fleet F_j Overlap Can Be Used as a Measure of the Likelihood That Mission M_i is a Member of Fleet F_j

The PMI method was used to identify the mission type associated with actual military aircraft engine usages. Raw RPM values (Figure 63) were obtained from engine flight recorder data and converted to stress values using an algorithm that accounts for local yielding [37, 38]. An established rainflow counting technique [35] was used to sort the stress data into min-max pairs. Rainflow stress values are shown in Figure 72 for two representative mission types (Live Fire, Instruments and Navigation). The grouping of data is similar for both mission types, with most values located within a region of minimum and maximum stress range values ranging from 360 to 720 MPa.

Probability densities were estimated using the adaptive kernel method based on 10 flights for each mission type, shown in Figure 73. The probability density estimates for both mission types appear to capture the correlation among minimum and maximum stress values associated with the original data set. The PDF associated with the Live Fire mission (Figure 73(a)) appears to have a single dominant mode, whereas the PDF associated with the Instruments & Navigations mission (Figure 73(b)) is characterized by two modes with similar intensities.

To evaluate the performance of the PMI method, rainflow stress probability densities associated with usages of known mission type were compared to fleets of usages of known mission type. Two test missions of known type (Live Fire, Instruments and Navigation) were selected to evaluate the PMI method. Probability densities obtained using the adaptive kernel method are shown in Figure 74, and probability contours associated with the test missions are shown in Figure 75.
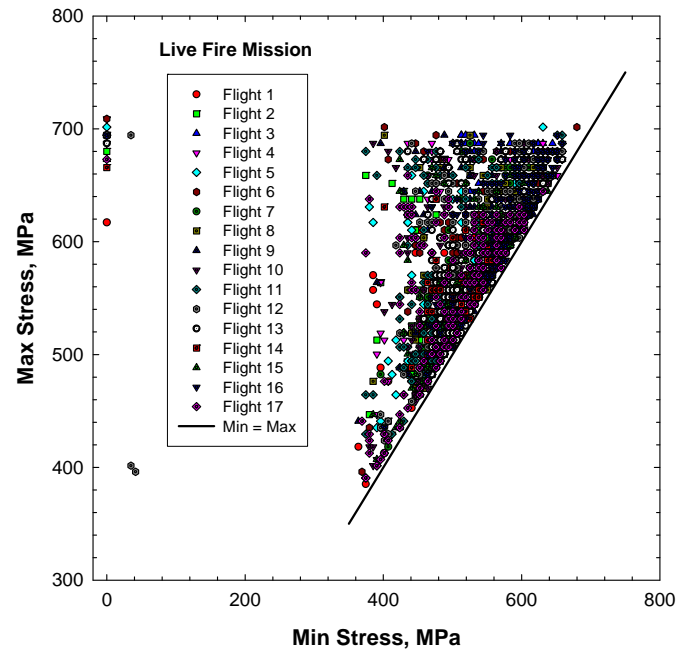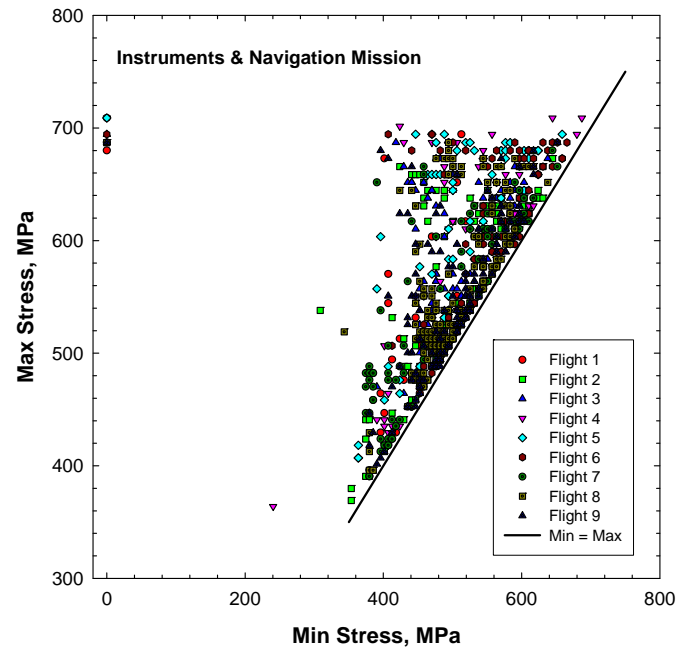
Figure 72. Rainflow Stress Pair Values Associated with the Following Aircraft Usage Classifications: (a) Live Fire, and (b) Instruments & Navigation
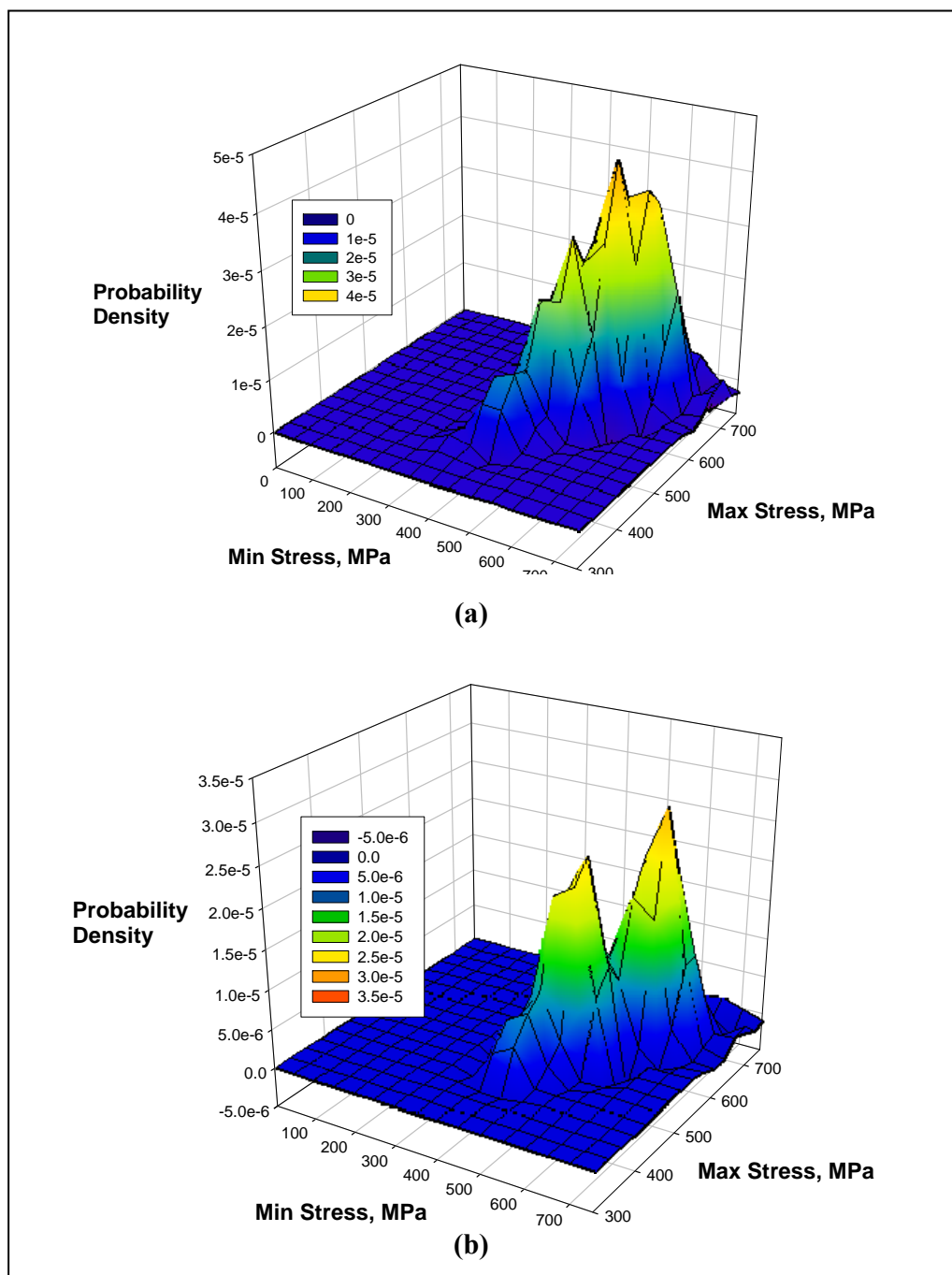
Figure 73. Estimated Joint Probability Densities Associated with the Following Aircraft Usage Classifications: (a) Live Fire, and (b) Instruments & Navigation

(a)

(b)
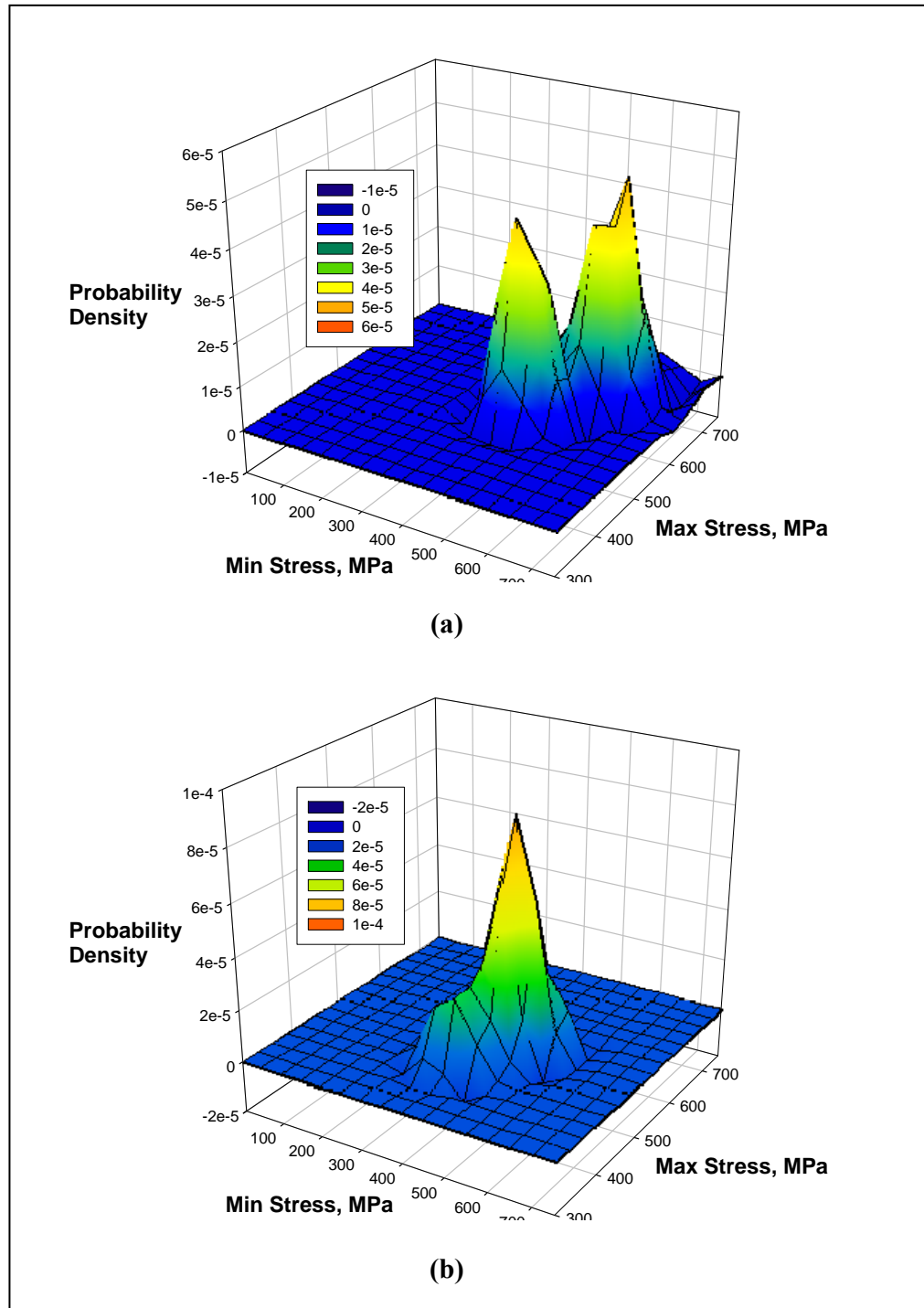
Figure 74. Probability Densities Associated with Individual Flights of Known Mission Type Were Used to Illustrate the Performance of the Probabilistic Mission Identification (PMI) Method: (a) Live Fire Test Mission 1, and (b) Instruments & Navigation Test Mission 1
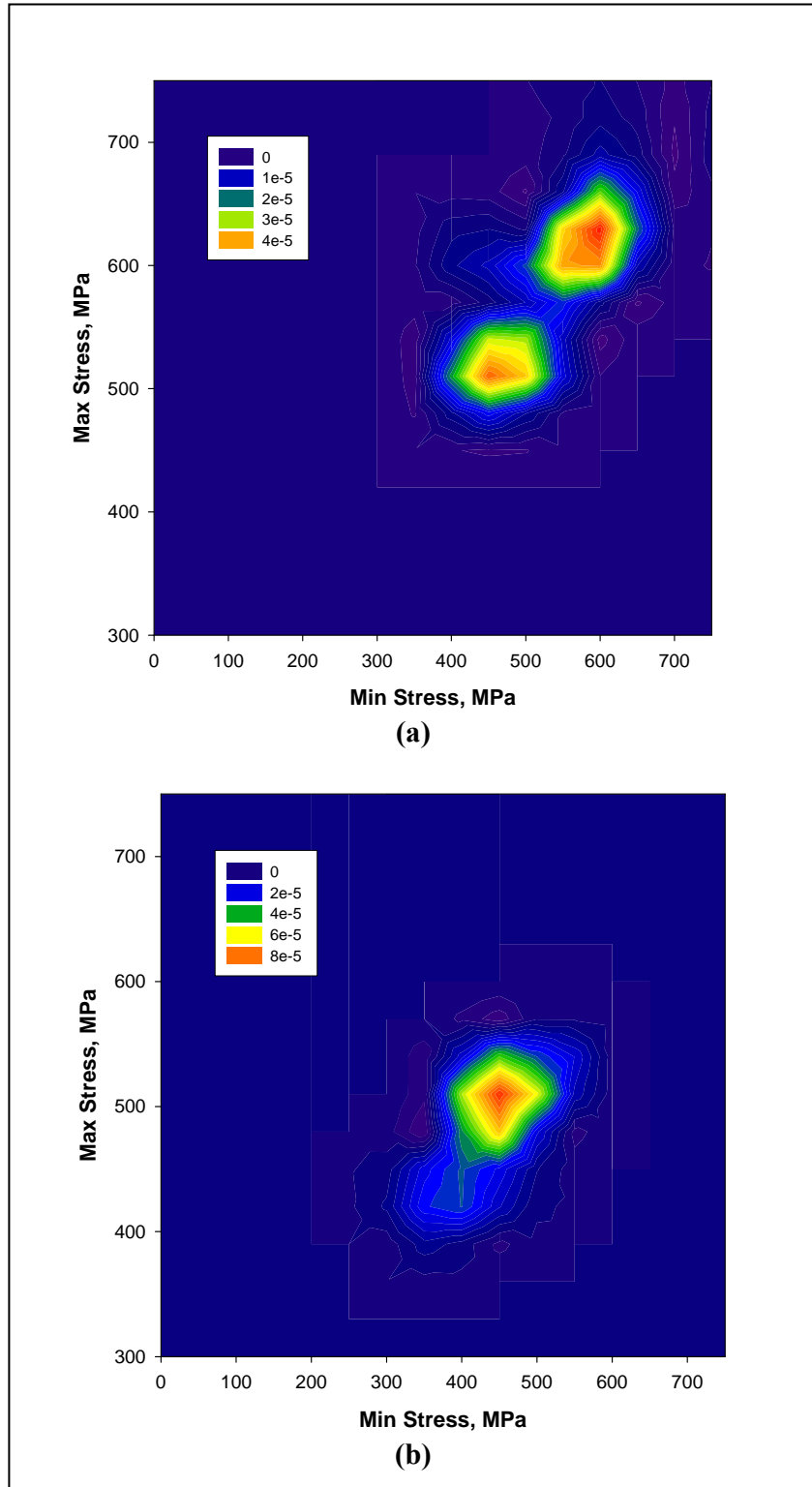
Figure 75. Probability Contours Associated with Individual Flights of Known Mission Type: (a) Live Fire Test Mission 1, and (b) Instruments & Navigation Test Mission 1

The PMI method was first applied to a test mission of type Live Fire. Probability densities and contours associated with the Live Fire test mission and the Live Fire and Instruments & Navigation fleets are shown in Figures 76(a) and 77(a), respectively. The bimodal shape of the Live Fire test mission suggests that it may belong to the Instruments and Navigation fleet. However, when the probability densities of the overlap among the test mission and the fleets are considered (Figures 77(a) and (b)), the region of relatively high density shown in Figure 77(a) suggests that the test mission belongs to the Live Fire fleet. Volume integration of the overlap density (Table 3) confirms that the test mission most likely belongs to the Live Fire fleet.

Table 3. Overlap Probabilities Associated with Test Missions

Test Mission	Overlap Probability	
	Live Fire Fleet	Instr. & Navigation Fleet
Live Fire	0.254	0.193
Instruments & Navigation	0.057	0.073

The PMI method was next applied to a test mission of type Instruments and Navigation. In contrast with the Live Fire test mission, the Instruments and Navigation test mission has a unimodal appearance which suggests that it may belong to the Live Fire fleet. However, as shown in Figure 78, the peak density of the test mission is very close to one of the modes of the Instruments and Navigation fleet. Volume integration of the overlap density (Figure 79, Table 3) confirms that the test mission most likely belongs to Instruments and Navigation fleet. For this example, the PMI method correctly identified the mission type associated with both test missions.

PMI has a critical role in the probabilistic treatment of aircraft engine usage as indicated in the conceptual framework shown in Figure 80. The framework consists of the following four stages: (1) data retrieval, (2) mission identification, (3) stress characterization, and (4) risk prediction. In the data retrieval stage, raw RPM values from engine sensors are converted to stress values and sorted using a standard rainflow procedure. In the identification stage, PMI is used to predict the most likely mission type of each flight based on volume integration of rainflowed stress pair values associated with the flight history and a standard mission. In the characterization stage, probability densities associated with each mission type are quantified using an adaptive kernel approach that addresses extreme behavior near the tails of the distributions, and can easily be updated as new data are acquired. Stress data are transformed to a stress ratio versus delta stress coordinate system to provide improved numerical treatment of the correlation among rainflowed stress pair values. In the final stage (prediction), future usage is simulated based on values obtained from the mission probability density functions and future mission mix values from fleet management projections.
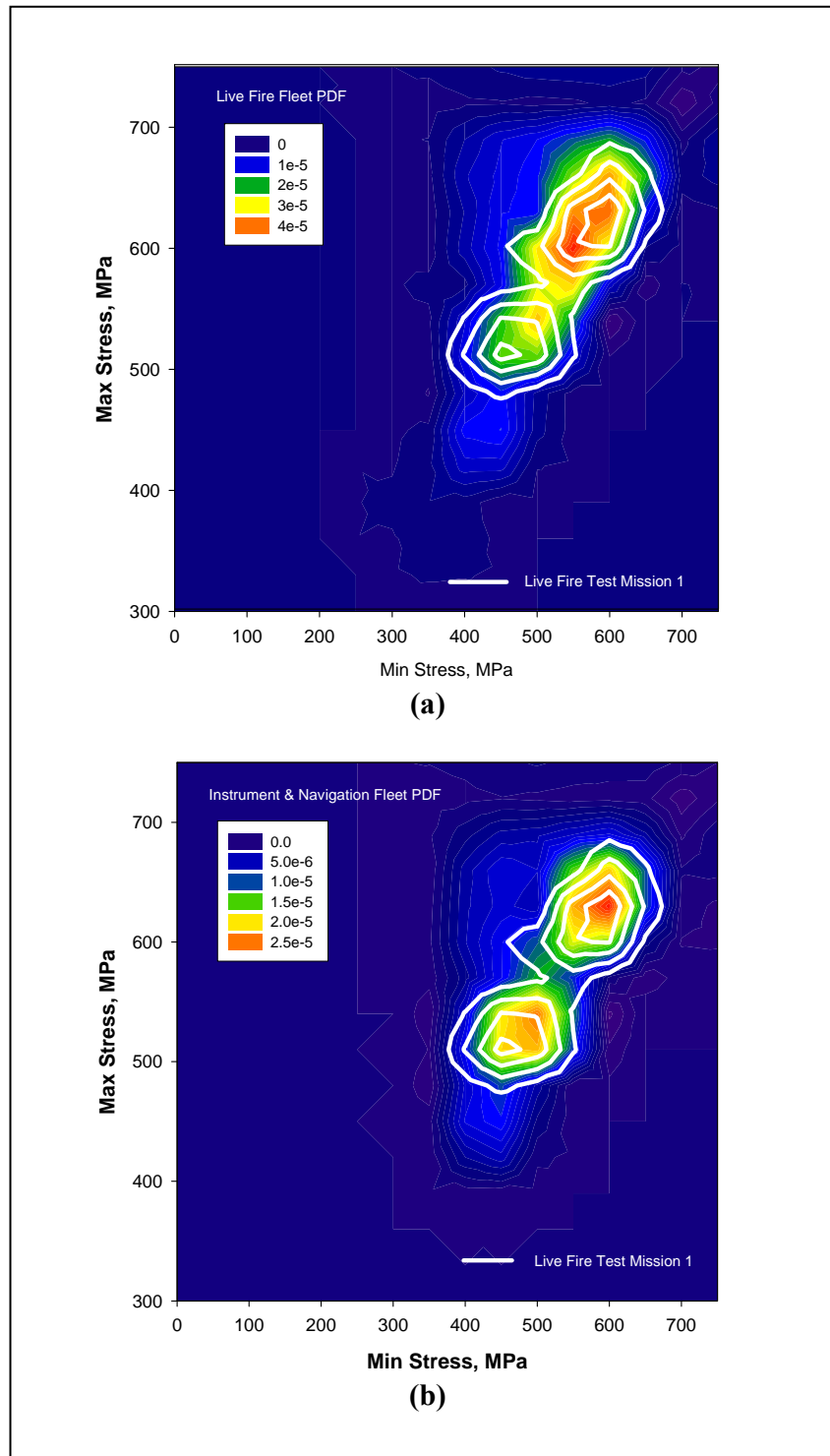
Figure 76. Probability Contours Associated with an Individual Flight of Known Mission Type (Live Fire Test Mission 1) and (a) Live Fire Mission, and (b) Instruments & Navigation Mission

85
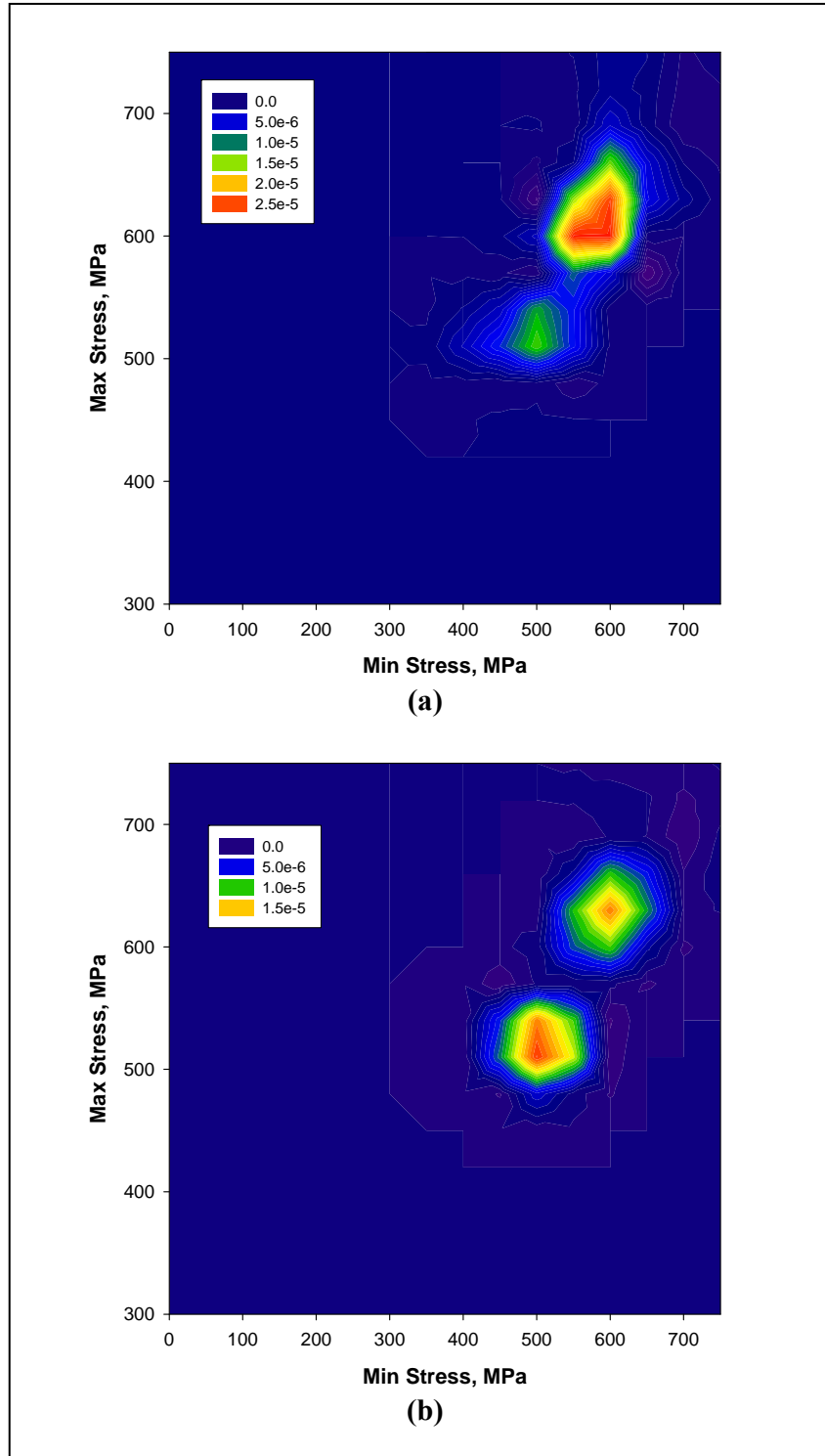
Figure 77. Overlap Probabilities for Live Fire Test Mission 1 and the Live Fire and Instruments & Navigation Missions, (a) and (b), Respectively

86
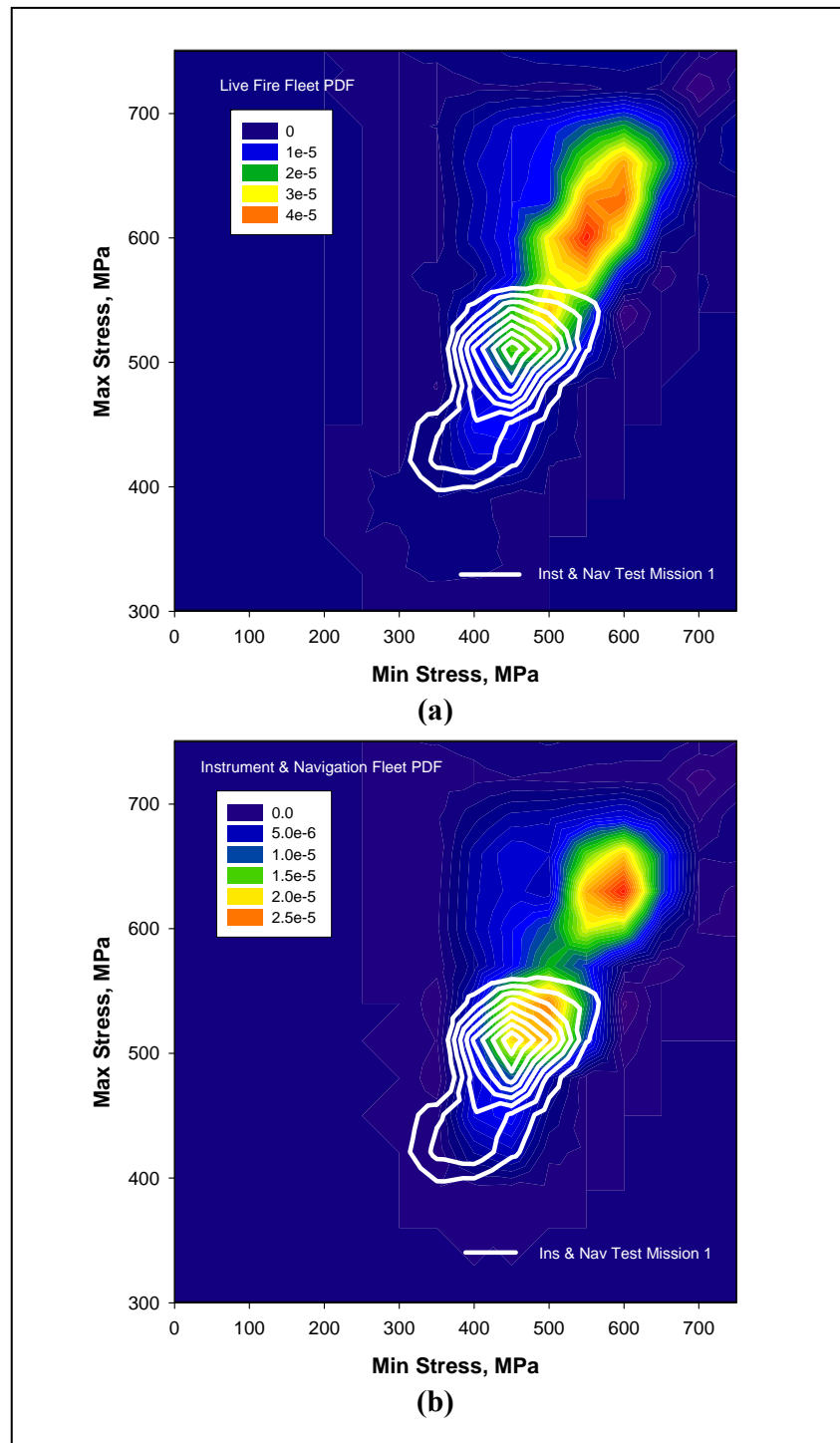
Figure 78. Probability Contours Associated with an Individual Flight of Known Mission Type (Instruments & Navigation Test Mission 1) and (a) Live Fire Mission, and (b) Instruments & Navigation Mission
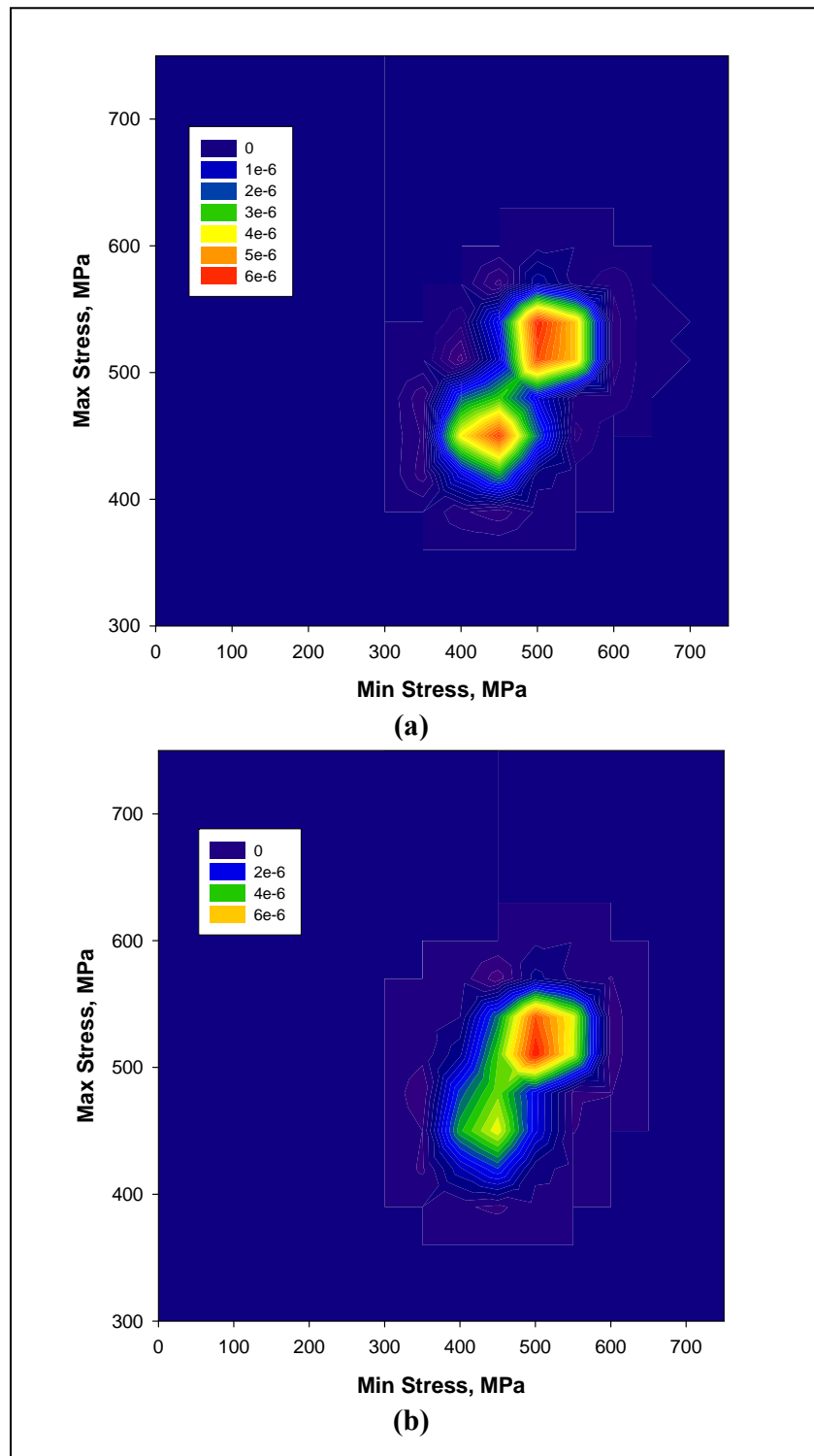
Figure 79. Overlap Probabilities for Instruments & Navigation Test Mission 1 and the Live Fire and Instruments & Navigation Missions, (a) and (b), Respectively
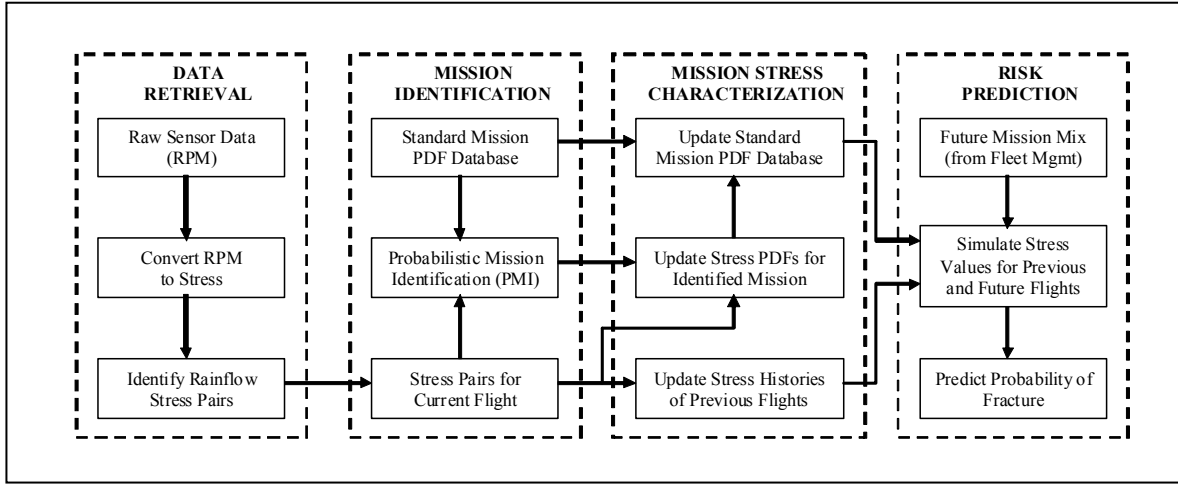
**Figure 80. A Conceptual Framework for Probabilistic Treatment
of Aircraft Engine Usage**

4.4   Probabilistic Sensitivity Methods

The development of probabilistic sensitivities is frequently considered an essential
component of a probabilistic analysis and often critical towards understanding the physical
mechanisms underlying failure and modifying the design to mitigate and manage risk.
One useful sensitivity is the partial derivative of the probability-of-failure with respect to
the parameters of the input random variables' PDF e.g., $\partial P_f/\partial\mu$, $\partial P_f/\partial\sigma$, where μ is the
mean value and σ is the standard deviation. The score function method, described below,
is a convenient method to compute these sensitivities because the equations are formulated
such that the same Monte Carlo samples used to compute the probability-of-failure of the
system can also be used to compute the probabilistic sensitivities. Therefore, the
sensitivities are obtained for negligible additional cost.

4.4.1   Methodology

The score function method has been published previously [39] but was extended in this
program to consider issues pertinent to DARWIN analyses; namely, the zone-based
analysis approach.

The essence of the method for independent random variables and a single zone is presented
below. More details on the DARWIN implementation are contained in the appendix in
Ref. [40].

The probability-of-failure is computed as

$$P_f = \int_{g(\mathbf{x})\leq 0} f_x(\mathbf{x}) \cdot d\mathbf{x} \tag{19}$$

where $\mathbf{X}$ is a vector of random variables, $f_{\mathbf{x}}(\mathbf{x})$ is the joint density function of $\mathbf{X}$, and g is the limit state function defined such that $g(\mathbf{x}) \leq 0$ denotes failure.

Inserting the indicator function $I(\mathbf{x})$, which is defined as equal to one if $g(\mathbf{x}) \leq 0$ and zero otherwise,

$$P_f = \int_{-\infty}^{\infty} I(\mathbf{x}) f_{\mathbf{x}}(\mathbf{x}) d\mathbf{x} \tag{20}$$

The derivative of P_f with respect to a parameter of the joint PDF e.g., mean, standard deviation, correlation coefficient, shape, scale factor, etc., denoted θ, can be written

$$\frac{\partial P_f}{\partial \theta} = \int_{-\infty}^{\infty} I(\mathbf{x}) \frac{\partial f_{\mathbf{x}}(\mathbf{x})}{\partial \theta} \frac{1}{f_{\mathbf{x}}(\mathbf{x})} f_{\mathbf{x}}(\mathbf{x}) d\mathbf{x} = E[I(\mathbf{x}) \cdot \mathbf{\kappa}_\theta(\mathbf{x})] \tag{21}$$

where

$$\mathbf{\kappa}_\theta(\mathbf{x}) = \frac{\partial f_{\mathbf{x}}(\mathbf{x})}{\partial \theta} \frac{1}{f_{\mathbf{x}}(\mathbf{x})} = \frac{\partial \ln(f_{\mathbf{x}}(\mathbf{x}))}{\partial \theta} \tag{22}$$

denotes the kernel functions.

As examples, for independent random variables, the kernel functions for a normal random variable are

$$\kappa_\mu = \frac{x - \mu}{\sigma^2} = \frac{1}{\sigma} U$$
$$\kappa_\sigma = \frac{1}{\sigma}(U^2 - 1) \tag{23}$$

where $U = (x - \mu)/\sigma$, and for a lognormal random variable defined in terms of the median $\tilde{X}$ and coefficient of variation COV,

$$\kappa_{\tilde{X}} = \frac{\ln(x) - \ln(\tilde{X})}{\tilde{X} \cdot \ln(1 + COV^2)}$$
$$\kappa_{COV} = \frac{COV \cdot \left(-\ln(1 + COV^2) + (\ln(\tilde{X}) - \ln(x))^2\right)}{(1 + COV^2) \cdot \ln(1 + COV^2)^2} \tag{24}$$

4.4.2 DARWIN Implementation

A DARWIN hard alpha analysis consists of three stages: single zone conditional risk assessment (assumes a defect is present in the zone), a single zone unconditional risk assessment (considers the probability of having a defect), and a multi-zone risk assessment. The sensitivity results from each level feed into the next DARWIN analysis for hard alpha has three random variables: exceedance curve, stress scatter and life propagation scatter. The mathematical development of the requisite equations are provided in the appendix in Ref. [40] (particularly Equations 7, 8, and 15 in the referenced document.)

Stress and propagation scatter are represented as lognormal random variables; therefore, sensitivities with respect to the median and COV are computed. The exceedance curve is nonparameteric tabular input, defined in part by the min and max bounds , a_{min} and a_{max}, of the exceedance curve. Sensitivities with respect to these bounds are computed by DARWIN. The bounds of the exceedance curve (e.g., the standard hard alpha anomaly distributions included in the Federal Aviation Administration Advisory Circular 33.14-1 [41]) have generally been set with the expectation that they are far enough above or below the range of expected behavior as to have no significant impact on the calculation. Therefore, it is anticipated that the sensitivities should be insignificant; otherwise, the exceedance curve should be extended as needed to reduce the sensitivity.

Since the sensitivities are computed using Monte Carlo sampling, the sensitivity estimates are random variables. An estimate of the variance of the sensitivities were derived. In addition, the distribution of the sensitivities follows a normal distribution. As such, the 95% lower and upper confidence bounds were developed and implemented. That is, it is 95% likely that the true sensitivity falls with the values computed by DARWIN. The bounds are set as

$$S_\theta - 1.96\sqrt{V} \le S_\theta \le S_\theta + 1.96\sqrt{V} \tag{25}$$

where V is the variance estimate. Equations for V are provided in the Ref. [40].

4.4.3 Numerical Example

The model consists of a rectangular cross-section titanium ring modeled by 24 zones (Figure 81). The titanium ring is under rotation, and has an external load applied at the rim to simulate blade loading. The maximum principle stress is in the circumferential direction. The crack grows under constant amplitude cyclical loading e.g., start up-shut down, until fracture, defined as when the stress intensity factor exceeds the fracture toughness. The probability-of-fracture of the disk before twenty thousand cycles is computed using Monte Carlo sampling.

The sensitivity results for a single zone unconditional probability of fracture (POF) are compared against finite difference estimates in Table 4. The finite difference estimates are computed by perturbing each parameter by a small percentage and rerunning. We note that it is exceedingly laborious to obtain finite difference estimates in that a very large number of Monte Carlo samples must be used in order to prevent the difference in the POF from being masked by sampling variance, or a very refined importance sampling method must be used. In addition, a separate analysis must be performed for each sensitivity estimate. In the examples below, six additional analyses are required to obtain the finite difference estimates, whereas, the sensitivity equations provide all sensitivities in a single analysis without any additional sampling.

The sensitivity results for the disk (with 24 zones) are compared against finite difference estimates in Table 5. In both tables, the comparison between the sensitivity equations and finite difference estimates are quite good.

**Table 4. Comparison of the Conditional POF Sensitivity Equations
with Finite Difference Estimates**

Random Variable Parameter	Sensitivity Method	Finite Difference*
Propagation Scatter Median	-5.148E-2	-5.195E-2
Propagation Scatter COV	4.765E-3	5.500E-3
Stress Scatter Median	2.037E+2	2.093E+2
Stress Scatter COV	9.042E-2	9.860E-2
Exceedance Curve a_{min}	6.497E-3	6.416E-3
Exceedance Curve a_{max}	3.260E-10	3.602E-10

* 2E6 samples used for all analyses

**Table 5. Comparison of Disk POF Sensitivity Equations
with Finite Difference Estimates**

Random Variable Parameter	Sensitivity Method	Finite Difference*
Stress Scatter Median	1.035E+0	1.066E+0
Stress Scatter COV	7.409E-4	7.796E-4
Exceedance Curve a_{min}	8.883E-9	6.580E-8
Exceedance Curve a_{max}	5.989E-12	5.258E-12
Propagation Scatter Median – cumulative	-2.369E-4	-2.553E-4
Propagation Scatter COV – cumulative	5.891E-5	4.938E-5

* Importance sampling

4.4.4   Concluding Remarks on Probabilistic Sensitivities

The score function method has been modified to fit the zone-based methodology in DARWIN. The score function method has advantages in that the sensitivities are computed without any additional sampling and, therefore, are obtained at negligible additional cost. This is in stark contract to finite differencing which requires a separate analysis for each sensitivity. Variance estimates have been obtained such that the lower and upper 95% confidence bounds for each sensitivity is output.

Since the completion of the probabilistic sensitivity information into DARWIN under DUST funding, a number of continuing enhancements have occurred, most under parallel USAF funding. These enhancement are not implemented into DARWIN but are relevant for fatigue lifing and probabilistic analysis in general.

Using the same score function concept the sensitivity of the response mean and response standard deviation can be computed as

$$\frac{\partial \mu_Z}{\partial \theta} = E[Z(\mathbf{x})\,\kappa_\theta(\mathbf{x})] \tag{26}$$

93

and

$$\frac{\partial \sigma_Z}{\partial \theta} = (E[Z(\mathbf{x})^2 \boldsymbol{\kappa}_\theta(\mathbf{x})] - 2\mu_Z E[Z(\mathbf{x}) \, \boldsymbol{\kappa}_\theta(\mathbf{x})])/(2\sigma_Z) \tag{27}$$

where Z denotes the response, e.g., cycles-to-failure.

Also, kernel functions for correlated normal random variables have been developed.
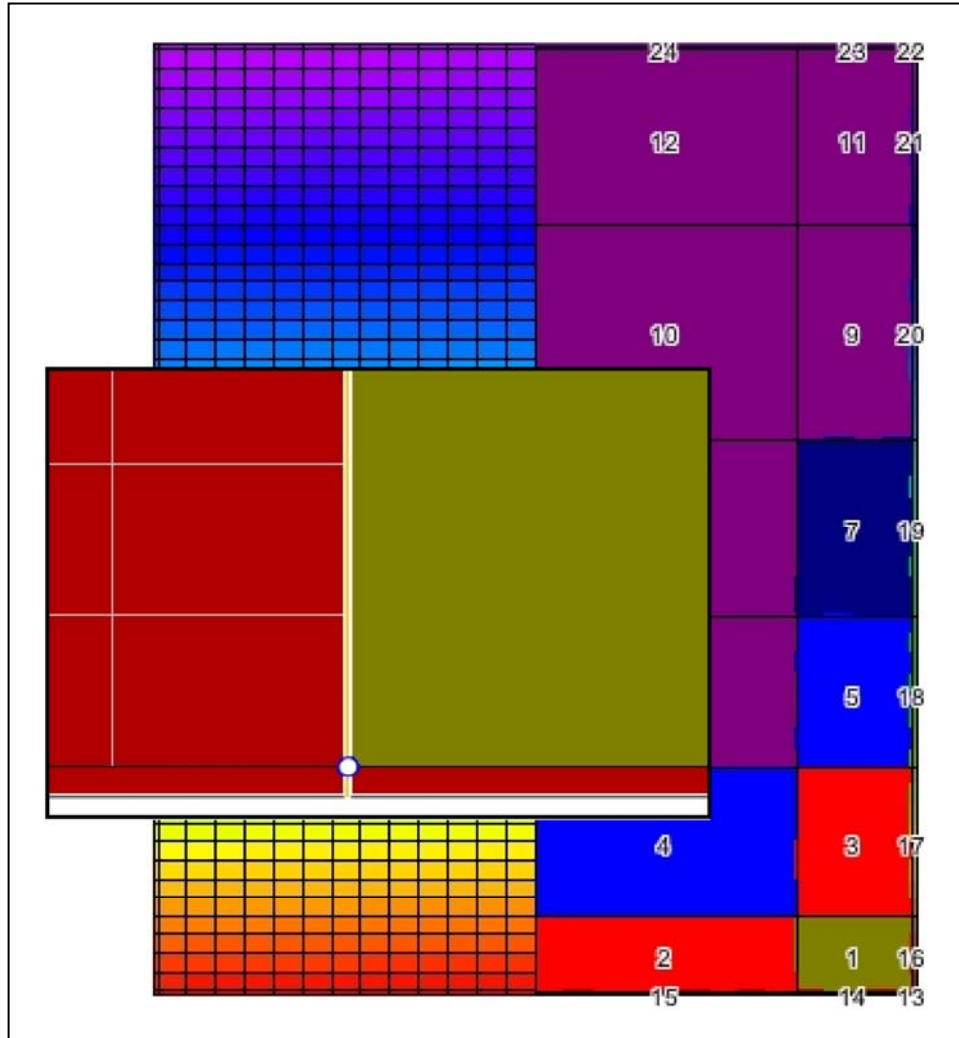
Figure 81. Zone Discretization of Rectangular Cross Section with Blow-up of Zone 2

4.5 Bayesian Updating

The objective for this task was to demonstrate the fusion of data from modeling (fatigue crack growth model) and testing (NDE estimate of crack size).

The mathematics for combining the information from the model and sensor regarding the crack size PDF are based on Bayesian updating. The fundamental equation is

$$f''(x) = kf'(x) \cdot f(x) \tag{28}$$

where $f(x)$ is the likelihood PDF, $f'(x)$ the prior PDF, $f''(x)$ the posterior PDF, and k is a normalizing constant such that $f''(x)$ integrates to one, i.e., $k = 1/\int_{-\infty}^{\infty} f'(x) \cdot f(x) dx$.

For our analysis, $f(x)$ represents the sensor PDF, $f'(x)$ represents the fracture mechanics model-based crack size PDF after a flight and $f''(x)$ denotes the updated PDF that combines the information from the model and sensor. $f''(x)$ denotes the crack size that will be used as a starting crack size for the next flight. Equation 28 is rewritten specific to our analysis as

$$f_M^{i+1}(x) = kf_{M+G}^i(x) \cdot f_S^i(x) \tag{29}$$

where the subscript "M" represent the fracture mechanics model, "$M+G$" stands for the model plus crack growth, "S" denotes the sensor, and i denotes the flight number. After the ith flight, the crack size from the model is $f_{M+G}^i(x)$ and the sensor estimate of the crack size is $f_S^i(x)$. From Equation 29, the starting crack size for the simulation of the next flight using the fracture mechanics model is $f_M^{i+1}(x)$. This process is repeated after each flight.

A synopsis of the methodology is shown in Figure 82; the crack size PDFs are fused through a Bayesian updating equation. The result of the fusion becomes the input distribution to the model for the next flight.

Bayesian updating: model pdf & sensor pdf

$$f_M^{i+1}(x) = k f_{M+G}^i(x) \cdot f_S^i(x)$$

i	-flight no.
f_S^i	-Sensor pdf
f_M^{i+1}	-Model + Growth pdf
f_{M+G}^i	-Updated pdf for next flight (input to model)

Red Curve is crack size PDF predicted from the fracture mechanics model, blue curve is the prediction of the PDF by the sensor, green is the resulting fused PDF the becomes and input to the next flight.
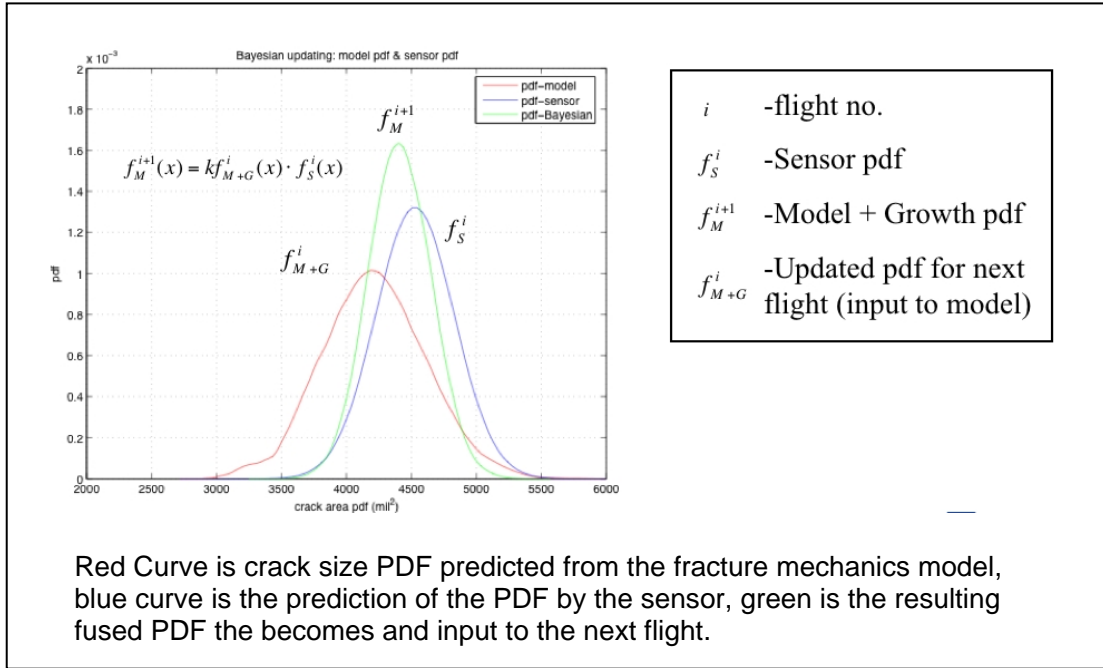
Figure 82. Notional Application of Bayesian Updating

4.5.1 Demonstration

The implementation of Bayesian updating was accomplished through a combination of Matlab (Bayesian updating) and DARWIN (crack growth analysis). The implementation is nonparametric, that is, no assumptions are made about the form of the crack size distributions (either DARWIN or the sensor). The Monte Carlo crack size results from DARWIN were output to a file and analyzed using a density estimation method to generate $f_{M+G}^i(x)$. This density was fused with the sensor density $f_S^i(x)$ to produce $f_M^{i+1}(x)$, see Equation 29. This density was then discretized numerically and input to DARWIN for the next flight.

Some general notes about Bayesian updating: (1) there is no resulting density unless distributions overlap, and (2) the density with the tightest variance dominates. That is, the "tightest" density contains the most information about the probable location of the crack size. A "non-informative" prior density that contains no information on the probable crack size outside of the given bounds would be a uniform distribution. Therefore, the resulting distribution after Bayesian updating more closely takes the shape of the tighter distribution.

The sequential analysis, grow the defect N flights, fuse the model and sensor PDFs, and input the fused data into the model for the next flight, has been automated through a combination of Matlab and DARWIN, see Figure 83. The implementation makes no assumptions about the DARWIN analysis, that is, whatever content is contained in the DARWIN template file will get executed. This provides great flexibility regarding the analyses that can be considered. The Bayesian implementation modifies only the initial

crack size distribution entered into DARWIN and reads the crack size results after a DARWIN analysis.
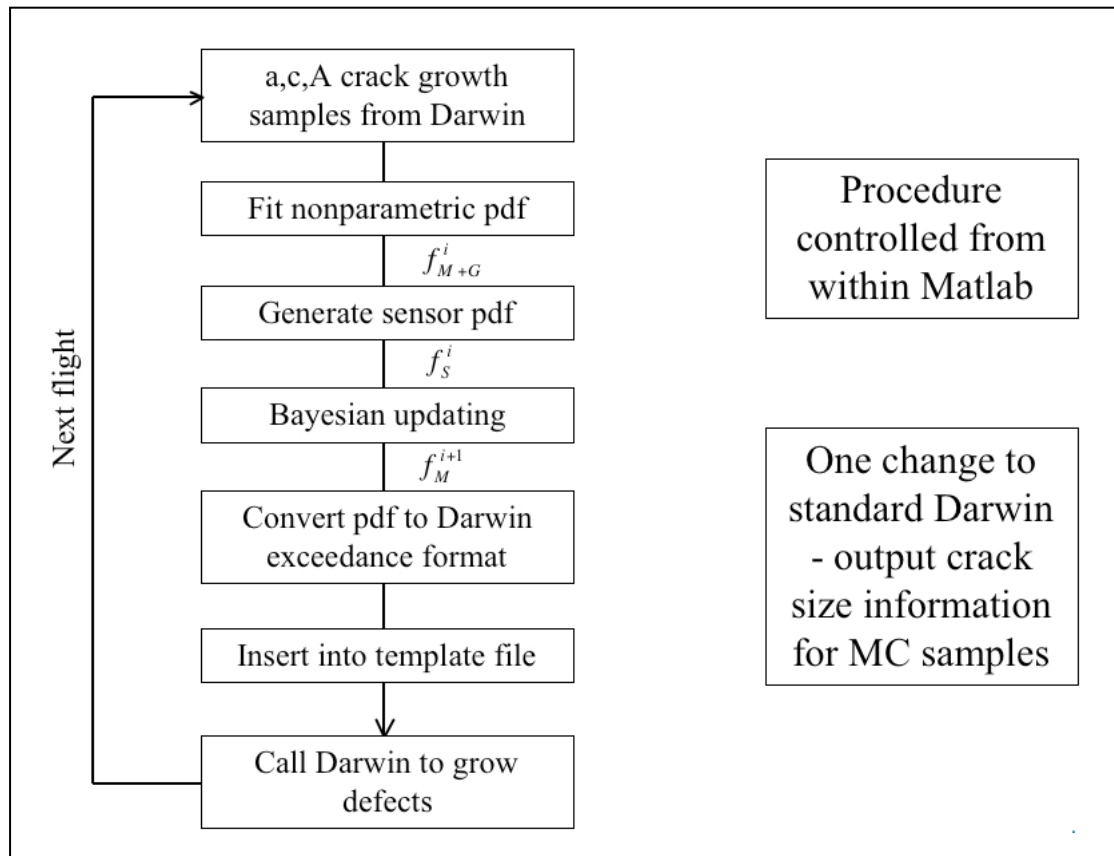
Figure 83. Schematic of Bayesian Updating Procedure

4.5.2 Demonstration Problem

The analysis procedure is demonstrated using a notched beam in pure bending containing two thin-film magnetostrictive ultrasonic sensors. The crack was grown in fatigue and interrogated using the sensors.

4.5.3 Initial Crack Size Distribution

A central issue in a probabilistic analysis is the initial crack size distribution. Under FAA-sponsored efforts, the original equipment manufacturers (OEMs) have developed a crack size distribution for machined holes in disks which represents results that can be expected for a fleet of disks, see Figure 84 [42]. The probability density is "exponential-like" in that it has a high probability of small cracks with a long right tail to capture the possibility of remote large cracks. This distribution is used as a starting distribution for the demonstration problem. As will be shown, the initial crack size distribution is modified significantly based upon the sensor crack size estimation.
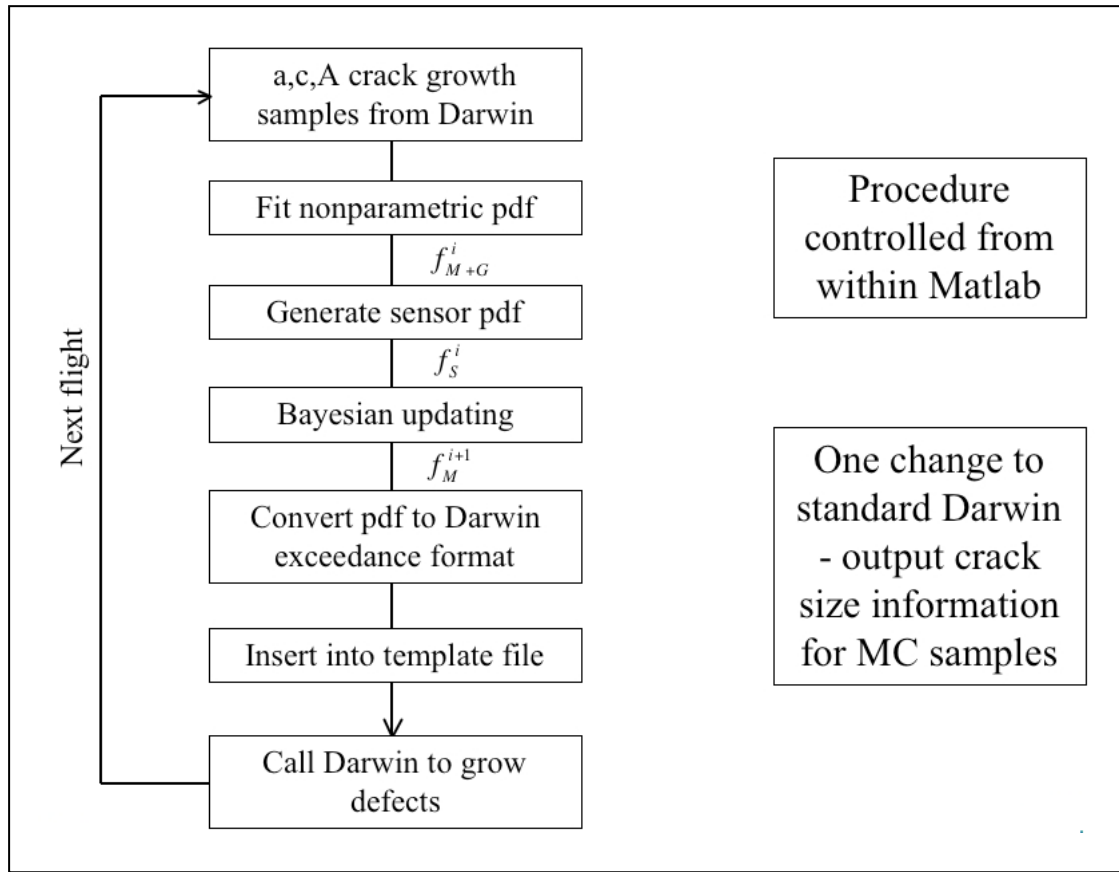
Figure 84. Initial Crack Size Distribution

4.5.4 Thin-Film Sensor (TFS)

The signal-to-noise ratio from the TFS was compared against known crack area obtained from observation of post-inspection marker bands on the specimen. The regression results are shown in Figure 85. The regression results indicate a constant standard deviation of approximately 2349 mil^2. For analysis purposes, the TFS result was truncated at a crack size of 2670 mil^2 (S/N = 1), i.e., no size information is provided below this crack size. This truncated value was set at -2 standard deviations which set the mean size as 7370 mil^2 (a = c = 66 mil). In summary, the crack size density estimate from the sensor was modeled as a normal distribution with mean 7370 mil^2 , standard deviation 2349 mil^2 and truncated in the left tail at 2670 mil^2.
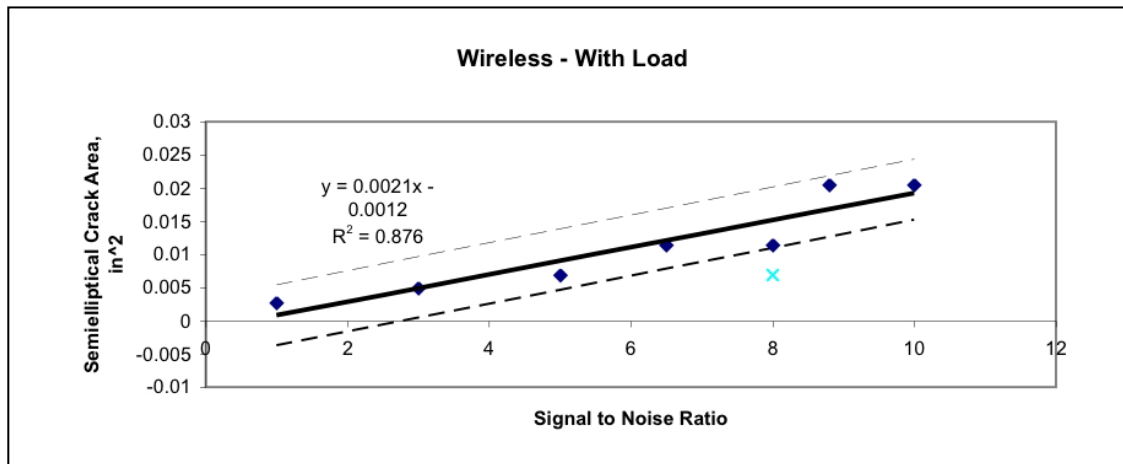
Figure 85. Thin-Film Sensor Experimental Regression Results

4.5.5   Analysis Results

Constant Sensor Reading

Various scenarios can be considered using the developed analysis tools. Figure 86 shows the results as a function of flights with the sensor density unchanged with the number of flights. The results show the model PDF becoming more narrow and approaching the mode of the sensor. Most interestingly is the plot summarizing the behavior of the mean and standard deviation of the fused PDF. The results from flight 1 represent the initial crack size distribution grown 1 flight. After fusing with the sensor, the mean value jumps significantly from approximately 1800 mil^2 to 6000 mil^2 because the sensor has found an indication of a defect. Note however, that the standard deviation reduces from 3500 mil^2 to 2000 mil^2. In other words, we have a much stronger belief in the crack size after the sensor detects an indication.

Sensor Drift to the Right

Figure 87 shows the results of a simulation where the sensor reading is taken every 1000 flights and the sensor drifts to the right by 400 mil^2 per every 1000 flights. In this scenario, the model initially under predicts the PDF relative to the sensor but later over predicts relative to the sensor. The mean and standard deviation show a similar behavior as discussed previously; the mean has a large jump initially then increases more slowly and the standard deviation drops significantly after the first flight then reduces more slowly.
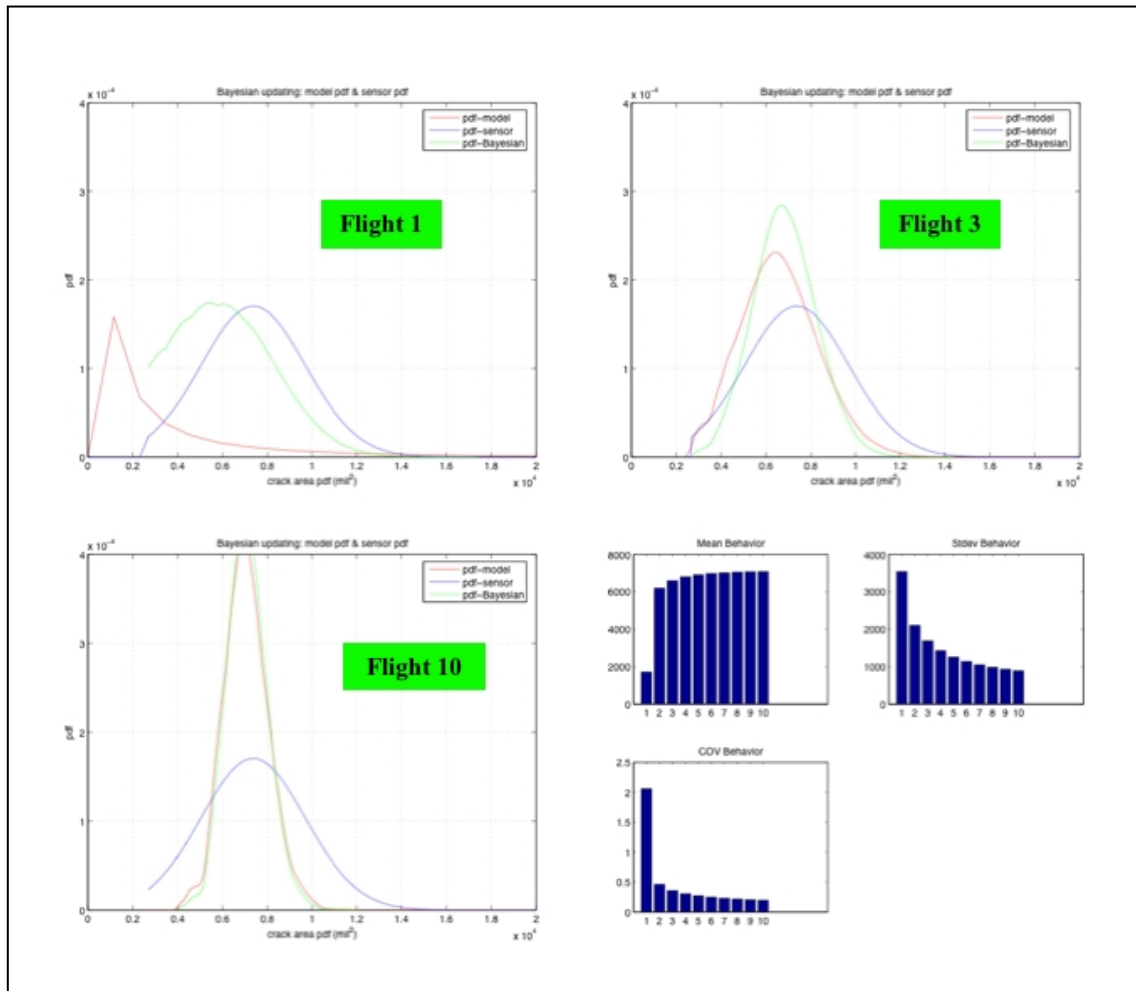
Figure 86. Result of Bayesian Updating of Model and Sensor – Fixed Sensor
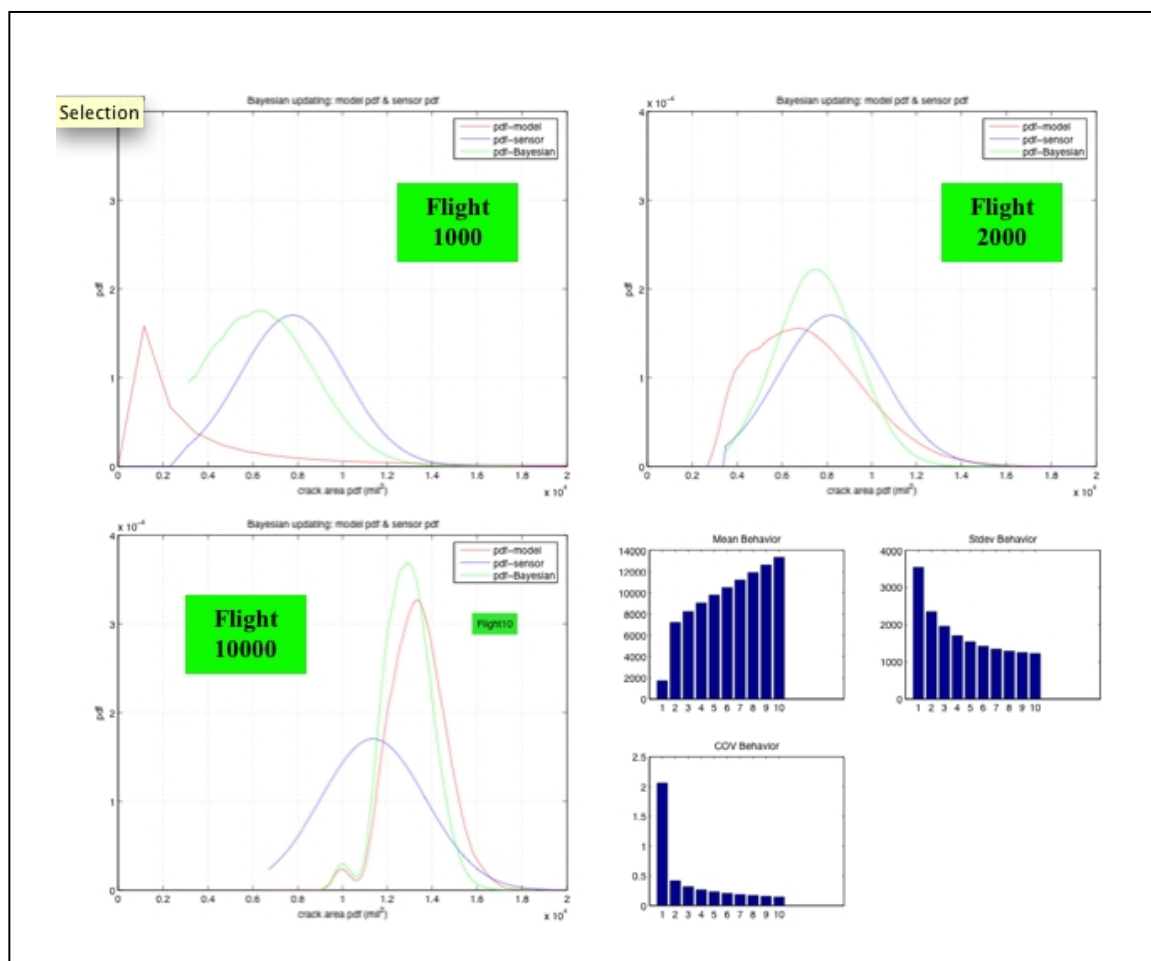
**Figure 87. Result of Bayesian Updating of Model and Sensor –
Sensor Drift 400 mil²/1000 Flights**

4.5.6   Summary

The mathematics necessary to combine information on crack size from models and sensors is contained in Bayesian updating. This technology provides a straightforward way to update the crack size PDF given data from both sources.

The Bayesian updating algorithm was implemented in software using DARWIN for the crack growth analysis and Matlab for the Bayesian updating. The methodology makes no assumptions on the DARWIN model nor any assumptions on the crack size distribution type.

Two demonstration problems were exercised, one with a fixed sensor reading (no change with flight number) and one with a sensor that drifted 400 mil^2 with each 1000 flights. The problems demonstrated the large reduction in standard deviation of crack size from the assumed initial damage PDF achieved by having a sensor reading.

4.6   Benefits of Parallel Processing

The objective of this task was to perform an introductory look into parallel processing methods for DARWIN and to see what, if any, low cost items could be handled under DUST.

Probabilistic fracture mechanics is inherently computationally time consuming. Although numerous efficiency enhancements have been implemented into DARWIN over the years, new capabilities have also been added which require increased computational time. Most importantly, analysis requirements for military missions (many time points), prognosis (cycle-by-cycle integration), residual stress analysis, etc. are exceptionally demanding. Table 6 below shows a schematic of real scenarios and the corresponding computational time using a desktop personal computer purchased circa 2003. Although other analyses will have different execution times, it is clear that an improvement in execution time is needed. Fortunately, parallel processing offers an avenue to address this issue.

Table 6. Analysis Scenarios Driving the Need for Increased Computational Efficiencies in Probabilistic Fracture Mechanics Analyses

Topic	Reason for Computational Expense	Time to execute – desktop PC
Simulation of onboard sensor	Cycle-by-cycle fatigue crack growth, single inspection scenario, Monte Carlo sampling	24 hrs with 5000 samples (more samples needed). Multiple inspection scenarios required
Bayesian updating of engine prognostics using a virtual crack sensor concept	Cycle-by-cycle fatigue crack growth, Bayesian updating of crack size, neural network training, Monte Carlo sampling	Similar but slightly longer to "Simulation of onboard sensor", see row 1.
Probabilistic risk assessment of fatigue disk life subject to inherent defects	Multiple zone analyses required for inherent defects, Monte Carlo sampling	50-100 hrs for 2000 samples. More samples required.
Residual stress effects on probabilistic lifing of engine disk materials	Multiple probabilistic fatigue analysis required to implement GCE algorithm	20 hrs with 2000 MC samples, only 1 zone

4.6.1 Parallel processing approaches

There are several levels of parallel processing typically organized by "granularity" of the method. OpenMP is well-suited for fine grained parallelism (low amounts of communication time), Message-Passing Interface (MPI) is well-suited for coarse grained, and grid computing for multiple independent analyses.

4.6.2 Multi-Threading (OpenMP)

OpenMP is a parallel programming model for shared memory computers (multi-processor machines where all processors can see all memory). OpenMP is administered by an independent oversite board (www.openmp.org). As such, it is now a standard for Fortran and C and supported by multiple compiler vendors. The OpenMP web site also contains tutorial information and there are books available [43].

OpenMP is a multi-thread approach to parallel programming – a master execution thread is forked into any number of threads to execute a user-defined sequence of code, see Figure 88. The forking and joining of threads is determined by the user using compiler directives.

One of the advantages of OpenMP is that an executable can be parallelized "piece by piece" over time. That is, compiler directives can be inserted in the source code to multi-

thread sections of code as time permits. This is in contract to MPI which often requires a whole scale modification.

OpenMP compiler directives are designed such that compilers that do not support OpenMP see the directives as comments. Thus, there is no decrement to behavior for compilers that do not support OpenMP. The compiler directives are documented in the OpenMP specification, tutorials and books.

The limitation of OpenMP is that it is designed for shared memory machines and the number of processors on shared memory machines is limited; although this is changing. For example, a top end desktop machine 5 years ago contained 2 processors. Now, 4 processor machines are routine and 8 processor machines are common. This trend is likely to continue; however, shared memory machines with hundreds or thousands of processors are not expected in the foreseeable future. This fact puts a limit on the scalability of parallel algorithms using OpenMP.
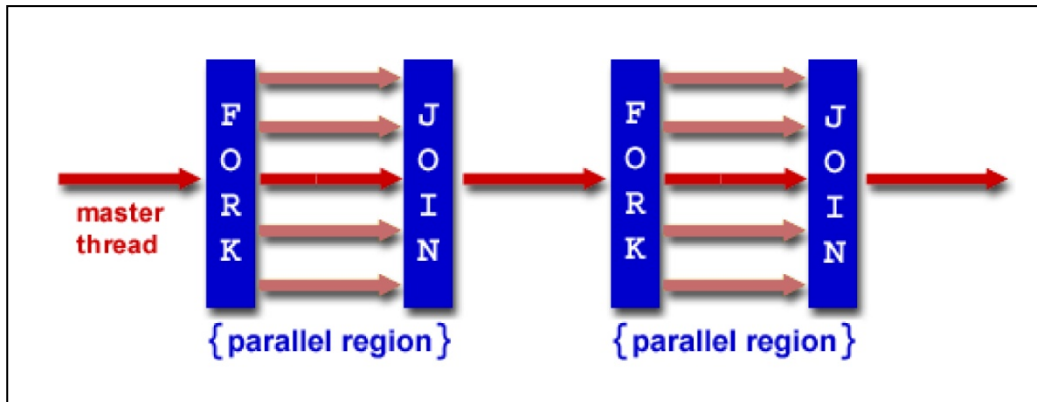
Figure 88. Example of OpenMP Fork-Join Thread Process

4.6.3   Message-Passing Interface

MPI is the most general method for parallel processing. MPI requires only local memory for each processor and a means of communicating between processors to share information [44]. This model matches many inexpensive "clusters" and maps to the Internet in general.

MPI is a standard governed by an oversite board (www.mpi-forum.org). MPI is a library not a compiler enhancement, hence use of MPI requires installation of a library on each system.

The essence of MPI is the message; the sender packs data into a message, sends the message to a specific user or users, each user agrees to receive the message, then unpacks the data.

A key element that often defines the usefulness of MPI is the computation to communication time ratio. Packing data, sending, then receiving data obviously consumes central processing unit (CPU) and wall time. A good algorithm will optimize the time spent computing versus communicating.

Because MPI is well suited to distributed memory machines or clusters, theoretically, it can scale to any number of processors, depending upon the algorithm. Hence, well designed and highly parallel algorithms can take advantage of hundreds or thousands of processors.

4.6.4   Grid Computing

Grid computing is the coarsest method and involves decomposing the problem into a number of independent analyses. As defined by Wikipedia: "Distributed" or "grid" computing in general is a special type of parallel computing which relies on complete computers (with onboard CPU, storage, power supply, network interface, etc.) connected to a network (private, public or the Internet) by a conventional network interface, such as Ethernet. This is in contrast to the traditional notion of a supercomputer, which has many processors connected by a local high-speed computer "bus." The advantage of grid computing over MPI or OpenMP is that open-source software exists that can be easily installed and used to coordinate the independent analyses.

There are several grid computing "engines": CONDOR (http://www.cs.wisc.edu/condor/), Sun Grid Engine (http://gridengine.sunsource.net/), Globus (www.globus.org), IBM's Grid and Grow (http://www-03.ibm.com/grid/gridandgrow.shtml), etc. The web site http://www.gridcomputing.com/ offers more information about grid computing.

4.6.5   Application of Grid Computing

Under FAA funding, DARWIN was modified such that the zone-based analysis would fit within the grid computing paradigm through a domain-decomposition approach. In effect, each zone is mapped to a different computer. In practice, to reduce communication time, multiple zones may be bundled into one analysis and passed to a computer.

Under DUST funding, the multi-input file capability was exercised using the grid computing program CONDOR from the University of Wisconsin using a bank of standard personal computers running the Windows operating system located at UTSA. The approach and results are contained in the paper "Application of Parallel Processing to Probabilistic Fracture Mechanics Analysis of Gas Turbine Disks" presented at the 2004 AIAA Structures, Dynamics, and Materials conference, see the Appendix.

The results revealed the effectiveness of the approach; an efficiency of 77% was obtained for a problem consisting of 6250 zones, with the zones divided into 121 different input files and run over 18 computers.

4.6.6 Summary

Parallel processing is a critical technology for applying DARWIN to analyses of military scenarios. Parallel processing paradigms of MPI, multi-threading (OpenMP) and grid computing were briefly reviewed. Several grid computing examples were developed using a parallel network of personal computers running Windows 2000 and the CONDOR public domain program. The approach was effective, yielding an efficiency 77% was obtained for a problem consisting of 6250 zones. The efficiency is largely controlled by the ratio of the communication/computation time. This ratio can be approximately controlled by the user by setting the number of zones written to an file. Our opinion is that the best choice for the number of files is a small multiple, say 3 or 4, times the number of computers in the network. This allows some dynamic load sharing without excessive communication time. However, this approach does not address the requirements for many military missions that require large execution times for a single zone.

4.6.7 Future Efforts

The grid computing approach is effective for multiple zones yet has some significant deficiencies. Foremost, the method cannot be applied to single zone problems. As shown in Table 6, cycle-by-cycle crack growth with inspection needed for prognosis combined with large loading histories indicate that even single zone problems may be very computationally demanding problems and cannot be addressed with grid computing. As such, it is proposed that a significant effort be expended to enhance DARWIN with OpenMP and or MPI capabilities. The logical application of these methodologies would be to parallelize the Monte Carlo sampling algorithm. OpenMP is a logical first step but it is limited to shared memory computers. However, the recent progress in microprocessors is towards single chips with many CPU cores. Thus, implementation of OpenMP may not be as limiting as at first glance. MPI is the most general approach and can scale to any size however the level of effort to implement and debug is substantially higher. Therefore, it is recommended that the OpenMP and MPI paradigms be explored for implementation into future versions of DARWIN.

4.7 Combining Classical and Physics-Based Diagnostics and Prognostics

Two distinctly different approaches to diagnostics and prognostics have been pursued, and continue to evolve, within the technical community:

> *1) Classical diagnostics and prognostics* – these methods are largely data-driven and employ signal processing of on-board data to define baseline operating conditions, deviations from these baselines (faults), from which fault limits are established and used to trigger inspection and/or maintenance actions.

2) Physics-based diagnostics and prognostics – these methods are based on an underlying physical model for material damage or structural degradation – for example, the deterministic and probabilistic fatigue crack nucleation and growth models described in the preceding section of this report. The damage rate and final instability (failure) of the material is independently measured and expressed in terms of a physical "driving force" such that the result is a material property (that can in some instances also depend on environment and loading rate). These material properties are then combined with finite element stress analysis of the component of interest to predict the nucleation and growth of damage, as well as final failure of the component.

Each of these approaches has certain advantages and disadvantages. For example, the physics-based methods have the advantage of being more rigorous and potentially more accurate – particularly for prognosis. However, the disadvantage of these methods is that they can be computationally intensive for certain applications, and thus may not be amenable to real-time component assessments; they also require a detailed understanding of the damage or degradation process, which is not always known. In contrast, classical diagnostics and prognostics approaches are generally faster, since they employ more efficient probabilistic methods based on artificial intelligence, neural networks, and Bayesian statistics that do not require detailed knowledge of the physics. Consequently, they are applicable to a wide range of systems (mechanical, electrical, fluid), as well as to higher levels within the system – for example, a system or sub-system that may contain many components. However, this lack of an underlying physical model means that classical methods must be carefully trained (calibrated) for each specific application, and depending on the availability of empirical data their selected fault limits may not be optimum or universal. One consequence of the fuzzy nature of the fault limit is that classical methods are generally more diagnostic than they are prognostic.

In view of the above trade offs between the two approaches, it would seem that some combination of these methods would be optimum for diagnostics and prognostics. Thus, the goal of this task was to assess the feasibility and potential benefits of combining classical diagnostic and prognostic methods with physics-based methods. The specific approach in this case was to look for turbine engine diagnostic and prognostic problems that might demonstrate enhanced solutions by combining the capabilities of Smiths' Probabilistic Diagnostic and Prognostic System (ProDAPS) and SwRI's probabilistic fracture mechanics software (DARWIN). A common point of departure for this exercise is that both methods recognize the considerable uncertainty that can exist in diagnostics and prognostics, thus both methods are probabilistically based.

ProDAPS was developed on a parallel DUST Program. ProDAPS was used to develop and demonstrate advanced Prognostic Health Management (PHM) capabilities for a range of engine and aircraft applications. All ProDAPS elements were built as software components and were designed in an open architecture to enable technology insertion into both airborne and ground-based systems for existing and future applications. ProDAPS uses advanced artificial intelligence tools to provide a probabilistic, knowledge rich,

framework to: Integrate all available types of health, usage, maintenance and reliability data; Provide advanced data analysis capabilities to maximize the available information; Fuse and reason with data from all sources to provide accurate diagnostics and prognostics; Support the user in optimum decision making, and; Adapt and improve its performance through the mining of historical data to discover new knowledge

Several approaches to assessing the effectiveness of ProDAPS and DARWIN capabilities were pursued. The goal of one of these efforts was to assess if ProDAPS could detect fault events that would be potentially detrimental to the operating environment of rotor/disks and pass them to DARWIN for more effective treatment of actual engine usage and its influence on component fatigue life. The output from DARWIN could also be fed back to ProDAPS for further prognosis and decision support. This exercise was focused on detection stalls and over-speeds since these faults should be detrimental to rotor/disk health and component life. This exercise required that data be fused from two separate data bases: 1) the Engine Diagnostic Unit (EDU) from the Comprehensive Engine Tracking and Diagnostic System (CETADS), which among other things, records transient data when fault events on engines are detected; and 2) data from Flight Data Recorders (FDRs), which among other things, records usage in terms of engine RPM vs. time histories as part of the Aircraft Structural Integrity Program (ASIP). The latter data are required to compute fatigue crack growth lives using DARWIN.

Although a total of 192 stall events and 1 over-speed event were indicated in the CETADS data base, we were able to find the corresponding FDR full usage data for one stall event. This is due in part to the fact that FDRs are only on 20% of the fleet. Moreover, FDR data sets are identified by aircraft tail number (not engine serial number), and CETADS data is only identified by the download date, which is not necessarily the flight date. In addition, further scrutiny of the data determined that of the 192 indicated stall events only one was found to be a valid stall, and there was no matching FDR data for this event. Thus no correlated data were found to meet the exercise objective. The major conclusion was that extracting correlated data from CETADS and FDRs is both inefficient and non-productive because of lack of common identifiers for engines, the limited number of aircrafts that contain FDRs, as well as the inaccuracies that exist in the EDU/CETADS data.

As indicated previously in Section 4.3, statistical analysis of usage data is hampered by the fact that mission type is often not recorder in the FDR database, thereby providing the motivation to develop an automated procedure from identifying the mission given the usage (RPM vs. time). Thus, an attempt was made to develop a data-driven Mission Classifier using cluster analysis. Cluster analysis is a data mining tool that can reveal associations and structure in data that is not initially evident. Using statistical analysis this method can sort cases (e.g. missions, people, things, events) into groups, or clusters, so that the degree of similarity is strong between group members and weak among non-members. Cluster analysis was assessed for its ability to define a formal classification scheme for mission types based on analysis of the characteristics of flight histories.

The specific data employed in this exercise was from F100-229 engines on F-15 aircraft at Lakenheath, Nellis, Mountain Home, and Elmendorf between 2002 and 2003. Although FDR data was available from nine different mission types, the analysis focused on the two missions – Live Fire and Instruments and Navigation. The data metric used to classify the missions was the percentage of flight time spent at various Power Lever Angles (PLAs) as follows: IDLE to 18°, 18°-30°, 30°-50°, 50°-83°, and greater than 83°. Seven different cluster models were generated having two and eight clusters in each model. Using the Bayesian Information Criterion (BIC), the best cluster model for both mission types was determined to be the model with five clusters. However, the results showed no clear distinction between the to different mission types. Thus, the number of PLA intervals was reduced from seven to four as in the industry definition of TACs. In this case, the Live Fire missions were best described by a cluster model with five clusters, while the instrument and navigation missions were best characterized by a cluster model with three clusters. However, as shown in Figure 89, it was found that the characteristics of the above cluster models were very close; thus, a clear characterization parameter to distinguish between the two mission types did not emerge.

It is hypothesized that the lack of success in using the above cluster analysis to automatically identify missions types from usage is due either to the relative lack of data for each mission type, or to the fact that the missions may have been improperly identified since these designations are currently manually logged by the pilot following the flight – a subjective process that may be prone to error or inconsistencies.

The ordinate in the figure is Bayesian Information Criterion (BIC) and the abscissa shows intervals of Power Lever Angle (PLA) per the industry definition of Total Accumulated Cycles.
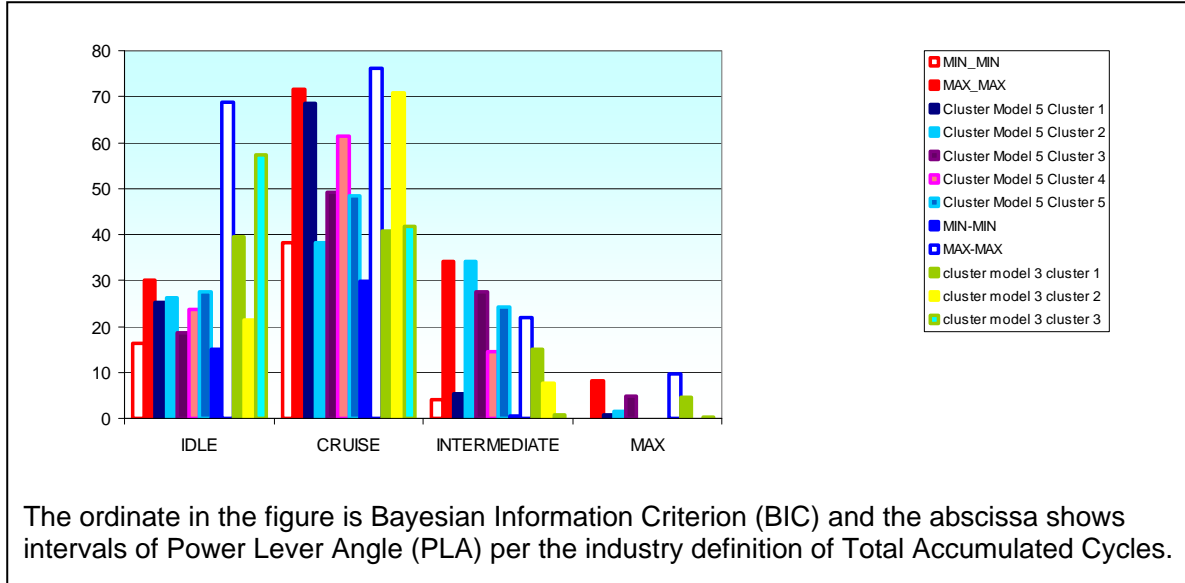
Figure 89. Cluster Analysis Indicated That Cluster Model Five Best Characterized the Live Fire Missions, and Cluster Model 3 Best Characterized the Instrument and Navigation Missions; However, These Characteristics Were Not Sufficiently Different to Uniquely Discriminate Between the Two Mission Types

The above analyses served to highlight two important issues: 1) the limitations in using current data bases for the tasks performed here – specifically, data are not consistently cross referenced from one data base to the next so that they can be fused for a given mission, and 2) the difficulties encountered in attempting to develop an automated mission classifier stimulated thought that led to the eventual development of the Probabilistic Mission Identification method described in Section 4.3.

Regarding the need for data strategies that facilitate sharing and processing data across data bases and organizational boundaries, the current situation not only limited the above tasks, but would also limit diagnostics and prognostics in general, as well as the broader Department of Defense (DoD) goals under the Condition Based Maintenance Plus (CBM$^+$) initiative [45]. Fortunately, this limitation has been recognized in the guidelines that are being prepared to implement these important initiatives [46].

5. Results and Discussion on Technology Transition: New DARWIN Capabilities

5.1 Summary of DARWIN Enhancements

The following new DARWIN features were implemented under this project:

- FaNG Model (General Inherent Analysis Mode, 1D Surface Damage Analysis Mode)
- Residual Stress Capability (General Inherent Analysis Mode)
- Mission Mixing (All Analysis Modes)
- Probabilistic Sensitivities (General Inherent Analysis Mode).

A brief description of the implementation and use of these features is provided in the sections that follow.

5.2 Implementation in DARWIN

5.2.1 FaNG Model Implementation

A new DARWIN capability was implemented that allows the User to select the FaNG model for crack nucleation and growth computations. The FaNG model predicts the crack nucleation and growth lives for a specified initial crack size. It consists of (1) a smooth specimen total life computation, (2) a smooth specimen crack growth life computation, and (3) a surface crack in plate crack growth life computation. The smooth specimen total life calculation is performed using equations that are defined in a separate module (the DARWIN "formation module"). This module is called during execution of DARWIN, and can be edited by the User as necessary for definition of the equations associated with smooth specimen total life. The smooth specimen crack growth life is performed within DARWIN using a surface crack in round bar stress intensity solution (SC07) that was recently implemented specifically for this purpose. The surface crack in a plate crack growth life computation is performed using existing stress intensity solution SC17. Note that the FaNG model is currently limited to surface crack in plate geometries.

During execution, the smooth specimen nucleation life is obtained by subtracting the smooth specimen crack growth life from the smooth specimen total life. For smooth specimen crack nucleation life computations, the stress value is set to the value at the User-specified nucleation (initial crack) depth. This stress value is also used for the smooth specimen crack growth life computations, where a uniform stress field is assumed. A small crack correction factor is applied to all crack growth computations to account for changes in the crack growth rate associated with small fatigue cracks.

5.2.2   Residual Stress Capability Implementation

A new DARWIN capability was implemented for treatment of surface residual stress values. This new capability allows the User to define a residual stress field that appears as a rectangular region that is superimposed on the 2-dimensional axisymmetric finite element model that appears in the DARWIN GUI. Stress values within the region that are applied to crack nucleation and growth life computations are based on the sum of the residual stress values and the finite element stress values.

5.2.3   Mission Mixing Implementation

The existing DARWIN mission mixing feature provides the capability to assess the life and probability of fracture of a component that has the same mission mix over the entire design life. For example, consider a mission mix that consists of three missions (Missions A, B, and C) that have equal mix percentages. If the existing DARWIN mission mixing capability is used, the mission sequence "ABCABCABC …" is applied repeatedly over the lifetime of the component.

Under this project, the DARWIN mission mixing capability was enhanced to allow the User to specify changes in the mission mix at specified flight intervals. For example, consider two mission mixes (Mission Mixes 1 and 2) that begin at different flight intervals. Mission Mix 1 consists of missions A, B, and C, and Mission Mix 2 consists of missions D and E. Mission Mix 1 begins at 0 flight cycles, and Mission Mix 2 begins at 5001 cycles. For this scenario, the mission sequence "ABCABCABC …" is applied repeatedly over the first 5000 cycles, and then the mission sequence "DEDEDE …" is applied over the remainder of the life.

5.2.4   Probabilistic Sensitivities Implementation

The sensitivity methods developed by Karamchandani [47] and Wu [48] were extended for application to additional parameters of random variables. Analytical expressions for probabilistic sensitivities were developed for the stress scatter, life scatter, and initial anomaly area random variables. Variance and associated confidence bound estimates were also developed for these variables. Probabilistic sensitivities and confidence bound expressions were implemented in DARWIN for these three random variables. A significant feature of the implementation is that sampling-based sensitivities are computed directly from the Monte Carlo results associated with failure probability computations, and are therefore very inexpensive to compute. Complete details regarding the equations are provided in [40].

5.3   New DARWIN GUI Features

5.3.1   Enabling New Features in DARWIN GUI

The DARWIN enhancements associated with this project were implemented as password protected features. To enable these features, the User must provide a unique password (Figure 90).
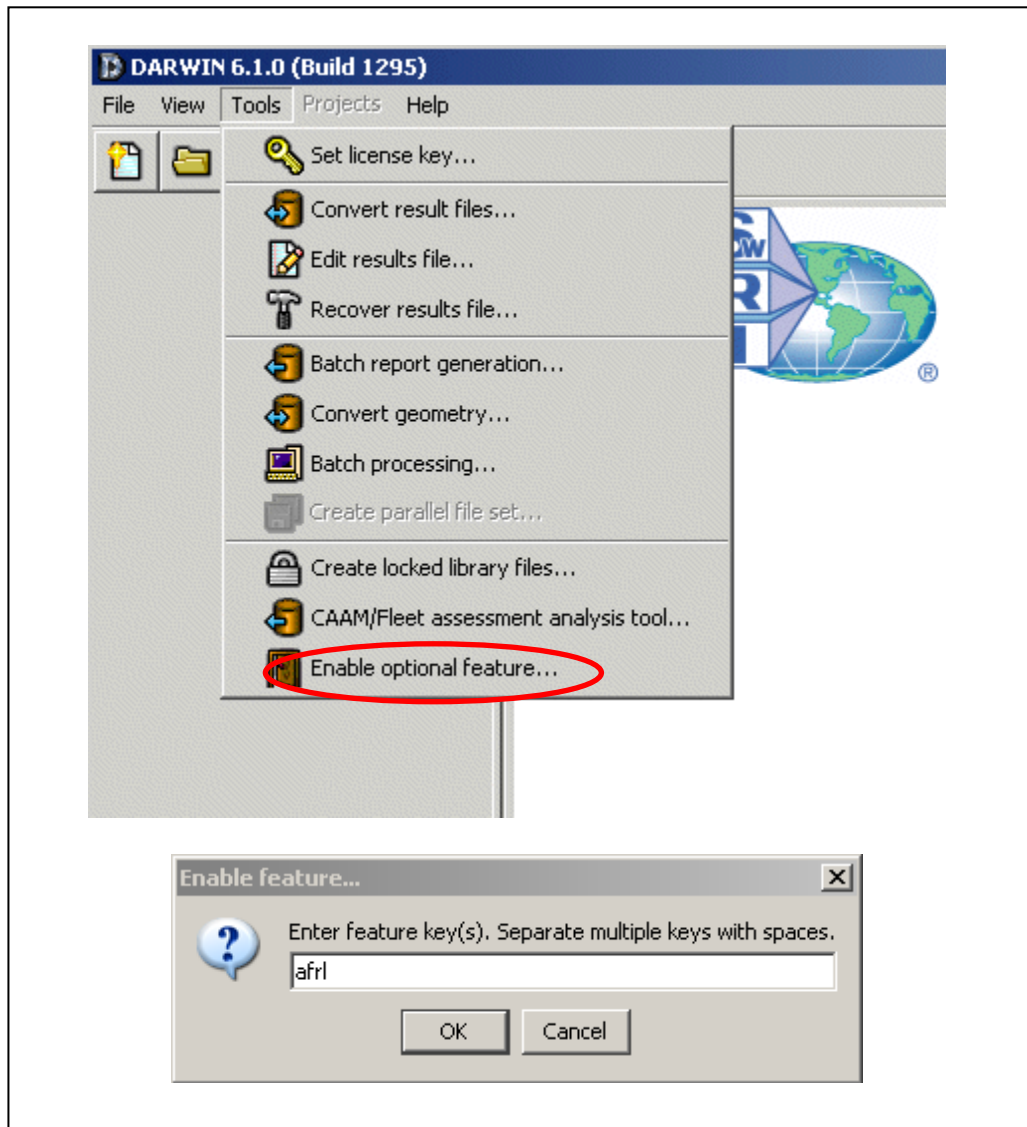
**Figure 90. The DARWIN Enhancements Associated with This Project
Were Implemented as Password-Protected Features**

5.3.2 Use of FaNG Model in DARWIN GUI

As shown in Figure 91, the FaNG model was implemented as a life option associated with the DARWIN Formation module. When the FaNG option is selected, the User must specify values for the a_0 constant (small crack correction) and the diameter of the specimen associated with smooth specimen crack growth life (SC07 diameter).
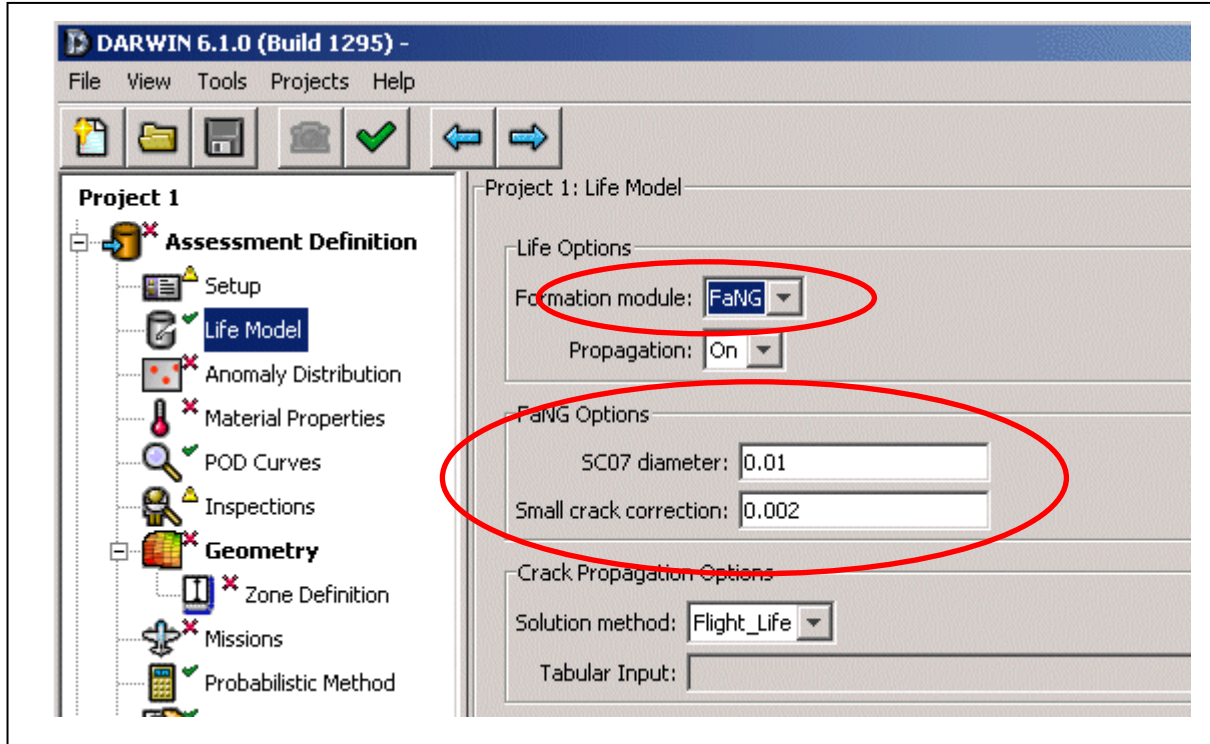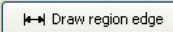
Figure 91. The FaNG Model Was Implemented as a Life Option Associated with the DARWIN Formation Module

5.3.3 Use of Residual Stress Capability in DARWIN GUI

A capability for treatment of residual stress (RS) values was implemented in DARWIN. This feature is activated by selecting use of "residual stress profiles" located in the DARWIN "Setup" menu (Figure 92). Definition of residual stress profiles in DARWIN consists of the following steps:

(1) Create an RS region. Click the [KB] button in the **Geometry** menu to bring up the **Stress Region Editor** window, (Figure 93). In the **Stress Region Editor** window, click the [+] button to create a stress region. The RS region is defined by a region edge (width of the RS region) and values of the RS versus physical distance from the starting edge (length of the RS region).

(2) Draw Region Edge. Click the [↔ Draw region edge] button to draw the region edge. On the finite element geometry, click at the starting point of the region edge, hold the mouse, drag it to the end point of the region edge, then release the mouse.

114

This feature is activated by selecting use of "Residual Stress Profiles" located in the DARWIN "Setup" menu.
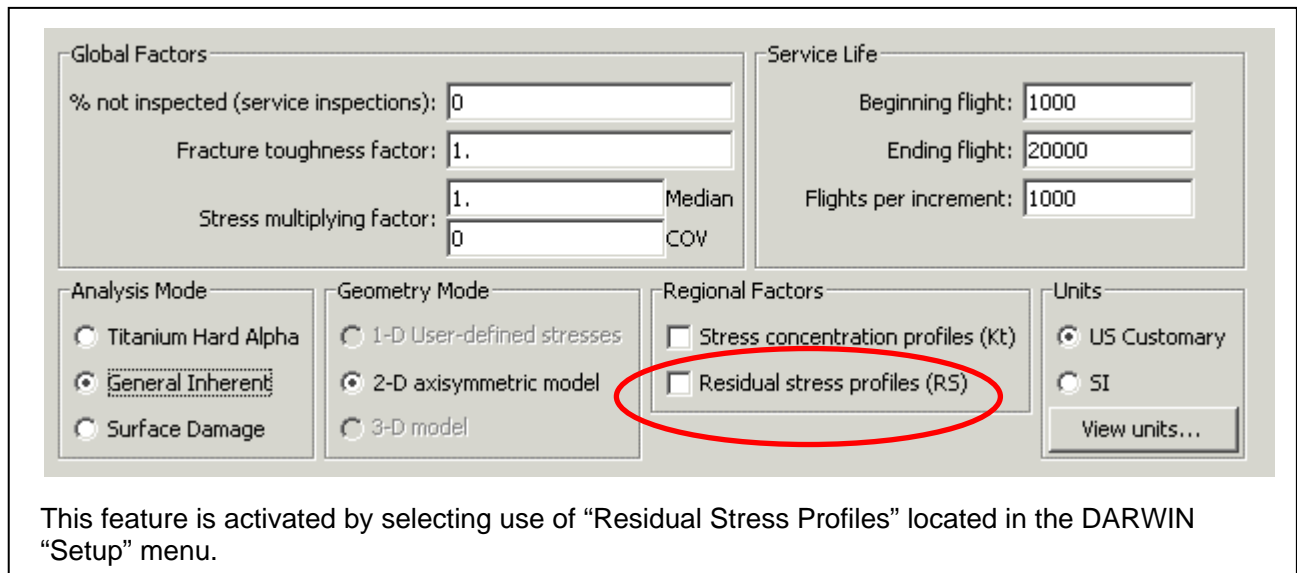
Figure 92. A Capability for Treatment of Residual Stress Values Was Implemented in DARWIN
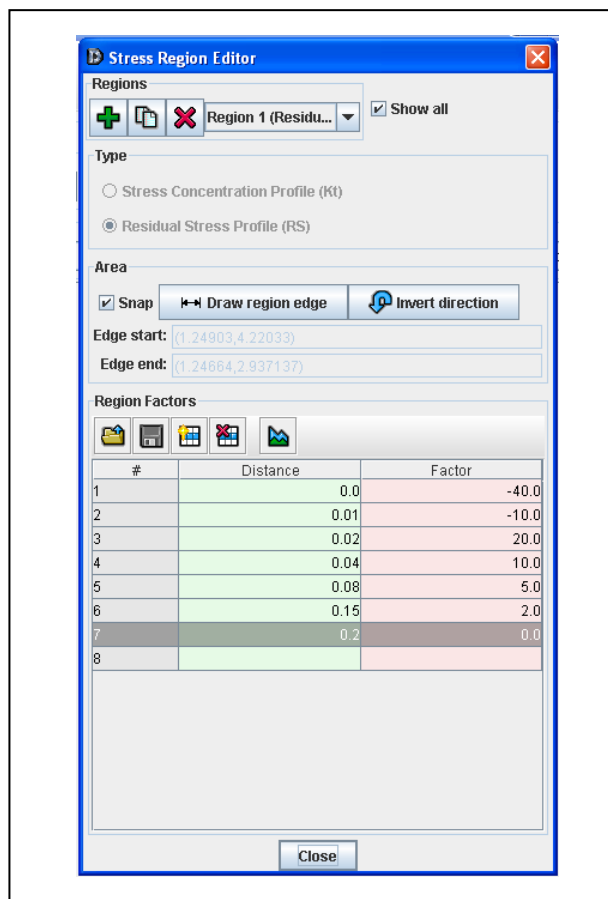
Figure 93. The DARWIN Stress Region Editor Allows the User to Define Residual Stress Gradient Values

115

(3) <u>Edit Region Factors</u>. Enter values of RS vs. distance in the **Region Factors** table. Click the button to insert a new row and click the button to delete a row. The values can also be imported from a text file. Click the button to open the text file containing region factors. To export region factors, click the button to specify the filename. The region factor vs. distance plot can be viewed by clicking the button.

The resulting residual stress field appears as a rectangular region that is based on the length of the residual stress gradient and the length of the user-specified line near the surface of the model. The region is superimposed on the 2-dimensional axisymmetric finite element model, and stress values within the region are based on the sum of the residual stress and the finite element stress values (Figure 94).

5.3.4 Use of Mission Mixing in DARWIN GUI

The existing DARWIN mission mixing capability was enhanced under this project to allow the User to specify changes to the mission mix as a function of flight cycles. As shown in Figure 95, a mission mix scenario menu was added for this purpose. The capability can be used in conjunction with the FaNG and residual stress models.

To use the enhanced mission mix capability,

1. Select the **Mission editor** tab on the **Missions** menu to define missions.
2. Select the **Mission mixer** tab to define mission mixes. By default, DARWIN creates a mission mix (Mix 1) with the first mission. Edit the mission mix by adding/deleting missions or changing the order of missions. Click the button to create and edit more mission mixes.
3. Specify the mission mixes in the **Mix scenario** table (located at the bottom of the Mission Mixer tab). Click the button to add mission mixes to the table and specify the starting flight cycle for each active mission mix.
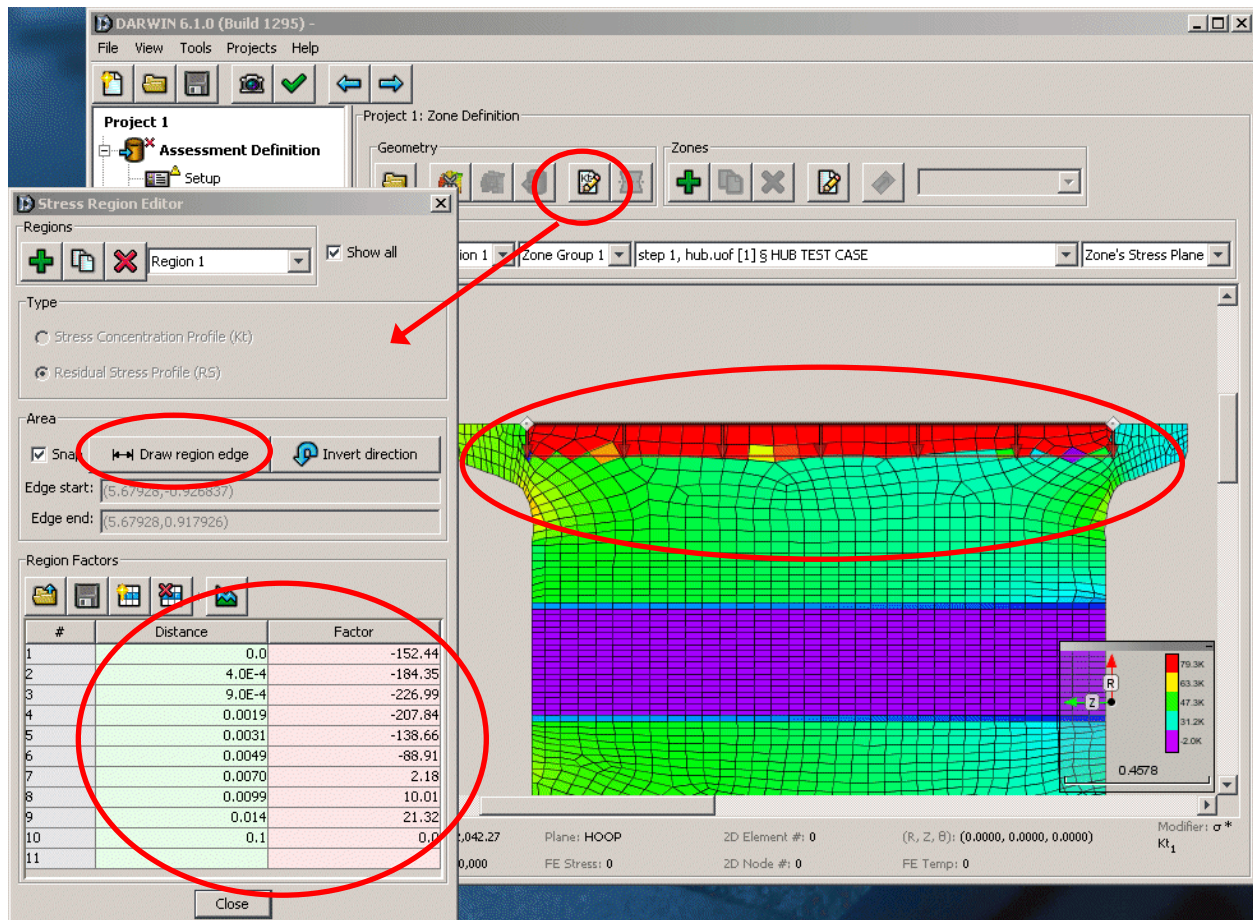
The resulting residual stress field appears as a rectangular region that is superimposed on the 2-dimensional axisymmetric finite element model.

Figure 94. Definition of Residual Stress Profiles in DARWIN
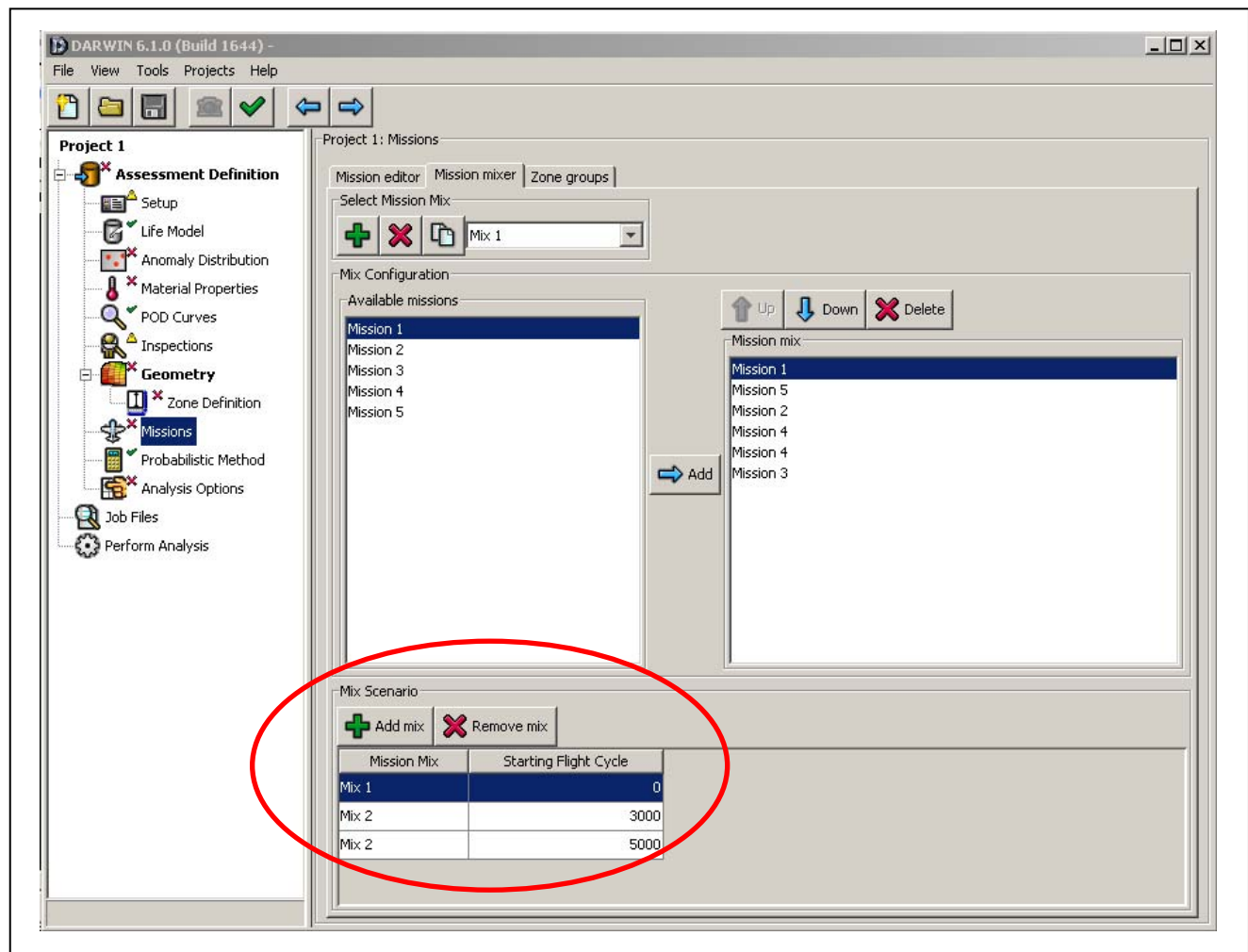
Figure 95. A New DARWIN Capability Was Developed That Allows the User to Specify Changes to the Mission Mix

6.   Results and Discussion on Probabilistic Simulations

6.1   Mission Mixing

In this section, the DARWIN mission mixing capability is described briefly and illustrated for representative engine usage histories. As shown in Figure 96, the load steps associated with each mission are specified using the DARWIN Mission Editor menu. The mission mix is defined by specifying the sequence and number of repetitions of each mission (Figure 97). The load steps associated with a representative mission mix are shown in Figure 98.

The DARWIN mission mixing capability was illustrated for the representative gas turbine engine hub component shown in Figure 99. Raw RPM values were obtained from engine flight data recorder data for several F-16/F100 missions. The RPM values were converted to stress values using an empirical algorithm and sorted into min-max pairs using the DARWIN rainflow cycle counting algorithm.

Normalized probability of failure values associated with representative engine usages are shown in Figure 100. In Figure 101, the influence of mission mix ratio on normalized probability of failure values is shown for the representative mixes indicated in Table 7. It is interesting to note that when the mix percentages are equal (Mix 1), the probability of failure is not equal to the average of the probability of failure values of the individual missions. This is probably due to the increased K values associated with large crack sizes associated with the most damage mission (similar to sequence effects). As expected, the probability of failure is greater for mission mixes with a higher percentage of damaging missions (Mixes 2 and 3).
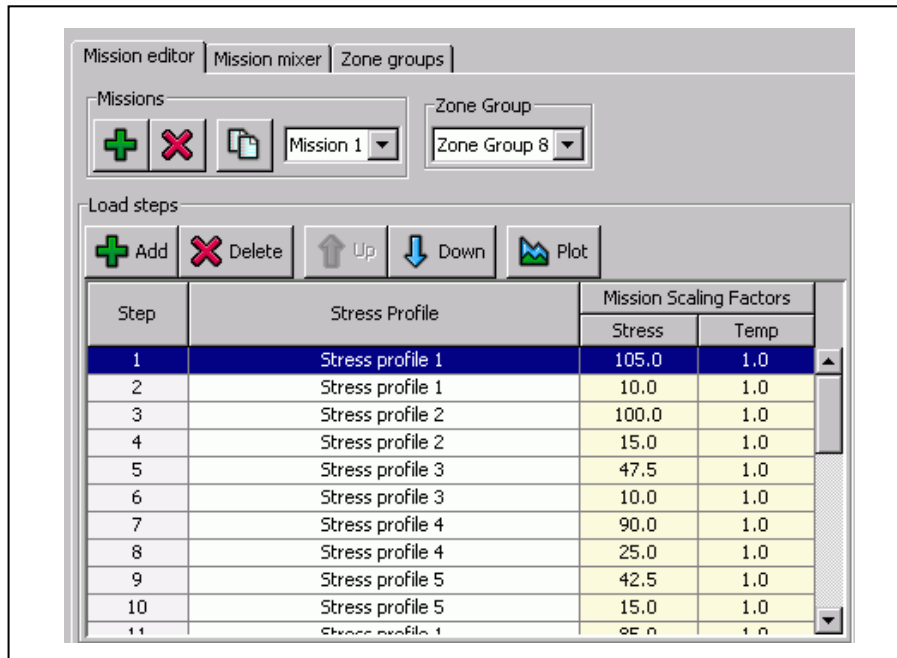
Figure 96. Specifying the Load Steps Associated with a Mission in DARWIN
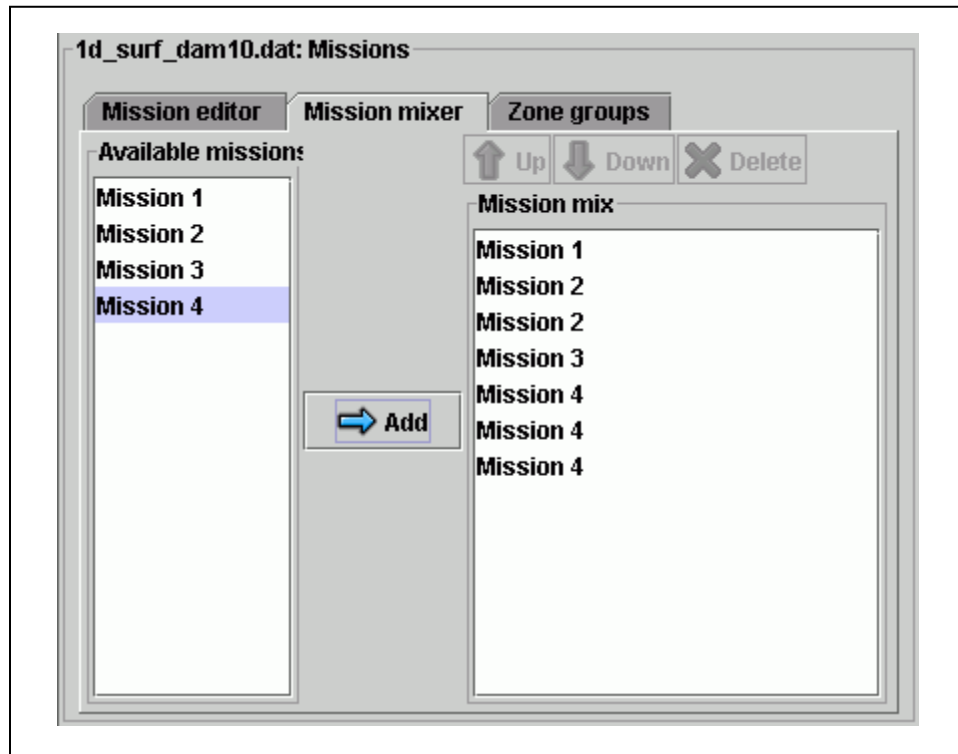
Figure 97. Specifying the Mission Mix in DARWIN
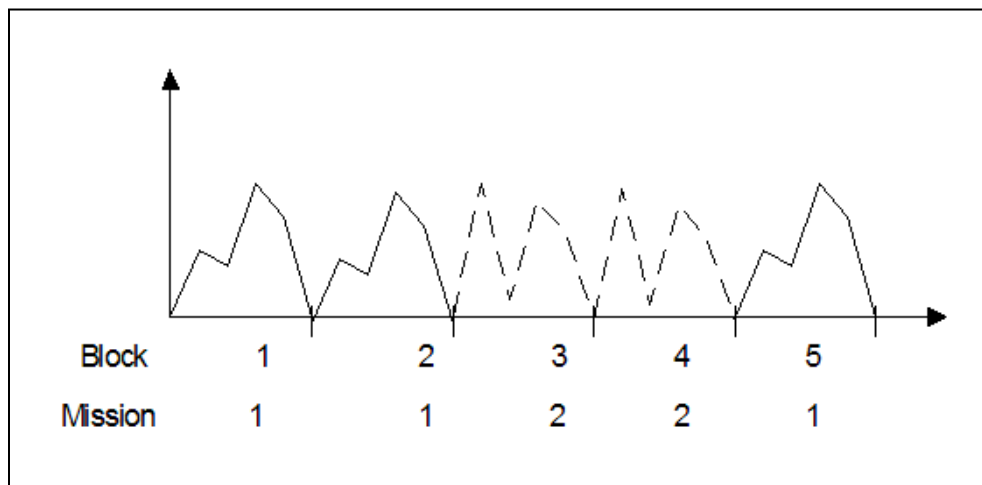
Figure 98. A Representative Mission Mix
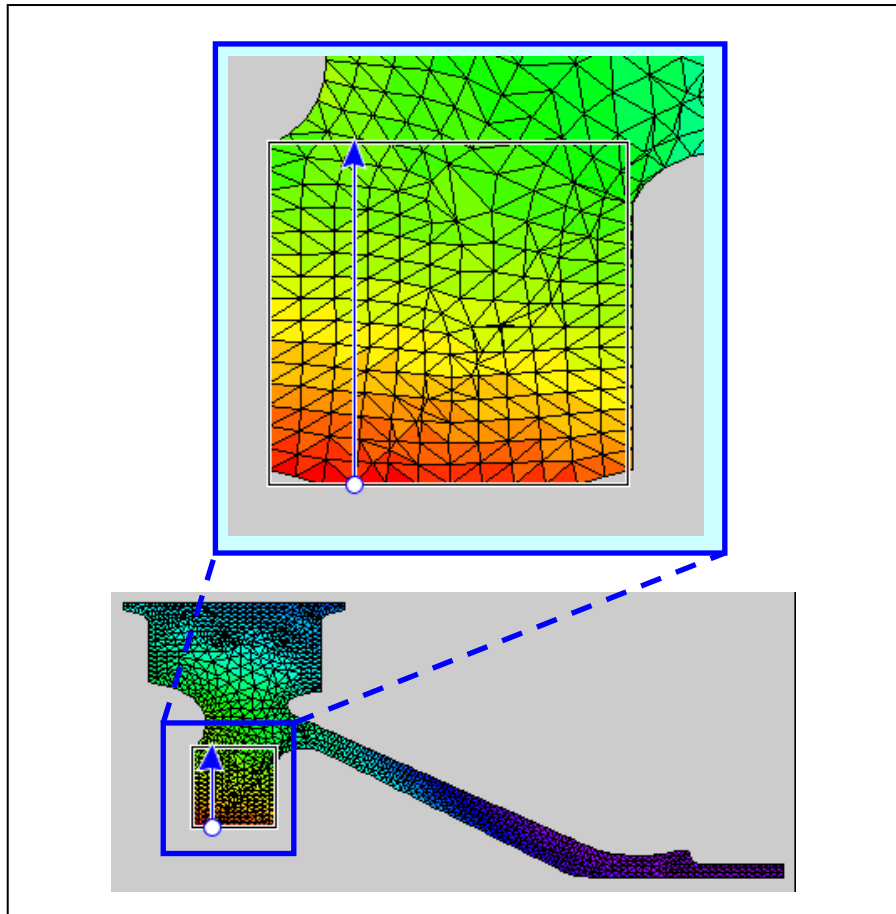
**Figure 99. The DARWIN Mission Mixing Capability Was Illustrated
for a Representative Gas Turbine Engine Hub Component**

Table 7. Mission Mix Percentages for Illustrative Example

Mission ID	Mix 1	Mix 2	Mix 3
Live Fire	25%	50%	16.7%
Instruments & Navigation	25%	16.7%	50%
ACBT	25%	16.7%	16.7%
Live Fire Missiles	25%	16.7%	16.7%
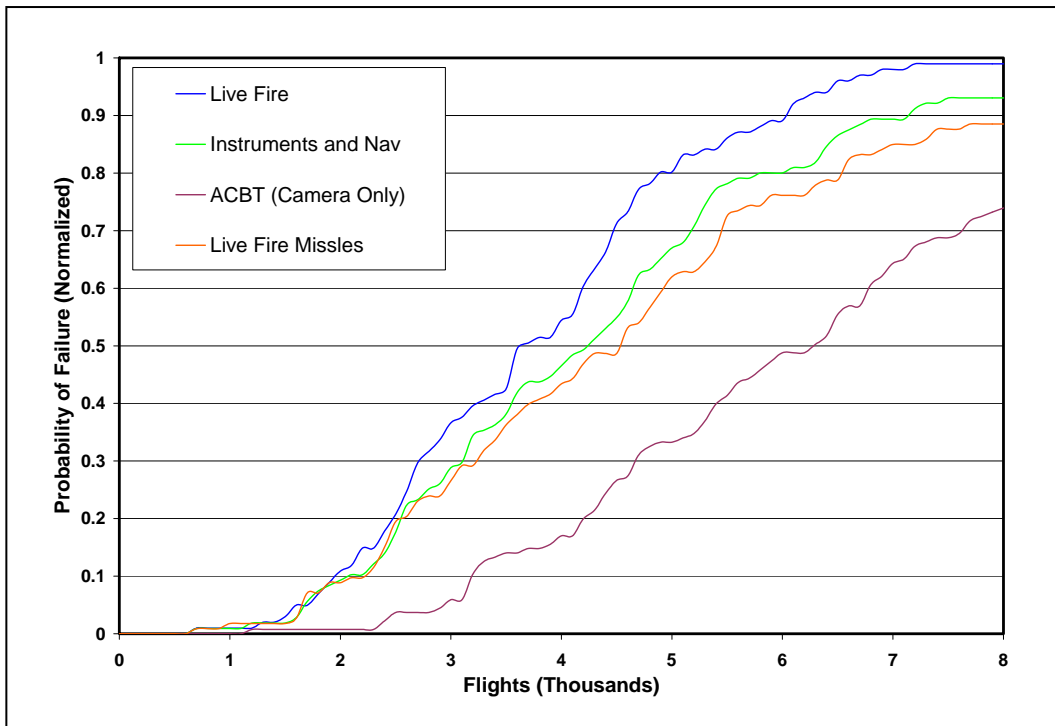
**Figure 100. Normalized Probability of Failure Values Associated
with Representative Engine Usages**
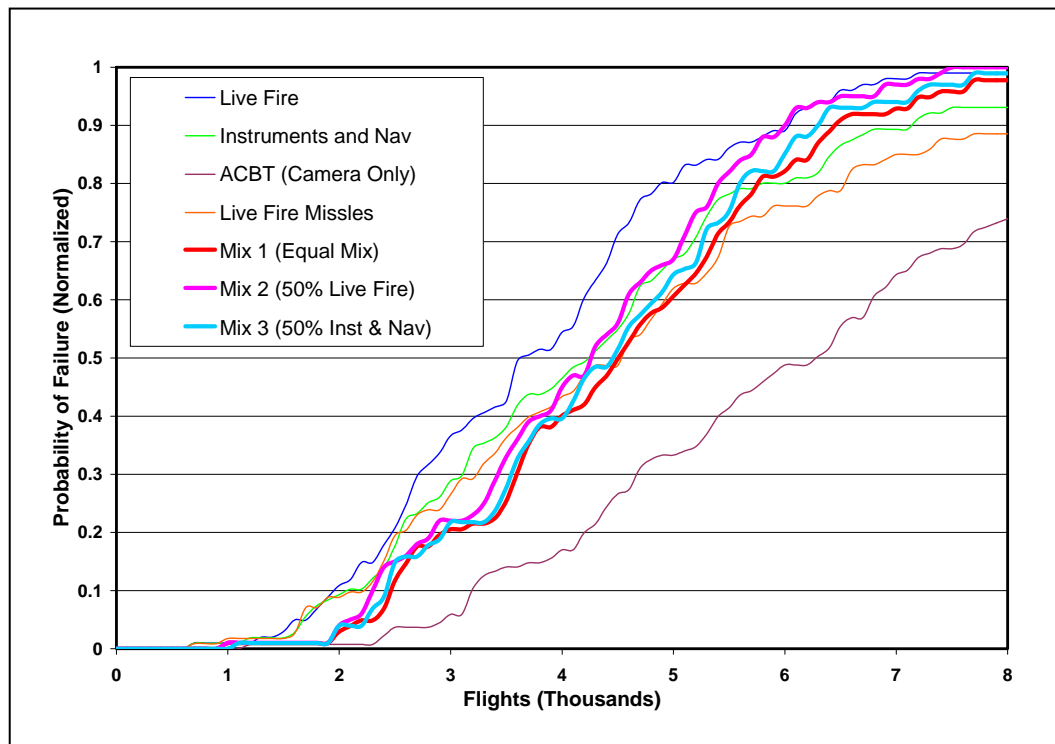
**Figure 101. Influence of Mission Mix Percentage on Normalized Probability
of Failure Values for Several Representative Mixes**

122

6.2   Forecasting Reliability

Previous versions of DARWIN provided a framework for forecasting the reliability of a component that has the same mission mix over the entire design life. As described in Section 5, DARWIN was enhanced under this project to allow the User to specify changes in the mission mix at specified flight intervals. This enhancement extends the reliability forecasting capability for potential application to fleet management decisions, because it allows the analyst to predict the influence of changes in applied usage on the overall risk of fracture.

The DARWIN mission mixing enhancement was illustrated for the representative gas turbine engine hub component shown in Figure 99 (see Section 6.1 for further details). Three mission mix scenarios were considered as indicated in Table 8. Although DARWIN can be used for assessment of large numbers of missions and mission scenarios, these simple scenarios were selected to demonstrate the maximum influence of changes in a single mission type over the service life of a component. The results are shown in Figure 102. For this example, it can be observed that the probability of fracture is usually largest for mix scenario 2, in which the most damaging mission mix is applied during the first half of the design life. Note that DARWIN currently includes only a single stress scatter random variable, so the stress scatter values associated with the mix scenarios were based on an average of the values associated with the individual missions within each mix.

Table 8. Mission Mix Scenarios for Illustrative Example

Mix Scenario	Mix 1 0 to 4000 flights	Mix 2 4000 to 8000 flights
1	50% Live Fire 50% ACBT	50% Live Fire 50% ACBT
2	100% Live Fire	100% ACBT
3	100% ACBT	100% Live Fire
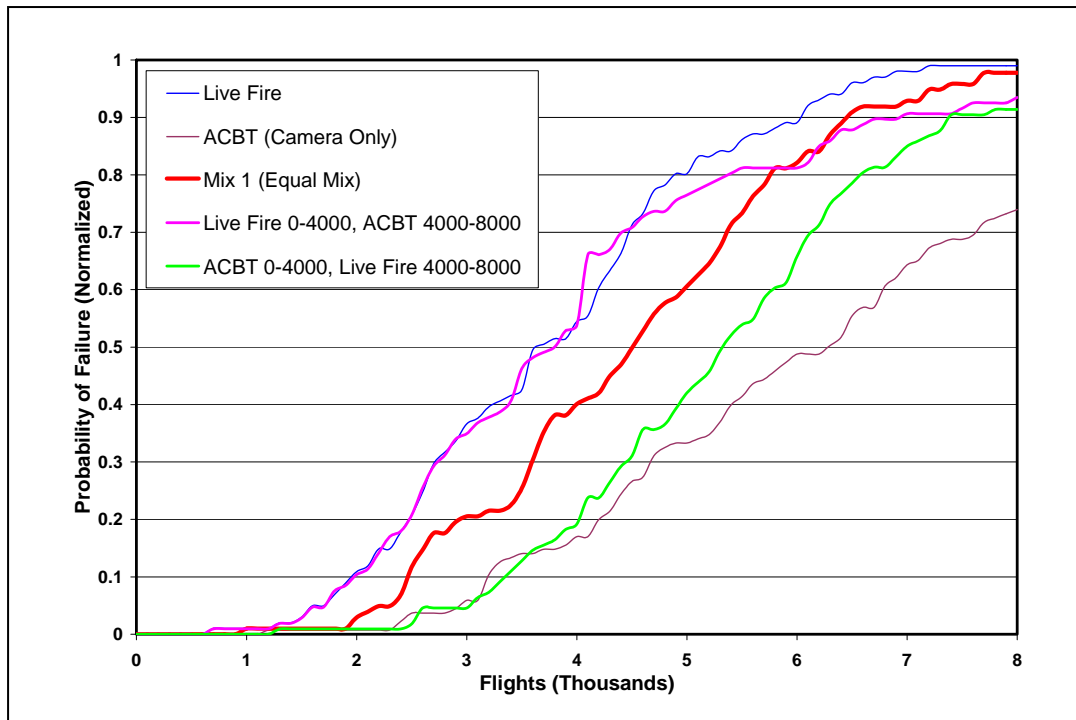
Figure 102. Influence of Mission Mix Scenario on Normalized Probability of Failure Values for Several Representative Mix Scenarios

6.3 Probabilistic Simulation of On-board Monitoring

The objective of this task was to compare the effectiveness of an accurate midlife depot inspection versus a coarser continual (once per flight) onboard inspection.

The traditional approach to inspection simulation is to assume each inspection is independent from the previous. This assumption is appropriate for the traditional application of inspections, i.e., different operators, equipment, and location, and widely separated by the time of inspection. Well-established computer models for determining probability-of-fracture (POF) estimates for aircraft structures [49]; and gas turbine rotor disks [50] consider infrequent or opportunity inspections, and; therefore, model the inspections as independent.

However, the assumption of independent inspections leads to dramatic predictions of non-realizable efficacy for continual inspections and the results are frequency dependent; almost any size crack can be detected by inspecting more and more frequently, even without any crack growth. The assumption of independent inspections is severely non-conservative and provides a false estimate of the accuracy of continual inspections.

Conversely, it is asserted and discussed below that continual inspections should not be treated as independent from previous inspections but as dependent; since the same sensor is performing subsequent inspections on the same defect, the sensitivity of the sensor in detecting the crack should be the same as for previous inspections, or nearly so.

Dependant inspections enforce that the sensitivity of a sensor at one inspection is the same at subsequent inspections.

An examination of redundant fluorescent penetrant inspection (FPI) substantiated the fact that repeated inspections should not be treated as independent and that doing so is nonconservative [51]. In this study, specimens were inspected using the same FPI method by two inspectors of approximately the same skill level. The resultant probability-of-detection from both inspections was quantified using data and compared with the independent assumption. The data-based Probability of Detection (POD) considering both inspections is significantly lower than the independent-based POD (which can be obtained by a multiplication of one minus the probabilities). As stated [51], "The fluorescent penetrant inspection process is not independent inspection-to-inspection and therefore the probability of detection for redundant FPI cannot be obtained by a simple multiplication of probabilities. The correct POD in a multiple inspection system is determined assuming dependence."

Mathematical bounds prove that independent and dependent inspections provide the upper and lower bounds, respectively, on the cumulative probability of detecting a defect. That is, assuming dependent inspections is a conservative assumption. Intermediate results between the independent and dependent assumptions can be obtained by correlating the inspections with a correlation coefficient between zero (independent) and one (dependent). The sum-of-uniforms method [52, 53] is ideal to implement any amount of correlation between inspections.

Given the assertion of dependent inspections, it is shown that the efficacy of an on-board sensor is principally determined by the probability of detecting a crack of critical size and, by and large, unaffected by the shape of the POD curve. This information can be used to: a) determine the effectiveness of implementing a particular sensor on a structural component, or b) determine the necessary design specification a sensor must satisfy to make an implementation effective for component safety and management of the asset.

6.3.1 Numerical Example

The problem consisted of a surface crack on the bore of a gas turbine disk. The stress spectra applied to the crack is derived from RPM values versus time obtained from a flight data recorder representative of an Air-to-Ground military mission. The mission contains 115 min-max fatigue loads which were applied per each flight simulation. The initial crack size was a semi-circular defect with an initial crack depth specified by an exponential probability distribution and a 1-to-1 aspect ratio with a mean 0.432 mm (17 mils). The initial crack size distribution was representative of the cracks initiated on holes in compressor disks due to machining. Other initial defect size distributions can be considered without altering the main conclusions. Material properties for a titanium material were used. The material fractured at a critical crack surface length of approximately 15.24 mm (600 mils) under the applied loading. Table 9 provides a summary of the problem inputs. The paper in the Appendix has more details.

Table 9. Example Problem Definition

Property	Description	Comment
Loading	Spectrum loading representative of an Air-to-Ground mission	11600 time points, 231 load pairs
da/dN-ΔK	C=5.248E-11 (9.25E-13 SI), m=3.87, Kc=58.7 ksi-in^-1/2 (64.6 MPa-m^-1/2)	Paris law with no threshold (C – constant, m – exponent, Kc – fracture toughness) US – units: da/dN (in/cycle), ΔK (ksi-in^-1/2) SI - units: da/dN (m/cycle), ΔK (MPa-m^-1/2)
Initial crack size	Probability distribution representative of crack at holes of compressor disks	Surface crack in the bore of a gas turbine disk. 1-1 aspect ratio

The POD curve was modeled with a lognormal distribution,

$$POD(A \le a) = \Phi\left[\ln(a/\tilde{X})/\sigma_y\right] \tag{30}$$

where a represents crack size, $\tilde{X}$ is the median, COV is the coefficient of variation, $\sigma_y^2 = \ln\left[1 + COV^2\right]$, and Φ represents the standard normal cumulative distribution function. The COV used for the POD curves is chosen as thirty-two percent based on analysis of existing industry ultrasonic POD curves.

The reduction in POF obtained by a single but precise mid-life inspection was compared to the results from less-precise but frequent continual inspections. All continual inspections were modeled as dependent; therefore, these results are conservative. Figure 103 shows the normalized POF versus flight cycles (the results are normalized to the POF without inspection at 8000 flight cycles) considering: a) no inspection, b) a single mid-life inspection with a median POD value of 0.762 mm (30 mils) and a COV of 32%, c) continual inspections (once per flight) with a median POD value of 5.080 mm (200 mils) and a COV of 32%, d) continual inspections with a median POD value of 10.16 mm (400 mils) and a COV of 32%, e) continual inspections with a median POD value of 15.24 mm (600 mils) and a COV of 32%.
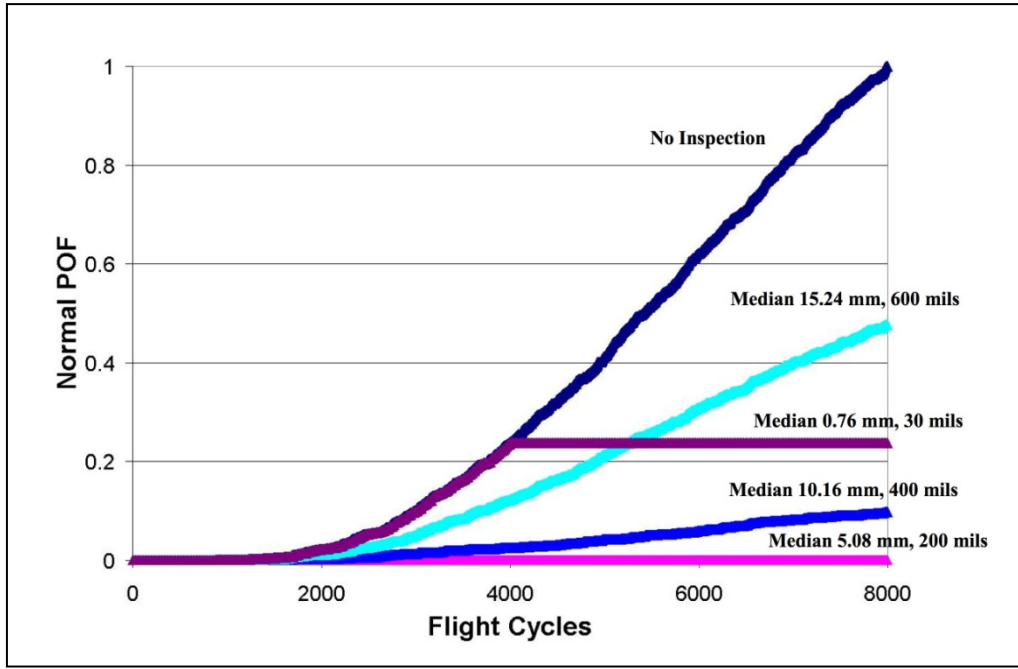
Figure 103. Comparison of Continual and Single Mid-Life Inspections

Figure 103 demonstrates that a single mid-life inspection reduces the POF to approximately 22% relative to the POF without inspection and effectively detects almost all defects that could case fracture within the ensuing 4000 flight cycles. Continual inspections with a sensor that exhibits a POD of median value equal to 5.080 mm (200 mils) and a COV equal to 32% is far superior than a single more precise mid-life inspection, reducing the POF to near zero even though the precision of the on-board sensor is far less than the depot inspection. Continual inspections with a sensor that exhibits a POD of median value equal to 10.16 mm (400 mils) and a COV equal to 32% reduces the POF to 11% relative to the POF without inspection. Continual inspection with this POD is still superior to a single more precise mid-life inspection through 8000 cycles although the slopes indicate that at some number of flight cycles the single mid-life inspection will be superior. Continual inspections with a sensor that exhibits a POD of median value equal to 15.24 mm (600 mils) and a COV equal to 32% reduces the POF to 50% relative to the POF without inspection and clearly is inferior to the single mid-life inspection. We note that the critical crack size for this problem is approximately 15.24 mm (600 mils).

For dependent inspections, the probability of detecting a flaw before fracture is approximately equal to the value of the POD curve at the critical crack size. Therefore, the reduction in POF is $P_{F,reduced} \approx [1 - POD(a_{crit})]$ and the POF with inspection can be closely approximated given the POF without inspection for any number of cycles M as

$$P_{F,wi}(M) \approx P_{F,reduced} \cdot P_{F,woi}(M) = [1 - POD(a_{crit})] \cdot P_{F,woi}(M) \tag{31}$$

127

Equation 31 has been verified by considering four vastly different contrived POD curves developed such that $POD(a_{crit}) = 70\%$ for each curve, see Figure 104. In this case $P_{F,reduced} = 1 - POD(a_{crit}) = 30\%$ for each POD curve. As a result, the POF with inspection was approximately the same regardless of which POD curve was used, see Figure 105. These results indicate that an estimate of the reduction in POF due to continual inspections can be ascertained by knowing the sensor's POD value at the critical defect size.
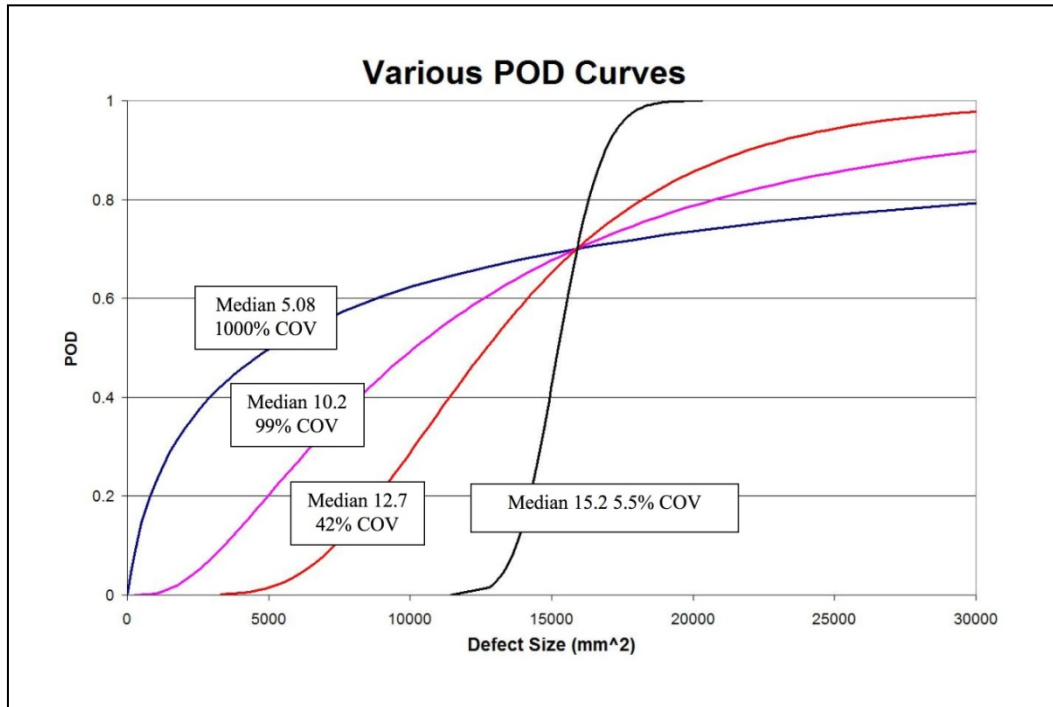
Figure 104. Contrived POD Curves
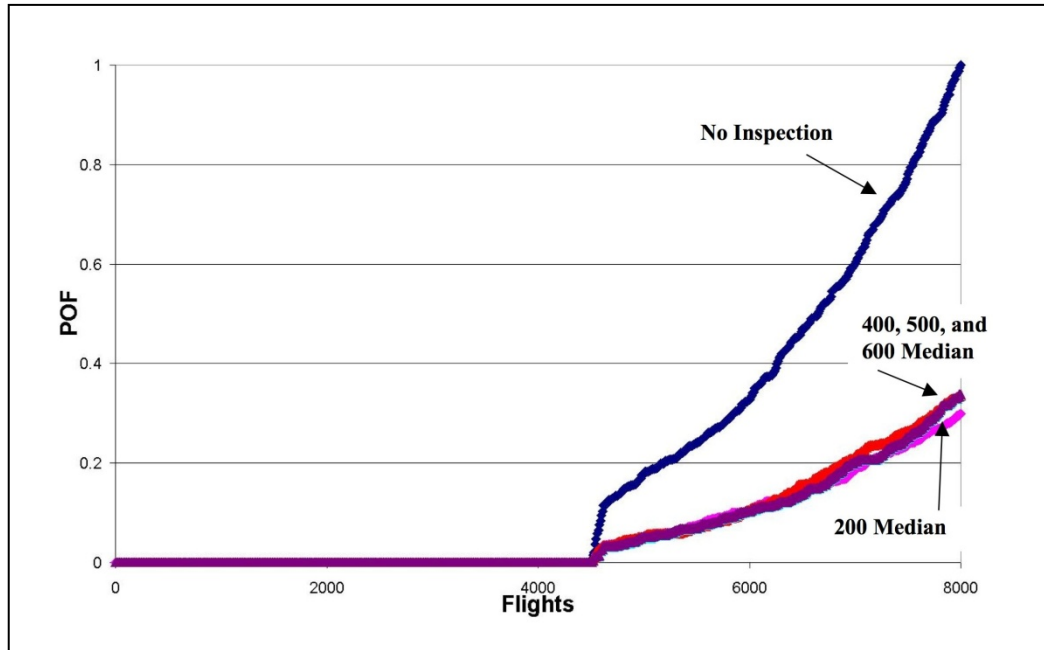
Figure 105. Reduced POF Resulting from Contrived POD Curves

6.3.2 Summary

During this research, a methodology was developed and implemented to compute the reduction in POF due to continual (once per flight) inspections based upon the concept of on-board crack sensors. This issue was investigated through the analysis of fracture of a gas turbine disk. A critical outcome of the research was that accurate simulation of continual inspections requires that inspections be treated as dependent rather than the traditional modeling approach of independent inspection. Dependent simulation is conservative whereas independent simulation may be grossly unconservative.

A second critical outcome is that the reduction in POF obtained by continual inspections depends almost solely upon the probability of detection of the sensor at the critical crack size, $POD(a_{crit})$. This information can be used to determine the required accuracy for an on-board sensor to prove effective. This assertion was verified from the analyses of four drastically different POD curves with the same POD value at the critical crack size; the resulting reduced POF from the analyses were all the same.

Finally an analysis comparing the reduction in POF from a precise single depot inspection versus various much coarser but continual inspections demonstrated that continual inspection may provide a significant reduction in POF compared to the depot inspection, even if the onboard sensor is several times less sensitive than the depot inspection. This is due to the fact that with a large number of on-board inspections, multiple opportunities exist to detect larger (but non-critical defects) than the single mid-life inspection.

6.4 Application of Bayesian Updating to Health Monitoring and Prognosis

The utility of the Bayesian updating method described in Section 4.5 was demonstrated by employing it to fuse data from an embedded sensor with probabilistic life predictions obtained from DARWIN. These fused predictions were compared with measurements from laboratory demonstration of the thin-film sensor under the DARPA Material Prognosis Program. The demonstration consisted of a growing fatigue crack in a Ti-6Al-4Ti beam specimen that was being monitored with a magnetostrictive, thin-film (ultrasonic) wireless sensor as described in Ref. [54].

6.4.1 Crack Detection Experiment with the Thin-Film Sensor

The experimental set-up is shown in Figure 106. The Ti-6Al-4V three-point bend specimen, containing a central surface crack, was subjected to fatigue loading. Note that the sensor was placed on the opposite side of the crack to demonstrate that bulk waves were being generated. Crack size measurements were made at both 25 °F and 500 °F. Results from the sensor were transmitted both wired and wirelessly. The sensor was also powered through a wired power supply since energy harvesting has not yet been developed to power the sensors. The surface crack was generated by first introducing a small electro-discharge machine notch followed by fatigue pre-cracking to extend the crack. During crack extension, marker bands were periodically generated on the fracture surface, as shown in Figure 107, by increasing the mean load and decreasing the load range to alter the crack surface morphology. These marker bands provided precise information on crack depth, shape, and area as summarized in Table 10.
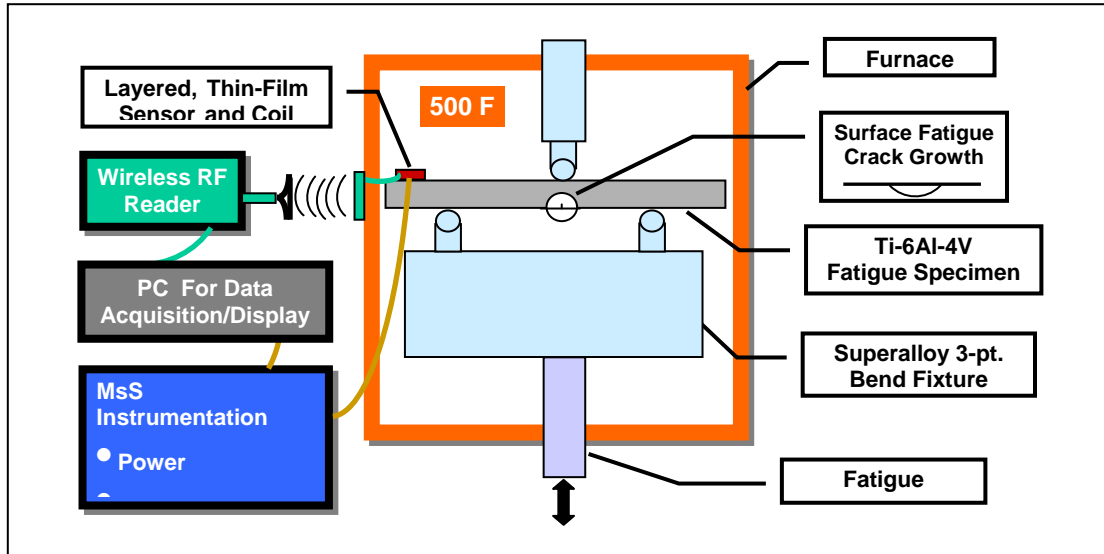
Figure 106. Experimental Setup of Fatigue-Cracked Beam Being Monitored with Thin-Film Sensor

Dimensions in the figure indicate total surface crack length for each marker band.
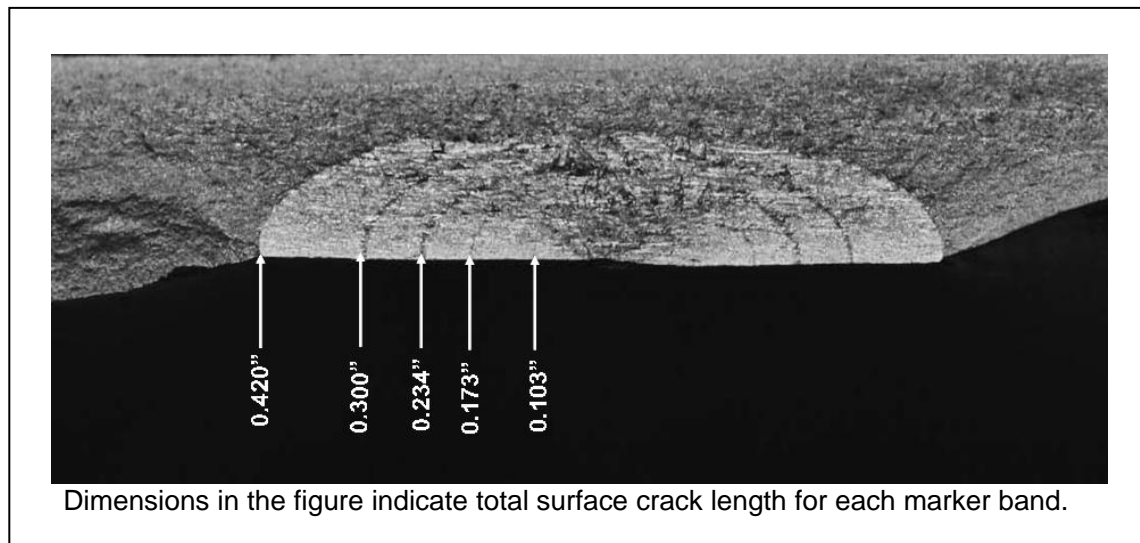
Figure 107. Fracture Surface of Fatigue Crack in Ti-6Al-4V Showing Fatigue Marker Bands

**Table 10. Crack Sizes and Areas Measured from the Surface Crack in Figure 107
That Were Detected Using the Thin-Film Sensor Operating at 500 ºF**

Crack Length (in.)	Crack Depth (in.)	Crack Area (in.^{2})
0.103	0.033	0.0034
0.173	0.036	0.0062
0.234	0.039	0.0091
0.300	0.05	0.015
0.420	0.062	0.026

6.4.2   Thin-Film Sensor Uncertainty Model

The signal-to-noise ratio obtained from the wirelessly-transmitted, TFS results at 25 ºF and 500 °F were compared against known crack area obtained from observation of post-inspection marker bands on the crack surface (see Table 10 and Figure 107). It was determined that results at both temperatures were similar, thus all data were combined to characterize the sensor uncertainty on crack size determination. Regression results, shown in Figure 108, were used to quantify the uncertainty in the sensor-derived crack area. The regression results indicate a constant standard deviation of approximately 2349 mil^2. For analysis purposes, the TFS result was truncated at a threshold crack size of 2670 mil^2 (S/N = 1), i.e., no size information is provided below this threshold crack size since for this size crack the sensor signal could not be readily distinguished from the background noise. This threshold size value was set at -2 standard deviations which set the mean size as 7370 mil^2 (for a = c = 66 mil). In summary, the crack size density estimate from the sensor response was modeled as a normal distribution with mean 7370 mil^2 and truncated in the left tail at 2670 mil^2.
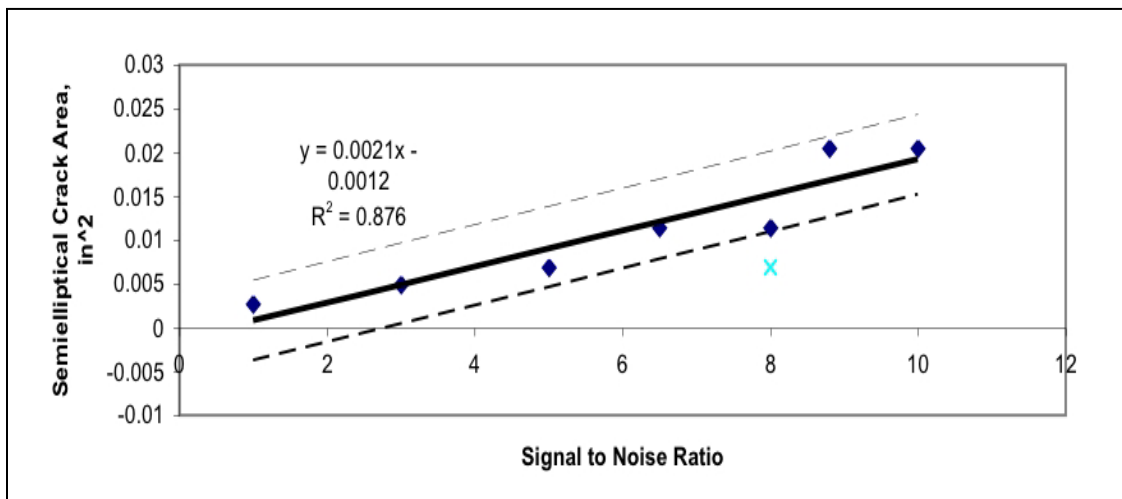
**Figure 108. Thin-Film Sensor Experimental Regression Results Used to
Establish Sensor Detection Threshold and Measurement Uncertainty**

It is significant to note that the minimum detected crack area of 2670 mils^2, which would, for example, correspond to a semicircular surface crack size of about 51 mils (2 mm) is 2.5 times smaller in size and 15 times smaller in area than the crack size shown to be effective in maintaining low failure rates based on the probabilistic simulations in Section 6.3 (Figure 103). These results are encouraging since they suggest that the current thin-film embedded sensing technology may have adequate margin to enable the successful transition from the lab to the turbine engine, or other applications, with temperature of 500 ºF or less.

6.4.3 Initial Crack Size Distribution

A central issue in any probabilistic fracture mechanics analysis is the initial crack size distribution. Under an FAA-sponsored effort, the turbine engine manufacturers have developed a crack size distribution for machined holes in disks [42]. These results are shown in Figure 109, which represents results that can be expected for a fleet of disks. The probability density is "exponential-like" in that it has a high probability of small cracks with a long right tail to capture the remote possibility of large cracks. This distribution is used for the demonstration problem. As will be shown, the initial crack size distribution is modified significantly based upon the sensor crack size estimation.
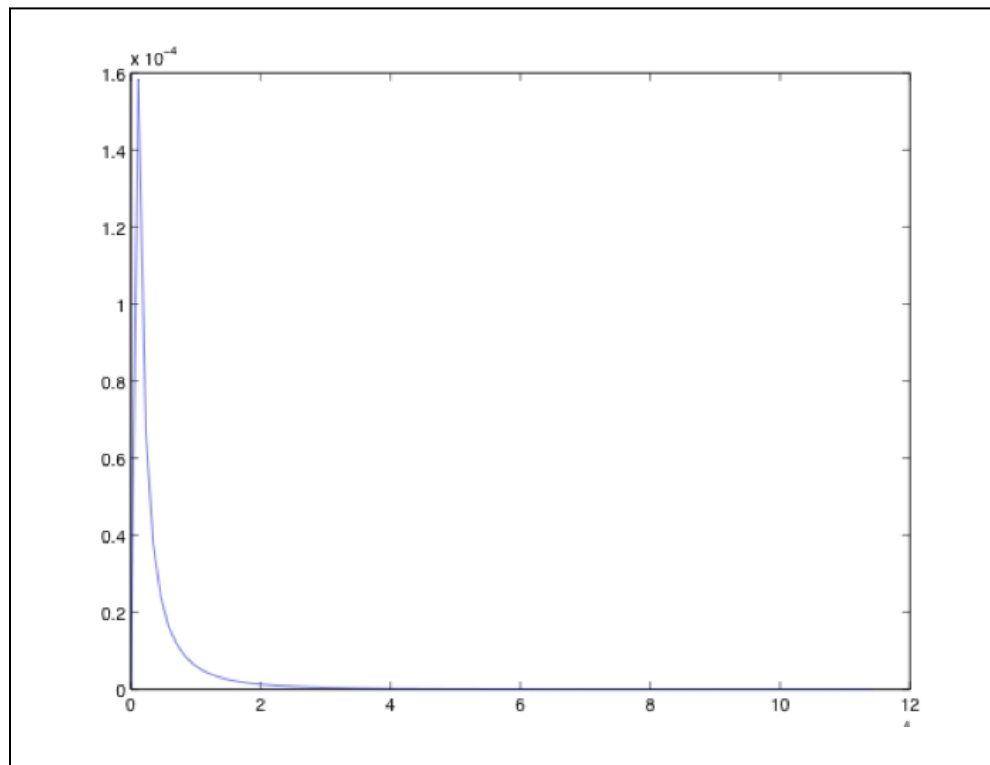
Figure 109. Initial Crack Size Distribution for Flaws at Machined Holes from Ref. [42]

6.4.4 Uncertainty in Fatigue Crack Growth Rates

The uncertainty in fatigue crack growth rates was captured by analyzing an extensive data base on Ti-4Al-4V obtained in an Advisory Group for Aerospace Research and Development (AGARD) round robin test program [55]. These results are summarized in Figure 110, along with results probability density functions (PDFs) at various fixed values of ΔK. As can be seen in the figure, the COVs of these distributions varied as a function of ΔK. Specifically, they increased at both low and high ΔK values. However, in the intermediate region of interest in the current simulation the COV was relatively constant and equal to 20% on average. A value of 50% was also used in the computations to simulate the larger uncertainty that would be associated with different heats of material, as would be the case in fusing data in an actual component.
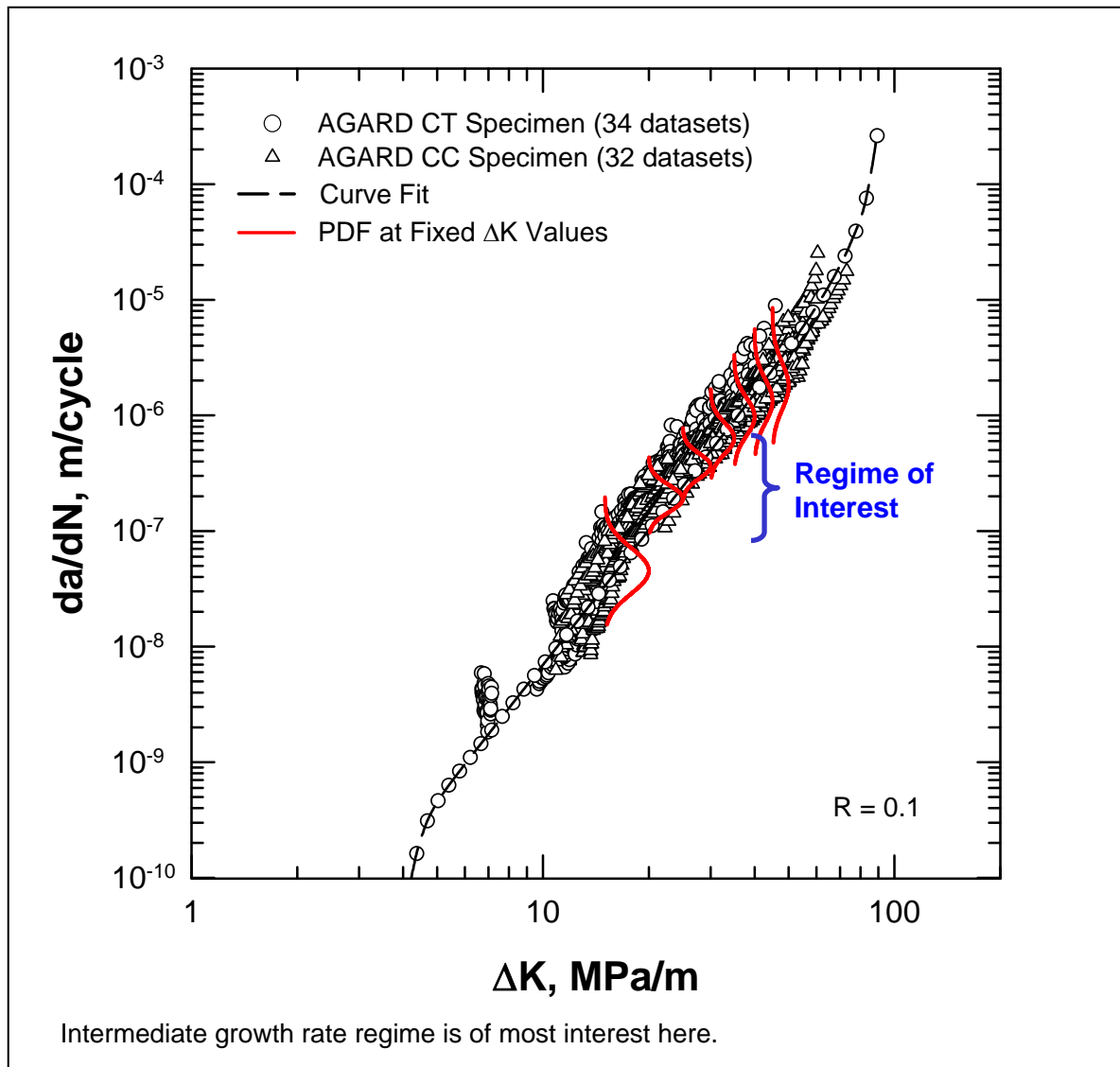
Figure 110. Fatigue Crack Growth Data in Ti-6Al-4V from AGARD Round Robin Study [55], Along with PDFs at Various ΔK Values

6.4.5 Fused Sensor and Fracture Mechanics Prediction Results

The method used to fuse the sensor and life prediction information is illustrated in Figure 111. An sample is randomly selected from the initial flaw size distribution (Figure 109) and appropriate loading cycles (23,500 cycles) are applied to the DARWIN life prediction software to grow the crack to the point of the initial sensor measurement in the experiment. Since the sensor predictions at this point are in terms of crack area, the crack aspect-ratio computed by DARWIN is fed to the sensor model to enable conversion of the sensor-predicted area to a crack depth and length. This procedure is performed numerous times using Monte Carlo simulation with all of the random variables indicated by the inner loop in Figure 111. The simulation results are then used to formulate a non-parametric PDF of crack length from the sensor and predictions are then formulated using the adaptive kernel method previously described in Section 4.2. The above procedure is then repeated for each of the crack lengths where sensor measurements were made in the experiment using the Bayesian updating procedure; this process is indicated by the outer loop in Figure 111. The above simulation procedure result is predicted PDFs as shown in the lower left of Figure 111 for the sensor (blue), life prediction model (red), as well as for the fused results (green).
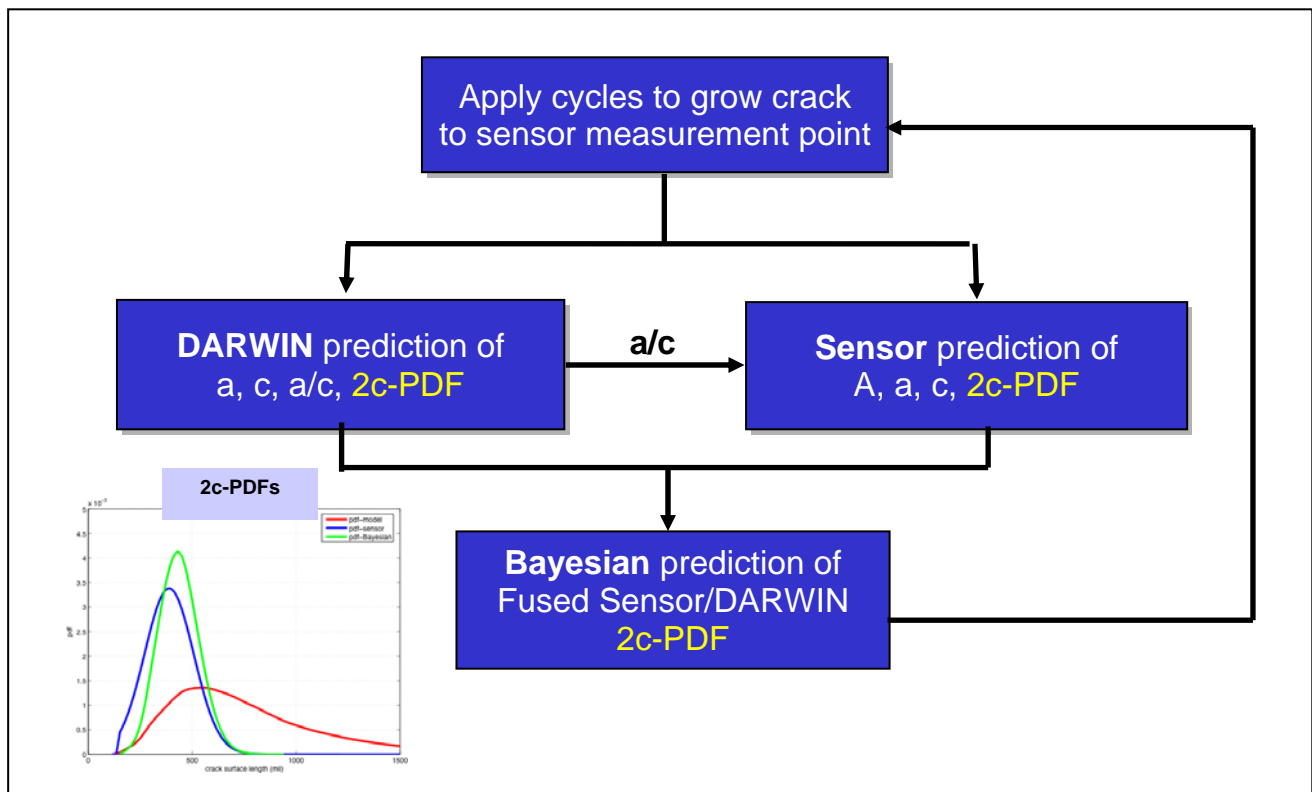
Figure 111. Method Used to Fuse Sensor Measurements and DARWIN Life Predictions, and with Example of Resulting Probability Density Functions

The Bayesian analysis at each cycle count was based on 10,000 Monte Carlo simulations with a Standard Deviation of 0.0023 in.[2] for the sensor model, and COV values of either 20% or 50% for life scatter – that was assumed to be controlled by the fatigue crack growth rate uncertainty. The results for the simulations with the life scatter of 20% in the DARWIN predictions are shown in Figure 112 for applied cycles of 23,500, 30,500, and 39,500 corresponding to the cycle counts for which sensor measurements and marker bands were applied in the experiment. As shown in the figure, the initial Bayesian results at 23,500 cycles favor the DARWIN predictions because of the relatively low COV of the DARWIN predictions relative to the sensor model predictions. However, the mean values of both of these distributions exceed the actual surface crack length, as well as that predicted by the sensor model. At both 30,500 cycles and 39,500 cycles, the DARWIN predictions continue to over-predict the actual crack length which is now close to the predictions of the sensor model, as well as the Bayesian analysis. This over prediction by the DARWIN analysis is likely due to the fact that the mean of the fatigue crack growth rate distribution is larger than that of the actual heat of Ti-6Al-4V used in the experiments. Thus, the availability of the sensor date serves to in this example resist the tendency of the DARWIN analysis to over-predict the crack length and consequently the Bayesian updating provides a significantly better prediction of the actual crack length in the experiment.
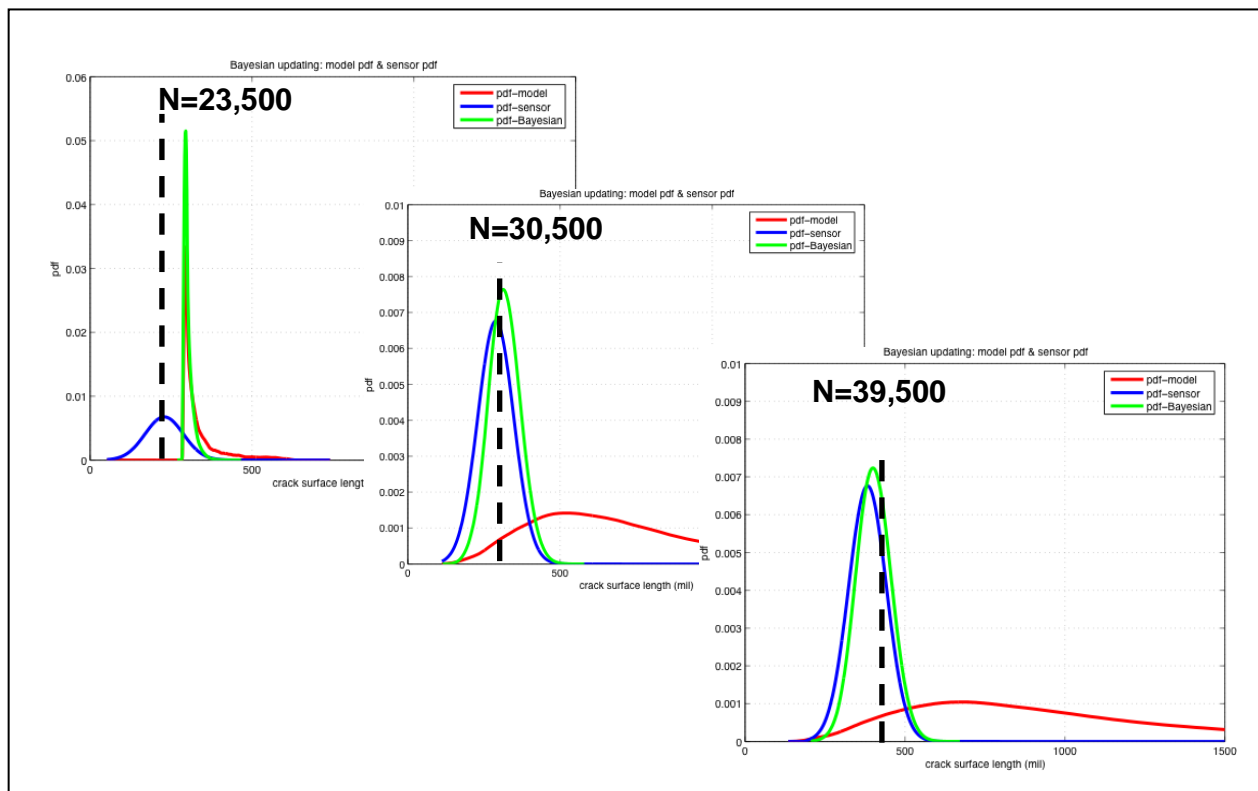
Figure 112. Comparison of Actual Crack Lengths (Dashed Lines) with Bayesian Predictions (Green) from Fusion of Sensor Model Results (Blue) and Fracture Mechanics Model Predictions (Red) with Crack Growth COV = 20%

The results for the simulations where the life scatter was increased by 2.5 X to 50% (versus 20% in the analyses shown in Figure 112) are shown in Figure 113. The overall trends in these results are similar to those for the smaller life scatter case in Figure 112. However, the increased uncertainty in the DARWIN analysis eventually results in all of the predictions having greater uncertainty as reflected in the broader distributions. Nevertheless, the mean values of the sensor and Bayesian predictions remain closer to the actual crack length than the mean value of the DARWIN analysis as the result of the smaller influence of the DARWIN analysis because of its higher uncertainty.

The results in summarized in Figures 112 and 113 demonstrate the advantage of making predictions having both sensor information and analytical life predictions, as well as the benefit of using Bayesian analysis in fusing both sources of information.
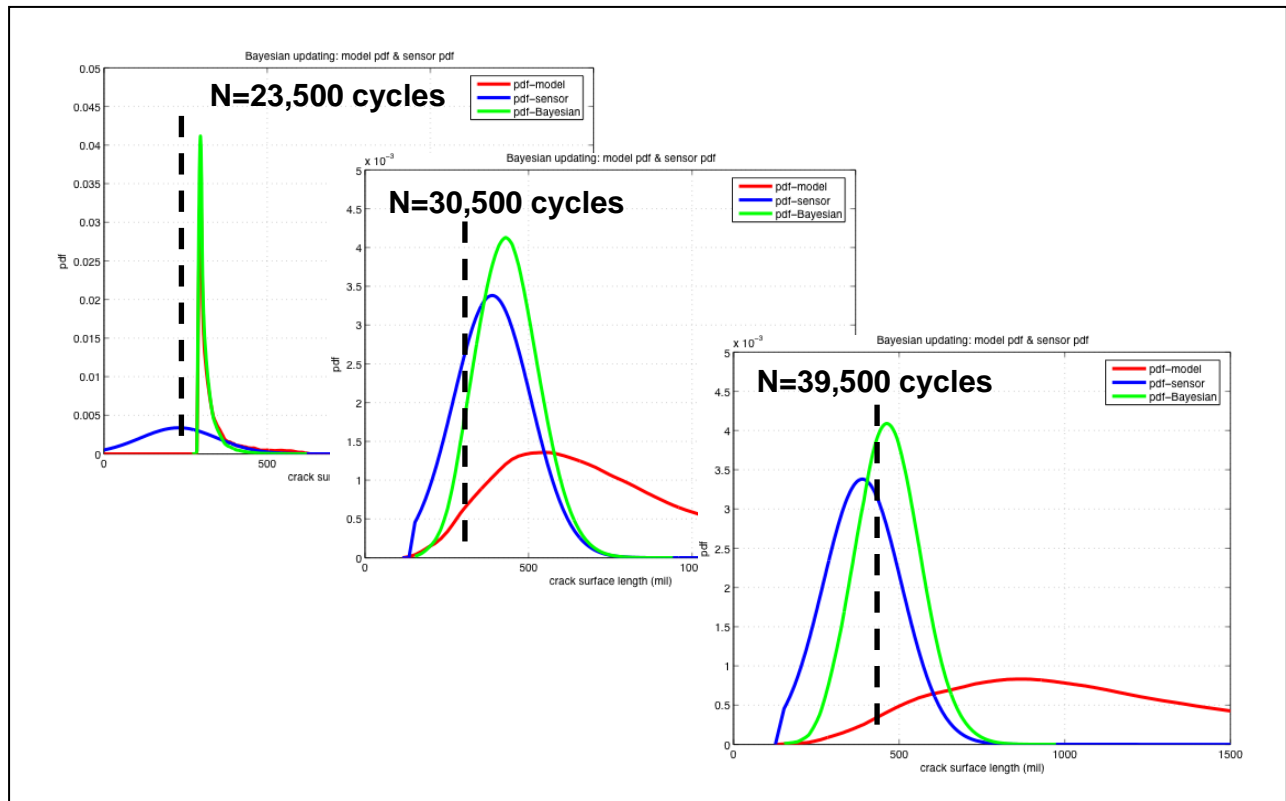
Figure 113. Comparison of Actual Crack Lengths (Dashed Lines) with Bayesian Predictions (Green) from Fusion of Sensor Model Results (Blue) and Fracture Mechanics Model Predictions (Red) with Crack Growth COV = 50%

7.   Conclusions

The following points summarize the key accomplishments and significant conclusions that can be drawn from the current program:

1.   A new FaNG model was developed based on the use of small fatigue crack growth behavior to link crack nucleation and classical large-crack growth regimes; the model is particularly useful for fatigue analyses involving steep stress gradients – for example, residual stresses, sharp notches, foreign object damage, fretting fatigue, and thermal stresses.

2.   The FaNG Model was validated by comparing predicted versus measured life of notched fatigue specimens, and peened fatigue specimens of Ti-6Al-4V for which residual stress measurements were also available, thereby enabling crack growth to be computed under the influence of the steep near-surface residual stress field.

3.   The FaNG Model was demonstrated to give results consistent with classical analyses for mild stress gradients.

4.   Computing fatigue lives in a fracture critical component feature (i.e. bolt hole in a generic compressor disc) based on TACs was shown to be conservative by a factor of two to five compared to computed fatigue lives based on actual usage from a variety of mission types. These results provide further documentation of the potential benefits of using actual mission usage instead of TACs to track fatigue damage, schedule inspections and maintenance, and manage the life fracture critical components.

5.   A multi-component da/dN(ΔK) model was developed and used to quantify fatigue crack growth rate uncertainty in Ti-6Al-4V. This model will facilitate the explicit incorporation of fatigue crack growth rate material properties in probabilistic analysis, which can aid in materials development, as well as materials selection for turbine engine applications.

6.   Enhanced probabilistic methods were developed that can increase the efficiency and effectiveness of probabilistic analyses including:
    a.   Quantification of the computational benefits of parallel processing for probabilistic fracture mechanics analysis of military engines, and
    b.   Development and validation of efficient analytical methods for computing probabilistic sensitivity factors using readily available computational results.

7.   The utility of a non-parametric distribution function, based on an adaptive kernel method, for characterizing uncertainty in mission usage data was demonstrated. This method can be used to automatically update mission usage as additional data are captured over time.

8. An automated method for PMI was developed using the adaptive kernel method Initial validation of the PMI method for automated identification of mission type from given usage data was successfully demonstrated for several different mission types. This tool will facilitate the automated characterization of uncertainty in mission usage and thereby lead to better forecasting of the impact of changes in mission mix on evolving fatigue damage.

9. Using the above tool, a conceptual design was formulated to synthesize mission usage and forecast the effect of changes in mission or mission mix on component reliability.

10. The benefits of Bayesian updating for fusing information from on-board, embedded sensing and probabilistic life predictions were demonstrated. This demonstration provided further evidence for the feasibility of real-time, or near real-time, prognosis of the reliability of fracture critical turbine engine components.

11. The above results also demonstrate that monitoring component fatigue damage (i.e. cracking) with embedded sensors having measurement sensitivities that are five times less sensitive than those used for depot inspection are beneficial for ensuring high reliabilities in fatigue and fracture critical turbine engine components since the lower sensitivity is compensated for by the ability of embedded sensors to continually interrogate the component damage state – for example, differential damage measurements acquired for each flight.

12. Many of the enhanced life prediction and probabilistic analysis methods developed in the current program have been transitioned to the commercial computer code DARWIN, which is available royalty-free to the government and through commercial licensing to industry; these methods which are accessible through the user friendly GUI include:
    a. FaNG model
    b. Residual stress analysis for surface cracks
    c. Enhanced mission mixing
    d. Probabilistic sensitivities.

13. The current work identified several technical challenges to hybridizing physics-based probabilistic analysis (DARWIN) and data-driven (ProDAPS) including:
    a. Physics-based models are available for fracture-critical components, while data driven methods have not been developed and matured for the same damage modes
    b. For those limited cases where the two methods are compatible, data are often lacking because of inaccessibility to software needed to interpret raw data, incompatibility between different data bases, and/or a general lack of infrastructure for storing and processing large amounts of data.

8.   Recommendations

1.   Explore the use of the probabilistic version of the FaNG model to elucidate the bimodal distribution of coupon S-N fatigue data. This will require a consistent set of representative material properties [S-N, da/dN(ΔK), and small crack data (optional)], as well as initial defect distributions inherent to the material.

2.   Perform further validation of the FaNG model over a broader range of materials (e.g. Ni-base alloys), stress gradients (geometries, thermal stresses, and/or beneficial residual stresses). This will require representative material properties [S-N], as well as coupon, subcomponent or component test data with known local stress distributions at fatigue critical locations, known loading history, as well as characterized residual stresses – if they exist in the coupon or component.

3.   Perform further assessment of the viability of the PMI to accurately identify mission type for a given usage (time history); testing robustness of the method will require access to more usage data from a wider range of mission types for which the mission type is known.

4.   Add the multi-component fatigue crack growth model to DARWIN so that the software code can be used as a research tool to examine the potential impact of new materials, with improved crack growth behavior, on turbine engine reliability.

5.   Implement current Air Force plans to develop data storage and data mining tools, as well as the ability of share data among the existing Air Force data bases for engines, as well as airframes. This would facilitate the validation of existing and new prognostic and diagnostic tools. It is also important to develop procedures to allow researchers to access data while preserving the confidentiality of the information.

9. References

[1]   G. M. Light, S. J. Hudak, Jr. and R. C. McClung, Turbine Engine Inspection and Life Extension Technology, SwRI Final Report to AFRL/MLLMN, SwRI Project 15.02950, October 2000.

[2]   "Improved High Cycle Fatigue Life Prediction," Final Report, USAF Contract F33615-96-C-5269 AFOSR/NA Structural Mechanics, Arlington, Virginia.

[3]   D. C. Slavik, T. Dunyak, J. Griffiths, and P. Kurath, "Crack Initiation Modeling in Ti–6Al–4V for Smooth and Notched Geometries," *Proc. 5th National Turbine Engine High Cycle Fatigue Conference*, Chandler, Arizona, 2000.

[4]   J. W. Sheldon, K. R. Bain, and J. K. Donald, "Investigation of the Effects of Shed-Rate, Initial K_{max}, and Geometric Constraint on ΔK_{th} in Ti–6Al–4V at Room Temperature," *International Journal of Fatigue,* Vol. 21, 1999, pp. 733-741.

[5]   B. L. Boyce and R. O. Ritchie, "Effect of Load Ratio and Maximum Stress Intensity on the Fatigue Threshold in Ti-6Al-4V," *Engineering Fracture Mechanics*, Vol. 68, 2001, pp. 129-147.

[6]   J. C. Newman, Jr., "A Crack-Opening Stress Equation for Fatigue Crack Growth," *International Journal of Fracture*, Vol. 24, 1984, pp. R131-R135.

[7]   Y. N. Lenets, R. S. Bellows, and H. F. Merrick, "Propagation Behavior of Naturally Initiated Fatigue Cracks in Round Bars of Ti-6Al-4V," *Proc. 5th National Turbine Engine High Cycle Fatigue Conference,* Chandler, Arizona, 2000.

[8]   H. Kitagawa and S. Takahashi, "Applicability of Fracture Mechanics to Very Small Cracks or the Cracks in the Early Stage," *Proc. 2nd Int. Conf. Mechanical Behavior of Materials*, Boston, Massachusetts, 1976, pp. 627-631.

[9]   M. H. El Haddad, K. N. Smith, and T. H. Topper, "Fatigue Crack Propagation of Short Cracks," *Journal of Engineering Materials and Technology, Trans. ASME*, Vol. 101, 1979, pp. 42-46.

[10]   K. S. Chan, "Fatigue Crack Growth Threshold of TiAl Alloys," *Proc. 2nd Int. Symp. Gamma Titanium Aluminides*, TMS, 1999, pp. 517-525.

[11]   K. Tanaka, Y. Nakai, and M. Yamashita, "Fatigue Growth Threshold of Small Cracks," *International Journal of Fracture*, Vol. 17, 1981, pp. 519-533.

[12]   C. W. Brown and D. Taylor, "The Effects of Texture and Grain Size on the Short Fatigue Crack Growth Rates in Ti-6Al-4V," *Fatigue Crack Growth Threshold Concepts,* TMS-AIME, 1984, pp. 433-445.

[13]   S. J. Hudak, Jr., K. S. Chan, G. G. Chell, Y.-D. Lee, and R. C. McClung, "A Damage Tolerance Approach for Predicting the Threshold Stress for High Cycle Fatigue in the Presence of Supplemental Damage," *Fatigue—David L. Davidson Symposium*, TMS, 2002, pp. 107-120.

[14]   J. A. Hines, J. O. Peters, and G. Lütjering, "Microcrack Propagation in Ti-6Al-4V Alloys," *Fatigue Behavior of Titanium Alloys*, TMS, 1999, pp. 15-22.

[15]   NASGRO® Fracture Mechanics and Fatigue Crack Growth Analysis Software, Version 5.2, Southwest Research Institute, San Antonio, Texas, 2008.

[16]   DARWIN®, Design Assessment of Reliability With INspection, Version 6.0, Southwest Research Institute, San Antonio, Texas, 2007.

[17]   D. F. Socie, J. Morrow, J., and W.-C. Chen, "A Procedure for Estimating the Total Fatigue Life of Notched and Cracked Members," *Engineering Fracture Mechanics*, Vol. 11, 1979, pp. 851-860.

[18]   N. E. Dowling, "Fatigue at Notches and the Local Strain and Fracture Mechanics Approaches," *Fracture Mechanics, ASTM STP 677,* American Society for Testing and Materials, 1979, pp. 247-273.

[19]   P. S. Prevéy, M. J. Shepard, and P. R. Smith, "The Effect of Low Plasticity Burnishing (LPB) on the HCF Performance and FOD Resistance of Ti-6Al-4V," 6th National HCF Conference, Jacksonville, 2001.

[20]   P. S. Prevéy, D. J. Hornbach, and P. W. Mason, "Thermal Residual Stress Relaxation and Distortion in Surface Enhanced Gas Turbine Engine Components," *Proceedings of the 17th Heat Treating Society Conference and Exposition and the 1st International Heat Treating Symposium*, ASM, 1998, pp. 3-12.

[21]   SAE International, "Guide to Life Usage Monitoring and Parts Management for Aircraft Gas Turbine Engines," Aerospace Information Report 1872, Rev. A, Warrendale, Pennsylvania, 1998.

[22]   A. Saxena, S. J. Hudak, Jr., and G. M. Jouris, "A Three Component Model for Representing Wide Range Fatigue Crack Growth Rate Behavior," *Engineering Fracture Mechanics,* Vol. 12, No. 1, 1979, pp. 103 115.

[23]   A. Saxena and S. J. Hudak, Jr., "Evaluation of the Three Component Model for Representing Wide Range Fatigue Crack Growth Rate Data," *Journal of Testing and Evaluation*, JTEVA*,* Vol. 8, No. 5, 1980, pp. 113 118.

[24]   W. G. Clark, Jr. and S. J. Hudak, Jr., "Variability in Fatigue Crack Growth Rate Testing," *Journal of Testing and Evaluation*, JTEVA, Vol. 3, No. 6, 1975, pp. 454-476.

[25]   A. H-S. Ang and W. H. Tang, *Probabilistic Concepts in Engineering Planning and Design,* John Wiley, New York, 1975.

[26]   A. Haldar and S. Mahadevan, *Probability, Reliability, and Statistical Methods in Engineering Design,* John Wiley, New York, 2000.

[27]   B. M. Ayyub, and R. H. McCuen, *Probability, Statistics, and Reliability for Engineers and Scientists,* Chapman & Hall, New York, 2003.

[28]   K. Dressler, M. Hack, and W. Kruger, "Stochastic Reconstruction of Loading Histories from a Rainflow Matrix," *Zeitschrift Fur Angewandte Mathematik und Mechanik,* Vol. 77, No. 3, 1997, pp. 217-226.

[29]   D. F. Socie and M. A. Pompetski, "Modeling Variability in Service Loading Spectra," Probabilistic Aspects of Life Prediction, ASTM STP 1450, 2004, pp. 46-57.

[30]   D. W. Scott, *Multivariate Density Estimation,* John Wiley, New York, 1992.

[31]   S. E. Rigdon and A. P. Basu, *Statistical Methods for the Reliability of Repairable Systems,* John Wiley, New York, 2000.

[32]   B. W. Silverman, *Density Estimation for Statistics and Data Analysis*, Chapman & Hall, New York, 1986.

[33]   M. P. Enright, S. J. Hudak, R. C. McClung, and H. R. Millwater, "Application of Probabilistic Fracture Mechanics to Prognosis of Aircraft Engine Components," *AIAA Journal,* AIAA, Vol. 44, No. 2, 2005, pp. 311-316.

[34]   "DARWIN[®] User's Guide," Southwest Research Institute, San Antonio, Texas, 2004.

[35]   J. A. Bannantine, J. J. Comer, and J. L. Handrock, *Fundamentals of Metal Fatigue Analysis,* Prentice Hall, New Jersey, 1990, pp. 193-195.

[36]   A. H-S. Ang and W. H. Tang, *Probabilistic Concepts in Engineering Planning and Design – Vol. II*, John Wiley, New York, 1990.

[37] S. J. Hudak, M. P. Enright, R. C. McClung, H. R. Millwater, A. Sarlashkar, and M. J. Roemer, "Enhanced Prognosis Through Probabilistic Damage Assessment – Final Report," Materials Directorate, Wright Laboratory, Air Force Materiel Command, Wright-Patterson AFB, Ohio, 2002.

[38] "DARWIN® User's Guide," Southwest Research Institute, San Antonio, Texas, 2008.

[39] R. Y. Rubinstein and A. Shapiro, *Discrete Event Systems, Sensitivity Analysis and Stochastic Optimization by the Score Function Method,* J. Wiley & Sons, Chichester, England, 1993.

[40] H.R. Millwater and R. W. Osborn, "Probabilistic Sensitivities for Fatigue Analysis of Turbine Engine Disks," *International Journal of Rotating Machinery,* Vol. 2006, Article ID 28487, 12 pages, 2006, doi:10.1155/IJRM/2006/28487.

[41] "Damage Tolerance for High Energy Turbine Engine Rotors," Advisory Circular No. AC 33.14-1, Federal Aviation Administration, January 8, 2001.

[42] R. Corran, M. Gorelik, D. Lehmann, and S. Mosset, "The Development of Anomaly Distributions for Machined Holes in Aircraft Engine Rotors," Paper GT2006-90843, ASME Turbo Expo, Barcelona, Spain, May 2006.

[43] R. Chandra, L. Dagum, D. Kohr, D. Maydan, J. McDonald, and R. Menon, *Parallel Programming in OpenMP,* Academic Press, San Diego, California, 2001.

[44] W. Gropp, E. Lusk, and A. Skjellum, *Using MPI, Portable Parallel Programming with the Message-Passing Interface,* Second Edition, The MIT Press, Cambridge, Massachusetts, 1999.

[45] Draft DoD Instruction 4151.ee, *Condition Based Maintenance Plus for Materiel Maintenance*.

[46] Draft Condition Based Maintenance-Plus (CBM+) Guidebook, October, 2007.

[47] A. K. Karamchandani, "New Approaches to Structural System Reliability," Ph.D. Thesis, Dept. of Civil Engineering, Stanford University, 1990.

[48] Y.-T. Wu, "Computational Methods for Efficient Structural Reliability and Reliability Sensitivity Analysis," *AIAA Journal,* AIAA, Vol. 32, No. 8, 1994, pp. 1717-1723.

[49] A. P. Berens, P. W. Hovey, and D.A. Skinn, "Risk Analysis for Aging Aircraft, Vol. 1-Analysis, Flight Dynamics Directorate," Wright laboratory, Wright-Patterson AFB, Ohio, WL-TR-91-3066, 1991.

[50] G. R. Leverant, R. C. McClung, H. R. Millwater, and M. P. Enright, "A New Tool for Design and Certification of Aircraft Turbine Rotors," *Journal of Engineering for Gas Turbines and Power,* ASME, Vol. 126, No. 1, 2004, pp. 155-159.

[51] K. Erland, *Quantifying the Benefit of Redundant Fluorescent Penetrant Inspection, Review of Progress in Quantitative Nondestructive Evaluation,* Vol. 8B, 1988, pp. 2221-2228.

[52] T. R. Willemain and P. A. Desautels, "A Method to Generate Autocorrelated Uniform Random Numbers," *Journal of Statistical Computation and Simulation,* Vol. 45, 1993, pp. 23-32.

[53] J. Chen, J., "Using the Sum-Of-Uniforms Method to Generate Correlated Random Variates with Certain Marginal Distribution," *European Journal of Operational Research,* Vol. 167, 2005, pp. 226-242.

[54] S. J. Hudak, Jr., B. R. Lanning, G. M. Light, K. S. Chan, J. A. Moryl, and J. R Pruitt, **"**Embedded Thin-Film Sensor for Crack Detection and Monitoring in Fracture Critical Turbine Engine Components," Paper GT2006-91206, Proc. ASME Turbo Expo 2006, Barcelona, Spain, May 2006.

[55] A. J. A. Mom, and M. D. Raizenne, *AGARD Engine Disc Cooperative Test Programme,* AGARD Report 766, August 1988.

APPENDIX

List of Publications and Presentations
Based in Whole or in Part on Results from the Current Program

Publications:

1. Enright, M. P. and Hudak, S. J. (2007). "Probabilistic mission identification of aircraft engine usage using nonparametric density estimation techniques," Paper GT2006-27176, *Proceedings of the 52nd ASME International Gas Turbine & Aeroengine Technical Congress*, ASME, Montreal, Canada, May 14-17, 2007.

2. Enright, M. P., Hudak, S. J., McClung, R. C., and Millwater, H. R. (2006). "Application of probabilistic fracture mechanics to prognosis of aircraft engine components," *AIAA Journal*, AIAA, 44 (2), pp. 311-316.

3. Enright, M. P., McClung, R. C., and Hudak, S. J. (2006). "Nonparametric risk assessment of gas turbine engine usage," Paper AIAA-2006-49448, *47th AIAA Structures, Structural Dynamics, and Materials Conference*, AIAA, Newport, RI, May 1-4, 2006.

4. Enright, M. P., McClung, R. C., Hudak, S. J., and Francis, W. L. (2006). "Probabilistic treatment of crack formation and growth for gas turbine engine materials," Paper GT2006-90813, *Proceedings of the 51st ASME International Gas Turbine & Aeroengine Technical Congress*, ASME, Barcelona, Spain, May 8-11, 2006. *(**Best Paper Award from ASME Structures & Dynamics Committee**).*

5. Enright, M. P., McClung, R. C., Hudak, S. J., and Millwater, H. R. (2006). "Application of nonparametric methods to rainflow stress density estimation of gas turbine engine usage," Paper GT2006-90780, *Proceedings of the 51st ASME International Gas Turbine & Aeroengine Technical Congress*, ASME, Barcelona, Spain, May 8-11, 2006.

6. Momin, F. N., Millwater, H. R., Osborn, R. W., and Enright, M. P. (2005). "Application of the generalized conditional expectation method for enhancing a probabilistic fatigue design code," Paper AIAA-2005-2146, *46th AIAA Structures, Structural Dynamics, and Materials Conference*, AIAA, Austin, TX, April 18-21.

7. Shook, B., Millwater, H. R., Enright, M. P., Hudak, S. J., and Francis, W. L. (2005). "Impact of continual inspection on cumulative probability of detection," Paper GT2005-68585, *Proceedings of the 50th ASME International Gas Turbine & Aeroengine Technical Congress*, ASME, Reno, NV, June 6-9.

8. Shook, B., Millwater, H. R., Enright, M. P., Hudak, S. J., and Francis, W. L. (2005). "Optimization of inspection frequency and sensitivity in engine health monitoring," Paper AIAA-2005-2215, *46th AIAA Structures, Structural Dynamics, and Materials Conference*, AIAA, Austin, TX, April 18-21.

9. Hudak, S. J., Enright, M. P., McClung, R. C., Francis, W. L., and Millwater, H. R. (2004). "A probabilistic analysis of the benefits of in-service fatigue damage monitoring for turbine engine prognosis," *Proceedings of the 45th Structures, Structural Dynamics, and Materials Conference*, AIAA, Palm Springs, CA, April 19-22, 2004, AIAA Paper AIAA-2004-1953.

10. Hudak, S. J., Lanning, B. R., Light, G. M., Major, J. M., Moryl, J. A., Enright, M. P., McClung, R. C., and Millwater, H. R. (2005). "The influence of uncertainty in usage and fatigue damage sensing on turbine engine prognosis," *Proceedings of the TMS MS&T Symposium on Materials Damage Prognosis*, TMS, New Orleans, LA, Sept. 27-29, 2004.

11. Momin, F., Millwater, H. R., Osborn, W., and Enright, M. P. (2004). "Application of a conditional expectation response surface approach to probabilistic fatigue," *Proceedings of the 9th ASCE Specialty Conference on Probabilistic Mechanics and Structural Reliability*, ASCE, Albuquerque, NM, July 26-28, 2004, paper PMC2004-204, 6 pages.

12. Shook, B., Millwater, Enright, H., M., Hudak, S., Francis, L., "Simulation of Recurring Automated Inspections on Probability-of-Fracture Estimates," submitted to *Journal of Structural Health Monitoring.*

Presentations:

1. Hudak, Jr., S. J., McClung R. C., Millwater H. R., and Enright M. P., "Enabling Life Prediction, Sensing and Probabilistic Analysis Technologies for Enhanced Engine Health Management," Integrated Systems Health Management Conf., Cincinnati, OH Aug. 6-9, 2007.

2. Enright, M. P., McClung, R. C., and Hudak, S. J. (2007). "Probabilistic mission identification of engine usage using nonparametric density estimation techniques," *Propulsion Safety and Affordable Readiness (PSAR) Conference,* San Diego, CA, March 13-15, 2007.

3. Hudak, S. J., Enright, M. P., and Millwater, H. R (2007). "A probabilistic assessment of the benefits of embedded sensors for structural health monitoring and management," *Propulsion Safety and Affordable Readiness (PSAR) Conference,* San Diego, CA, March 13-15, 2007.

4. McClung, R. C., Lee, Y-D., Enright, M. P., and Fitch, S. (2007). "Advances in fracture mechanics methods for propulsion applications," *Propulsion Safety and Affordable Readiness (PSAR) Conference,* San Diego, CA, March 13-15, 2007.

5. Enright, M. P., McClung, R. C., and Hudak, S. J. (2006). "A probabilistic framework for crack formation and growth in gas turbine engine materials," *Propulsion Safety and Affordable Readiness (PSAR) Conference,* Jacksonville, FL, March 28-30, 2006.

6. Hudak, S. J., Lanning, B., McClung, R. C., Light, G., Enright, M. P., Moryl, J., and Pruitt, J. (2006). "Benefits of usage tracking and health monitoring for turbine engine reliability forecasting," *Propulsion Safety and Affordable Readiness (PSAR) Conference,* Jacksonville, FL, March 28-30, 2006.

7. Millwater, H. R., and Osborn, R. (2006). "Probabilistic sensitivities for fatigue analysis of gas turbine engine disks," *Propulsion Safety and Affordable Readiness (PSAR) Conference,* Jacksonville, FL, March 28-30, 2006.

8. Millwater, H. R., Larsen J. and John, Reji, "Probabilistic Sensitivity Modeling of Residual Stress Effects on Life of Engine Component," *Propulsion Safety and Affordable Readiness (PSAR) Conference,* Jacksonville, FL, March 28-30, 2006.

List of Acronyms, Abbreviations, and Symbols

Acronym/ Abbreviation	Description
AFOSR–HCF	Air Force Office of Scientific Research–High Cycle Fatigue
AFRL	Air Force Research Laboratory
AGARD	Advisory Group for Aerospace Research and Development
ASIP	Aircraft Structural Integrity Program
BIC	Bayesian Information Criterion
CBM^+	Condition Based Maintenance Plus
CETADS	Comprehensive Engine Tracking and Diagnostic System
COTR	Contracting Officer's Technical Representative
COV	Coefficient of Variation
CPU	Central Processing Unit
DARWIN®	Design Assessment of Reliability With Inspection
DEN	Double Edge Notch
DoD	Department of Defense
DUST	Dual Use Science and Technology
EDU	Engine Diagnostic Unit
ERLE	Engine Rotor Life Extension
FAA	Federal Aviation Administration
FaNG	Fatigue Nucleation and Growth
FCG	Fatigue Crack Growth
FDR	Flight Data Recorder
FOD	Foreign Object Damage

FPI	Fluorescent Penetrant Inspection
FTC	Full-Throttle Cycle
GUI	Graphical User Interface
HCF	High-Cycle Fatigue
LC	Large Crack
LCF	Low-Cycle Fatigue
LPB	Low-Plasticity Burnishing (a surface treatment)
LSP	Laser Shock Peened
MURI	Multidisciplinary University Research Initiative
N1	Low-Speed Spool
N2	High-Speed Spool
NASGRO	National Aeronautics and Space Administration (NASA) Flaw Grow
OEMs	Original Equipment Manufacturers
OPS	Optimum Point Spacing used in developing weight-function stress intensity factor solutions in steep stress gradients.
PDF	Probabilistic Density Function
PDO	Probability of Detection
PLAs	Power Lever Angles
PMI	Probabilistic Mission Identification
POF	Probability of Fracture
PRDA	Program Research and Development Announcement
(ProDAPS)	Probabilistic Diagnostic and Prognostic System
PTC	Part-Throttle Cycle

RPM	Revolutions Per Minute
RS	Residual Stress
SAE	Society of Automotive Engineering
SC	Small Crack
S-N	stress versus number of cycles to failure
SP	Shot-Peening (a surface treatment)
SwRI	Southwest Research Institute
SWT	Smith-Watson-Topper
TACs	Total Accumulated Cycle(s)
TFS	Thin-Film Sensor
TRMD	Turbine Rotor Material Design
USAF	United States Air Force
UTSA	University of Texas at San Antonio

Symbol	Description
C_i	Pre-exponential constants in multicomponent crack growth law
E	Young's modulus, ksi
F_j	jth fleet
K	Applied stress intensity factor range
K_c	Fracture toughness measured during a fatigue crack growth test under non-plane strain conditions (typically $K_C > K_{IC}$)
K_{IC}	Plane-strain fracture toughness

M_i	ith mission
M_i	Exponents in multicomponent crack growth law
N_{LC}	Cycles of large crack growth
N_{SC}	Cycles of small crack growth
N_f	Cycles to failure
N_f^*	Flights to failure at 100% Design RPM TACs per Flight
N_i	Cycles to initiation
N_i^{SWT}	Cycles to initiation computed from Smith-Watson-Topper criterion
N_{tn}	Cycles to "true" crack nucleation
P_f	Probability of Failure
R	Load (or stress) ratio used to characterize fatigue loading
S/N	Signal-to-noise ratio
S_θ	Confidence bound
a	Crack size
a_0	Small fatigue crack parameter
da/dN	Fatigue crack growth rate, in./cycle
f_{M+G}^i	Bayesian updated PDF for next flight (input to model)
f_M^{i+1}	Model PDF for $i+1$ growth cycle
f_S^i	Sensor PDF for flight i
h	Kernel window width
n	Number of data points

ΔK Applied stress intensity factor range

ΔK_{eq} Equivalent stress intensity factor range that accounts for increased crack-driving force of small fatigue cracks

ΔK_{th} Fatigue threshold stress intensity factor range, ksi√in.

$\Delta \sigma_e$ Fatigue endurance limit in a smooth specimen

Φ Standard normal cumulative distribution function

$\varepsilon_{a,max}$ Maximum principal strain amplitude

μ Mean value of a distribution

σ Standard deviation of a distribution

σ_{max} Maximum normal stress on the critical plane of $\varepsilon_{a,max}$

$\dfrac{\partial \sigma_Z}{\partial \theta}$ Probabilistic sensitivity of random variable θ with respect to uncertainty in mean σ of the response Z

$\dfrac{\partial \mu_Z}{\partial \theta}$ Probabilistic sensitivity of random variable θ with respect to uncertainty in mean μ of the response Z